CZECH TECHNICAL UNIVERSITY IN PRAGUE

Faculty of Nuclear Sciences and Physical Engineering

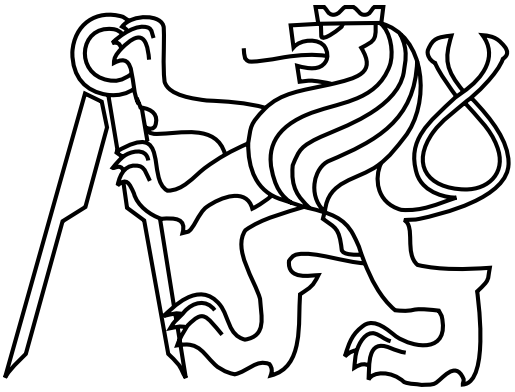

DOCTORAL THESIS

Influence of Laser Shock Peening on corrosion resistance and stress corrosion cracking

Prague 2022 Jan Kaufman

Bibliografický záznam

Autor:	Ing. Jan Kaufman České vysoké učení technické v Praze Fakulta jaderná a fyzikálně inženýrská Katedra fyzikální elektroniky
Název práce	Vliv laserového vyklepávání na korozní odolnost a korozní praskání
Studijní program:	Aplikace přírodních věd
Studijní obor:	Fyzikální inženýrství
Školitel:	doc. Ing. Ladislav Pína, DrSc. České vysoké učení technické v Praze Fakulta jaderná a fyzikálně inženýrská Katedra fyzikální elektroniky
Školitel specialista:	Professor Seetha Ramaiah Mannava University of Cincinnati College of Engineering and Applied Science Department of Mechanical and Materials Engineering Cincinnati, Ohio, Spojené státy americké
Akademický rok:	2021/2022
Počet stran:	161
Klíčová slova:	námořní hliníkové slitiny, laserové vyklepávání, laserové vyklepávání bez ochranné vrstvy, zcitlivění, mezikrystalická koroze

Bibliographic entry

Author:	Ing. Jan Kaufman
	Czech Technical University in Prague
	Faculty of Nuclear Sciences and Physical Engineering
	Department of Physical Electronics
Title	Influence of Laser Shock Peening on corrosion resistance and stress corrosion cracking
Degree programme:	Application of Natural Sciences
Field of study:	Physical Engineering
Supervisor:	doc. Ing. Ladislav Pína, DrSc.
	Czech Technical University in Prague
	Faculty of Nuclear Sciences and Physical Engineering
	Department of Physical Electronics
Supervisor specialist:	Professor Seetha Ramaiah Mannava
	University of Cincinnati
	College of Engineering and Applied Science
	Department of Mechanical and Materials Engineering
	Cincinnati, Ohio, United States of America
Academic year:	2021/2022
Number of pages:	161
Key words:	marine aluminium alloys, Laser Shock Peening, Laser Peening without Coating, sensitization, intergranular corrosion

Abstrakt

V této práci jsme využili technologie laserového vyklepávání k řešení problémů mezikrystalické koroze (IGC), mezikrystalického korozního praskání (IGSCC) a korozní únavy (CF), které ovlivňují hliníkové slitiny bohaté na hořčík využívané v námořním průmyslu. Konkrétně se jednalo o zcitlivěnou hliníkovou slitinu 5083-H116, která byla zpracována technologií laserového vyklepávání jak s (LSP) tak bez ochranné vrstvy (LPwC). Po zpracování byla slitina podrobena sérii mechanických a elektrochemických zkoušek. LSP and LPwC do slitiny vložily hluboká zbytková napětí, která byla doprovázna zvýšením tvrdosti. Modifikovaný test s kyselinou dusičnou na úbytek hmotnosti (NAMLT) ukázal, že LSP má vliv na stupeň zcitlivění materiálu, a že tento efekt přímou úměrou souvisí s mírou protváření a plastickou deformací materiálu. Elektrochemické zkoušky odhalily, že LPwC zpracování vytváří na povrchu materiálu unikátní přetavenou vrstvu skládající se z modifikované tenké oxidické vrstvy, která vznikla během tepelné interakce laserových pulsů s povrchem materiálu bez ochranné vrstvy. Bylo ukázáno, že tato vrstva chrání materiál proti IGC v mořském prostředí. V případě LSP s ochranou vrstvou se přetavená vrstva nevytvořila. CF zkoušky ukázaly silné zlepšení meze únavy zcitlivěného materiálu po zpracování laserem. Toto zlepšení bylo nejpatrnější pro LPwC proces aplikovaný pod vodou. Tahové zkoušky (SSRT) ukázaly silnou míru protváření materiálu po zpracování, nicméně vliv na IGSCC nebyl jasně prokazatelný.

Abstract

In this work, the problems of intergranular corrosion (IGC), intergranular stress corrosion cracking (IGSCC) and corrosion fatigue (CF) on Mg-rich marine grade aluminium alloys were addressed using the Laser Shock Peening (LSP) technology. Specifically, LSP with and without protective coating (LPwC) was applied to sensitized AA5083-H116 followed by electrochemical analysis and mechanical testing. Both LSP and LPwC treatments imparted deep residual stresses in the material accompanied by increased hardness. Modified Nitric Acid Mass Loss Test (NAMLT) showed that LSP treatment does effect the degree of sensitization and that the effect is correlated with the amount of plastic deformation induced in the material. Electrochemical testing revealed that that the LPwC treatment produced a unique recast surface layer composed of a modified oxide film created during laser pulse interaction with the surface when no coating was applied. This layer was absent in the LSP treatment and was shown to prevent IGC in sea water environment. CF testing showed greatly improved fatigue strength of sensitized samples after both LSP and LPwC treatments with strongest improvement for LPwC underwater treatment. Slow strain rate test (SSRT) showed strong strain hardening of samples after treatment although the direct effect on IGSCC was not clear.

Acknowledgements

I would like to express my deepest gratitude to my supervisor specialist and mentor professor Seetha Ramaiah Mannava from University of Cincinnati who fully introduced me to the field of Laser Shock Peening and helped me to overcome the first out of many hurdles to come. The same gratitude goes to professor Vijay K. Vasudevan from University of North Texas who helped a great deal to make my stay in the states full of happy memories and always provided me with support and advice whenever needed. Similarly, I would like to thank professor Matthew A. Steiner who provided me with great insights regarding sensitized aluminium alloys and helped me with corrections and paper publishing.

My thoughts and gratitude also go to my former supervisor Dr. Kálal from the Czech Technical University in Prague who passed away unexpectedly before this thesis could be finished. I would also like to thank Dr. Ladislav Pína from the Czech Technical University in Prague who was kind enough to take after Dr. Kálal and became my supervisor for the last two years of my doctoral degree. My gratitude also goes to the whole HiLASE team who provided me with great opportunities and conditions to work on my thesis.

And finally, I would like to thank my family and friends for providing with unlimited emotional support throughout the years and who never stopped pushing me to finish the work.

Contents

Introduction

Laser Shock Peening (LSP) is a technology that utilizes high-energy laser pulses to create localized plastic deformation on metallic surfaces. It bears resemblance with classical peening process which uses ball-peen hammers to harden metallic surfaces by impact. The nature of the impacts in LSP, however, is very different. In a typical LSP setup, nanosecond laser pulses irradiate metal parts covered with thin water layer to create rapidly expanding plasma. The expansion is confined by the water layer against the surface which leads to extreme pressure rise (~GPa) [1]. The locally generated pressure then sends shock waves inside the underlying material which causes its plastic deformation and compressive residual stresses are created as a result. Prior to the laser impact, the surface is additionally covered by a black vinyl tape or paint to protect it against heat effects associated with the laser absorption. LSP is therefore sometimes considered a cold-working process and holds a special spot among other laser processing technologies which often revolve around direct material heating or ablation. The generated stresses stay in the surface layer permanently, even after the external force is removed. Compressive residual stresses can be extremely beneficial to numerous mechanical applications, most noticeably in preventing crack related failures often associated with material fatigue.

Although the principle mechanisms and potential benefits of LSP have been known since 1970s [2], it took more than 20 years for the first industrially viable application to emerge. In the 1990s, the U.S. Air force faced a serious problem concerning foreign object damage (FOD) affecting fatigue life of fan engine blades of the Rockwell B-1B Lancer bomber [3]. Unable to address the problem with conventional methods such as Shot Peening (SP), General Electric tested the LSP process which uniquely managed to solve the problem and industrialized production of the engine fan blades commenced in 1998. After this major breakthrough, more applications followed although most of them were narrowly focused on aerospace industry and some niche cases in nuclear industry [4]. The major obstacle of the LSP technology to spread into other application areas since its inception has always been its high cost. A much cheaper although less efficient technology of shot peening was used instead and many problems were left unresolved. However, due to the rapid development of laser systems in the last decade, new powerful and cheap nanosecond laser sources are now commercially available. This opened new economically viable areas for the LSP technology. One such area is the marine industry which has for some time been trying to implement high-strength light-weight aluminium structures to lower fuel costs and increase payload capacity without losing structural integrity. The aluminium alloys primarily used are the 5xxx series with increased magnesium content and high corrosion resistance. However, after years of service, ships manufactured from these strengthened aluminium alloys encountered a new problem in the form of material weakening (sensitization) as a result of long-term exposure to increased temperatures (as low as 50 °C)[5]. It turned out that combined with the aggressive salt environment of the sea water, this can lead to intergranular corrosion (IGC) and subsequent inter-

granular stress corrosion cracking (IGSCC) or corrosion fatigue (CF) which can result in catastrophic structural failures. This work addresses these newly encountered problems using the LSP technology with focus both on the mechanical and electrochemical effects.

In chapter 1, the problem of sensitization, IGSCC and CF in the 5xxx aluminium series is investigated. The sensitization process is described in detail and clear link to the IGC is established. The sensitization process is further quantified and various factors affecting the degree of sensitization (DoS) are analysed. Lastly, 3 approaches (metallurgical, electrochemical and mechanical) toward preventing IGSCC and CF are outlined and discussed in relation to LSP.

Chapter 2 focuses on the LSP technology itself. The process physics is described in depth and a simplified analytical model is presented which links the laser pulse power density to the residual stresses generated. The second part of the chapter explores the influence of various laser parameters and processing parameters which will be utilized in the experimental part.

In chapter 3, the experimental hardware along with experimental methods and material used are presented. The LSP process is discussed from the experimental standpoint where a synchronization loop between the laser systems and robotic arm movement is maintained to ensure correct patterning strategies. An overview of the various diagnostics methods used such as X-ray diffractometry, electrochemical analysis, slow strain rate testing (SSRT) and fatigue testing is provided.

Chapter 4 presents the experimental results with selected aluminium alloy 5083. First, a parametric study to determine optimal processing parameters is shown. A set of experimental parameters comprising 3 distinct peening scenarios is selected and applied for the rest of the tests. Corrosion behaviour of AA5083 is investigated in terms of IGC and an extensive electrochemical analysis is provided. Finally test samples are subjected to SSRT and CF tests followed by fracture and microstructure analysis.

Motivation and goals of the work

The 5xxx series aluminium alloys are high strength-to-weight ratio, weldeable materials with excellent general corrosion resistance. These alloys are for example used extensively throughout the U.S. Navy fleet, ranging from deck elevators at the Nimitz class aircraft carrier to serving as a primary structural material for the Independence-class littoral combat ship [5]. The 5xxx aluminium series can also be referred to as aluminium-magnesium alloys due to high magnesium content which is responsible for the enhanced strength.

Despite their initial good corrosion resistance, it has been established that alloys containing more than 3.5% of Mg can become sensitized when exposed to elevated temperature for prolonged periods of time. The temperatures required can be as low as <50 °C when a sufficiently long time period is considered (years) [6]. This can be a common occurrence in marine service environment where in hot climate, the temperature of a ship deck exposed to direct sunlight can reach over 70 °C. A sensitized material becomes susceptible to localized corrosion, particularly intergranular corrosion (IGC) which can lead to mass loss through grain fall-off and also to intergranular stress corrosion cracking (IGSCC). Between 2001 and 2002, for example, over 200 commercial ships made of AA5083 were found to be susceptible to IGC and needed to have their hulls and other structures completely replaced [7]. In more recent years, the U.S. Navy has reported over 1 meter long cracks in Ticonderoga combatant ship superstructures made of AA5456 that were attributed to IGSCC (Fig. 1). On one of the ships, the discovered cracks were severe enough that the ship had to be temporarily put out of service for a $14 million extend repair period [8].

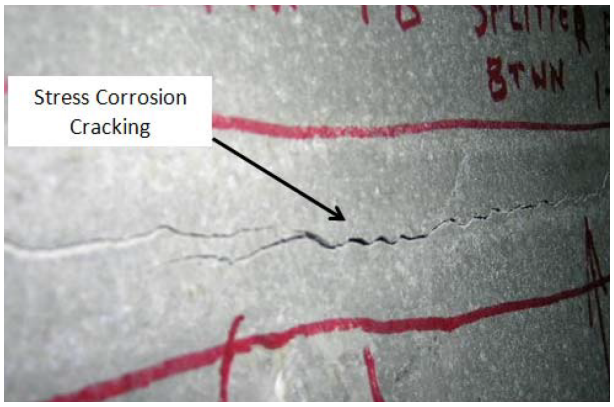

Figure 1: Stress corrosion crack generated in the Ticonderoga class cruiser AA5456 superstructure [9].

Overall, more than 3000 cracks have been found across the whole Ticonderoga class fleet [10]. Fig. 2 shows an upward trend in the average number of cracks found per ship

inspection, covering the time period of 1990 – 2015. As of 2015, more than 6000 cracks have been documented in ship reports. It is important to note that these numbers include fatigue cracks as well, however, most of the cracks have been identified as due to SCC [5].

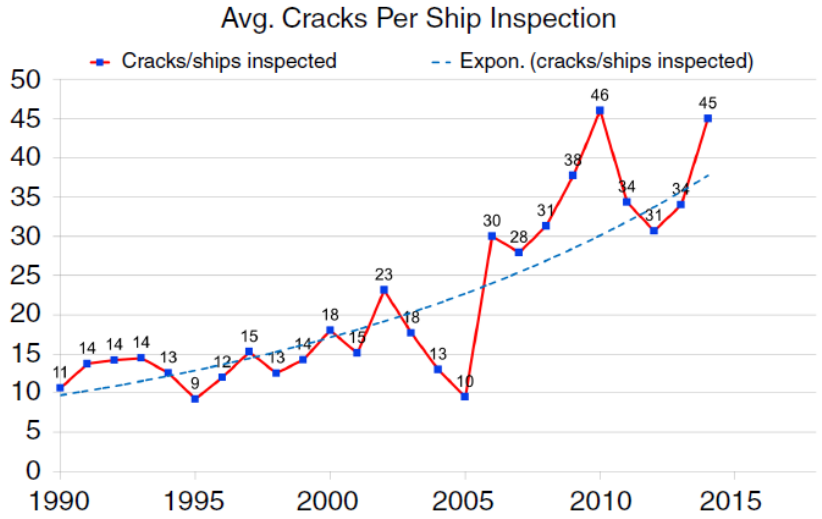

Figure 2: The average number of cracks identified per ship inspection between years 1990-2015 [5].

Several approaches were tried to address the problem, mainly through metallurgy and electrochemical inhibition but the results were unsatisfactory. In this work, we investigate the stress removal option where tensile stresses in critical areas are replaced with compressive stresses using LSP. While the positive effects of LSP on SCC [11, 12, 13, 14] are well documented using other materials, studies conducted both with [15, 16] and without protective coating [17, 18] indicate that LSP could also have a direct positive effect on corrosion behaviour. The main corrosion mechanism in these studies, however, is pitting. Very little to no investigation has been carried out when it comes to the influence of LSP on IGC which is the driving force behind IGSCC. This work will attempt to investigate both the mechanical effects of LSP on the marine grade aluminium alloys as well as the corrosion effects with a focus on IGC and IGSCC . The work is further expanded to cover CF of AA5083 in aggressive marine environments [19, 20, 21] since LSP has also been shown to positively influence CF in other materials [22, 20, 21]. The fatigue loading in marine environment is introduced by wind and wave motion, ship machinery vibrations, thermal expansion, and contraction and operational loading events [23, 24].

Chapter 1

Stress Corrosion Cracking and Corrosion Fatigue of 5xxx series aluminium alloys

1.1 Mechanism of Stress Corrosion Cracking

Stress corrosion cracking (SCC) or environment induced cracking is classified as catastrophic form of corrosion, as the detection of fine cracks that are associated with it can be very difficult and the damage not easily predicted. Experimental SCC data is therefore notorious for a wide range of scatter. In order for SCC to occur, three conditions must be met simultaneously: susceptible material, specific corrosive environment and tensile stresses. The process is sometimes described as synergistic because only the combined effect of all the required mechanical and chemical forces results in crack propagation (Fig. 1.1) whereas neither factor acting independently or alternatively would bring the same effect [25].

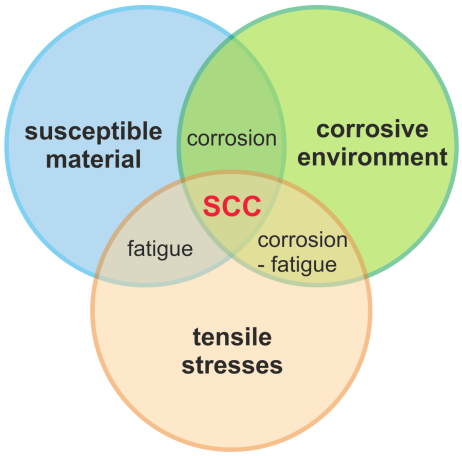

Figure 1.1: Mechanical and chemical factors necessary for SCC to occur.

SCC often progresses rapidly, and is more common among alloys than pure metals. As for the environment, the process tends to be highly chemically specific. Alloys will undergo SCC when exposed to only a small number of chemical environments such as stainless steels in various halide solutions and copper alloys in ammoniacal solutions. In case of aluminium, well known specific environments include water vapour, aqueous

solutions, organic liquids and liquid metals. Common alloys with corresponding SCC favourable environments are summarized in Table 1.1.

Alloy	Enviroment
Carbon steels	Hot nitrate, hydroxide, carbonate/bicarbonate solutions, anhydrous liquid ammonia, aqueous amines, molten Na-Pb alloy, liquid Li
High-strength steels	Aqueous electrolytes (containing H_2S)
Ferritic steels	Hydroxide, nitrate, phosphate solutions, anhydrous liquid ammonia, high temperature water, CO and CO_2 in H_2O, CS_2 in H_2O
Martensitic steels	Aqueous solutions of hydroxides, nitrates, sulphides, and chlorides
Austenitic stainless steels	Chlorides (in liquid water and steam), bromides, hydroxides, polythionic acids, ($H_2S_xO_y$), sulphurous acid, Cl^- + H_2S (aqueous)
Nickel alloys	High-purity steam, caustic soda solutions, polythionic acids, chlorides, fluorides, HF
Copper and copper alloys	Ammoniacal solutions (ammonia and amines), nitrites, nitrates, steam, liquid Li, Hg, Bi
Aluminium alloys	Chlorides, bromides and iodides in water, high-purity hot water, CCl_4; liquid Hg, Ga, Zn
Titanium alloys	Chlorides, bromides and iodides, red fuming nitric acid, anhydrous N_2O_4, methanol-halides, HCl, CCl_4; liquid Hg

Table 1.1: SCC environments for commonly used alloys. Adapted from [25].

The stresses required to cause SCC are small, below the macroscopic yield stress. Another definition narrowing of the SCC process comes from the fact that the tensile stresses are static. If the load varies over time (cyclic loading), the term corrosion fatigue (CF) is used instead. Another difference is that in the case of CF, combinations of environmental conditions and metal types are not specific as in the case of SCC. What makes SCC especially dangerous is that the stresses can be well within the design ranges and most of the surface remains unattacked wile fine cracks penetrate into the material. Furthermore, tensile stresses may be residual or applied. Tensile residual stresses are formed as a result of inhomogeneous deformation in materials and usually involve heat treatment or other fabrication methods where cold deformation is utilized such as bending and drawing.

SCC occurs in 3 stages:

1. Initiation or incubation
2. Spreading
3. Failure or arrest

The crack typically initiates at a surface flaw, serving as a stress amplifier, and then selectively propagates along a path of higher corrosion susceptibility. Flaws can either pre-exist due to poor manufacturing procedures or can develop at locations of discontinuities or high stress concentration such as grooves or corrosion pits. Once a crack is initiated, it will grow as long as

$$K_I \geq K_{ISCC} \tag{1.1}$$

where K_I denotes the stress intensity factor and K_{ISCC} the SCC resistance parameter. K_{ISCC} is a material and environment dependent property and can be acquired through experimental fracture testing of materials in specified environments. K_I is a function of the crack length and its calculation requires knowledge of the stress field at the crack tip

and the crack length at any given time. In most practical cases, closed-form solutions for calculation of K_I are not available due to non-uniform stress distributions and complicated geometries and numerical algorithms such as finite element modelling need to be employed.

The most common active path for the crack to spread along is the grain boundary which is described as intergranular stress corrosion cracking (IGSCC). The cracks generally propagate perpendicular to the applied stress and its morphology can very from a single crack to a branching formation reminiscent of a river delta. A typical crack created by IGSCC is shown in Fig. 1.2a. Transgranular SCC where the cracking advances without preference for boundaries is also possible but it is more rare [26] (Fig. 1.2b). Final macroscopic fracture will occur when the crack has reached a critical crack length denoted by K_{IC} and thus

$$K_I \geq K_{IC} \tag{1.2}$$

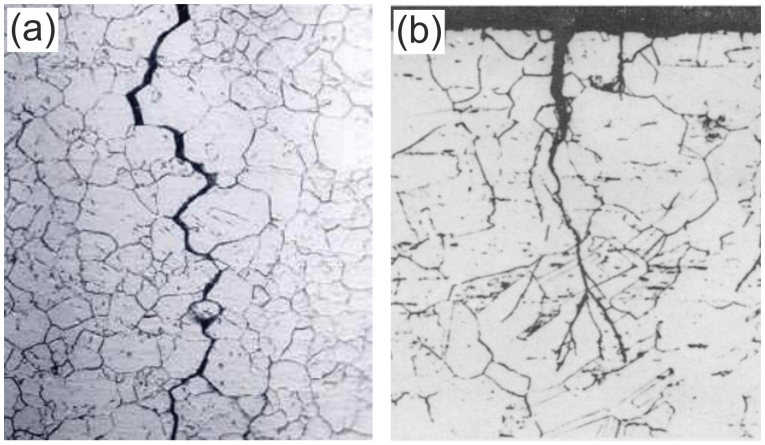

Figure 1.2: (a) Intergranular stress corrosion crack of an Inconel heat exchanger tube [27] and (b) transgranular stress corrosion crack in type 304 austenitic stainless steel [28].

From the time of initiation of the crack, the failure can occur within minutes to several years, depending on the specific conditions. From the macroscopic point of view, SCC fractures have brittle appearance which is a result of brittle phase formation at the crack tip and its periodic rupture during the crack propagation. Due to the brittle nature of the crack, the fracture under stress is sudden and rapid.

1.2 IGSCC in marine environment

The operating environment of Navy ships readily provides 2 of the conditions necessary for SCC to take place: (1) corrosive environment in the form of salt water and (2) tensile loading, both external and internal. External stresses are represented by structural loading due to wind, the hogging and sagging motion of a ship cruising through waves, operation of machinery, payload and thermal loading which all together create a dynamic stress environment. The internal loading is caused by tensile residual stresses resulting from thermal processing during ship manufacture and fit up. A common place for tensile residual stresses to develop is around welds, bolts, riveted joints, notches and crevices. In case of welds, for example, as the weld area is heated and cooled, its expansion and contraction is limited by the bulk of the surrounding unaffected material,

leaving the material in the heat affected zone (HAZ) in tension. The third SCC condition, susceptible material, is achieved through a sensitization process when the initially corrosion resistant aluminium alloy undergoes critical microstructural changes that leave it vulnerable to IGC.

The 5xxx aluminium series can also be referred to as aluminium-magnesium alloys due to high magnesium content which is responsible for the enhanced strength. The specific weight content of magnesium in currently used 5xxx alloys, along with their typical applications is listed in Table 1.2.

Alloy	Mg content (wt%)	Application
5052	2.2-2.8	fuel lines, ducts
5454	2.4-3.0	uptake trunks
5086	3.5-4.5	shapes, stiffeners
5083	4.0-4.9	hulls
5456	4.7-5.5	deck plates

Table 1.2: Examples of selected commercial 5xxx aluminium alloys in service. Adapted from [5].

The high Mg content is of critical importance. In heat unaffected material, Mg atoms exist in the form of a solid solution (α-phase) distributed uniformly across the aluminium matrix where the atoms act as obstacles to dislocation movement which is what gives the alloys their characteristic high strength. When the material is exposed to elevated temperatures for prolonged periods of time, however, the Mg atoms diffuse from the matrix to low energy sites such as the grain boundaries. Eventually, solid state β-phase precipitates (Mg_2Al_3) at the grain boundary are formed and the material becomes sensitized (Fig. 1.3). The general consensus is that the driving force for the β-phase precipitation becomes appreciable when the Mg content is more than 3.5 wt% [29].

When the β-phase is formed, the matrix becomes electrochemically heterogeneous. The electric potential of the grain boundaries, specifically the β-phase precipitates, is lower (-0.95 V_{SCE}) than the electric potential of the alloy (-0.75 V_{SCE})[31]. An electrochemical reaction takes place in the near neutral salt solutions of sea water where the grain boundary acts as an anode to the adjacent magnesium depleted cathodic regions, causing dissolution of the anodic precipitates.

Under normal fresh water conditions with pH from 4.0 to 8.5, aluminium naturally forms a protective, passivating oxide layer on its surface. The layer is self-renewing meaning that when the thin film is damaged by abrasion or other means, it is repaired rapidly. In salt water environment of 3.5% NaCl, however, the effectiveness of the passivating layer is lowered due to the chloride ions (Cl^-) which attack the passive film [32, 33] and hinder its reformation [34], providing more initiation sites for the corrosion to take place. The reaction generates hydroxide ions, increasing local pH, causing further removal of the protective oxide layer and exposing more area to more anodic dissolution. The dissolution happens in the form of matrix trenching and cavity formation of β-phase pitting surrounding the intermetallic particles. The β-phase dissolution causes local acidification and high chloride concentration inside the pits which further decreases the breakdown potential and increase the dissolution rate. Eventually, the corrosion spreads to neighbouring precipitates resulting in a network of corroded grain boundaries across the surface (Fig. 1.4). The IGC propagation rate may vary with pene-

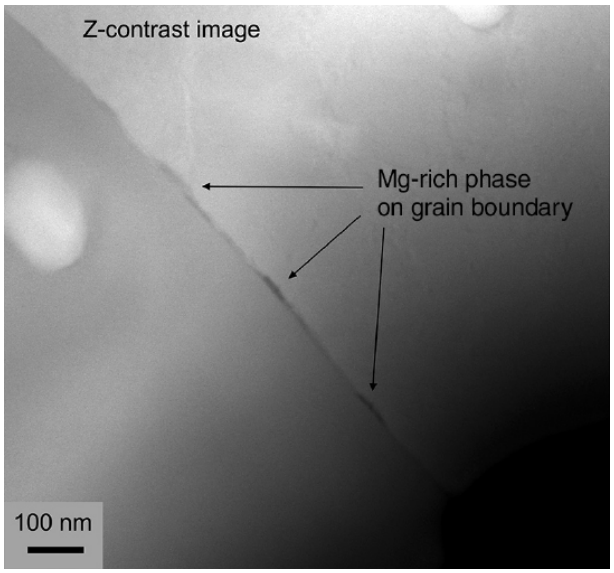

Figure 1.3: TEM image showing thin (<10 nm) and discrete β-phase in a field retrieved sample of AA5083 exposed to low temperatures (<50 °C) for period of 40 to 50 years [30].

tration depth and local chemical conditions. At some point, reduction in the IGC propagation rate or stifling occurs due to further chemical unbalancing until the corrosion stops completely which leads to IGC arrest.

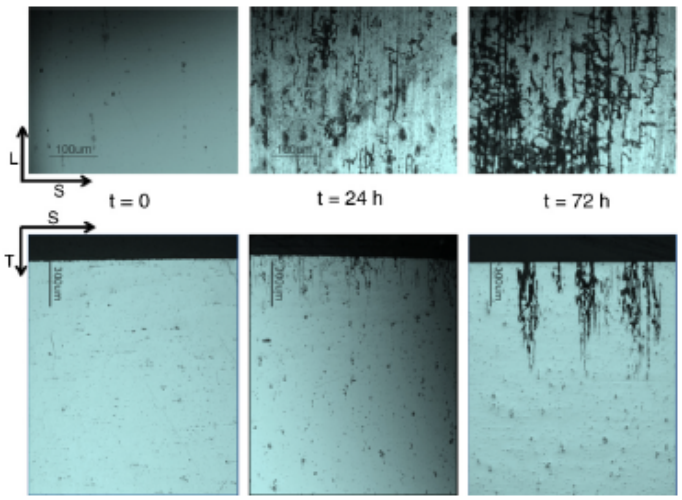

Figure 1.4: Surface (top) and in-depth IGC spreading (bottom) for an AA5083-H131 over period of 72 hours [35].

The IGC is primarily driven by chemical forces and thus no stresses are required for the corroded network to develop. A special type of IGC associated with aluminium alloys is called exfoliation which occurs on elongated grain boundaries where IGC spreads parallel to the surface along selective subsurface paths. The corrosion products that form have a greater volume than the volume of the parent metal and the increased volume forces the material layers apart, causing the material to delaminate or exfoliate (Fig. 1.5).

However, having tensile stresses present during IGC provides the optimal environment for IGSCC to develop. The cracks spread along the corroded grain boundaries, perpendicular to the direction of stresses. When the crack reaches a critical length, fracture occurs. The IGSCC mechanism is depicted in Fig. 1.6.

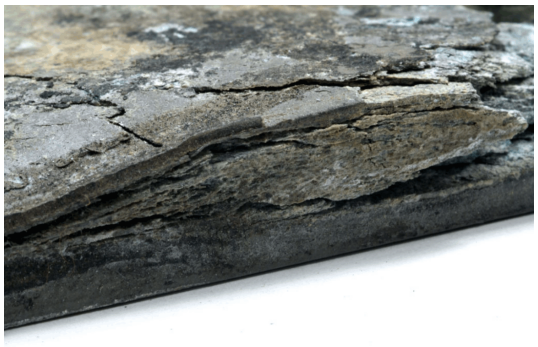

Figure 1.5: Exfoliation in aluminium sheet [36].

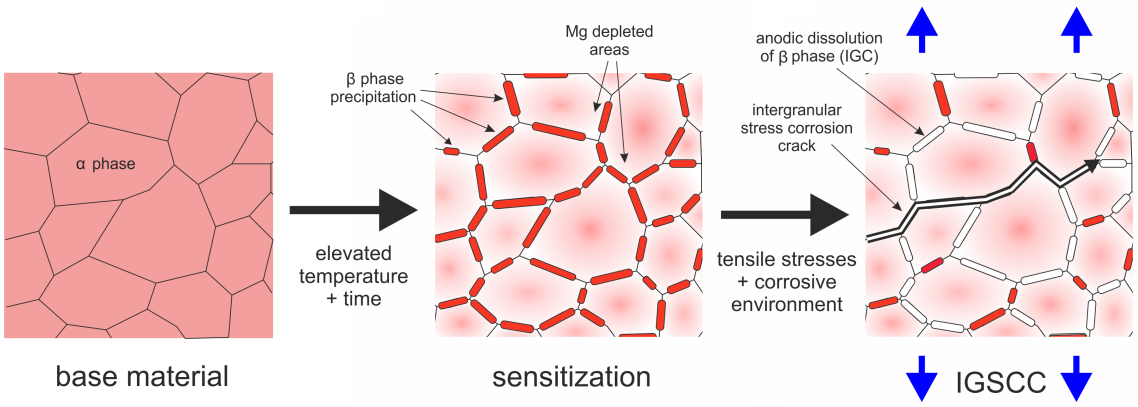

Figure 1.6: Schematic representation of the IGSCC process in Mg rich aluminium alloy.

While the continuity of the β-phase is an important factor in the crack propagation [6], a fully corroded interconnected network is not necessary when tensile stresses are present. Instead, the β-phase forms a nearly continuous network through the sensitized specimen. The β-phase precipitates themselves are expected to remain discrete though densely populated under the particular sensitization conditions used, each sensitizing a region of the boundary much larger than their direct footprint [37]. Crane et al. [38] proposed a hydrogen environment assisted cracking mechanism (HEAC) under which cracks propagate despite gaps present between the β-phase anodic dissolution sites (Fig. 1.7). An appreciable amount of hydrogen is produced at the crack tip as a product of hydrolysis of water due to the presence of Al^{3+} and Mg^{2+} atoms released during the β-phase (Mg_2Al_3) anodic dissolution [39]. The abundance of hydrogen and low pH then triggers a low rate dissolution of the interconnecting α-phase regions [40]. More hydrogen is produced in hydrolysis and pH is lowered even further. The hydrogen then gets trapped in the concentrated stress field around the crack tip, causing local embrittlement and facilitating the crack growth.

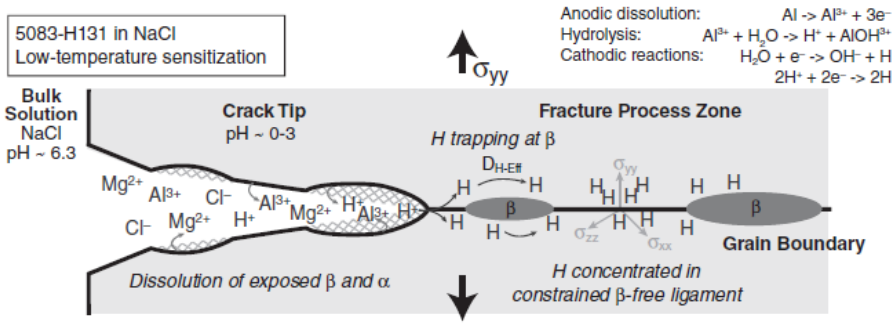

Figure 1.7: Hydrogen assisted cracking to breach cracks in discontinuous β-phase precipitated on the grain boundary [38].

1.3 Degree of sensitization

The degree of sensitization (DoS) or susceptibility to IGC is measured using the nitric acid mass loss test (NAMLT) as defined by the ASTM G67 standard [41]. Samples of defined dimensions are submerged in concentrated nitric acid for a period of 24 hours at fixed temperature of 30 °C. As the IGC spreads, the exposed sample faces experience grain fall-off which translates into a weight loss at the end of the test. The G67 standard defines Al-Mg alloys as resistant when DoS < 15 mg/cm^2, as intermediate for 15 mg/cm^2 < DoS < 25 mg/cm^2 and as susceptible for DoS > 25 mg/cm^2 (Fig. 1.8). In the intermediate region, the sensitization needs to be determined by metallographic inspection. The measured DoS depends on several factors such as the alloy composition, sensitization time and temperature, microstructure and thermomechanical treatment. All of the numerous factors are significant and largely cross-related which makes it difficult to separate their effects on the sensitization process. One should therefore be careful when drawing conclusions as more than just one factor could contribute to observed results.

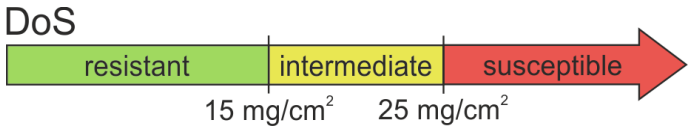

Figure 1.8: 5xxx series aluminium alloys susceptibility to IGC as defined by G67 ASTM standard.

The empirical relationship between microstructure and IGSCC shows that higher DoS values as measured by the NAMLT test result in increased IGSCC velocities [38, 42]. The NAMLT, however, is viable for laboratory conditions only. In service conditions (e.g. shipboard) where samples of specific dimensions cannot be independently obtained, other in-situ methods have to be used. One such method has been developed by ElactraWatch, Inc. in the form of a portable DoS probe that can run non-destructive measurements in service conditions (Fig. 1.9). The probe uses diluted 2% nitric acid solution and measures electric current from the anodic dissolution of β-phase in the probed surface. The current is then correlated with DoS. The probe can also perform in-situ microscopic observation of an etched surface and determine whether sensitization took place. This method, however, is qualitative only and does not provide any DoS value.

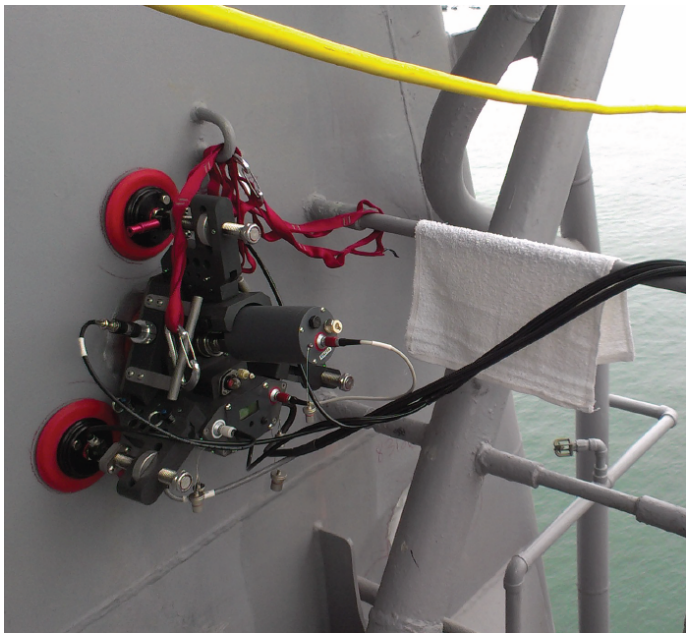

Figure 1.9: Portable DoS probe for in-situ non-destructive measurements in service environment [43].

1.3.1 Time and temperature of senzitization

A simplified way to estimate the sensitization damage of the 5xxx aluminium series is to quantify the amount of β-phase precipitation. From a metallurgical perspective, the growth of a precipitate at a grain boundary is a diffusional-transformation process where thermodynamic and kinetic forces compete with each other and where temperature plays a crucial role. In equilibrium, the β-phase volume fraction decreases with rising temperature up to a point where all the precipitates are dissolved into a homogeneous solid solution. In fact, thermal stabilization of sensitized alloys at temperatures below the solvus line (<220 °C) is one of the possible ways to prevent IGC in Al-Mg alloys and will be discussed more in detail in section (1.4.1). On the other hand, increased temperature can lead to faster diffusion kinetics, thus promoting the precipitation at grain boundaries. The competition between the driving force for precipitation (thermodynamic) and diffusion (kinetics) leads to a local maximum in DoS within a certain range of sensitization temperatures. The variation of DoS with time and temperature of sensitized AA5083 collected over a large range of experimental data can be seen in Fig. 1.10.

The temperatures range from 50 °C to 225 °C from several hours up to many years of sensitization in service conditions. The data are divided into 4 distinct regions with regards to their IGC susceptibility:

(i) **Immune** - the equilibrium β-phase volume fraction is high but the diffusion kinetics of Mg and thermal driving forces are low. The segregation of Mg would require much longer time for the material to become sensitized.

(ii) **Immune** – in spite of high diffusion rates and thermal forces, the equilibrium β-phase volume fraction near the solvus temperature is very low which leads to very low DoS.

(iii) **Susceptible** – the balance of kinetic and thermodynamic factors in this region,

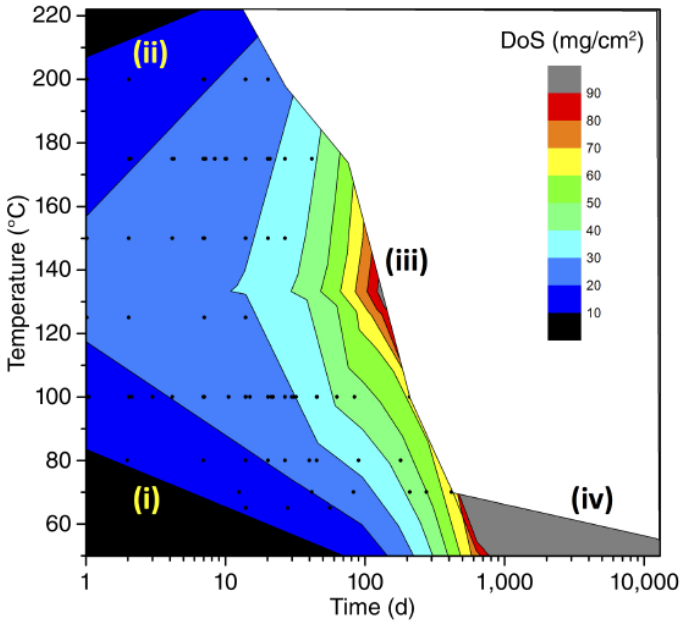

Figure 1.10: A graphical compilation of AA5083 DoS data collected via NAMLT test as a function of sensitization time and temperature [6].

where both the β-phase volume fraction and diffucion rate are considerable but not at their maximum, results in a local DoS maximum and susceptibility to IGC.

(iv) **Highly susceptible** – this region has the highest DoS and represents field retreived specimens sensitized at low temperatures of <60 °C. The exceptionally high DoS shows that despite the very low diffusion rate at this temperature range a severe condition can be achieved when enough time (years) is taken into consideration. The β-phase volume fraction can be as much as several time higher at 50 °C than that at 200 °C.

Apart from the DoS, it appears that the temperature of sensitization also influences the thickness of the β-phase at the grain boundaries. Holtz et al. [20] investigated the β-phase thickness in AA5083-H131 as a function of temperature and concluded that the precipitate thickness decreases with decreasing temperature, despite longer time exposures for lower temperatures (Fig. 1.11). This effect cannot be accounted for by bulk diffusion, since that would lead to the opposite result, and rather suggests that grain boundary diffusion becomes more dominant at lower temperatures which would explain the thinner β-phase. The observation also fits with well with field retrieved AA5083 specimen that displays similarly thin β-phase [30].

To predict the thickness of β-phase along the grain boundary, Goswami and Holtz proposed a phenomenological model that is based on the solute diffusion within the grain [44, 45]. Even more recently, the JMAK model (based on the Johnson-Mehl-Avarami-Kolmogorov theory) that links the DoS to thermal exposure has been proposed. Unlike other models, the JMAK model establishes a direct connection between the DoS and the coverage of grain boundary with β-phase which seems to be an important factor in the IGC spreading. Steiner and Agnew [46] make an assumption that the correlation between the DoS and boundary coverage in the JMAK model is linear (Fig. 1.12) which leads them to good experimental fit for sensitized AA5083 with DoS below 25 mg/cm^2. Studies on

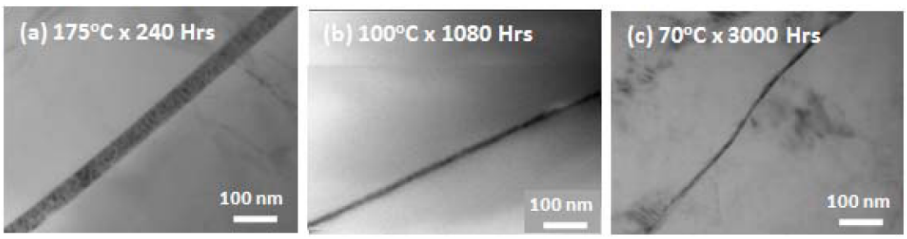

Figure 1.11: Thickness of β-phase precipitate as a function of sensitization temperature and time in AA5083-H131 [20].

β-phase morphology and and distribution show that in high DoS material, 50% of grain boundaries become almost completely covered with β-phase while a low DoS material will only have discrete β-phase [35]. Recent investigation of AA5083 suggests, however, that material reaches a saturated DoS well before a continuous boundary coverage forms on most boundaries (though a continuous boundary will eventually form with extensive over-aging). This implies that changes in the DoS are driven largely by the shape, number density, and size of discrete grain boundary β-phase precipitates prior to reaching a saturated state [39]. As such, it is rather the amount and the proximity of β-phase that determine the IGC susceptibility and subsequent IGC spreading.

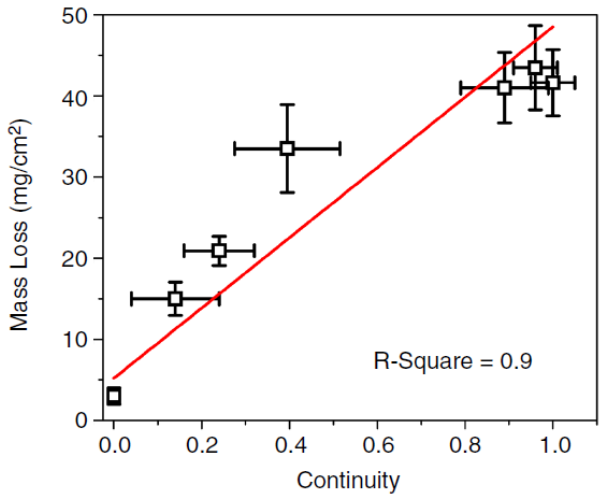

Figure 1.12: Experimental DoS data of AA5083-H131 sensitized at 70 °C for different times showing linear dependency between DoS and β-phase continuity [47]

.

1.3.2 Magnesium content

It has been established that the increased Mg content in the 5xxx (2 wt% to 6 wt%) Al alloy series is what gives the alloys their characteristic high strength via solid solution strengthening and strain hardening [48]. While the high Mg content does not significantly affect ductility or general corrosion resistance, it leaves the material vulnerable to sensitization. The β-phase precipitation has negative impact not only on IGC by rendering the grain boundaries preferential sites for anodic dissolution but also on the mechanical performance of the material. The β-phase is not a hardening particle and offers

no significant improvement in strength while at the same time it is weakening the matrix by draining the Mg solute. The result is a drop in hardness after sensitization [49]. The increase in Mg content is directly linked to increase in SCC and IGC as shown in Fig. 1.13. However, there is a threshold of 3.5 wt% below which no sensitization occurs, regardless of sensitization time and temperature. After the initial increase in DoS above the 3.5 wt% threshold, the DoS continues to increase monotonically after 4 wt% Mg [29]. The increase in DoS is also correlated with the linear increase of β-phase volume fraction at equilibrium at higher Mg content.

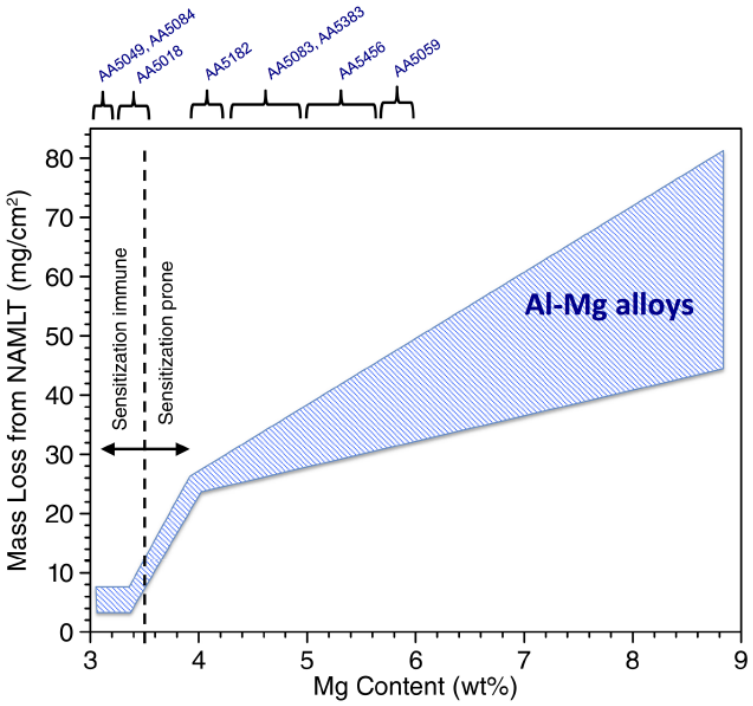

Figure 1.13: DoS of cold rolled 5xxx aluminium alloys as a function of Mg wt% after sensitization at 150 °C for 7 days [29].

1.3.3 Grain size and boundary misorientation

IGC is an intergranular phenomenon and thus microstructure related which makes grain size a relevant factor in the context of sensitization. The grain size of the 5xxx series can vary, significantly depending on the fabrication and processing conditions such as cold rolling, recrystallization or friction stir welding. Moreover, grain refinement as a method to enhance mechanical properties of the 5xxx series is gaining on popularity [50, 51] which puts even more emphasis on understanding the effect of grain structure on DoS. For example, it was found that the DoS of sensitized AA5059 (220 °C for 2 hours) is decreased by 50% from 65 mg/cm^2 to 33 mg/cm^2 when cold rolling reduction ration increased from 16.7% to 54.2% [52]. One of the factors the result was attributed to was the non-linear grain boundary length increase during the cold rolling grain size refinement. Since the amount of Mg available to populate grain boundaries with β-phase is the same, the overall β-phase coverage should decrease. However, there is little consensus in the literature what the effect of grain size actually is. This is mainly because the processing technologies that are used to refine the grain size also influence defect

type and its density (vacancies, dislocations, etc.), and the grain boundary characteristics such as the misorientation angle. Davenport et al. [53] reported that low misorientation angles (<20°) hinder the formation of β-phase on the grain boundary while preferential corrosion occurred inside the matrix which was attributed to more noble elements such as Si diffusing to the grain boundary rather than Mg atoms. On the other hand, D'Antuono [54] reported that β-phase formed preferentially on low-angle grain boundaries. Nonetheless, both studies agreed that β-phase precipitate growth occurs along high angle boundaries with precipitate size and thickness of β-phase increased with misorientation angle as confirmed by TEM in-situ tests. D'Antuono further postulated that the difference in β-phase thickness was related to grain boundary energy and that the grain boundary character dominates over the grain size as far as DoS is concerned. Nevertheless, more data needs to collected in this regard. Additionally, the enhanced diffusivity of Mg caused by new vacancies produced by severe plastic deformation was reported to have significant effect on DoS [54, 55]. Zhang et al. [56] report that there exists a competition between the effect of grain size and grain boundary misorientation on the resultant DoS. Depending on the grain size, the DoS response to grain refinement can be divided into grain size dominated regime and texture dominated regime as depicted in Fig. 1.14. Similar grain size can give a large variation in DoS depending on the grain misorientation distribution with higher DoS for higher fraction of high misorientation angle boundaries.

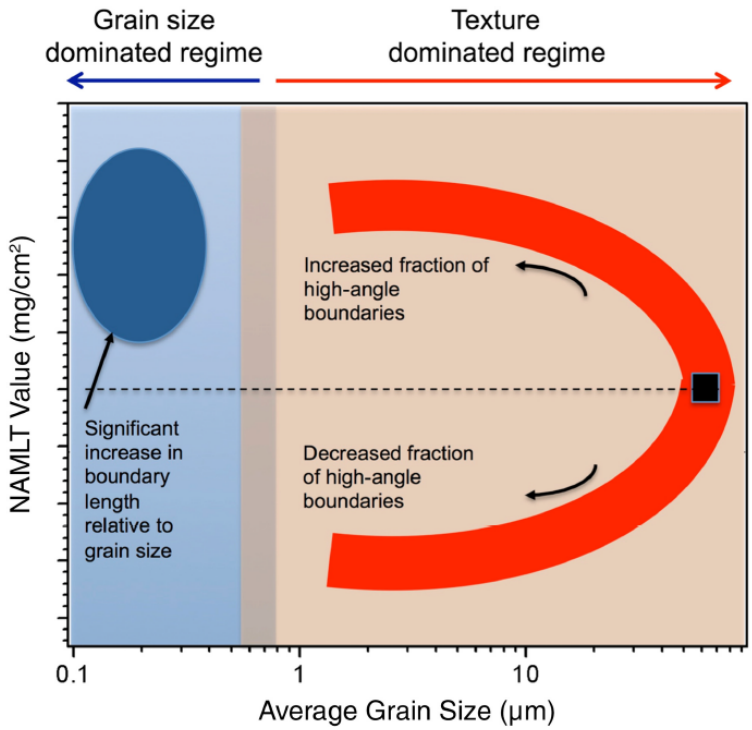

Figure 1.14: Relationship between grain size and DoS as measured by NAMLT. For larger grain sizes, the regime is texture dominated and grain boundary precipitation is dictated by grain boundary misorientation. For Sub-micrometer grain sizes, the regime becomes grain size dominated and the precipitation is mainly dictated by boundary length and finer grain core [56].

1.3.4 Grain orientation

Finally, the DoS and subsequently IGC spreading is also affected by the grain shape and its orientation within the overall structure. Alloys that have been strain hardened display anisotropy in grain geometry due to the uneven strain application. Grains are expected to be elongated in the rolling direction (RD) while shortened in the transverse (TD) and normal direction (ND), forming a pancake-like microstructures. Such directionality in the grain shape has been found to severely impact the exfoliation and IGC propagation in precipitation hardened and strain hardened Al alloys [57, 58, 59]. Hunt et al. [60] used the NAMLT test to measure the dependence of mass loss on sample orientation by preparing flattened samples with each of the three planes being preferentially exposed to the acid attack. They report that samples with preferentially exposed TD-RD plane suffered significantly less mass loss than samples with exposed ND-RD and ND-TD plane. Specifically, AA5083-H116 samples sensitized at 100 °C for 30 days showed mass loss of 87.3 mg/cm^2 for ND-RD plane, 81.0 mg/cm^2 for ND-TD plane and 20.0 mg/cm^2 for TD-RD plane which corresponds to 43%, 46% and 11% percentage mass loss, respectively. Fig. 1.15 shows a model of nitric acid penetration into the matrix on the cross-sectional ND-RD plane through both the top surface of the TD-RD plane and that of the ND-TD plane during NAMLT. The diagram shows two connecting arrow paths of the intergranular attack. Assuming that the grain boundaries have been indiscriminately sensitized, meaning that the nitric acid attacks all boundaries at constant rate, the two paths have equal length. Due to the non-uniform grain orientation, the corrosion attack starting at the TD-RD plane has to progress along more zigzag path as opposed to rather straight path of corrosion attack starting at the ND-TD plane. The depth reached by the TD-RD attack is thus lower which results in less grains falling off, providing an explanation for lower DoS measured.

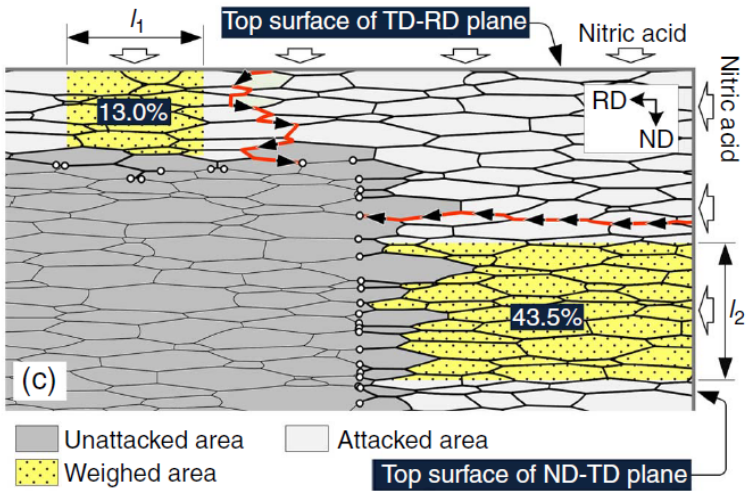

Figure 1.15: Schematic representation of acid penetration during the NAMLT test in RD-ND plane microstrucure cross-section. Deeper penetration is achieved in the grain elongation direction (ND-TD plane) as opposed to the normal direction (TD-RD plane) where the acid has to take less direct route [60].

1.4 Countermeasures to SCC

As was mentioned before, in order for SCC to occur, 3 conditions - susceptible material, corrosive environment and tensile stresses have to be met simultaneously. All methods that aim to prevent or counter SCC therefore revolve around denying or eliminating one or more of these requirements.

1.4.1 Metallurgical

Careful control of the manufacturing process in order to ensure proper structure refinement has been one of the valid avenues of research. Conventional 5xxx series alloys are used in annealed or strain hardened states. For certain Mg wt%, the grain morphology and size is controlled both by the level of cold work and the final annealing treatment. When manufacturing Al-Mg alloys with > 3.5 wt% Mg, the basic requirement is related to control of the β-phase precipitation (form and distribution). The final structure should discourage continuous β-phase precipitation along grain boundaries while promoting microstructures with β-phase precipitates within the grains. This can be achieved through the process of thermal stabilization. The alloy is heated to a temperature just below the β-phase solvus but it needs to stay above the sensitization range. The treatment in practice is difficult as the proper temperature range is narrow and varies with rolling conditions. If the stabilization temperature is too low, the result will be accelerated sensitization and more precipitated β-phase on the grain boundaries. If the stabilization temperature is too high, the Mg will redissolve back into the aluminium matrix (α-phase) but the alloy will be annealed, removing any previous strain hardening and resulting in significant loss in strength. In addition, Mg in solution is not stable and can lead to new sensitization over time [61, 62]. The situation is depicted in Fig. 1.16.

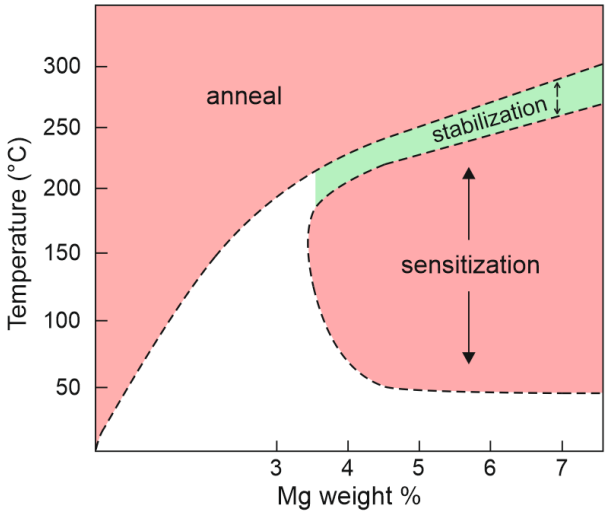

Figure 1.16: Stabilization temperature range for aluminium alloys with >3.5% Mg content. Temperature below the narrow range leads to sensitization, temperature above leads to annealing and removal of strain hardening. Adapted from [61].

The effect of β-phase dissolution has been observed after friction stir welding (FSW) where FSW[1] of sensitized AA5083-H321 (14 days at 100 °C) lead to low DoS of 5 mg/cm^2

[1] FSW of unsensitised AA5454 [63] also showed better IGSCC and localized corrosion resistance in FSW

in the weld area compared to the DoS of 50mg/cm^2 of the parent matrix [64]. When the temperature remains just below the solvus temperature, the β-phase precipitation takes place on sites that are away from the grain boundaries. If the β-phase is already present on the grain boundaries, it does not dissolve back into the aluminium matrix but rather coarsens into discrete large precipitates with lower continuity, thus lowering the IGC susceptibility. The stabilization treatment is therefore invariably sensitization treatment, albeit only low levels of susceptibility to IGC are developed. The treatment can be applied both to plates right after fabrication as well as to already fully sensitized plates from service. The temperature window for stabilization is quite narrow, usually between 220 °C and 240 °C, but it depends on the Mg wt%. For example, alloy with 7 wt% Mg will have the stabilization window between 260 °C and 290 °C.

Besides the thermomechanical treatment during and after the manufacturing process, one can also approach the problem through microalloying additions. Next to Mg, small amounts of Mn, Cr and Ti are added to further improve strength and prevent grain growth upon recrystallization (Table 1.3).

Alloy	Mg	Si	Mn	Fe	Cr	Ti	Cu	Zn	Other
5005	0.5-1.1	0.3	0.2	0.7	0.1	-	0.20	0.25	0.15
5052	2.2-2.8	0.25	0.1	0.4	0.15-0.35	-	0.10	0.1	0.15
5083	4.0-4.9	0.4	0.4-1.0	0.4	0.05-0.25	0.15	0.10	0.25	0.15
5086	3.5-4.5	0.4	0.2-0.7	0.5	0.05-0.25	0.15	-	0.25	0.15
5154	3.1-3.9	0.25	0.10	0.40	0.15-0.35	0.20	0.10	0.20	0.15
5182	4.0-5.0	0.20	0.2-0.5	0.35	0.10	0.10	0.15	0.25	0.15
5456	4.0-4.5	0.40	0.4-0.7	0.50	0.05-0.25	0.15	0.10	0.25	0.15

Table 1.3: Chemical composition (wt%) of selected commercial 5xxx aluminium alloys [35].

Together with elemental impurities, the additional additives create a range of different intermetallic or constituent particles distributed over the alloy microstructure. The effect of Mg content on DoS has been discussed in (1.3.2) and is rather straightforward. Lowering the amount of Mg makes the alloy less susceptible to IGC. At the same time though, the alloy loses its strength. There are other additional alloying elements, however, that can have an impact on IGC as well although their role is less well understood. Studies showed that Al-Mg alloys with higher percentage of Zn [65, 52] and to some extend Cu [66, 67] show lower DoS. The role of Zn and Cu addition, which preferably precipitates in the form of τ-phase Al-Mg-Zn/Cu, is to disrupt the continuity of β-phase along grain boundaries. The addition of 0.6 wt% Zn decreased the DoS considerably from 100 mg/cm^2 to 55 mg/cm^2 for 4-5 wt% Mg samples sensitized at 100 °C for 7 days. However, the authors did not study the effect of alloying Zn on the mechanical properties which can be critical for industrial use. A decrease in DoS has also been achieved with the addition of Sr [68, 69] and Nd [70, 71] although the mechanism of improvement in IGC resistance is not very well established. While Sr seems to be very promising for negating the sensitization alone, the hardness of sensitized samples, however, decreased as the Sr content increased. A similar decrease in hardness may be expected for samples with higher Zn content [65]. So far, the only element that showed both enhancement in hardness and IGC resistance properties is Nd [70]. The amount of Nd additions in the aforementioned study ranged from 0-0.17 wt%. It is also worth mentioning that chro-

location when compared to the parent matrix and tungsten arc welded structure.

mate, silicate and rare earth elements have been used as cathodic inhibitors to prevent localized corrosion attacks by forming films on cathodic sites [72, 73, 74, 75]. While the corrosion rates have been reduced, none of the studies considered DoS as a variable and thus no direct comparisons can be made.

1.5 Environmental

From the electrochemical perspective, protection against corrosion by means of manipulation of external factors can be achieved in 2 ways: cathodic protection and anodic protection. In the former case, the surface to be protected acts as an anode, whereas in the latter case, the surface to be protected acts as a cathode. The principle of anodic protection is bringing the anodic metal to its passive region where it forms a natural protective layer using higher electric potential. Searles et al. [76] performed slow strain rate tests (SSRT) on sensitized AA5083 using various electric potentials. They assumed that the IGC mechanism of sensitized Al-Mg alloys is driven by β-phase anodic dissolution along the grain boundaries and found that samples potentiostatically polarized below the β-phase breakdown potential showed almost no evidence of IGSCC. The newly created potential corresponded to the passive regime for β-phase. Seong et al. [77, 78] chose a different approach and studied the effect of chromate, silicate, or vanadate ions based chemical additives as corrosion inhibitors. They used the SSRT to show that the addition of K_2Cr0_4 and $NaVO_3$ into the 3.5 wt% NaCl environment resulted in strain curves essentially equal to those in air while sodium silicate additive was ineffective. The mechanism of inhibition in this case was mainly through the inhibition of cathodic reaction rather than the anodic dissolution. Despite their effectiveness, the anodic protection methods are not well suited for marine environment where large bulks of material need to be protected.

The most common solution in the cathodic protection approach is galvanic and sacrificial protection. Since the galvanic method is not viable for large structures such as long pipelines or ship hulls, localized sacrificial protection must be utilized. In this case, a sacrificial metal with corrosion potential lower than that of the protected metal is used. The sacrificial metal then becomes the new anode and corrodes instead of the protected now cathodic bulk metal. The three most commonly used sacrificial materials are magnesium, aluminium and zinc. In the case of marine salt water environments, it is zinc. Park et al. [79] studied the effect of zinc sacrificial anode on AA5083-H321 in seawater and found that the open circuit potential (OCP) of zinc anode was about –0.2 V relative to the aluminium which resulted in preferential corrosion of the zinc anode and calcareous deposits formed on the Al surface. Sacrificial anodes are normally supplied in the form of blocks, rods, plates or cast-m straps to facilitate their attachment to ship hulls (Fig. 1.17). The amount of sacrificial anodes used is determined by a balance between the additional mass they add to the ship and the depletion period. Usually, they need to be replaced annually or when they have corroded to half their original size. This brings additional cost and time investment into the ship maintenance schedule.

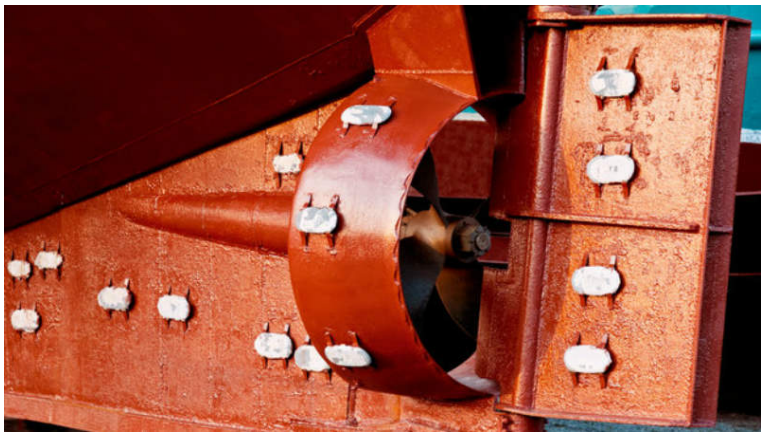

Figure 1.17: Sacrificial cast-m strap anodes attached to a ship hull [80].

1.6 Stress removal

The last, yet for this work most relevant approach toward preventing SCC, is the removal of tensile stresses via specialized mechanical treatments. Tensile stresses in general are a necessary component for crack initiation and propagation and need to be monitored carefully during the manufacturing process. A faulty technological procedure leading to tensile stress pile up in critical area may result in a quick failure of a component. Although the penetration depth can vary significantly, the treatments usually target the material surface since that is where the cracking usually initiates and propagates further into the material. Nevertheless, there are also cases where cracks can initiate within the material, usually due to uneven heat treatments, bubbles, impurities, ultra-high cycle material fatigue.

All of the methods presented in this section, namely Shot Peening (SP), Ultrasonic Impact Peening (UIP) and Laser Shock Peening (LSP) are part of the severe plastic deformation (SPD) group. There is some evidence that the recrystallization that accompanies surface plastic deformations may have a positive impact on the IGC. Seong et al. [78, 81] investigated the OCP of a solutionized and sensitized AA5083 and found that the small plastic deformation of the surface induced during diamond solution polishing prevents IGC from happening. The altered surface layer is only about 1 μm thick but it was enough to cause recrystallization of the surface layer which removed the β-phase from the grain boundaries. In contrast, it has been also proposed that the vacancies produced by SPD could enhance Mg diffusion rate during the sensitization process [82]. Nevertheless, the influence of near-surface deformed layers on the corrosion properties of aluminium alloys is not widely understood.

It is important to point out that as far as stress removal is concerned, the SPD processes merely cause redistribution of residual stresses rather than their removal as the total sum of residual stresses, both tensile and compressive, must remain equal to zero. If the sum is not equal to zero, the material macroscopically deforms (bends or twists) until a balance is restored. This is especially important when a larger volume of material is affected, as in the case of Laser shock peening, which can lead to undesired geometrical changes of the treated component.

1.6.1 Shot peening

Shot peening (SP) is a cold working and work hardening process and is an industrially widespread method for tensile stress elimination. In this case, the surface of a material is bombarded with high velocity spherical projectiles (shots) accelerated by means of compressed air or centrifugal forces. The shots can be made of metal, glass or ceramics, within the typical size range of 0.1 mm up to 3 mm. The speeds vary between 10-100 m/s, depending on the material and application. Each of the shots acts as a little ball-peen hammer, leaving a small dimple in the place of impact. Compressive residual stresses are induced around the peened surface region along with some tensile stresses further below. Additionally, a thin nanocrystal layer is created, refining the grain size close to the surface [83]. The mechanism is depicted in Fig 1.18. The process is similar to sandblasting, except unlike sandblasting, SP operates by the mechanism of plasticity rather than abrasion and thus no material is intentionally removed.

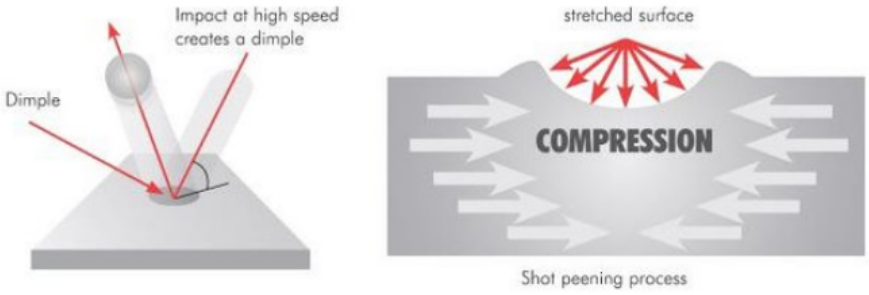

Figure 1.18: A schematic of the shot peening process [84].

The key parameters during the SP treatments are the intensity and coverage. The intensity is governed by the shot velocity, size and time of exposure. It is measured with an Almen strip which is a thin sheet of plain carbon steel with defined dimensions (75 x 19 x 0.7–2.4 mm) supported on 2 knife edges or 4 small metallic balls [85]. The strip is peened from one side which causes its bending due to uneven compressive residual stress distribution. The degree of bending then determines the peening intensity. The second important factor is coverage which is given by the percentage of the surface indented once or more. Due to the inherent randomness of the SP process where individual shots cannot be controlled, coverage is subjected to statistical determination. It is affected by the angle of shot blast incidence which varies either due to the shape of the treated part or the natural cone shaped beam. The coverage can be increased by slower or repeated passes and it was shown to have a direct impact on the amplitude and uniformity of the induced compressive stresses which are positively correlated with fatigue life improvement [86, 87]. It is important to note that excessive coverage can have a negative or diminishing impact on the fatigue life improvement as the surface may be damaged with too many impacts.

The main advantage of the SP process is its relative technological simplicity and low cost, making it the conventional tensile stress removal technique. The downside is the superficial compressive stresses induced which usually do not reach further than about 250 μm. Moreover, the treatment causes higher surface roughness which may require additional grinding and polishing, typically with applications that revolve around wear. And lastly, some areas such as notches and fillets are not accessible for SP and require a different technique. Nevertheless, SP has been successfully applied to extend the fatigue

life of AA5083-H11 T-welded joints [88] and has been reported to have a positive effect on exfoliation properties of AA5083 [89].

1.6.2 Ultrasonic impact peening

Ultrasonic Impact Peening (UIP) operates on the principle of an ultrasonic transducer which converts alternating current into ultrasonic vibrations, usually by means of piezoelectric crystals that change size and shape when voltage is applied. Specially hardened steel pins (indenters) attached to the transducer transfer the vibrations to the treated surface where a direct contact between the pins and surface is maintained. A basic scheme of the process is shown in Fig. 1.19. The peened metal responds to the pre-calibrated resonant frequency of the indenter by high rate straining and heating near the material surface, causing plastic deformation. Energetically stable dislocations are created, inducing compressive residual stresses as a result. Depending on the desired effects, a combination of different frequencies (ranging from 15 to 80 kHz) and pin displacement amplitudes (20 um to 80 um) is applied.

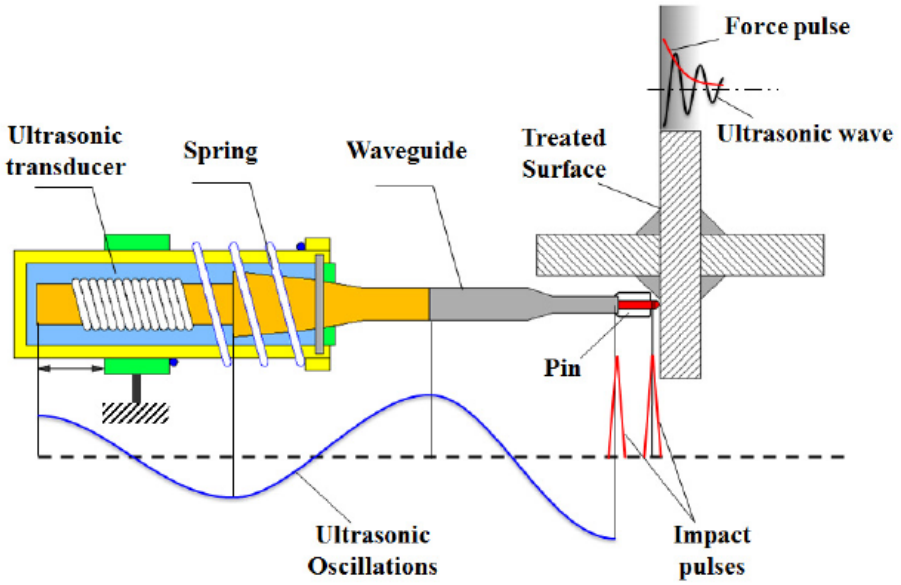

Figure 1.19: A schematic of the shot ultrasonic impact peening mechanism [90].

UIP was originally developed in Russia for the shipbuilding industry in the 1970s [91] and became prominent at the end of 1990s in USA, in particular tied to federal highway construction works where it was applied for fatigue strength enhancement of steel bridges [92]. Since 2008, the US Navy uses the process to aid in repairs of SCC caused surface cracking of AA5456-H116 ship structures. The repairs specifically involve treatment of sensitized and heat affected areas around welded SCC cracks (Fig. 1.20) and repairs that require insertion of a new material. UIP was specifically shown to impart deep compressive stresses in sensitized AA5456 accompanied by a refined microstructure resulting in improved resistance to IGSCC [93]. Similarly, the surface layer nanocrystalization and fatigue life improvement was observed with AA2024 [94] and AA7075 alloys [95] where in the latter the effect of UIP on exfoliated material was investigated. Similar effects can be observed with other materials such as stainless steel [96], low carbon steel and various titanium alloys [97]. A considerable upside of the process

when compared to SP is that UIP can be implemented using hand-held devices allowing access to hard to reach locations. However, leading the pins over the surface by hand will negatively affect the uniformity of the impact distribution when compared to a static machine where the sample is mounted to translation stages and the indenter speed and pattern can be precisely controlled. As far as the surface roughness is concerned, UIP in general does not cause gross damage to the surface of the material although some flaws in the form of microcracking and microtearing may appear, usually as a result of uneven treatment.

Figure 1.20: Application of ultrasonic peening technology to localized AA5456-H116 aluminum crack repair [93].

1.6.3 Laser shock peening

Unlike the previously described SP and UIP processes which are both mechanical in nature, LSP is based on interaction of high-energy nanosecond laser pulses with solid material and will be the main focus of this work. During the process, a laser pulse with typical energy of several Joules is focused on a specimen surface covered with a thin protective layer and a laminar water layer on top. As the laser pulse gets absorbed, a strong shock wave is generated which travels into the material creating plastic strain and compressive residual stresses similar to the other SPD processes. Treatment of areas is achieved via placing laser shots next to each other in a controlled fashion. The process can be applied to a wide range of materials, most notably to various steel, aluminium and titanium alloys. The details of the process will be extensively described in the following chapter. For the sake of continuity, however, let us now elaborate on LSP in context of SP and UIP.

First practical applications of LSP has been developed in the 1990s as an alternative method to SP which has been used in the industry since 1940s. It turned out that SP proved insufficient in dealing with certain problems which required deeper compressive residual stresses than what SP offers which proved to be an insurmountable technological limitation up to this day. Apart from the deeper compressive stresses, LSP offers precise control over the laser shot impact location which removes the randomness associated with the SP coverage and provides higher stress uniformity. LSP also produces smoother surfaces as evidenced by Montross et al. [98] and Hatamleh et al. [99] who studied surface roughness R_a of AA7075 after both treatments. The roughness improvement in direct comparison of LSP to SP is roughly 3-10 fold, depending on the material and parameters used. And lastly, LSP can be utilized in areas inaccessible both to SP and UIP usually associated with various cavities, complex geometries or underwater environment. The comparison with SP is graphically summarized in Fig. 1.21. The obvious

downside to LSP is its cost which is, however, getting progressively lower as new cheap laser sources are developed.

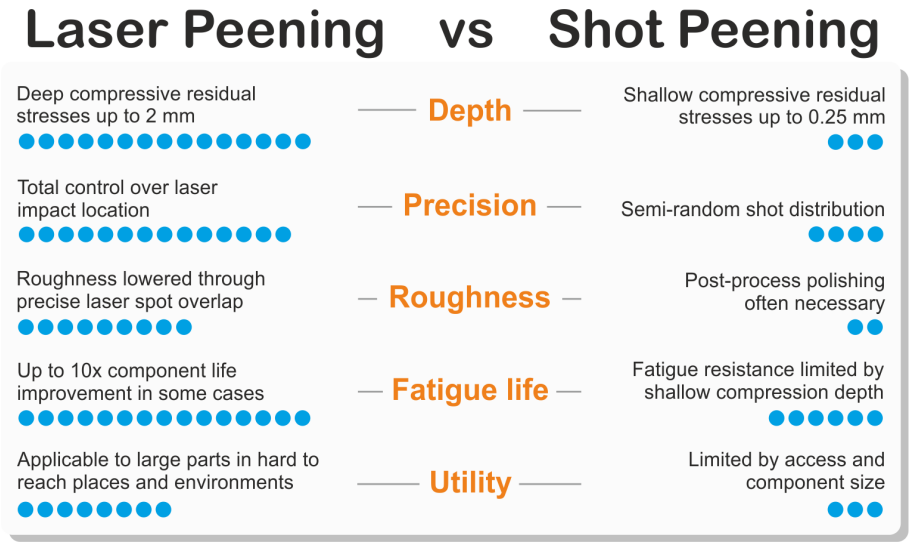

Figure 1.21: Comparison between LSP and SP.

When it comes to UIP, a comparison to LSP is harder to assess as it seems to be highly material dependent. Both Mordyuk et al. [100] and Wang et al. [101] studied the effects of LSP and UIP on stainless steels AISI 321 and AISI 316L, respectively. Both studies reported significantly higher surface compressive residual stresses for the UIP treatment although a depth profile is absent in both studies. Similarly, a significant increase in hardness has been observed for UIP (125%) as opposed to LSP (20-30%) where the difference is attributed to the much higher impact number and total energy for UIP. The effect of the treatments on microstructure is discussed in detail with the conclusion that UIP causes much higher nanocrystallization (10-90 nm) compared to LSP (>70 nm) characterized by different deformation mechanisms, namely dislocation and twinning, respectively. Hamzah et al. [102], on the other hand, performed similar comparative study on AA7075 and found better hardness results with LSP of 23% improvement as opposed to 5% with UIP. LSP also showed better high cycle fatigue life improvement but worse low cycle data. It seems that both LSP and UIP should be regarded as valid alternatives differentiated by specific application. Traditionally, UIP was applied using portable hand-held devices which allows it to be used in many small scale scenarios where high precision is not required. In recent years, UIP has also been automated using robotics giving it precise control over the peening location. LSP tends to perform better with complex geometries where it can be difficult to maintain contact between the surface and peening pins. Due to the deep nature of LSP induced compressive residual stresses, more surrounding bulk material around the treated area is needed to counteract the compression. This means that deeper stresses can be obtained with thicker samples. Moreover, a great level of automation for high-throughput industrial manufacturing incoporating LSP has been achieved using advanced robotic control [103]. The two conventional approaches to industrial LSP are presented in Fig. 1.22. In one case, the part is fixed to a robotic arm which moves around a static laser beam. In the second case, the part is fixed and laser is delivered through special mirror tracking system and laser head mounted to the robot. The second approach allows for treatment of very large parts such as wings in aerospace industry.

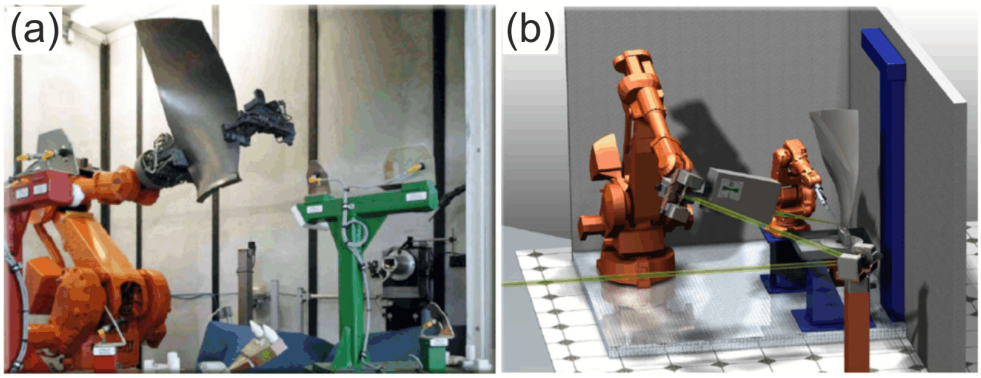

Figure 1.22: Robotic control of the LSP process. (a) Part is carried by robotic arm and moved through a static laser beam. (b) Part is fixed to a positioner while laser beam is delivered via advanced beam guiding system mounted to the robot [103].

When it comes to LSP influence on SCC, studies focusing on AISI 304 and AISI 316L steels [11, 12], AA7075 [104] or AZ31B magnesium alloy [14] have been carried out and all point to positive effect of LSP. These studies approach the problem mostly via the stress route where SCC is supressed through the introduction of compressive residual stresses. Despite LSP being primarily utilized for the generation of compressive stresses, this work also aims to investigate the microstructural aspect of LSP and its effect on sensitization of AA5083 and its susceptibility to IGC. We have already established in (1.3.3) that the grain size and grain boundary orientation have an effect on the DoS although the precise mechanisms are unclear. Various studies suggest that LSP does have a refining effect on the grain structure. For instance, Lu et al. [105] studied the influence of LSP on grain refinement of LY2 aluminium alloy. The ultra-high plastic strain caused by multiple laser impacts caused a grain refinement at the top surface to a 100-200 nm size. Similarly, Trdan et al. [106] used 6082-T651 aluminium alloy and report exceptional increase of dislocation density after LSP with the result of producing ultra-fine (60-200 nm) and nano-grains (20-50 nm) in the surface layer. Moreover, electrochemical studies performed with aluminium alloys subjected to LSP treatment also speak in favour of LSP. In different study, Trdan et al. [107] investigated corrosion resistance of AA6082-T651 under LSP and showed improvement in open circuit potential, corrosion current and electrochemical impedance. The results were attributed to modification of surface film and residual stresses caused by LSP. Amar et al. [16] report that LSP on AA2050-T8 prevented IGC although the IGC mechanism is different than with AA5083-H116. Wang et al. [15] used AA7075 and linked the 50% reduction in corrosion current to grain refinement.

Despite the intrinsic heat effects associated with nanosecond laser pulse absorption, LSP is often considered a cold-working process due to the fact that the heat gets dissipated in the protective layer. Removing the protective layer causes burning and melting of the surface layer followed by creation of surface tensile stresses. This process is referred to as Laser Peening without Coating (LPwC). It was shown, however, that the tensile stresses can be minimized when using low energy pulses with high pulse density [108]. A unique aspect of the LPwC process, often associated with the previously mentioned negative effects, is the creation of a modified oxide layer on top of the treated material. Aluminium surface in aqueous environments naturally forms a thin oxide passive layer that hinders the corrosion processes. A hypothesis is put forward where the

modified oxide layer created by LPwC could fulfil a similar role in a more aggressive sea water environment.

To the author's knowledge, very few studies touched the subject of the effect of LSP on IGC and IGSCC of AA5083. H. Mattern in her thesis [9] investigated the effect of laser peening on SCC in metal-inert-gas welds of AA5083 in corrosive 3.5% NaCl environement. Although the slow strain rate tests showed a systematic increase in maximum stress applied with increasing LSP intensity, the fracture surfaces of the laser peened and control weld samples all showed primarily ductile failure without any evidence of SCC. Without any prolonged sensitization, she concludes that the heating associated with the welding process may not have been sufficient to sensitize the tested specimens. The second work is by Tsao [109] with a focus on the effect of LSP on dislocation morphology and microstructural evolution of AA5083-H116 after LSP supported by FE modelling.

1.7 Corrosion fatigue

While significant attention in the literature was paid to investigating IGSCC behaviour of the 5xxx aluminium alloys, only a limited number of studies have investigated the effects of corrosion fatigue (CF) in aggressive marine environments [19, 20, 21]. CF refers to the process in which a metal fractures prematurely under conditions of simultaneous corrosion and repeated cyclic loading at lower stress levels or fewer cycles than would be required to cause fatigue of that metal in the absence of the corrosive environment. In this case, the fatigue loading is introduced by wind and wave motion, ship machinery vibrations, thermal expansion, and contraction and operational loading events [23, 24]. The fatigue process is thought to cause rupture of the protective passive film, upon which corrosion is accelerated.

CF behaviour is dependent on the interactions among loading, environmental, and metallurgical factors although less stress is put on the state of the material which in the IGSCC case plays a critical role. For a given material, the fatigue strength (or fatigue life at a given maximum stress value) generally decreases in the presence of an aggressive environment. For the majority of engineering alloys, the fatigue limit or fatigue strength refers to the stress level below which failure does not occur within a specified number of cycles, usually 10^7 or 10^8 cycles. A typical S-N graph which plots stress level against the number of cycles is shown in Fig. 1.23.

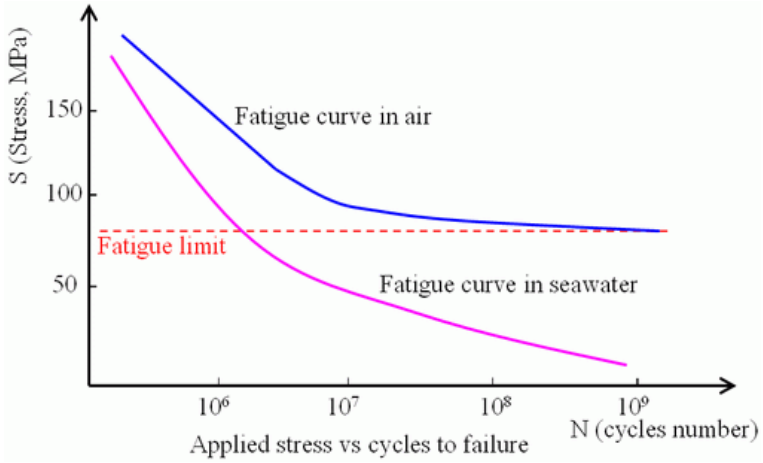

Figure 1.23: Corrosion fatigue S-N curve.

The fatigue fracture is brittle and the cracks are most often transgranular [110] although intergranular cracks are not uncommon [111, 112] especially when the alloy is sensitized [113, 114]. The corrosive environment can cause a faster crack growth and/or crack growth at a lower tension level than in dry air. Even relatively mild corrosive atmospheres can reduce the fatigue strength of aluminium structures considerably, down to 75 to 25% of the fatigue strength in dry air. No metal is immune from some reduction of its resistance to cyclic stressing if the metal is in a corrosive environment.

CF can be prevented through:

1. Reducing the fatigue by minimizing vibration and pressure fluctuation
2. Reducing the corrosion by using high-performance alloys resistant to corrosion fatigue
3. Reducing the corrosion by using coatings and inhibitors to delay the initiation of corrosion fatigue cracks

This work's LSP approach falls primarily into the second category which in this case means making the alloy more fatigue resistant by inducing compressive residual stresses in the critical area. Increasing fatigue life is the primary application of the LSP process and there are numerous studies covering its beneficial effects on various materials. Furthermore, similar to the goals regarding IGSCC, the impact of LSP on the surface film will be investigated where affecting the pitting behaviour could have a significant impact on the crack initiation sites. This approach would then fall into the third CF prevention category.

Chapter 2

Laser Shock Peening process

2.1 Nanosecond laser pulse interaction with matter

2.1.1 Light propagation in materials

When a laser pulse strikes a surface of a material, a portion of it will be reflected from the interface due to discontinuity in the index of refraction and the rest will be transmitted into the material. The fraction of incident power that is reflected from the surface, denoted by reflectance R, and transmitted into the material, denoted by transmittance T, can be calculated from the Fresnel equations which for normal angle of incidence are

$$R = \left(\frac{n_1(\lambda) - n_2(\lambda)}{n_1(\lambda) + n_2(\lambda)} \right)^2, \quad T = 1 - R \tag{2.1}$$

where n_1 and n_2 denote the real part of index of refraction for the two media. The index of refraction is a function of laser wavelength λ which will be important later when the influence of laser wavelength on the peening procedure will be discussed (2.5.2). Typical values of R of metals in the infrared (IR) range for the normal incidence case are between 0.8 and 0.99 for a mirror finish of the surface [115]. Despite the high reflectance, even smooth surfaces will be ablated as long as the laser fluence is high enough[1]. Fig. 2.1 shows reflectance of polished aluminium target when under various laser fluences [116]. We see that once the fluence threshold is reached, the reflectance drops sharply due to the screening effect of plasma created on the surface (2.1.5). The laser light absorption is further enhanced by surface nano and micro-dents present on the sample surface following mechanical polishing and their local overheating.

An important factor significantly influencing the reflectance/transmittance not included in the Fresnel approximation (2.1) is surface roughness. For light incident, normally (0^o) or with a relatively small angle (30^o), the laser absorption was found to increase with roughness (rms slope) after the threshold for multiple (double) scattering had been reached (Fig. 2.2a). The relation between the number of scattering events and surface roughness is shown in Fig. 2.2b. The increase in absorption with roughness is most pronounced for metals which are highly reflective in flat, smooth state. This is simply a consequence of diminishing returns where each new scattering point along a ray path contributes less and less energy for absorption due to the limited amount of energy available in the bundle.

Once inside the material, the light intensity decays with depth at a rate determined by the material absorption coefficient α which is in general a function of temperature

[1] The same effect occurs when a mirror is burnt by a laser pulse due to a random hot spot in the laser spatial profile.

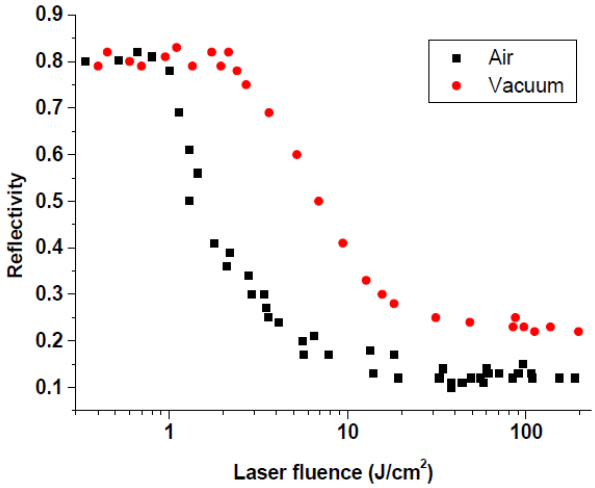

Figure 2.1: Hemispherical total reflectance of aluminium as function of laser fluence for ablation in 1-atm air and in vacuum [116].

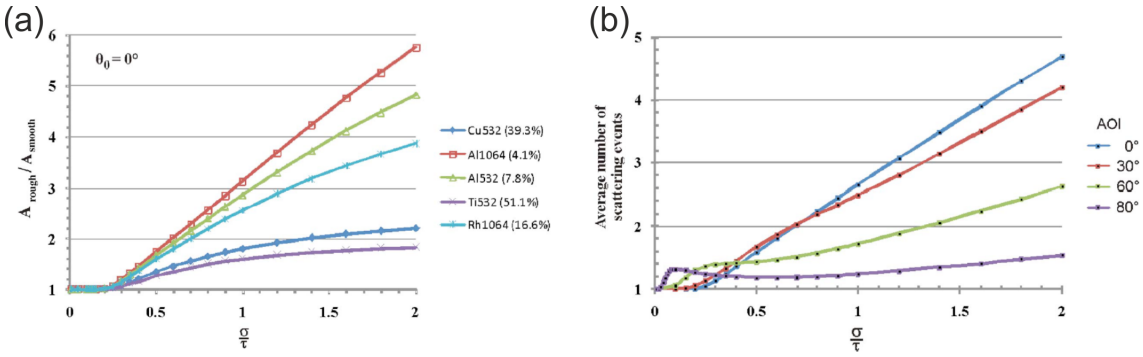

Figure 2.2: (a) Ratios of the absorptions of rough and smooth surfaces for normally incident light shown as a function of slope roughness (where σ is the rms height and τ the correlation length) for various metals (the number after the atomic symbol indicates the wavelength of the light involved) [117]. (b) The average number of scattering events per incident ray as a function of the rms slope roughness for different angles of incidence [117].

and wavelength. For constant α, the light intensity decays exponentially with depth z according to the Beer-Lambert law

$$I(z) = TI_0 e^{-\alpha z} \tag{2.2}$$

where I_0 denotes the light intensity before the reflection loss is accounted for. It is useful to define the optical penetration depth as $\delta = 1/\alpha$, which denotes the depth at which the light intensity drops to $1/e$ of its initial value at the interface. For metals, the optical penetration depth also known as 'skin depth' can be calculated as [118].

$$\delta = 1/\sqrt{\pi \mu f \sigma_0} \tag{2.3}$$

where μ is the magnetic permeability, σ_0 is the electrical conductivity and f is the electromagnetic wave frequency. Typical values for visible and near infrared wavelengths

are around 10-20 nm. The absorption in metals therefore takes place only in a very thin layer on the material surface, hence the name skin effect.

2.1.2 Laser pulse absorption in material

For relatively low laser intensities[2] associated with nanosecond pulses (10^8-10^{11} W/cm^2), the optical absorption in metals is dominated by free electrons through the collisional absorption mechanism, also known as inverse bremsstrahlung. Regular bremsstrahlung (Fig. 2.3a) is an electromagnetic radiation produced when a charged particle gets decelerated when deflected by another charged particle, typically an electron being deflected by an atomic nucleus. Since energy during the process must be conserved, the electron loses kinetic energy at the expense of a radiated photon. The energy of the radiated photon is $h\nu = \varepsilon_1 - \varepsilon_2$ where h denotes the Planck constant, f frequency and ε_1 and ε_2 the electron energies before and after the collision, respectively. Inverse bremsstrahlung (Fig. 2.3b) is an opposite process when an electron absorbs a photon while colliding with another ion or electron. The electron gets accelerated and spreads its newly acquired kinetic energy among other particles, in this case lattice phonons, by means of ordinary Coulomb collisions (thermalization)[3].

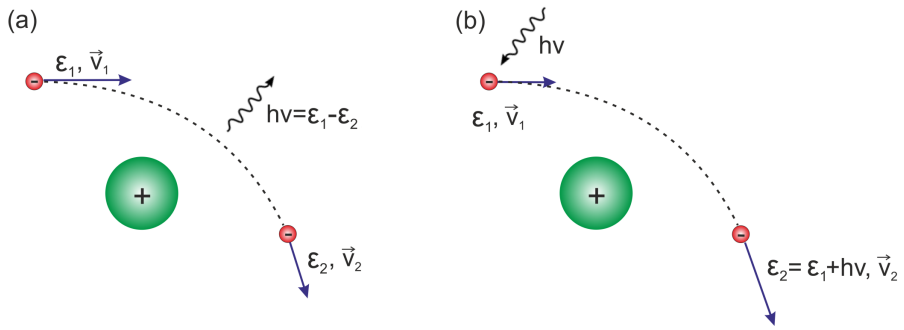

Figure 2.3: (a) Bremsstrahlung: an electron with energy ε_1 and velocity $\vec{v}_1$ emits a photon with energy $h\nu = \varepsilon_1 - \varepsilon_2$ as a result of deceleration in the ion field. (b) Inverse bremsstrahlung: an electron is accelerated by a photon absorption and spreads its newly acquired energy among other plasma particles.

A simpler way to think of inverse bremsstrahlung is to consider the motion of an electron in the oscillating field of an electromagnetic wave (incident laser beam). As the electrons oscillate in this field, they collide with ions, thereby converting the directed energy of the oscillation into the random energy of thermal motion. In other words, the oscillating electrons correspond to a current induced in the plasma by the incident light beam that then leads to resistive heating of the plasma due to charged particle (Coulomb) collisions. In this way, the incident light energy is deposited in the form of increased electron thermal energy. The rate of energy transfer between the electrons and ions ν_{ei} can be expressed through the collisional frequency formula [119]

[2]Low intensities in the context of ultrafast laser physics where the intensities of femtosecond pulses can realistically reach up to 10^{21} W/cm^2.

[3]In non-relativistic cases, energy loss of electrons to ions due to elastic Coulomb collisions dominates over energy loss of electrons via bremsstrahlung. The absorbed energy thus stays in the material and is not radiated back.

$$\nu_{ei} = \frac{3Z^2 e^4 n_i \ln\Lambda}{8\pi\epsilon_0^2 m_e^2 v_e^3} \tag{2.4}$$

where Z denotes the ion charge state, e the electron charge, m_e the electron mass, n_i the ion density, ϵ_0 the permitivity of vacuum, v_e the electron velocity and $\ln\Lambda$ the Coulomb logarithm which is a factor by which small angle collision are more effective than large angle collisions. In case of insulators, there are no free electrons and the laser energy is absorbed via excitation of electrons from valency bands into conduction bands or into their vibration states. The electrons then interact with neighbouring atoms and convert their energy into thermal energy.

The time it takes for the excited electronic states to transfer their energy to phonons and thermalize depends on the material and on the specific mechanisms within the materials. For most metals, the thermalization time is in the order of tens of picoseconds. Typically, the electron relaxation time τ_e is much shorter than the ion heating time, $\tau_e \ll \tau_i$. For a nanosecond laser pulse with a duration time τ_L, the condition $\tau_e \ll \tau_i \ll \tau_L$ is fulfilled, which means that in the case of sufficiently long laser pulses, electrons and ions can be considered reaching thermal equilibrium ($T_e = T_i$) instantaneously. When the laser-induced excitation rate is low in comparison to the thermalization rate, one can consider the absorbed energy as being directly transformed into heat as the details of the transient electronically excited states are not important. Such processes are called photothermal (pyrolytic) and the material response can be treated in a purely thermal way. Processing of materials or semiconductors with slow laser pulses (>ns) are typically characterized in this way.

2.1.3 Ablation

Laser ablation is the process of direct removal of material from a solid surface when irradiated by sufficiently intense laser pulse[4]. In order for ablation to occur, a threshold laser fluence needs to be exceeded which depends on the specific material properties, absorption mechanism, and laser pulse parameters. Typical threshold fluences for metals are 1 – 10 J/cm^2, for inorganic insulators 0.5 – 2 J/cm^2 and 0.1-1 J/cm^2 for organic materials [115]. At lower fluences, which are typical for ns pulses operated in air, photothermal mechanisms for ablation include evaporation and sublimation. The energy absorption rate is relatively slow when compared to the thermalization rate of most materials. That means that part of the absorbed energy will be dissipated into the material as heat before the irradiated material is evaporated, causing melting around the ablated crater also known as HAZ (Heat Affected Zone). This effect is most apparent in the ablation of metals due to their large thermal diffusiveness and low melting temperatures. The melting effect can be avoided with shorter laser pulses (ps to fs) where all the laser energy gets deposited into the material before thermalization can take place. In that case, the process is governed by photochemical ablation mechanisms such as direct ionization, electron-hole plasmas formation, direct bond-breaking and Coulomb explosion [120]. The difference in the ablation effect for ns and fs pulse is shown in Fig. 2.4b.

In all cases, the material removed from the irradiated zone is ejected in a highly directed and dense vapour plume. At high laser intensities, the plume becomes ionized and plasma is created (Fig. 2.4a). Due to their longer duration, ns pulses can interact with the plasma plume which absorbs the incident light and shields the material surface below. The thickness of material actually removed is therefore very low, in the order

[4] also possible with intense CW radiation

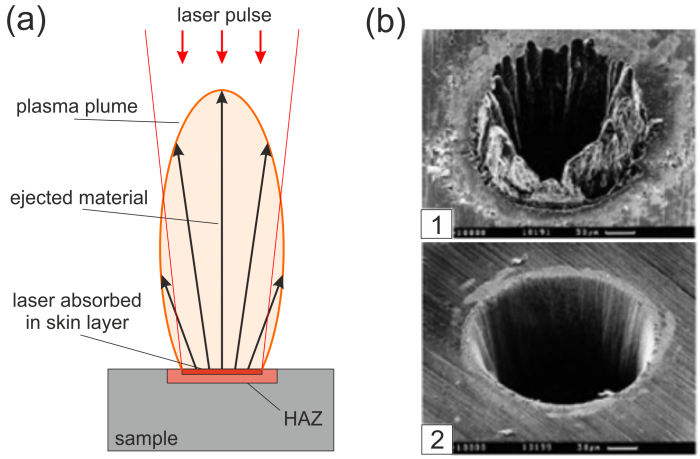

Figure 2.4: (a) Ablation: Laser pulse (ns) vaporizes surface layer of material, ionizes the ejected material and interacts with the created plasma plume. (b) Laser ablation of holes drilled in a 100 μm thick steel foil with (1) 3.3 ns, 1 mJ, and $F = 4.2$ J/cm^2 and (2) 200 fs, 120 μJ, $F = 0.5$ J/cm^2 laser pulses at 780 nm [121].

of μm. For instance, a 10 J pulse 30 ns long with intensity of 10 GW/cm^2 will ablate 1 to 3 μm of surface material. The importance of the plasma absorption phenomena will become clear in the following sections.

2.1.4 Ionization mechanisms

The ionization of a material by intense laser pulses can be generally divided into 2 stages: the initial ionization and the subsequent avalanche ionization. Let us start with the second stage. The basic mechanism of avalanche ionization can be written down as

$$e^- + M + h\nu \rightarrow 2e^- + M^+ \tag{2.5}$$

A free electron (e^-) is accelerated by the inverse bremsstrahlung mechanism ($h\nu$) and then interacts with an atom of a material (M), displacing a valency electron from its shell and ionizing it. At the end, there is an ionized atom and 2 free electrons ready to continue the process in a snowball fashion. However, the avalanche ionization process can only start when there are some free electrons in the medium. In case of dielectrics, there are no free electrons to begin with and the photon energy for the common wavelength of 1 μm, given by

$$E_{ph}(eV) = \frac{1.2398}{\lambda(\mu m)} \tag{2.6}$$

is less than the ionization energy of most atoms. However, in case of very high photon densities of intense laser pulses, multiphoton ionization can take place. The process can be described by the following equation

$$M + mh\nu \rightarrow e^- + M^+ \tag{2.7}$$

m photons are absorbed simultaneously with combined energy high enough to reach the ionization energy of a given atom. Other explanations for the initial ionization include the presence of impurities, and also a distortion of the atomic energy levels in the very high intensity laser electric field that effectively lowers the ionization potential.

2.1.5 Laser plasma interaction

An important parameter related to optical properties of plasma is the plasma frequency

$$\omega_p = \sqrt{\frac{e^2 n_e}{\epsilon_0 m_e}} \tag{2.8}$$

where n_e denotes the electron density. We see that the plasma frequency is proportional to density of free electrons in plasma. The dispersion relation of an electromagnetic wave propagating in plasma for non-relativistic case[5] is

$$\omega_L^2 = \omega_p^2 + k^2 c^2 \tag{2.9}$$

where ω_L denotes the laser angular frequency, k the wave number and c the speed of light.

Based on the dispersion relation (2.9), the plasma can be divided into 2 regions: underdense and overdense. The underdense region is marked by low electron density n_e such that $\omega_L > \omega_p$. The wave number k in this case is real and the electromagnetic wave can propagate through the plasma and deposit its energy through the inverse bremsstrahlung mechanism. The depth at which the laser light propagates is determined from the absorption coefficient [118]

$$\kappa = (2\pi)^{1/2} \left(\frac{16\pi}{3}\right) \frac{e^6}{c\,(m_e k_B T_e)^{3/2}} \frac{\ln\Lambda}{\omega_L^2 \sqrt{1 - \left(\omega_p/\omega_L\right)^2}} \tag{2.10}$$

where k_B is the Boltzmann constant, and T_e the electron temperature. Experiments show sharp cut-off in target surface reflectance when critical laser fluence is reached (Fig. 2.1). The critical fluence coincides with the moment of plasma creation, when the laser energy starts getting strongly absorbed in the underdense plasma region.

In the overdense region, where $\omega_L < \omega_p$, k in (2.9) becomes imaginary and the electromagnetic wave cannot propagate. It can only penetrate into the plasma via skin effect. The mechanism is the same as in the case of light absorption in metals where the electrons in plasma are replaced by free electrons in the crystal lattice. From a more physical point of view, the electron inertia is sufficient to keep the material current in phase with the displacement current in the underdense region where the light frequency exceeds the plasma frequency. In the overdense region, the light frequency is less than the plasma frequency and the material current opposes the displacement current in the light field. The wave is then not allowed to propagate. The critical electron density $n_{e,crit}$ marks the boundary between the underdense and overdense region where $\omega_L = \omega_p$. It can be derived from (2.8) as

$$n_{e,crit} = \frac{\varepsilon_0 m_e}{e^2} \omega_L^2 = \left(1.11 \times 10^{21}\,\mathrm{cm}^{-3}\right) \lambda_L^{-2}(\mu\mathrm{m}) \tag{2.11}$$

At this electron density, the plasma behaves as a mirror (Fig. 2.5). The reflectance is high and the absorption nearly zero. This effect is the basis of plasma mirrors which are used to increase laser contrast in femtosecond pulses [123, 124].

During the absorption in the underdense region, it is mainly electrons that are accelerated due to their low inertia compared to ions. The energy transfer between electrons

[5] For the interaction to be treated relativistically, the laser intensities would have to exceed 10^{18} W/cm^2 where the kinetic energy of the electrons oscillating in the electric field of the laser pulse is equal to their rest energy [122].

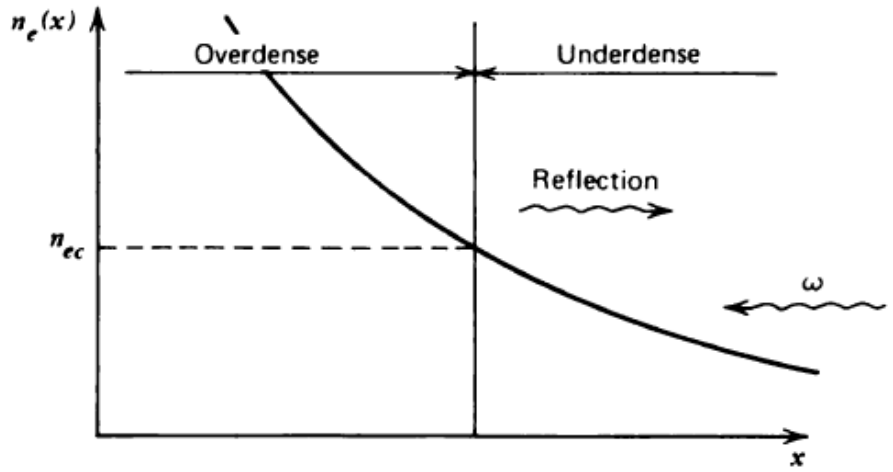

Figure 2.5: Incident laser light cannot propagate beyond the critical density which separates the underdense and overdense plasma regions [125].

and ions by means of Coulomb collisions is not very efficient because the maximum part of the electron energy that can be transferred to an ion is limited to $2m_e/m_i$. The energy is transferred mostly to other cold electrons where the collisional frequency is $\nu_{ee} = \nu_{ei}/Z$. The rate of energy transfer between electrons is therefore much faster than between electrons and ions (by a factor of $\sim 10^4$). As the laser intensity increases and $v_e \rightarrow c$, and considering that $\nu_{ee} \sim v_e^{-3}$, the plasma becomes transparent for the fast electrons and practically no collisions take place. This is another reason why lower intensity ns pulses are preferred over ultrashort pulses since it is in our interest to transfer as much energy into the plasma as possible. This will be shown in the analytical model calculations in the next section.

2.2 Laser Shock Peening mechanism

LSP processing (Fig. 2.6) starts with the application of an opaque overlay on the material surface. This layer is most often made of a black or aluminium tape or some kind of paint which is easily applied and easily removed when the process is finished. This overlay has 2 primary roles. First, it serves as a sacrificial layer which protects the material surface from heat effects such as melting and oxidation caused by heat diffusion from the target area during the laser pulse absorption phase (2.1.2). The effect on the processed material itself is then purely mechanical and can be treated as such. In special cases where no protective coating is applied, the surface is exposed to various heat effects which has in general a negative impact on the resultant characteristics. Secondly, the opaque layer enhances the pressure transmitted to the underlying metallic material.

Next, the sample with the applied overlay layer is fixed in place and a transparent confinement layer is placed on top of it. The most common type of confinement layer in production processing is water since it is cheap, easily applicable, readily conforms to most complex surface geometries and is easily removed. The water is usually applied with some kind of adjustable nozzle which ensures that the flow is laminar and stable in the target area. Other confinement media such as quartz or glass can also be used. Despite producing better results than the water confinement does, these are limited only to flat surfaces and must be replaced after every shot which is highly impractical in a

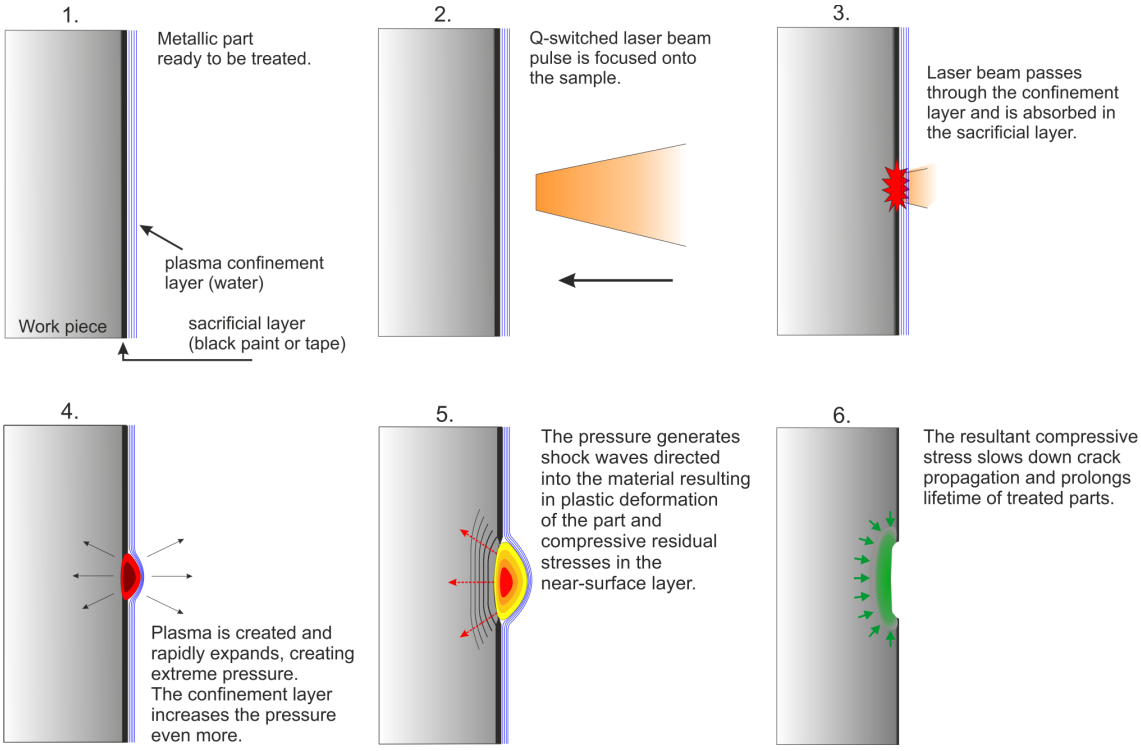

Figure 2.6: Step by step description of the LSP process.

production setting.

The part is now ready to be treated. The laser system is triggered. Before the laser pulse hits the target area, it is usually focused by a lens to a desired spot size. In more advanced systems, the beam profile is imaged by more complex system of optics to prevent beam profile distortion. The beam passes through the transparent confinement layer and strikes the opaque overlay, immediately vaporizing its surface (2.1.3). The vapour is trapped in the interface between the transparent and opaque overlays. As the pulse energy continues to be delivered, it rapidly heats and ionizes the vapour (2.1.4), converting it into a rapidly expanding plasma plume. The plasma keeps getting heated (2.1.5) and the sudden rise of pressure on the material surface due to the plasma expansion produces a high amplitude shock wave which propagates into the material. Without a confinement layer, the plasma plume would move away from the material surface and the resultant pressure would be significantly lower.

If the amplitude of the pressure wave exceeds the Hugoniot Elastic Limit (HEL), i.e. the dynamic yield strength of the material, the material is permanently plastically deformed during passage of the shock wave. As the wave propagates inside the material, magnitude of the plastic strain decreases due to attenuation. When the pressure drops below HEL, the plastic strain becomes zero and no more deformation takes place. Once the shock wave passes, the material is left with a compressive residual stress gradient created by the residual plastic strain. The residual stresses are usually highest on top of or just below the surface and then steadily decrease penetrating up to a few millimeters deep.

The post-process material characteristics such as surface roughness, residual stress depth profile, hardness, corrosion resistance and microstructure are dependent on many factors such as laser power density, pulse duration, wavelength, coverage, overlay mate-

rial and thickness, confinement medium, sample geometry and many more. The effects of individual factors will be discussed later in this chapter (2.5).

2.2.1 History of LSP

The first scientific discoveries directly leading to modern laser peening can be tracked back to the beginning of 1960s, shortly after the discovery of laser itself by Maiman in 1960 [126], when the very first pulsed laser sources started to emerge. Early investigations documented the laser pulse interaction with materials leading to creation of pressure on the material surface [127]. It turned out that the observed pressure was much higher than what could be created by the force of the laser beam alone. Studies of the phenomenon indicated that the high pressure is a result of a momentum impulse generated by expanding plasma created by vaporization of material on a surface which is rapidly heated by a short and intense laser pulse [128, 129]. In order to reach higher pressure, it was necessary to increase the laser power density by focusing the beam. To prevent dielectric breakdown of air (2.5.1), the interaction between the laser and material had to be confined to a vacuum chamber which meant that only small a number of researchers with sufficiently strong lasers were able to participate in the research [130, 131].

A major breakthrough occurred in 1970 when N.C. Anderholm discovered that much higher plasma pressures can be achieved by confining the expanding plasma against the target surface [2]. Rather than water which is most often used nowadays, Anderholm used quartz glass which he firmly placed over the target surface. With the transparent overlay in place, the laser beam passed right through it and created rapidly expanding plasma on the material surface which was now confined within the interface between the quartz overlay and the target surface. In this regime, the generated pressure was increased by an order of magnitude into the GPa levels. This meant that laser peening could now be performed in air without the need for a vacuum chamber. However, the problem of scarcity of sufficiently strong and affordable laser sources still remained.

The first study regarding improvement of mechanical properties of metals was published in 1972 by the researchers of Battelle Memorial Institute in Columbus, Ohio, USA. The study reported on beneficial effects of laser generated shocks on tensile aluminium samples using quartz overlay as plasma confinement medium [132]. More research in Battelle followed which investigated the effects on materials in more detail and showed the creation of deep compressive stresses inside the material accompanied by increase of fatigue life caused by laser peening [133, 134, 135, 136, 137] [6]. Eventually, Battelle was the first to patent LSP in 1974 with additional patents filed subsequently.

During the initial stages of development, laser peening was severely hindered by contemporary laser technology available. The Battelle laser encompassed one large room and was able to deliver laser pulses up to 500 J every few minutes at 1053 nm and 30 ns pulse duration (FWHM) [133]. In order for LSP to become economically and industrially viable, more time was needed for the laser technology to mature so that the laser sources would become more compact while having higher repetition frequency at the same time.

The first potentially viable laser arrived in 1987 when Wagner Castings Company approached Battelle with an interest to use LSP to improve fatigue properties of iron castings and powder metallurgy parts. Development of a new more compact laser design with faster repetition rate was funded aiming to demonstrate commercial and industrial viability of the process. Having the pre-prototype laser ready, Wagner Castings Company launched a marketing campaign to introduce LSP to potential industrial mar-

[6] Incidentally, large part for this thesis contains results acquired in 2018 in Ohio Centre for Laser Shock Processing in Cincinnati which has very close ties to the Battelle Institute in Columbus.

kets. In 1991, the U.S. Air force introduced the engineers of Battelle and Wagner to GE Aviation, to discuss potential utilization of LSP when dealing with the problem of foreign object damage (FOD) with fan blades of the General Electric F101 engine which propelled the Rockwell B-1B Lancer Bomber. The tests showed that after laser peening severely notched blades had the same fatigue life as new blades [3, 138]. After further development, GE Aviation licenced the LSP technology from Battelle and in 1998, in cooperation with U. S. Air Force, GE has developed the industrialized production process of the F101 fan blades and coined the phrase Laser Shock Peening using black tape as an ablative medium. Prior to that, only black paint was used in Batelle and it was called Laser Shock Processing. To meet the technical demand, part of the Battelle research team in 1995 founded the LSP Technologies, Inc. to become the first commercial supplier of laser peening systems.

With a major commercial breakthrough of LSP with the F101 engine blades treatment, the laser peening technology attracted some attention around the world and several LSP groups were created outside the USA. In the 1980s, it was the French group lead by Remy Fabbro of the Ecole Polytechnique. Fabbro visited Battelle in 1986 and carried on with research of his own [139]. The group made major contributions, both theoretical and experimental, to the overall understanding of the overall LSP phenomena, especially by investigating and modelling the shock wave propagation inside the target material under various conditions using the VISAR measuring system [1, 140, 141]. In the mid 1990s, independent of the laser peening development in USA and France, Toshiba company in Japan initiated their own investigation, lead by Yuji Sano, into mitigation of stress corrosion cracking of nuclear power plant pressure vessels. Their main contribution was the development of laser peening without protective coating (LPwC) as the pressure vessels had to be treated underwater where no coating could be easily applied [4]. Next, it was the Spanish group at the Madrid Polytechnic University lead by J. Ocana, established in the 90s. Their work encompassed both theoretical and experimental studies on various metals using low energy laser pulses [142, 143]. Later on, more countries with their own LSP programs such as China, Britain, Germany and several others joined in. In the second half of the 1990s, Metal Improvement Company (now part of Curtis Wright Surface Technologies) started cooperation with Lawrence Livermore National Laboratory (LLNL) to develop its own laser peening capabilities. One of the first applications was wing shape forming of Boeing 747-8 (Laser Forming). In Japan, Toshiba expanded its commercial applications of its LPwC for pressurized water reactors. In 2002, they included laser beam delivery via optical fibers which were connected with the underwater laser head. The whole system was redesigned to be more compact, making it possible to fit entirely into the pressure vessel [144]. Commercial use started in 2013.

Since its inception in the 1960s, the biggest obstacle laser peening faced on the way to become commercially and industrially viable were the high production and operation costs. Not only do the laser sources need to be compact and highly effective, they also need to be very robust in order to withstand suboptimal work environment full of vibrations and dust often with non-stop operational schedule. All these requirements add up to a very complex high-tech system. Add to it low processing rates, manual labour, overlay application and high training costs and it is easy to understand why the development of spread of the applications is relatively slow. At the beginning, the low processing rates were compensated by targeting low volume, high cost components as was the case with aerospace industry. In the 1990s and continuing through present day, the development was aimed at decreasing costs and increasing throughput to reach markets outside the expensive aeronautics parts. Numerous ongoing advancements addressing these challenges have reduced laser peening costs dramatically. The laser peening systems are now

being designed to handle more robust operations, the pulse rates and pulse stability are increasing and routine labour operations such as overlay application are increasingly automated. Thanks to these developments, more companies adopted laser peening to solve and prevent specific manufacturing problems. Some of the companies are Rolls-Royce, Siemens, Boeing, Pratt & Whitney, and others. More research groups are being created in order to continue in this endeavour to make laser peening more industrially viable and more widespread. HiLASE laser centre in the Czech Republic is one of these groups. With its state-of-the-art laser systems, it is aiming to further advance the LSP knowledge while looking for more affordable industrial applications.

2.2.2 Analytical model of the confined regime

The physical model presented here was proposed and developed by Fabbro et al. in 1990 [139] and since then has been accepted as a baseline for many experimental measurements in confined regime both for solid and liquid confinement media. More rigorous mathematical description including the plasma dynamic has been recently published by Zhang in [118]. In Fabbro's model, the process can be described in 3 steps:

1. **Heating phase** - laser is switched on and the laser pulse energy is being absorbed at the interface between the target and the confinement medium. Plasma is created and the generated pressure sets off 2 shock waves propagating into the target and the confinement layer and an opening at the interface is formed.

2. **Adiabatic cooling** - laser is switched off and the plasma still maintains pressure. As it continues to expand, the pressure decreases due to adiabatic cooling as the opening increases.

3. **Heated gas expansion** - for longer times, after complete recombination of the plasma, projectile like expansion of the heated gas inside the interface adds further mechanical momentum to the target.

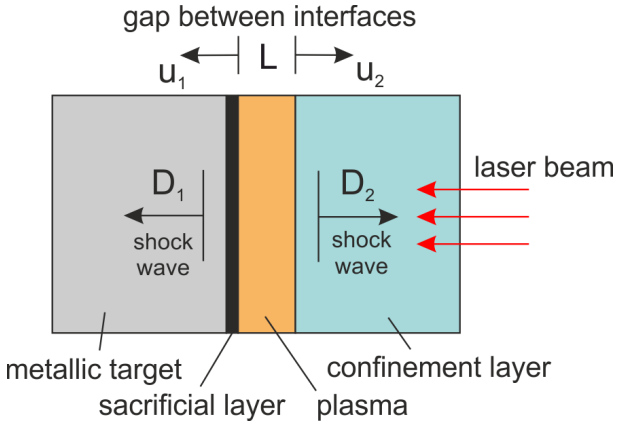

Figure 2.7: Geometry of the target assembly in confined ablation mode.

Let us now discuss these 3 steps in further detail. Fig. 2.7 shows schematic of the target assembly. Only a 1-dimensional solution to the problem will be presented.

Heating phase

The laser energy is absorbed at the interface between the target material and the transparent medium. Material in the affected zone is rapidly heated, vaporized, and ionized while being confined against the target material as the blow-off effect is being suppressed. As the pressure increases, two shock waves with velocities D_1 and D_2 propagating inside the two materials are created and an opening of thickness $L(t)$ forms on the interface. The opening is the result of the fluid motion behind the 2 shock waves which can be written as

$$L(t) = \int_0^t [u_1(t) + u_2(t)]\,\mathrm{d}t \tag{2.12}$$

where the velocities of the fluids are denoted by u_1 and u_2. The relation between the fluid velocity and the pressure force is given by [145]

$$P_i = \rho_i D_i u_i = Z_i u_i \tag{2.13}$$

where ρ_i, D_i, and Z_i are the density per unit surface, shock velocity and shock impedance of a material, respectively. We will assume that $Z_i = \rho_i D_i$ is constant. Equation (2.12) can then be written as

$$\frac{\mathrm{d}L(t)}{\mathrm{d}t} = \frac{2}{Z} P(t) \tag{2.14}$$

where Z is the reduced shock impedance

$$Z = \frac{2Z_1 Z_2}{Z_1 + Z_2} \tag{2.15}$$

After the initial ablation phase the ongoing laser energy influx is being used to increase the internal energy of the plasma inside the interface as well as to open the interface. The laser energy deposited per unit surface $I(t)\mathrm{d}t$, where $I(t)$ is the laser power density, is used to increases the plasma internal energy density $E_i(t)$ (Joules per unit volume) per unit area by $\mathrm{d}[E_i(t)L(t)]$ and as work of the pressure forces $P(t)\mathrm{d}L$. The law of conservation of energy states

$$I(t) = P(t)\frac{\mathrm{d}L(t)}{\mathrm{d}t} + \frac{\mathrm{d}[E_i(t)L(t)]}{\mathrm{d}t} \tag{2.16}$$

Only a constant fraction α of the plasma internal energy $E_i(t)$ represents the thermal energy $E_T(t)$ which is responsible for the actual pressure rise. The rest of the internal energy $(1-\alpha)E_i(t)$ is used for the ionization of the ablated, vaporized material. In the ideal gas assumption, the pressure P is related to the thermal energy E_T of the plasma by

$$P(t) = \frac{2}{3}E_T(t) = \frac{2}{3}\alpha E_i(t) \tag{2.17}$$

Substituting relation (2.17) into equation (2.16) gives

$$I(t) = P(t)\frac{\mathrm{d}L(t)}{\mathrm{d}t} + \frac{3}{2\alpha}\frac{\mathrm{d}[P(t)L(t)]}{\mathrm{d}t} \tag{2.18}$$

We obtain a system of 2 coupled differential equations (2.14)(2.18). Next, we assume the solution for $I(t)$ and $L(t)$ in the form of $I(t) = At^a$ and $L(t) = Bt^b$. Substitution into the equations and comparison of the exponential coefficients and constants gives the following relations between the A, B, a and b coefficients:

$$a = 2(b-1) \tag{2.19}$$

$$A = bB^2\frac{Z}{2}\left[b + \frac{3}{2\alpha}(2b-1)\right] \tag{2.20}$$

To obtain analytical solutions, we further assume constant laser power density I_0 ($a = 0$ and $A = I_0$) with duration τ and non-existence of the opening $L(t)$ before the laser was switched on ($L(0) = 0$). Finally, we obtain

$$P(\text{GPa}) = 0.01\sqrt{\frac{\alpha}{2\alpha+3} \times Z(\text{g/cm}^2\text{s}) \times I_0(\text{GW/cm}^2)} \tag{2.21}$$

$$L(t)(\mu\text{m}) = \frac{2\times 10^5}{Z(\text{g/cm}^2\text{s})} \times P(\text{GPa}) \times \tau(\text{ns}) \tag{2.22}$$

We see that for the time of the pulse duration with constant intensity, the pressure P in the interface opening is constant and the interface thickness $L(t)$ is only linearly dependent on the pulse duration. Moreover, equations (2.14) and (2.15) show that using confining material with very high shock impedance can only increase the pressure by a maximum factor of 1.41. Equations (2.21) and (2.22) do not explicitly contain dependence on the laser wavelength or the overlay material besides the acoustic impedance. All of these factors are, however, included in the α factor which can only be estimated based on fitting of experimental results. Typical values of α are between 0.1 and 0.4.

Adiabatic cooling

This phase starts at time $t = \tau$ when the laser pulse is switched off. To simplify the following equations for cooling, we will neglect the heat losses to the walls of the interface due to the short duration of the cooling process. The plasma will then experience an adiabatic cooling for times $t > \tau$ described by the adiabatic condition

$$PV^\gamma = constant \tag{2.23}$$

where γ denotes the ratio of specific heats for the gas. In 1D approximation the equation can be reduced to

$$P(t > \tau) = P(\tau)\left(\frac{L(\tau)}{L(t)}\right)^\gamma \tag{2.24}$$

When coupled to equation (2.14), the evolution of $L(t)$ will be

$$P(t > \tau) = L(t)\left(1 + \frac{(\gamma+1)}{\tau}(t-\tau)\right)^{1/(\gamma+1)} \tag{2.25}$$

Using equation (2.25) in equation (2.24) and considering that for ideal gas $\gamma = 5/3$, we see for example that the pressure will drop to half of its original value in time $t = 1.8\tau$. This tells us, that unlike in the case of direct ablation mode which will be discussed later, the pressure persists over a period much longer than of the laser pulse itself. We can also conclude that the main pressure peak lasts about twice as long as the pulse duration. Let us now see the effect on the impulse momentum delivered to the shockwave

$$J(t) = \int_0^t P(t)\mathrm{d}t \tag{2.26}$$

Using equation (2.14) and the fact that the pressure $P(0 < t < \tau) = constant$, we obtain from (2.26)

$$J(t) = Z\frac{L(t)}{2} = \frac{L(t)}{L(\tau)}\int_0^\tau P(t)\mathrm{d}t = \frac{L(t)}{L(\tau)}P(\tau)\tau = \frac{L(t)}{L(\tau)}J(\tau) \tag{2.27}$$

As an example, we can now see that when the pressure drops by an order of magnitude in time $t = 15.7\tau$ (2.24) accompanied by the increase of interface thickness $L(t)/L(\tau)$ by a factor of 4 (2.25), the impulse momentum increases by the same factor. Later, it will be shown that the impulse momentum is directly proportional to the plastically affected depth of the material (2.39).

Heated gas expansion

Even after complete recombination of the plasma, the heated gas can still apply pressure before reaching atmospheric pressure levels. Since the pressure is lower that the elastic limit of the material, it can no longer cause plastic deformation and thus contribute to the residual stresses. However, the additional momentum delivered to the target and the confinement medium causes their macroscopic 'cannon-ball' like acceleration. We can estimate the effect by calculating the time it takes for the system to obtain its final velocities and corresponding momentum in a laboratory frame. At time t_1 which roughly corresponds to the end of the previous cooling phase, the interface thickness is L_1, the pressure is P_1 and the corresponding internal energy per unit surface in the gas is E_1. Let us assume that the internal energy is equal to the initial energy delivered by the laser pulse decreased by energy dissipated in irreversible processes such as plastic deformation, heat conduction or lateral 2D expansion of the gas and others. The thickness of the target and the confining medium is l_1 and l_2, respectively. The equation of motion for the interface thickness can be written as

$$\frac{\mathrm{d}^2L(t)}{\mathrm{d}t^2} = P(t)\left(\frac{1}{m_1} + \frac{1}{m_2}\right) \tag{2.28}$$

where $m_{1,2} = \rho_{1,2}l_{1,2}$. Combining equation (2.28) with equation (2.14) where τ is replaced by t_1 we can calculate the time it takes to reach 80% of the final velocity [139] as

$$t_2 = \frac{6.3}{\sqrt{\frac{P_1}{L_1}\left(\frac{1}{m_1} + \frac{1}{m_2}\right)\left(\frac{2}{\gamma - 1}\right)}} \tag{2.29}$$

In order to determine the final velocities of the target and the confining medium, we use the equations for conservation of momentum and energy

$$E_1 = \frac{1}{2}m_1v_1^2 + \frac{1}{2}m_2v_2^2 \tag{2.30}$$

$$m_1v_1 = m_2v_2 \tag{2.31}$$

where v_1 and v_2 are the sought after velocities, respectively. The impulse momentum J_1 delivered during the process to the target and the confinement layer can then be derived as

$$J_{1,2} = m_{1,2} v_{1,2} = \sqrt{2E_1 \left(\frac{m_{1,2}}{1 + \frac{m_{1,2}}{m_{2,1}}} \right)} \tag{2.32}$$

2.2.3 Direct ablation mode

In the direct ablation mode, there is no confinement layer on top of the irradiated material. The pressure dependency on the laser intensity within the range of $10^9 - 10^{12}$ W/cm^2 can be estimated by an empirical relation [146]

$$P_d(\text{GPa}) = 0.393 \times I^{0.7}(\text{GW/cm}^2) \times \lambda^{-0.3}(\mu\text{m}) \times \tau^{-0.15}(\text{ns}) \tag{2.33}$$

Let us now compare the pressures from relations (2.21) and (2.33) for the intensity range of 1-100 GW/cm^2. The laser wavelength is 1.06 μm with a 10 ns pulse duration, the confinement medium is water with $Z = 1.7 \times 10^6$ g/cm^{2}s and we assume $\alpha = 0.1$. The ratio $P(\tau))/P_d$ then varies from 3.3-8.3 where the lower end is associated with the upper end of laser intensities and vice versa. For the typical laser intensity values in the order of GW/cm^2, the pressures generated in confined regime are nearly an order of magnitude greater than in direct ablation.

The second major difference between the two modes is related to the duration of applied plasma pressure. In the direct ablation mode, the pressure follows the temporal laser pulse profile due to very fast plasma expansion. In the confined mode, however, the pressure persists even after the laser is switched off during the adiabatic cooling phase as the plasma keeps opening the interface. As was shown before, the main pressure peak lasts about twice as long as the pulse duration. The mechanical impulse momentum transmitted to the target is then twice as much. Achieving the same effect in the direct ablation mode would require much higher laser intensities which is only possible in vacuum due to dielectric breakdown in standard pressure atmosphere. A solution involving vacuum is however not industrially feasible, at least for now.

2.2.4 Generation of residual stresses

Let us now move onto what happens inside the treated material itself when the outside pressure is applied. The generation of residual stresses greatly depends on the process parameters and usually follows a two-step sequence:

1. During the laser-matter interaction, the plasma expansion creates a uniaxial deformation of the irradiated area and a dilation of the surface layers

2. After the pressure wave passes, the surrounding matter reacts to the deformed area by generating the compressive stress field

The basic model to predict the mechanical effects induced by a short pressure pulse in a semi-infinite body presented here was developed by Ballard et al. in 1991 [147]. The model is based on several assumptions:

(a) shock waves propagating in a perfect elastic-plastic half space are longitudinal and plane

(b) plastic strain follows a Von Mises plasticity criterion

(c) the applied pressure is uniform on the impacted area

Using this model, one can determine the optimal process conditions for a specific elastic-plastic material and the plastic strain and residual stress fields induced by the impact pressure.

Materials undergo plastic deformations when subjected to strong shocks. The point where a material transitions from a purely elastic state to an elastic-plastic state is called the Hugoniot elastic limit (HEL). The pressure where the transition takes place is denoted by

$$HEL = \frac{1-\nu}{1-2\nu}\sigma_Y^D \tag{2.34}$$

where σ_Y^D is the compressive yield strength at high strain rate and ν is the Poisson's ratio[7]. The deformation process can then be divided into 3 steps:

1. $P < HEL$, no plastification occurs
2. $HEL < P < 2HEL$, plastic strain occurs with a purely elastic reverse strain
3. $2HEL < P$, elastic reverse strain gets saturated to $2HEL$ and plastic strain occurs. At this point, only detrimental superficial deformation effects occur

The process then follows the same chronological order of events. First, elastic deformation occurs, then a plastic one followed by an elastic release and a plastic ultimate release (Fig. 2.8). In order to cause maximum surface plastic strain while at the same time avoiding the additional superficial deformation effects, materials should be optimally treated with stresses in the $2-2.5HEL$ range.

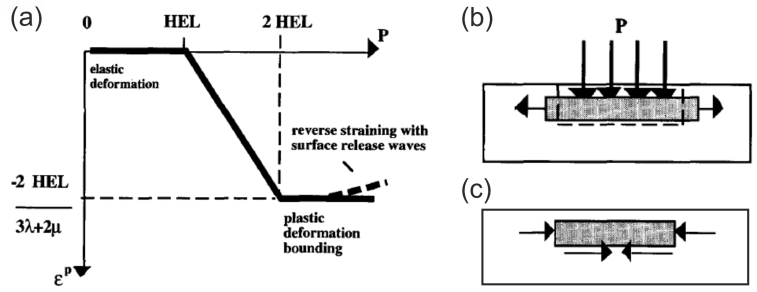

Figure 2.8: (a) Plastic deformation induced by LSP as a function of peak pressure where λ and μ are the Lame constants [147], (b) tensile stretching of the impacted area during the laser interaction [148], (c) reaction of the surrounding matter after the laser is switched off induces a compressive stress field [148].

Assuming biaxial (no shearing effects) and isotropic residual stress field and no initial residual stress, the surface residual stress for circular (radius r) and square (side a) laser spot geometries is given by [1, 149]

$$circularspot: \sigma_{surf} = \sigma_Y^D\left[1 - \frac{4\sqrt{2}}{\pi}(1+\nu)\frac{L_p}{r}\sqrt{2}\right] \tag{2.35}$$

[7] ratio of transverse contraction strain to longitudinal extension strain in the direction of stretching force

$$squarespot : \sigma_{surf} = \sigma_Y^D \left[1 - \frac{4\sqrt{2}}{\pi}(1+\nu)\frac{L_p}{a} \right] \tag{2.36}$$

where L_p is the plastically affected depth. An initial residual stress σ_0 modifies HEL of the base material and it also changes the induced residual stresses to [1]

$$circularspot : \sigma_{surf} = \sigma_0 - (\sigma_Y^D + \sigma_0)\left[1 - \frac{4\sqrt{2}}{\pi}(1+\nu)\frac{L_p}{r}\sqrt{2} \right] \tag{2.37}$$

$$squarespot : \sigma_{surf} = \sigma_0 - (\sigma_Y^D + \sigma_0)\left[1 - \frac{4\sqrt{2}}{\pi}(1+\nu)\frac{L_p}{a} \right] \tag{2.38}$$

If there is a compressive residual stress state in the base material, the plastification threshold of the material tends to increase under a laser-shock loading and allows reaching higher residual stress levels. The opposite effect can be associated with initial tensile stress.

The previous equations contain the term L_p which denotes the depth of the plastic deformation. The depth depends on given shock conditions (P and τ) and given material (HEL). It is also directly related to the dimple size which is left after the laser impact. For a Gaussian pressure profile induced by a laser pulse, the estimation of L_p then is [1]

$$L_p = \frac{C_{el}C_{pl}\tau}{(C_{el} - C_{pl})}\frac{P}{2HEL} \tag{2.39}$$

where C_{el} and C_{pl} are the elastic and plastic velocities, respectively. The estimation has been calculated with the assumption that the plastic deformation occurs only to depths where $P > HEL$. The model shows that the plastically affected depth is quasi-linearly proportional to the pulse duration τ. Many experimental studies show that the affected depths indeed increase both with P and τ but in case of τ to a much lesser extent than the model predicts.

These inconsistencies can be mostly attributed to the 1D planer geometry approximation of the model. The model does not account for the propagation of release waves as a consequence of the finite impact geometry. The phenomenon can be described as follows. At time $t = 0$, the plasma pressure is applied to the material which creates a plane longitudinal wave at the surface. The wave propagates along the surface normal and induces plastic deformation. At the same time, release waves are generated at the border of the impact. These waves are of two types: a longitudinal F wave corresponding to an edge effect due to the impossibility of a discontinuity existing between the inner and the outer sides of the impact. The second transverse wave S is created by shear occurring at the edge of the impact. The S wave forms a Rayleigh wave whose longitudinal component gets focused at the centre of the impact zone. The resulting plastification may suppress the plastic deformation from the initial longitudinal wave in the centre of the created dimple. After the Rayleigh wave passes, the underlaying matter reacts against the deformation of the affected layer and creates tensile stresses. As a consequence, a stress drop appears in the middle of the dimple (Fig. 2.9). In practice, the residual stress drop can be countered by overlapping of the laser spots.

The mechanical effects predicted by this planar model in terms of plastically affected depth L_p and surface residual stress σ_{surf} are summarized in Table 2.1

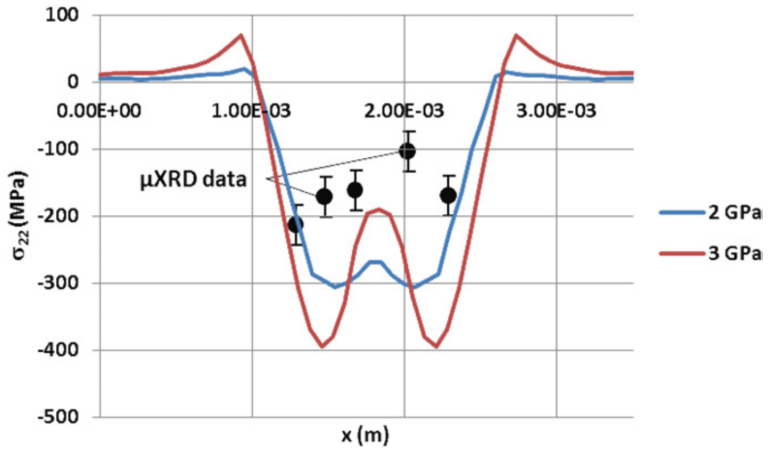

Figure 2.9: Residual stresses induced by a single laser impact on aluminium alloy 2050-T8 at $I_0 = 3.5$ GW/cm^2. Experiments versus simulation at impact pressures $P_0 = 2$ and 3 GPa [150].

When \ Then	ϵ_p (%)	σ_{res} (MPa)	L_p (mm)	Hardness (HV)	Surface depression (µm)
P increases	+	+	+	= to +	+
τ increases	=	= to +	+ +	= to +	+ +
σ_Y^D increases	-	+	-	+/-	-
a increases	=	+	=	=	=
Number of shots increases	+	= or +	+ +	= to +	+ +

Table 2.1: Influence of both laser impact (P-impact pressure, τ-laser pulse duration, a-spot size) and target (σ_Y^D-dynamic yield strength) parameters on mechanical surface states induced (ϵ_p-plastic strain, σ_{res}-residual stress, L_p-plastically affected depth) [1]. Legend: + increase; ++ large increase; – decrease; and = no effect.

2.3 Influence of processing parameters

2.3.1 Protective overlay

The importance of the protective overlay to the LSP process has been recognized soon during the initial development in the 1970s [137, 151]. Since the early works, many different coatings have been used. These coatings can be metallic or organic paints or adhesives. The influence of the protective overlay on the process is threefold:

1. Protection of the underlying material from thermal effects resulting from the laser irradiation
2. Acoustic impedance mismatch can increase the pressure transmitted to the underlying metal
3. Enhancement of the laser absorption

The first effect is probably the most important as it has large consequences for the resultant residual stresses. As was noted in (2.1.3), during the laser-material interaction

in the GW/cm^2 range, the energy deposition and the following ablation phenomenon occur only on a few micrometers of depth. The heat penetration depth ranges between 10 and 20 μm [149]. Therefore, if the protective layer is thick enough, thermal effects on the metallic underlying substrate are suppressed and the target experiences only pure mechanical loading. With no overlay, thermal effects dominate. As the heated zone is compressively plastified by the surrounding material during its dilation, it produces tensile residual stresses after cooling. The effects can be observed in Fig. 2.10b where the stresses are tensile near the surface when no overlay was applied. Furthermore, the overlay tends to move the stress profile towards the surface Fig. 2.10a which has positive effects on fatigue properties in general.

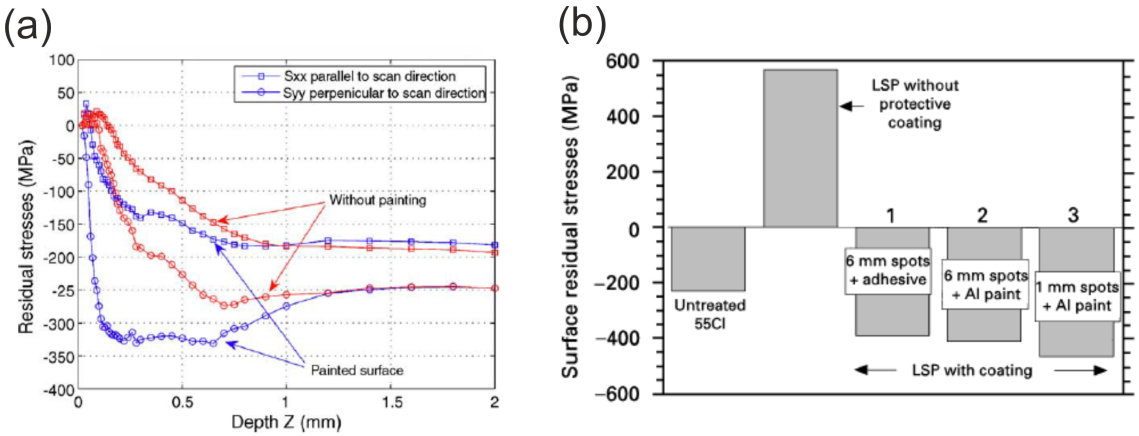

Figure 2.10: (a) Residual stress distribution induced by LSP in 6061-T6 samples with and without protective coating using a water jet arrangement [152]. (b) Average residual stress values determined at the surface of notched fatigue samples with different LSP conditions at 5 GW/cm^2 in the water-confining regime [149].

Fabbro et al. [1] studied the influence of various overlay materials on the peak pressure developed during the process. The coatings were thick enough to avoid complete ablation but thin enough to minimize impedance mismatch effects. All the materials, except for copper, probably due to lower laser absorption, show that the laser induced pressure is quite independent on the nature of the target material. This suggests that the plasma is primarily composed of the confining layer material which in this case is water as it is the only element common for all the measurements. A possible explanation could be that after establishment of some free electrons during the initial ablation phase through the multiphoton ionization process, the avalanche ionisation in the water takes over as water has lower ionization potential than the overlay material. Thus the plasma is primarily composed of the confining medium elements regardless of the overlay material. Benavides et al. [116] tried to explain this effect by suggesting that the fast electrons originate from thermally isolated surface micro and nanodefects of the irradiated material which are heated much faster than the rest of the surface. These hot spots then thermoionically emit the free electrons which trigger the avalanche ionization effect in the surrounding medium, causing its optical breakdown. Vorobyev et al. [153] report that the optical breakdown of air near metal surface results in a significant thermal energy transfer from the air plasma to the metal surface. On the contrary, there is no noticeable thermal energy transfer to the sample from the plasma in vacuum. This 'plasma assisted etching' due to enhanced thermal coupling also explains why the fluence threshold of plasma creation in vacuum is larger than in air (Fig. 2.1).

The second beneficial effect of the overlay can be considered more of a side-effect of the necessity of having a protective overlay in the first place. A mismatch in the acoustic impedance Z between the confining can increase the induced stress. By using thicker coatings with low Z compared to the base material, much higher pressure than the plasma pressure can be achieved inside the material. This phenomenon is for instance promoted in the cases when steel samples are protected by Al-based coatings. Fig. 2.11b shows an example of a 316 steel covered with a 100 μm thick Al-based coating [1, 149]. One can see that the peak pressures obtained with bare steel are very similar to those obtained with aluminium. However, the pressures are about 50% increased when the coating is used. As a result, lower power density can be used to achieve similar induced stress as compared to when no coating is used. However, such protective overlays must have very good adhesive properties to prevent spallation [154], especially in cumulative shock loadings. Spallation is a phenomenon when the overlay gets detached from the base material during the laser impact. This results into non-ideal shock wave coupling as well as very often thermal damage to the base material. Also, once the overlay is compromised, more spallation usually follows in the surrounding area especially when the laser pulse density is high.

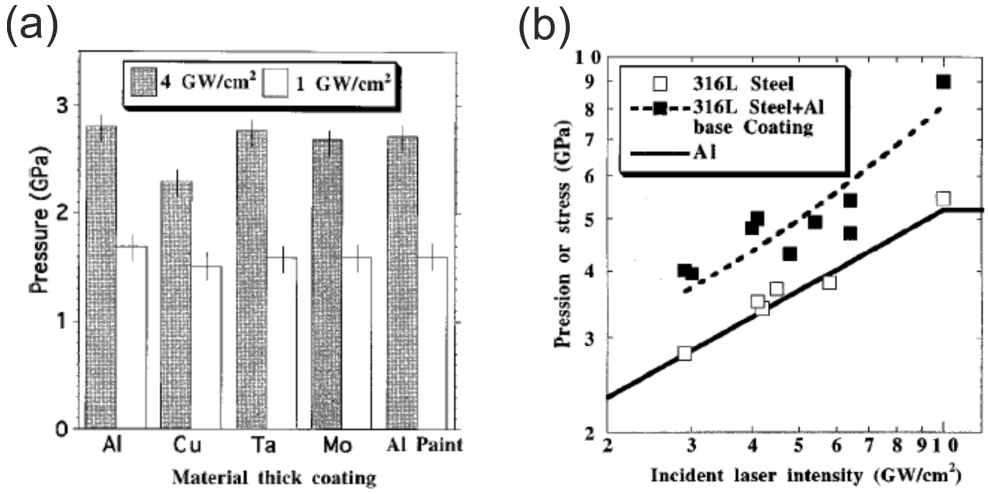

Figure 2.11: (a) Peak pressures obtained for different target materials for laser intensities 1 and 4 GW/cm^2 [1]. (b) Peak pressure levels induced by LSP on 200 μm 316L foils influenced by Al-based protective coatings [1].

The last effect has to do with the laser absorption efficiency. In the ablation section (2.1.3), we spoke about the threshold fluences that are necessary to ablate the irradiated material which leads to plasma formation and strong laser absorption (Fig. 2.1). Typical laser fluences for metals are in the range of 1-10 J/cm^2. As an example, let us take a 10 ns laser pulse with 10 GW/cm^2 intensity. Considering the fluence range, it takes 1-10 % of the total pulse energy to reach the point of plasma breakdown. With highly reflecting surfaces, the effect can be even stronger as can be observed in Fig. 2.11a in the case of copper which has very high reflectance compared to other metals. In order to prevent the energy losses, the protective coating is often opaque. Having low reflectance, the plasma is formed much sooner and the laser energy conversion efficiency is higher. Despite being highly reflective, some of the overlay types such as aluminium are still used. The reason for that is first, because of the impedance mismatch effect and second, because metallic tapes tend to withstand higher laser fluences than organic materials, making them more

suitable for applications with high pulse densities without the need to be replaced during the process.

No protective overlay

LSP is also possible without the protective overlay. The process is then called Laser Peening without Coating (LPwC). The idea emerged when classical peening with protective overlay was not applicable in certain situations such as treatment of pressure vessels in nuclear power plants [155]. These vessels are permanently under water which makes it impossible to apply the coating. As we discussed in the previous section (2.3.1), the absence of protective coating causes temperature rise in the material surface resulting in tensile residual stresses (Fig. 2.10b). However, studies showed that it is possible to obtain compressive residual stresses without protective coating when lower power densities, high pulse densities and shorter pulse durations are used [4, 156, 157, 158]. An example is shown in Fig. 2.12a. Typical process parameters for Laser Peening with and without protective coating are summarized in Table 2.2.

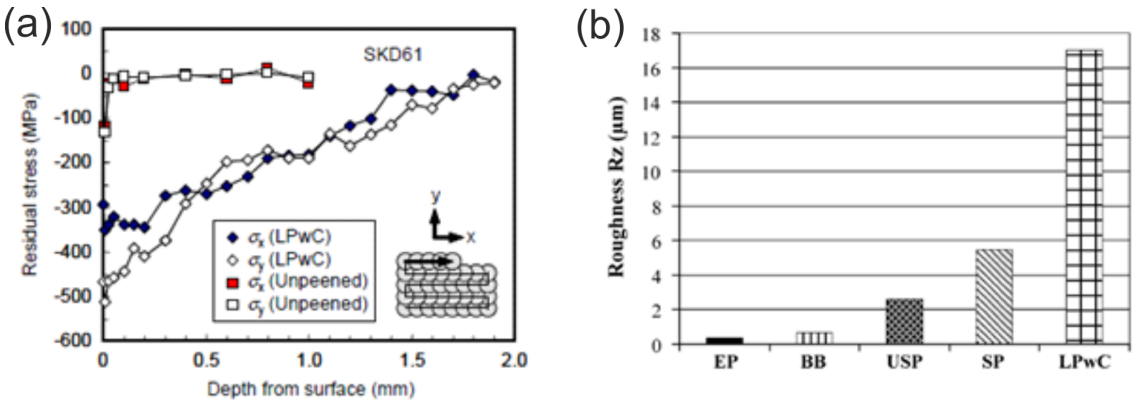

Figure 2.12: (a) Residual stress depth profile of tool steel (JIS SKD61) after LPwC with low pulse energies and high pulse densities used [4]. (b) Surface roughness after various surface treatments in Ti–2.5Cu (EP = electropolishing, BB = ball-burnishing, USP = ultrasonic shot peening, SP = shot peening) [159].

	with coating	without coating
Laser oscillator	Nd:glass (1.05 µm)	Nd:YAG (532 nm)
Pulse duration	< 100 ns	< 10 ns
Pulse energy	≤ 100 J	40 ∼ 250 mJ
Spot size	≤ 10 mm Φ	≤ 1.2 mm Φ
Delivery system	Mirror	Fiber or mirror
Developed in	USA, France	Japan

Table 2.2: Typical laser parameters for LSP with and without protective overlay.

Surface vaporization and melting is still induced by LPwC even with much smaller power and shorter pulse duration compared to LSP. This leads to resolidification of droplets leading to increase of surface roughness [159, 160]. Other methods such as

shot peening, ball burnishing and ultrasonic impact peening usually introduce roughness smaller in magnitude than LPwC as shown in Fig. 2.12b. This rougher surface associated with LPwC may lead to more significant deterioration in resistance to fatigue-crack initiation and corresponding fatigue life than that with the other treatments.

Another side-effect of the underwater environment is that the most commonly used wavelength can no longer be used or with very little effectiveness. This is due to strong absorption of the near IR wavelength of Nd:YAG laser (1064 nm) in water. The effect is not significant when only a thin confining layer of water of a few mm is used and the rest of the space between the treated sample and the beam delivery optics is air which is almost 100% transparent. But when a significant part of the space is occupied by water, the absorption becomes non-negligible[8]. The most common solution is frequency doubling of the Nd:YAG laser producing the 532 nm of green light which is less absorbed by water (Fig. 2.13) [161]. The process is referred to as second harmonic generation (SHG).

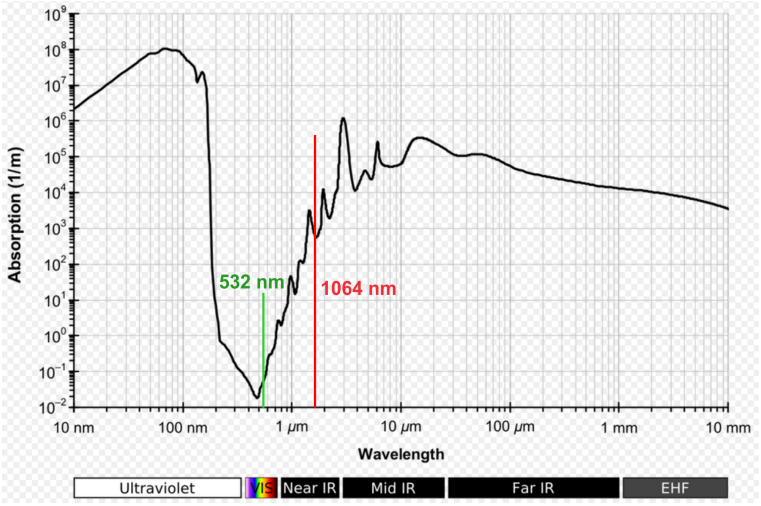

Figure 2.13: Liquid water absorption spectrum across a wide wavelength range [161].

2.4 Confinement medium

The introduction of the confinement regime in 1970 was a breakthrough in the LSP technology. It removed the necessity of the interaction taking place in vacuum and opened many real application possibilities. The crucial role of the confining medium is prolonging of the pressure effect created in the laser-matter interaction which consequently leads to more plastic deformation and higher residual stresses. As the plasma is trapped between the target and the overlaying water, the peak pressure level can be increased by a factor of 10 and pressure duration by a factor of 3 compared with direct ablation mode. Fig. 2.14 illustrates that the pressure decay is also much slower when compared to the laser pulse temporal shape.

Various types of confining media have been tried, both solid state and liquids. Among the most common solid state media are BK7 glass [162, 163, 164] and quartz [133]. These

[8]Beam dumps of high-power near IR lasers are often externally cooled vessels filled with water which fully absorbs the laser pulse.

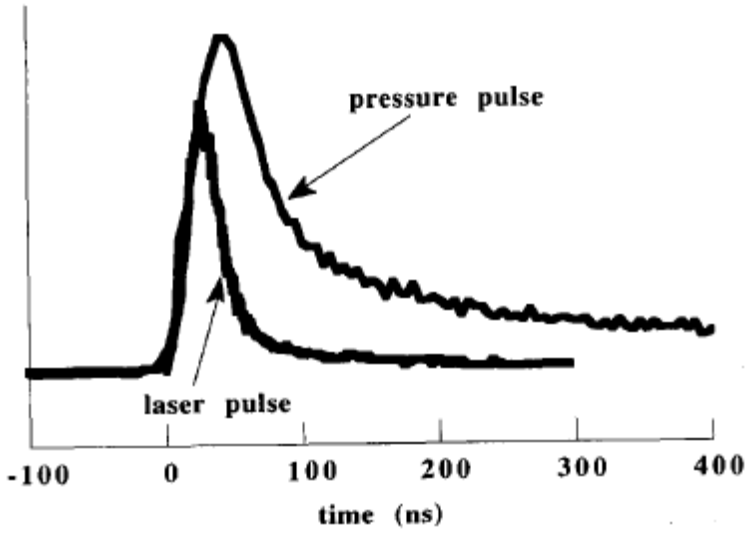

Figure 2.14: Gaussian laser pulse and resulting pressure pulse submitted to the target [148].

media were used especially in the early years of LSP when high energy (~50 J) low frequency (~0.1 Hz) laser pulses have been used. Also, BK7 has a higher shock impedance and larger breakdown threshold than the commonly used water. The reason for the decrease in utility nowadays is because these types of confining media are not reusable as they often take optical damage from the laser impact. This makes the process rather slow, especially with the high frequency lasers (~20 Hz) which we have at our disposal today. Among the liquid confining media used are water and silicon oil [162] with water being the most commonly used confining medium nowadays. There are several reasons for that. First, water is very easy to work with and can be easily delivered to the treated sample. Second, it self-replaces itself due to its constant flow, taking away any debris from the sacrificial layer. Third, it is suitable for peening complex non-flat geometries. And four, its density and acoustic impedance is compatible with most materials.

Generally, the choice of confining medium depends on the density and speed of sound in the target which is related to the reduced acoustic impedance given in equation (2.15). An instance when water as a confining layer is not suitable may arise due to its low evaporation point when the treatment is done at higher temperatures. In such case, the silicon oil is more suitable choice. In some cases, no confining layer is used when the laser intensity is too large and would case optical breakdown of the confining medium [165, 166].

2.5 Influence of laser parameters

2.5.1 Power density

We have mentioned earlier that the LSP process comprises a large amount of processing variables. Some of these variables such as laser wavelength and pulse duration are often fixed on one or a few discrete settings based on the laser system used. The main adjustable laser parameter then becomes laser power density defined as

$$I(\mathrm{GW/cm^2}) = \frac{E(\mathrm{J})}{\tau(\mathrm{ns}) \times A(\mathrm{cm^2})} \tag{2.40}$$

where E denotes the laser pulse energy, τ the pulse duration and A the spot size. Assuming that the pulse duration is fixed, there are generally 2 ways to change the power density. Either by changing the pulse energy or by changing the spot size. The former can be done either by attenuator or by varying the delay between the laser signal pulse and the pump and the latter can be done via changing the distance between the laser focusing element and the sample.

In order to create residual stresses, the pressure has to exceed the dynamic yield strength σ_Y^D of the material to cause plastic deformation at the surface. Opposite to that, the pressure cannot exceed the dynamic ultimate tensile strength of the metal σ_U^D to prevent spallation which leads to dramatic reduction of fatigue life of materials [167, 168, 169]. The reason for this reduction is the formation of internal cracks in the specimens during the laser treatment which act as large crack initiators and are larger than any surface discontinuities. Thus we have for the pressure [163]

$$2\sigma_Y^D < P < 2\sigma_U^D \tag{2.41}$$

Using equations (2.41) and (2.21), we obtain the optimal power density

$$\frac{4(2\alpha+3)}{\alpha}\frac{(\sigma_Y^D)^2}{Z} < I < \frac{4(2\alpha+3)}{\alpha}\frac{(\sigma_U^D)^2}{Z} \tag{2.42}$$

Dielectric breakdown

In addition to the just mentioned hard upper power density limit which is imposed by the material, there is another soft restriction which is imposed by the laser-matter interaction dynamics. The phenomenon is referred to as dielectric breakdown and occurs when the power density exceeds certain threshold, usually around 5-8 GW/cm^2. During the breakdown, a parasitic plasma is prematurely created further from the target surface and acts as a screening to the laser pulse. This limits the amount of energy that actually reaches the target behind.

As mentioned earlier (2.1.4), there are two mechanisms which lead to plasma formation – multiphoton ionization (MPI) and avalanche ionization (AI). The latter requires one or more free electrons in the focal volume[9] to get going which can be supplied either by the MPI process or by thermal ionization of absorbing impurities. One can speak of dielectric breakdown when the free electron density exceeds $10^{18} - 10^{20}$ cm^{-3}. The breakdown eventually happens in every medium as long as there are atoms present. The difference between various media such as air, water, glass, etc. is the power density at which the breakdown occurs. The phenomenon is of big importance in high peak power laser science where damage caused by the laser pulses to the optics is a common occurrence and is referred to as Laser Induced Damage Threshold (LIDT). Fig. 2.15 shows an example of an optical element damaged by high intensity laser pulse.

In order to determine the irradiance required to cause the optical breakdown, one needs to solve the rate equation which describes the free electron density evolution [163]

[9] Very often in laser science, it is necessary for the laser beam to go through focus (e.g. relay imaging) without being distorted by the optical breakdown of the medium. The focal point then has to be placed into vacuum. It is also the same reason why the first LSP tests had to be conducted in vacuum chambers before the invention of the confinement regime. The optical breakdown of air would occur before high enough power density on the target could be achieved to produce the pressure necessary to cause plastic deformation of the material.

Figure 2.15: Laser induced optical damage in a laser window caused by high laser fluence.

$$\frac{dn_e}{dt} = \left(\frac{dn_e}{dt}\right)_{MPI} + \eta_{casc} n_e - \eta_{diff} n_e - \eta_{rec} n_e^2 \tag{2.43}$$

The first two terms on the right-hand side describe the electron generation through MPI ($(dn_e/dt)_{MPI}$) and AI ($\eta_{casc} n_e$), respectively. The third term accounts for the free electron diffusion out of the focal volume ($\eta_{diff} n_e$) and the last term addresses recombination ($\eta_{rec} n_e^2$). Once the critical free electron density is reached, plasma is created and the laser gets strongly absorbed[10].

Let us now focus on the water confinement regime. Studies [1, 170, 151, 141] indicate that the pressures generated by the laser impacts with respect to the power density follow the trend set by the analytical model (2.21). Fig. 2.16a shows that the pressure rises with the power density until a point of saturation is reached which coincides with the critical power density when the breakdown plasma is formed. After that, the pressure no longer rises and is kept constant as part of the laser pulse is shielded. The high variance in the peak pressure after the critical power density is caused by the stochastic nature of the exact moment when the breakdown plasma is formed.
Fig. 2.17 shows snapshots of the process which were taken by a frame camera with 5 ns exposure time during the water confinement regime. At low power density (< 2 GW/cm^2), no plasma breakdown occurs (Fig. 2.17a). At higher power densities, the breakdown occurs at the outer water surface and the plasma at the sample-water interface is switched off by the screening effect (Fig. 2.17b and 2.17c).

When the breakdown occurs, the laser pulse duration impinging on the target can be considered as shortened (Fig. 2.18a). At high power densities which depend on the laser pulse parameters and the confinement layer used, the breakdown happens before the peak of the laser pulse is reached (Fig. 2.18b). Let us stick to our current example of 25 ns long laser pulses at 1064 nm and water confinement. In the 2-10 GW/cm^2 range, the maximum laser intensity reaches the target and the pressure is increasing (Fig. 2.16a). As the power density keeps increasing and the plasma breakdown occurs, the shortened laser pulse reaching the sample translates into shortened pressure wave propagating inside the material. The situation is covered in Fig. 2.16b, where 2 laser wavelengths of 1064 nm and 355 nm have been investigated. One can also see that the water breakdown occurs sooner for the shorter wavelength which will be further discussed in the following section (2.5.2).

[10] One can easily observe the screening effect of the plasma when a high intensity laser is focused in air and the pulse energy is measured in a safe distance in front of and behind the laser focus. One will find out that there is very little energy left from the original pulse as it gets shielded mid-air and the pulse energy is

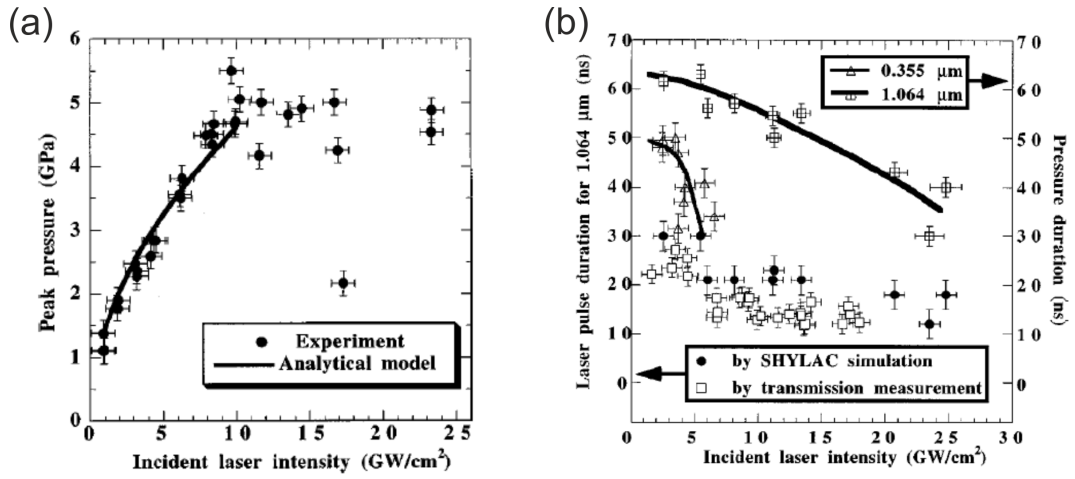

Figure 2.16: (a) Peak pressure variation vs incident peak laser intensity in Al target confined with water with 25 ns pulse duration. Continuous curve: analytical model given by Eq. (2.21) with $\alpha = 0.3$ [1]. (b) Variation of pulse pressure duration vs laser intensity at 1064 nm and 355 nm (measured with VISAR) [1].

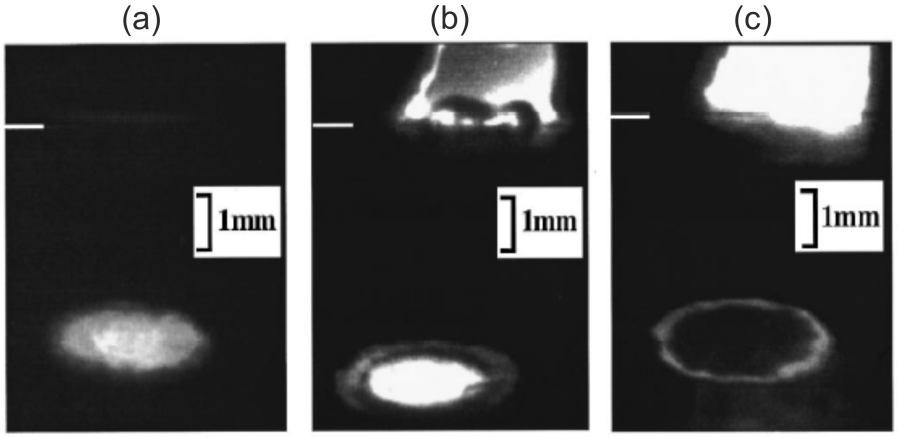

Figure 2.17: Examples of breakdown and confined plasma photographs obtained with a frame camera. Horizontal bar represents the water surface. (a) $I_0 = 2$ GW/cm^2, observation time: at peak laser intensity. No plasma at water surface. (b) $I_0 = 28$ GW/cm^2, observation time: in the laser rise time, before plasma breakdown. The water surface plasma increases in luminosity. The confined plasma is still readily heated. (c) $I_0 = 28$ GW/cm^2, observation time: after breakdown. The outer plasma disappears, only an outer ring remains [1].

In practice, the situation can be improved by artificially steepening of the pulse front. The technique is called pulse slicing and is being employed by fast switching of Pockels cells interacting with the polarized laser light. Slicing of the pulse front causes higher power density to reach the target before the plasma breakdown occurs which in turn produces higher pressures inside the target. Fig. 2.19 shows peak pressure measurements as a function of the power density for a water confinement mode and two different pulse

absorbed in the plasma via the inverse bremsstrahlung mechanism or it gets reflected.

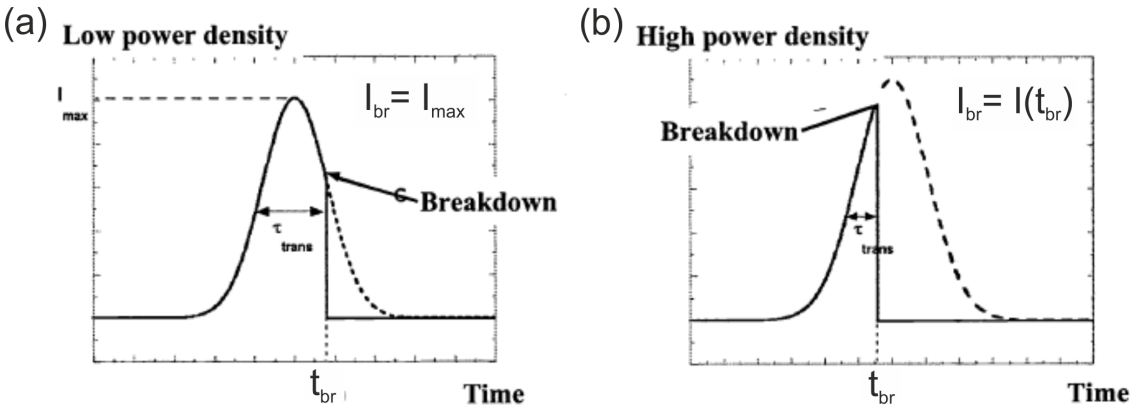

Figure 2.18: Plasma breakdown in the laser pulse time frame. (a) At low intensity, the plasma breakdown occurs in the falling part of the incident laser pulse at time t_{br}. (b) At high power density, the breakdown occurs in the rising part of the incident laser pulse. The width of of the transmitted part of the laser pulse is marked τ_{trans} [170].

temporal shapes: a classical Gaussian pulse and a sliced pulse with short rise time (SRT) [171]. While the Gaussian unsliced pulses would cause pressure saturation at around 4 GW/cm^2, the sliced pulses would saturate much later at 10 GW/cm^2. The peak pressure generated in the target material was thus larger with the sliced pulses. The effect is very beneficial since higher pressure in the material causes higher residual stresses.

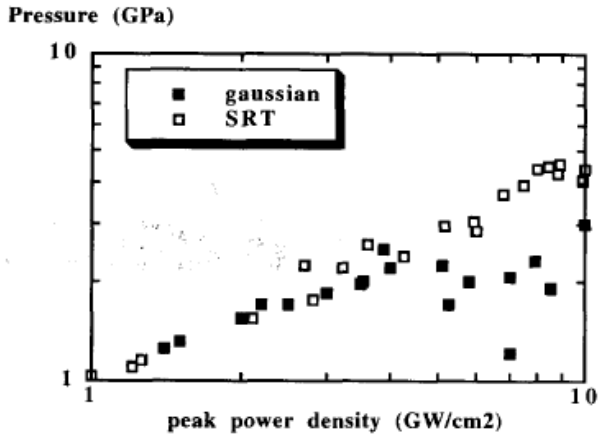

Figure 2.19: Peak pressure levels as a function of the peak power density for the water confinement mode using Gaussian and short rise time (SRT) pulse shapes [148].

2.5.2 Wavelength

The most commonly used lasers in the LSP industry up to date are based on the Nd:YAG solid state active medium which produces the fundamental wavelength of 1064 nm in the near infrared spectrum (NIR). Other commonly used wavelengths in the visible spectrum (VIS) are then acquired from this basic wavelength through second (SHG)[172] and third harmonic generation (THG)[173] using non-linear crystals. The conversion efficiency for SHG is usually capped at around 50-60% and at 30-40% for THG.

The wavelength of the laser pulse has direct impact on the laser-matter interaction in the LSP process. The effect in the confined regime can be characterized as two-fold. First, it affects the pressure saturation level and second, it affects the pressure pulse duration that propagates into the sample. Fig. 2.20a shows peak pressure measured against the incident power density for four different wavelengths. The pressure reaches saturation in all cases but the threshold power density and saturation pressure magnitude decreases with wavelength. On the other hand, for intensities below threshold, shorter wavelengths are slightly more efficient for pressure generation when compared to longer ones despite the lower ability of shorter wavelength photons to be absorbed by inverse bremsstrahlung. One of the reasons can be lower reflectance of the incident light but this is highly dependent on the material or the protective coating. A more generally applicable explanation seems to be that lower wavelengths enhance the MPI process which stands at the initial plasma creation which than absorbs the laser pulse and creates the pressure due to its expansion (2.1.4). The very same MPI process at the water surface however causes that the parasitic plasma breakdown occurs earlier with shorter wavelengths which limits the amount of energy that reaches the sample surface. In the case of the very short wavelengths (here 308 nm), the recoil pressure produced cannot exceed 2.5-3 GPa. This limits the range of materials where such lasers can be used. If the pressure is not high enough to cause the plastic deformation, no dislocations driving the residual stresses will be created and the process has no beneficial effect [4, 155, 156].

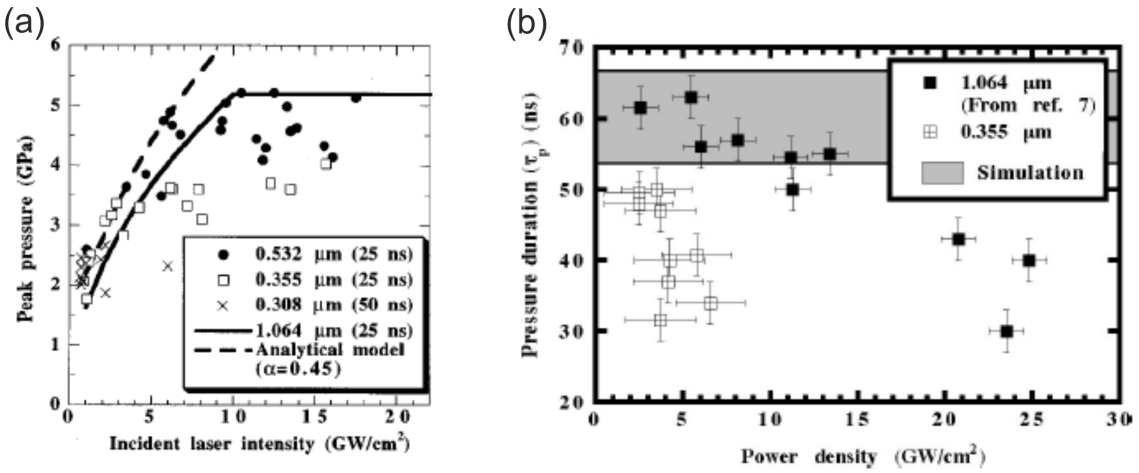

Figure 2.20: (a) Peak pressure variation vs laser power density for laser wavelengths (and duration) of 1064 (25 ns), 532 (25 ns), 355 (25 ns), and 308 nm (50 ns) [1]. (b) FWHM (τ_p) of shock-wave profile from the VISAR material velocity measurements as a function of power density for 1064 and 355 nm laser wavelengths [141].

Fig. 2.20b shows the shock-wave duration from the material velocity measurements as a function of power density at 1064 nm and 355 nm. The incident laser pulse duration was 25-30 ns. In both cases, the pressure pulse duration decreases as the power density increases. But the decrease occurs sooner in UV than in IR and the drop in UV is sharper. Thus the duration of a laser pulse irradiating the confined target is reduced when the power density increases and stays shorter in UV than in IR at the same incident power density. The reason is the plasma breakdown at the water surface which screens the laser pulse and which occurs at lower power density at shorter wavelengths.

It seems that there is not much reason to use anything besides the fundamental Nd:YAG laser wavelength of 1064 nm. Especially when one does not have to deal with

the energy loss during the wavelength conversion processes. However, as we have already mentioned in section (2.3.1), the fundamental wavelength is not suitable for underwater peening due to its high absorption in water (Fig. 2.13). The choice of proper wavelength is therefore governed by the specific application rather than by the material being peened. An example of such application is the peening of nuclear power plants in Japan which has to be performed underwater [4, 155, 156] or possibly peening of ship hulls to prevent various corrosion effects which is one of the objectives of this thesis.

2.5.3 Pulse duration

Typical pulse durations used for LSP lie in the range of 1-100 ns. The reason for the upper limit is that for too long pulses, the target will be thermally affected even when protective overlay is used because the hot plasma will be sustained for too long and transfer of heat will occur. Another reason is related to target thickness. The duration of the pressure is directly related to the pulse duration. Usually, it is about 2-3 times longer (Fig. 2.14). Longer lasting pressure means that the pressure wave will reach deeper inside the target before being attenuated resulting in deeper residual stresses. When the target is thin (a few mm), the pressure wave will get reflected at the other side of the material, sending a refraction wave back inside the material, causing tensile stresses and effectively lowering the efficiency of the process. If the pulse duration is too short (<0.1 ns), the laser pulse does not interact with the ablated material and the pressure effect of the rapidly expanding plasma is absent [174]. In this regime, the material is effectively ablated but no plastic deformations and thus residual stresses occurs. Fig. 2.21a shows peak pressures generated versus the laser power density of 3 different pulse durations. While the magnitude of the peak pressures is independent on the pulse duration, the saturation pressure increases with shorter laser pulses.

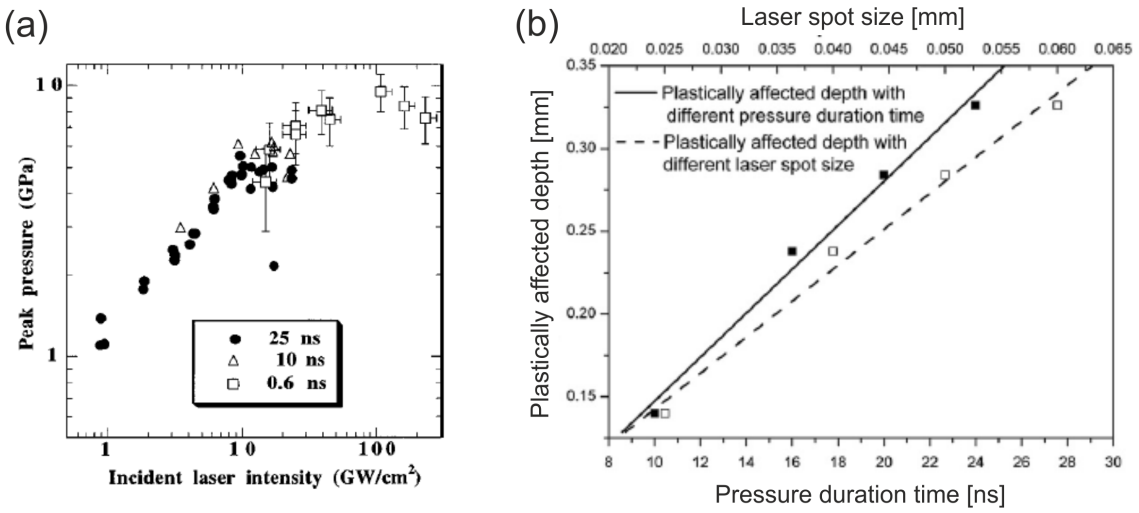

Figure 2.21: (a) Peak pressure variation as a function of peak incident laser intensity for laser pulse duration of 25, 10, and 0.6 ns [1]. (b) Plastically deformed depth as a function of laser spot size and pressure duration [175].

Based on the analytical model (2.2.4), the pulse duration has a direct effect on the plastically affected depth caused by the laser impacts since it affects the pressure wave duration (2.39). The trend can be observed in Fig. 2.21b. One also needs to realize that even if the dimple size increases, the surface residual stress remains constant or increases

slightly [175].

It is interesting to note that experiments with femtosecond laser pulses to produce laser driven shocks inside the material have also been performed [176]. Due to extremely high power densities (~PW/cm^2), the experiments have to be conducted in a vacuum chamber. In case of low energy femtosecond pulses and low power densities (~GW/cm^2), no vacuum is needed [177, 178]. The pressure in these cases is generated by the ejected material which causes compression of the material surface.

2.5.4 Multiple laser impacts and overlapping

It has been shown that multiple laser shocks have significant influence on improvement of the residual stresses induced in the treated material [179, 180, 181, 148, 182, 150, 183]. It is due to the fact that the higher the number of impacts, the higher the plastic deformation of the treated surface until a point of saturation is reached [184]. Fig. 2.22a shows surface deformation of 2050-T3 and 2053-T8 aluminium alloys [150]. In one case (T8), a decrease in depth per impact with the number impact loadings is found. In the case of T3, the depth per impact exhibits constant value.

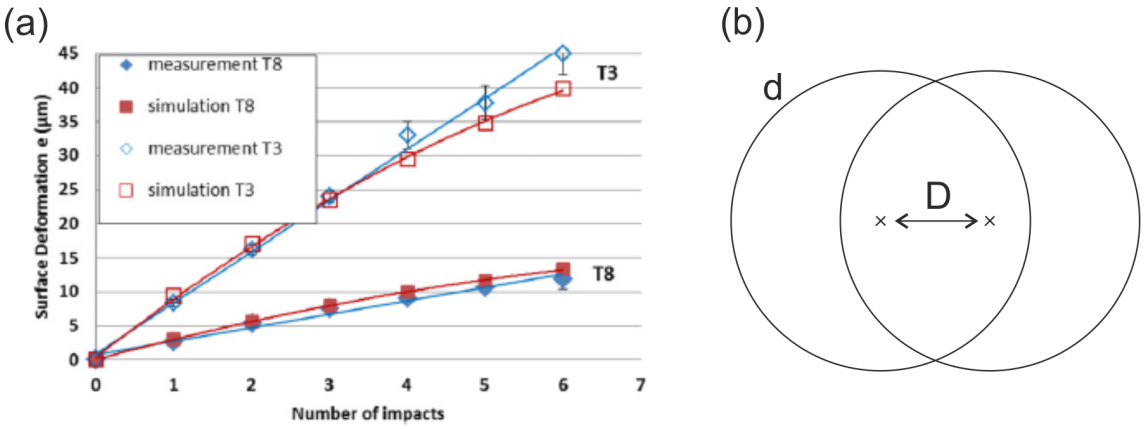

Figure 2.22: (a) Surface deformations induced by 1–6 laser impacts at I_0 = 6 GW/cm^2 (P_0 = 4 GPa) on 2050-T8 alloy [150]. (b) Laser spot overlap.

Due to the high power density requirements (2.5.1) and limitations of available laser systems, the effect of multiple impacts is often used in the form of overlapping to cover larger areas. In classical SP, the coverage ratio is an important factor in optimizing the generation of the residual stress fields. A similar effect also applies to LSP except that in case of SP, the coverage rate is determined statistically while in the case of LSP, it can be done precisely since one can control the exact position of every laser impact. The overlap ratio can be calculated as

$$overlap\ ratio = \frac{d - D}{d} \tag{2.44}$$

where d denotes the spot diameter (or in the case of square spot the square side) and D is the distance between the centres of neighbouring spots as shown in Fig. 2.22b.

Investigations showed (Fig. 2.23) that an increase in the coverage ratio (number of shots) leads to the residual stresses reaching deeper inside the material [1, 180, 148, 183]. This phenomenon may result from a purely elastic propagation of shock waves in the

pre-stressed layers. These have already been plastically deformed meaning that the consecutive shocks are less attenuated and thus reach deeper inside the material. Overlapping of the laser shots also helps to smoothen out the uneven residual stress distribution produced by a single shot impact (Fig. 2.9) on larger treated areas. Investigations also showed that there is a relatively uniform distribution of residual stresses across the overlapped regions after LSP. No indications of tensile residual stresses in the overlap region has been reported.

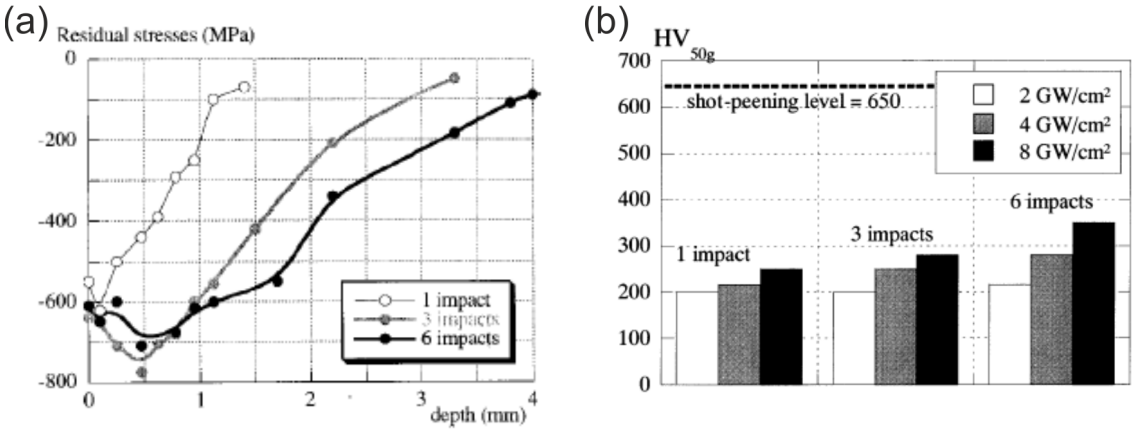

Figure 2.23: (a) In-depth residual stress profiles by LSP on 35CD4 steel (10 Gw/cm^2, 30 ns) showing the influence of the number of local impacts [1]. (b) Vickers measurement of hardness induced by SP and LSP for 1, 3 and 6 laser impacts [182].

It was also reported that multiple laser impacts also have an influence on hardness of the treated sample [182, 183]. Fig. 2.23b shows work hardening levels found by Vickers microhardness tests. It is also worth noting that even though work hardening levels increase with high laser intensities and numerous laser impacts, they remain smaller than after SP treatment, indicating a lower yield strength for the laser peened surface.

2.5.5 Laser spot size

The first obvious effect the laser spot size has is that it directly determines the power density. For a fixed laser pulse energy, one can change the power density simply by changing the distance of the sample and the laser focusing optics as described in equation (2.40). Similarly, by varying the lens distance and adjusting the laser pulse energy, one can easily achieve various laser spot sizes with the same power density.

A second, less obvious effect can be observed in the pressure wave propagation. A small diameter shock wave expands as a sphere which then attenuates at a rate of $1/r^2$ [185]. A larger diameter shock wave, however, behaves like a planar front and attenuates at a rate $1/r$. The situation is depicted in Fig. 2.24. The net result is that planar shock waves propagate further into the material as less energy gets lost due to attenuation and deeper compressive stresses are produced [186, 187].

Different spot sizes will also have an impact on the residual stress distribution within the created dimple. Assuming uniform power density distribution, larger spots will produce more uniform stress fields than their smaller counterpart of the same power density. Furthermore, the release waves which are generated on the laser impact boundaries will be affected by the spot size (2.2.4).

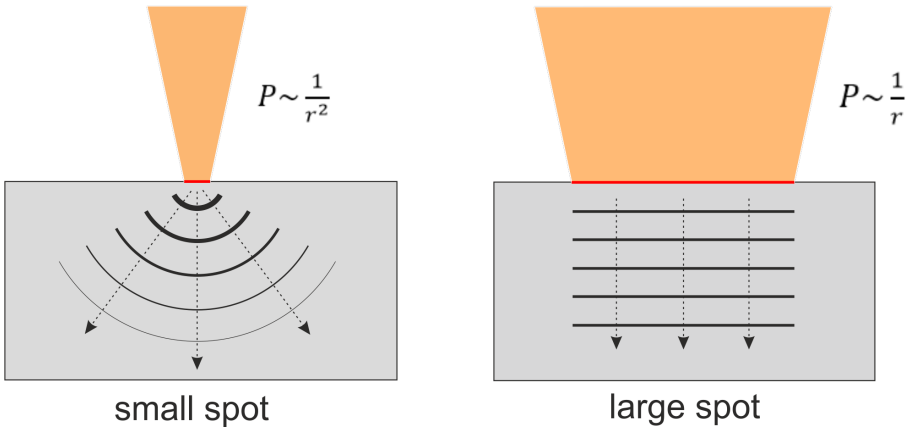

Figure 2.24: Pressure attenuation rate for small and large spot sizes.

2.5.6 Spatial beam profile and scanning strategy

The most commonly used spatial beam profile in the LSP process is circular profile[11]. Nevertheless, studies have shown that using square shaped laser beam is superior and yields better results [181, 188, 189, 190, 191, 192, 193]. It was observed that circular spots in a single impact arrangement cause a pressure drop in the middle of the impact area [150, 1]. The effect is much less pronounced in the case of square laser spots [181]. As we discussed in the previous section (2.5.4), non-uniform residual stresses caused by singular laser impacts can be avoided by proper overlapping. But even if the laser spots are sufficiently overlapped to cover the whole treated area, the total power density distribution for the circular and square beam shape can never be made identical due to the inherent geometrical restrictions. An example of 50% overlap and how it affects the total power density distribution for the two spot shapes is shown in Fig. 2.25. While every area is hit exactly 4 times in the case of the square spot, the total power density distribution is more complicated in the case of circular spot. Obviously, the situation will be different for different overlaps but the effect of square spots on higher uniformity of local residual stresses remains.

When it comes to patterning strategy, there are 3 strategies that are generally used. The first one is a simple zigzag pattern where the overlapping of neighbouring pulses happens all in one take (Fig. 2.26a). This strategy is often employed in LPwC (2.3.1) where no protective overlay is used or when the protective overlay is strong enough to withstand multiple shots. Such an overlay can for instance be an aluminium tape. As a result, this strategy is fast as the overlay does not need to be replaced during the process. The second strategy in Fig. 2.26b is a scanning pattern similar to the zigzag one but all the lines now start at the same side. This pattern is obviously slower but the advantage here as that with correct timing, it is guaranteed that each line will be directly above the previous lines with no horizontal offset between individual shots. The zigzag pattern generally lacks this feature. The third strategy depicted in Fig. 2.26c relies on sequential overlapping of several patterns (in this case 4) which are mutually shifted with respect to one another to achieve the target overlap. Individual sequences have zero or very small overlap in order to prevent the overlay disruption (i.e. black vinyl tape) and the overlay

[11] Typical lasers used for LSP are Q-switched and YAG crystal based. These crystals are in the shape of elongated rods which give the generated beam its characteristic circular shape. The reason the crystals are rod shaped is because they are easier to produce and they are also easier to uniformly pump using flash lamps.

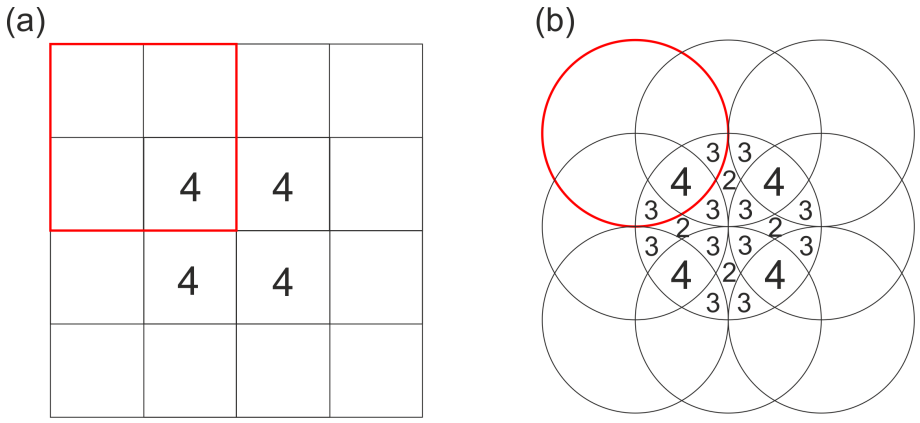

Figure 2.25: Overlap ratio 50% for (a) square and (b) circular laser spots. The numbers indicate how many times a particular area in the pattern was hit.

is replaced between each of the sequences. A common overlap used is 50%. This strategy is more time consuming but the sample surface is protected against heat effects.

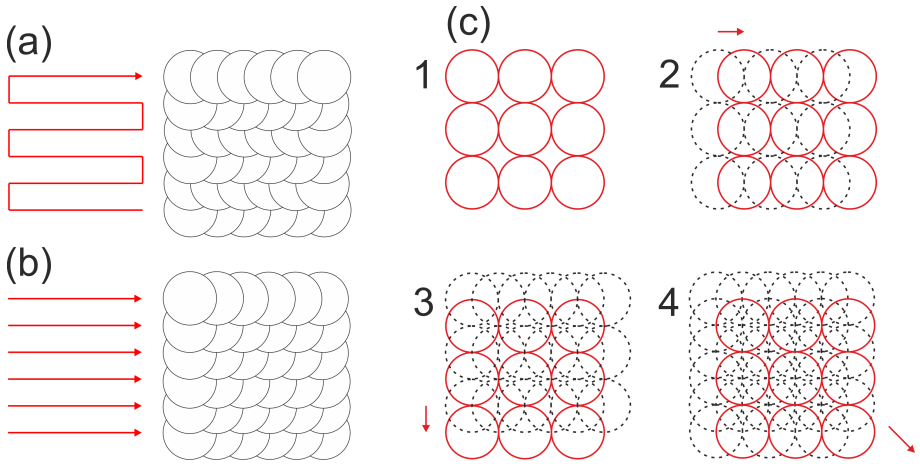

Figure 2.26: Scanning strategies: (a) zigzag pattern, (b) scanning pattern and (c) overlapping of 4 mutually shifted sequences.

Even though the coverage and resultant pattern is the same with all three strategies, studies show that the residual stress distribution varies as a result of different sequencing [194, 195]. The experimental and numerical results indicate that the zigzag and scanning patterns cause a residual stress anisotropy as a collateral effect. It is also numerically shown that using a random pattern significantly decreases the anisotropy [195]. From a practical point of view, however, using a random pattern algorithm has several disadvantages. First, the whole treatment would take much longer as lower pulse repetition frequencies would have to be used with respect to the maximum sample movement speed. Secondly, random patterning can cause local tearing (spallation) of the protective tape when too many spots are randomly assigned on the same place. Such tears tend to get larger as the peening continues which very often compromises the whole sample.

Chapter 3

Experimental methods, procedures and devices

This chapter covers the general experimental procedures as well as devices used throughout the course of this work. The laser treatment of samples and subsequent analysis took place partially in the laboratories of HiLASE laser centre in the Czech Republic and the Mechanical and Materials Engineering Department at the University of Cincinnati (UC), Ohio, USA.

3.1 Aluminium alloy 5083-H116

Due to its light-weight properties and the growth of fabrication processes, many industries seek to use aluminium as an alternative for steel in many applications. The mechanical properties of aluminium are derived from alloying elements such as copper, manganese, silicon, magnesium, and zinc. The alloys are then categorized based on the primary alloying element (Table 3.1). Additionally, aluminium can be cast or wrought.

Aluminium alloy series	Principal alloying element
1xxx	Minimum 99.00% of aluminium content (commercially pure aluminium)
2xxx	Copper
3xxx	Manganese
4xxx	Silicon
5xxx	Magnesium
6xxx	Magnesium + Silicon
7xxx	Zinc
8xxx	Other elements (e.g. iron)

Table 3.1: Aluminum wrought alloy series and its principal alloying element. Adapted from [196].

The alloys are supplied in different tempers which can be divided into two principal groups of heat treatable and non heat treatable alloys. Heat treatable alloys whose temper designation starts with T achieve their strength and mechanical properties via heat treatment followed by cooling and natural or artificial ageing. On the contrary, non heat treatable alloys whose designation starts with H acquire their strength and mechan-

ical properties through cold working (rolling, extruding, etc.). Cold working or strain hardening is a process of making a metal harder and stronger through plastic deformation. When a metal is plastically deformed, new dislocations are generated which interact with each other, becoming pinned and tangled. The result is decrease in the dislocation mobility and strengthening of the material. An important aspect of the process is that sufficiently low temperature must be maintained so that the atoms cannot rearrange themselves, thus cancelling the strengthening effect. Common tempers for non heat treatable alloys are summarized in Table 3.2.

Temper	Description
O	Annealed, recrystallized. Temper with the lowest strength and greatest ductility.
H1	Strain hardened.
H2	Strain hardened and partially annealed.
H3	Strain hardened and stabilized.
H18	Strain hardened during fabrication. Temper with Ultimate tensile strength (UTS) equivalent to about 75% cold reduction after full annealing.
H131	Strain hardened during fabrication. Temper with mean UTS equivalent to three-eights of the UTS of a full-hard condition (H18).
H321	Strain hardened during fabrication. Amount of strain hardening controlled during hot and cold working.
H116	Special strain hardened. Corrosion resistant temper for aluminium magnesium alloys.

Table 3.2: Temper designations for strain hardened alloys. Adapted from [197].

The specific alloy used in this work is the AA5083-H116 with chemical composition shown in Table 1.3. The testing material has been supplied by the Slim Fusina company in the form of sheets 12" x 18" wide and 0.25" and 1" thick. In total, several 0.25" thick plates have been used and one 1" plate. Since the Mg content is not strictly defined but rather in a range of 4-4.9 Mg wt%, the exact Mg content may vary between individual plates. As a result, slightly different Mg content dependent results may be obtained which was accounted for by using carefully selected control groups from each plate. The mechanical properties of AA5083-H116 are shown in Table 3.3.

Property	Value
Density	2.77 g/cm^3
Hardness, Vickers	96
Yield strength	228 Mpa
Ultimate tensile strength	317 Mpa
Elongation at break	16%
Young's modulus	71 Gpa
Poisson ratio	0.33
Fatigue strength	159 Mpa
Shear modulus	26.4 Gpa

Table 3.3: Mechanical properties of AA5083-H116 [198].

3.2 Laser systems

A typical laser for the LSP process is based on the Nd:YAG or Nd:Glass solid state active medium which is common for this type of high-energy nanosecond lasers. Compared to ultra-short laser systems which generate pulses on the pico and femtosecond scale, nanosecond systems are relatively simple and reliabe. The design consists of a Q-switched resonator and several power amplifiers pumped either by flash lamps or recently more common laser diodes. The lasers can either be single-pass or multi-pass and depending on the cooling efficiency, they can generate average power from 10 W up to 1 kW.

3.2.1 Q-switching

Unlike CW lasers (Continuous Wave) where the resonator cavity losses are constant and energy is released in a gradual manner, Q-switched laser utilize artificial cavity loss modulation with the result of energy being released in short powerful bursts[1]. At the start of the process, the resonator losses are kept high. No lasing occurs due to the lack of positive feedback from stimulated emission and energy from the external pumping is being accumulated. The laser gain rises as the electron population inversion increases. The amount of energy stored is only limited by spontaneous emission, amplified spontaneous emission (ASE)[2] or simply by the pump energy available. The losses are then abruptly lowered which leads to a quick build up of laser radiation in the resonator cavity. The energy build up starts form spontaneous emission noise. As the energy rises, the gains starts to be saturated. The peak of the pulse is reached when the gain becomes equal to the current low resonator losses. As the rest of the stored energy is depleted, the power drops and the cycle ends. The result is a short laser pulse with duration typically in the nanosecond range (corresponding to several resonator round trips). The process is depicted in Fig. 3.1.

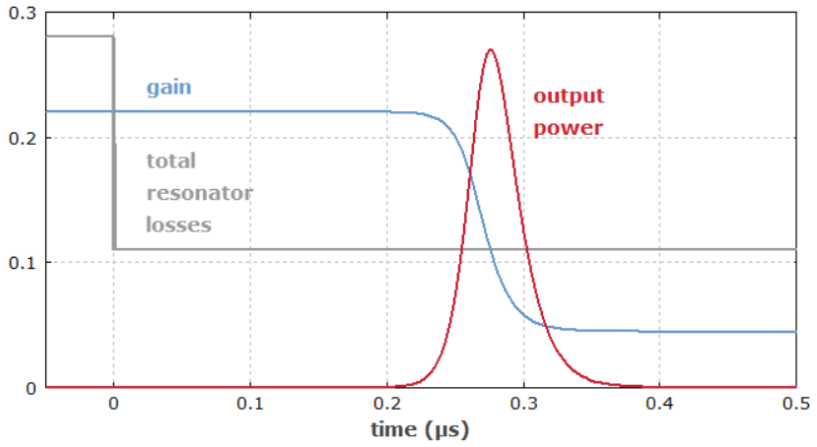

Figure 3.1: Temporal evolution of gain and losses in an actively Q-switched laser [199].

[1] Resonator losses are directly linked to the Q factor (quality factor) of a resonator, hence the name Q-switching.

[2] ASE is a process when a single pass through the high gain medium can generate strong laser pulse even in the absence of a resonator. It is commonly used for example in generation of X-ray laser pulses where the active medium is plasma generated either by high-voltage electrical discharge or secondary laser-matter interaction.

The sudden change in resonator losses can be achieved via passive or active means. An example of passive Q-switching is a saturable absorber which changes its absorption with light intensity. When enough energy accumulates in the resonator cavity, the absorber becomes semi-transparent for the radiation and fast build up follows. Active Q-switching can be for instance achieved via rotating mirrors or very often using ultrafast optical switching with Pockels cells [200]. In the Pockels cell configuration, the resonator contains polarizer which rejects the light. When the cells are switched, the light polarization is abruptly changed by 90° and can now pass the polarizer. The pulse energy after the resonator is typically in the mJ range and the short pulses are amplified further using power amplifiers.

3.2.2 PowerLite Plus laser

Two laser system have been used for this work. The first one is the Powerlite Plus commercial laser system manufactured by Amplitude [201] which is located in the UC laboratory (Fig. 3.2).

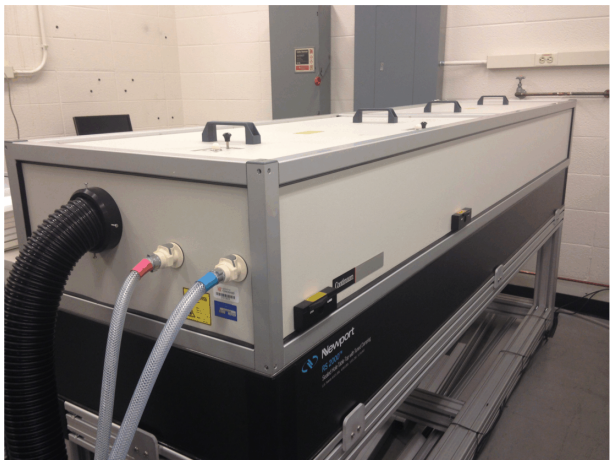

Figure 3.2: Powerlite Plus laser system at UC.

The system is based on the Nd:YAG laser medium, uses flashlight pumping and generates pulses at 1064 nm infrared (IR) wavelength. The beam profile is circular due to the rod shaped Nd:YAG crystals and the intensity profile is top-hat (Fig. 3.7a). The design is single-pass and comprises a resonator, one preamplifier and two amplifiers. The Q-switching happens via Pockels cells placed within the resonator cavity. Between the resonator and preamplifier, another Pockels cell can be found, this time in a pulse slicing configuration. The function is very similar to the one for Q-switching, except that the delay is now set so that only a front part of the pulse is cut off – sliced – and rejected via polarizer. This is specifically done to steepen the pulse ascending edge (Fig. 3.3) which increases plasma breakdown threshold in the LSP process (2.5.2).

A Faraday isolator is placed after the amplifiers to protect the laser system from backward propagating laser pulses. The Faraday isolator comprises strong homogeneous permanent magnetic field which acts as an anisotropic polarization rotator so that light can only pass in the forward direction. This is very important for the LSP process as laser pulses are fired at metallic parts at close to perpendicular angle which means that part of the pulses can be easily reflected back. Similarly, laser light can be reflected from the generated plasma (2.1.5). If the reflected pulse was allowed to propagate back into the

laser system, it could be further reamplified and potentially damage often expensive optical parts upstream. To lower the risk of reflection damage, the sample is usually peened at a slight angle (±3°) with respect to the laser beam.

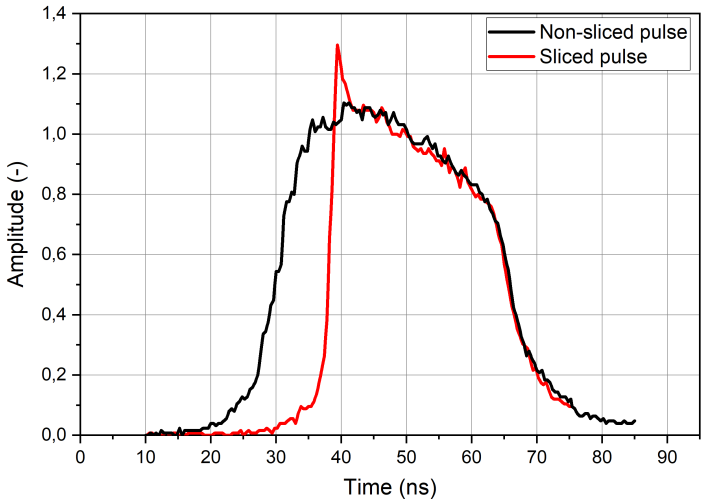

Figure 3.3: Temporal shape of non-sliced vs sliced laser pulse produced by the PLP laser at 3J and 1064 nm wavelength. The measurement has been done using a photodiode utilizing a mirror leak.

A removable mirror allows to divert the beam path into a KDP crystal for second harmonic generation (SHG). Each beam path has different exit aperture. No Faraday isolator is necessary for the SHG path since mirrors preceeding the KDP crystal are non-reflective for the halved wavelength. Additionally, the SHG pulse cannot be reamplified in the Nd:YAG laser medium. The emerging laser beam has a top-hat spacial profile which is achieved via specially optimized flashlight pumping of the Nd:YAG crystal in the resonator. As a result, relay imaging is required via a confocal non-magnifying telescope to prevent distortion of the beam profile. The overall parameters of the PLP laser are summarized in Table 3.4.

The laser operation is controlled by timing central unit (TCU) which synchronizes the flash lamp pumping with the Q-switch and pulse slicer Pockels cells. The pump and slicer delay can be adjusted via a PC with a customized software. When and how many laser pulses are coming out is controlled via gating of the Q-switch timing signal. When the gate is OFF, no Q-switching takes place and the resonator is in its default state of high losses. When the gate is ON, pulses are generated and amplified. The pulse energy is controlled via desyncing of the amplifiers with the signal pulse. This method of energy control is not ideal because the pulse spacial and temporal profile can vary between energies. In this case, the result is that the pulse FWHM is dependent on the output energy, starting at 20 ns for low energies and rising up to 30 ns for high energies. For example, the FWHM of 1J pulses at 1064 nm was measured to be 22 ns (Fig. 3.7a) while for 3J it was 30 ns.

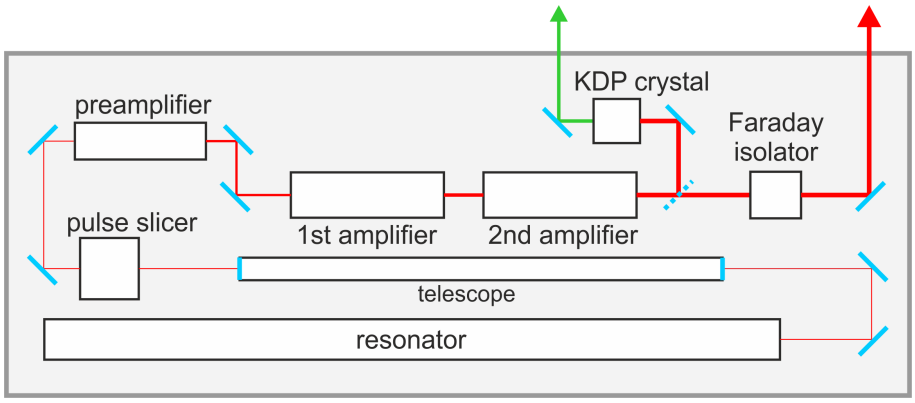

Figure 3.4: Structural schematic of the Powerlite Plus laser.

3.2.3 Bivoj laser

The second laser system named Bivoj [202] is situated at the HiLASE laser center. The state-of-the-art system was designed for high average power operation and is currently the world record holder for Q-switched laser pulses [203]. The efficient cooling required for the high power is achieved in three ways. First, it is laser diode pumped with about 30% conversion efficiency compared to the usual < 5% efficiency for flash lamps. Second, it is based on the Yb:YAG active medium with 1030 nm first harmonic which has lower quantum defect[3]. And third, the slab shaped laser crystals are cooled cryogenically by means of flowing helium cooled down to 150 K. The system is divided into 2 parts, one generating maximum 10 J at 10 Hz (Fig. 3.5) and the second, a scaled up copy of the first, generating 100 J at 10 Hz. Only the first part of the system was used for this study and its scheme is shown in Fig. 3.6.

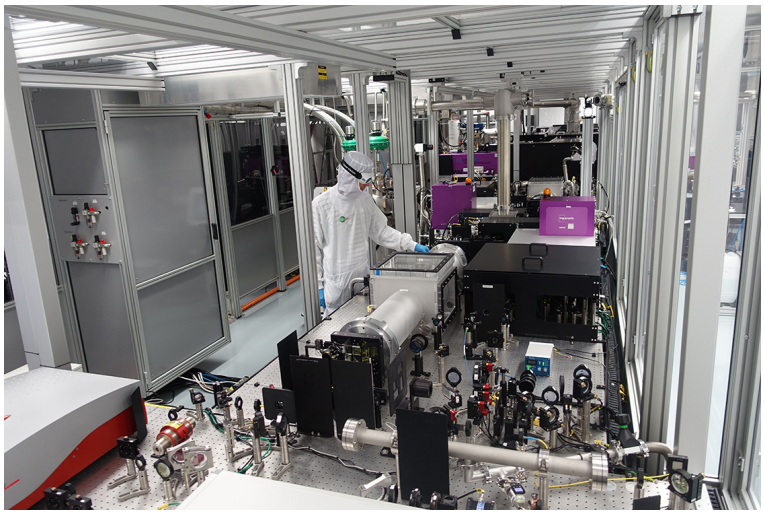

Figure 3.5: Bivoj laser system 10 J part.

Pulses are generated in a fiber resonator situated in a rack outside the optical table. The pulses are then transported via optical fiber into the 1st preamplifier. After that the

[3]Quantum defect refers to the photon energy difference between the pumping photon and signal photon. The lower the quantum defect, the less energy is getting transformed into heat

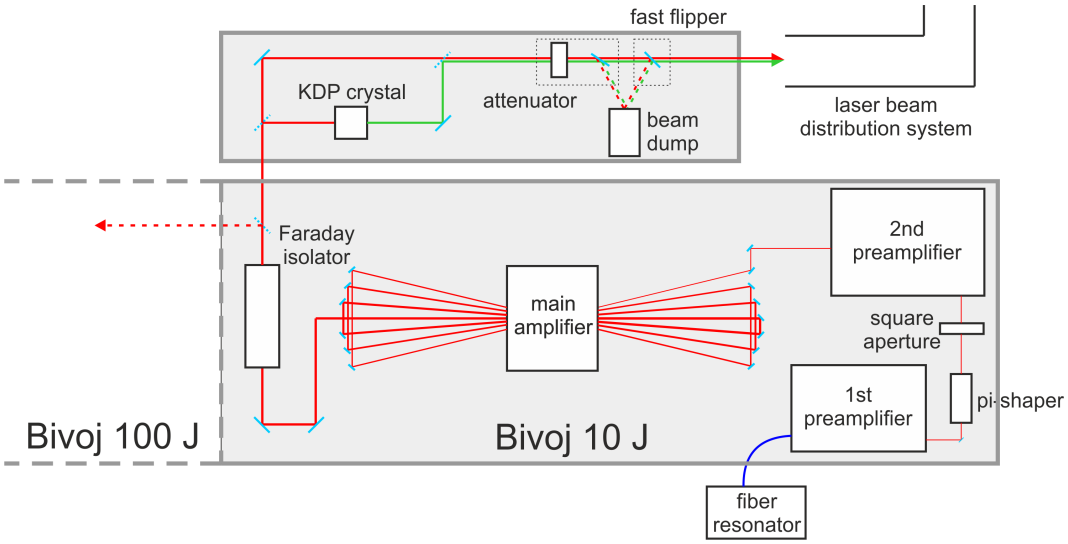

Figure 3.6: Structural schematic of the Bivoj laser.

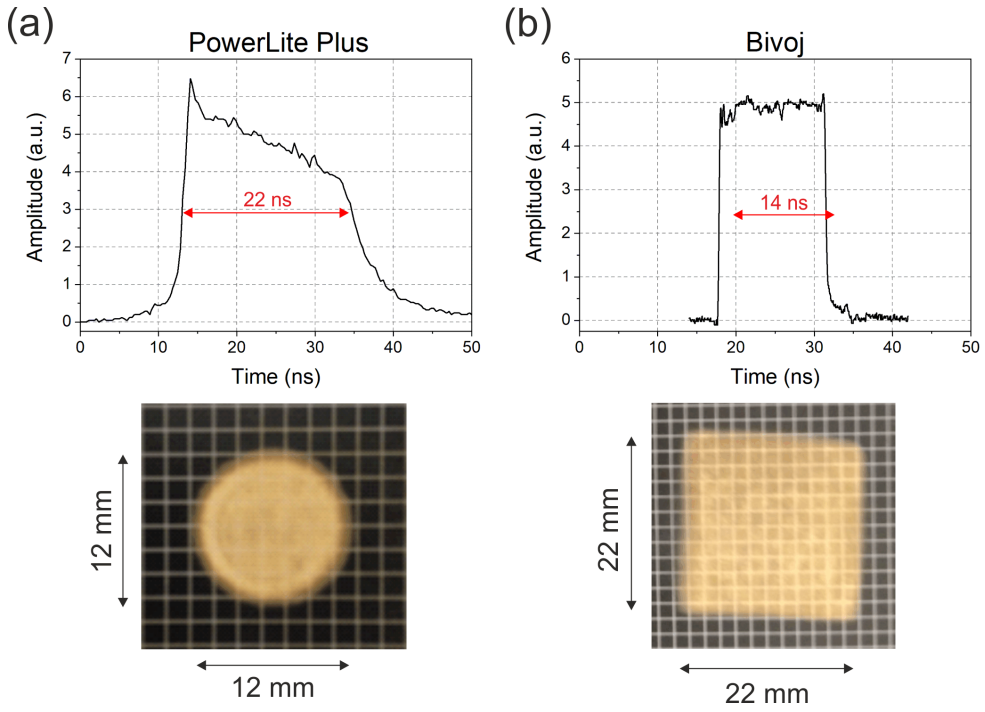

Figure 3.7: Temporal (top row) and spatial (bottom row) beam profiles of (a) the PowerLite Plus laser at 1J pulse energy and of (b) the Bivoj laser using IR wavelength.

pulses enter a pi-shaper which redistributes the intensity profile from Gaussian to top-hat using specially shaped lenses. Next, the pulses pass through square shaped aperture, giving the pulses their characteristic square shape (Fig. 3.7b). For the rest of the beam path, the image plane is relayed via multiple confocal telescopes which are absent from the scheme for simplicity. After the second preamplifier, the pulses enter multi-pass main amplifier with 7 passes in total. The end of the amplification area is marked by Faraday isolator. A mirror can be inserted to send the pulses into the 100 J part for

further amplification but in this case, the pulses were released into a distribution system leading to the LSP station. For SHG, the pulses are diverted into a KDP crystal and then sent into the distribution system following the same path as the first harmonic using dual wavelength optics. The energy is controlled via an attenuator which consists of a $\lambda/2$ wave plate and a polarizer. The waveplate is used to rotate the polarization vector of the laser pulse. Depending on the vector orientation, part of the beam gets reflected on the polarizer ending up in a water filled beam dump and part passes through. The attenuator is followed by a pneumatic fast flipper which can be directly controlled from the LSP station. When the flipper is closed, the pulses end up in the same beam dump. During the operation, the laser runs constantly on full power which means that all the attenuated pulses preserve the spatial and temporal beam profile. In this case the pulse duration (FWHM) was 14 ns (Fig. 3.7b). All the laser parameters are summarized in Table 3.4.

	Powerlite Plus	**Bivoj**
Wavelength	1064/532 nm	1030/515 nm
E_{max}	3.5J @1064 nm, 1.5J @ 532 nm	7J @ 1030 nm, 5J @515 nm
Pulse length	20 - 30 ns FWHM	10 - 14 ns FWHM
Temporal profile	steep rise, gradual fall	steep rise, steep fall
Spacial profile	top-hat circular	top-hat square
Energy control	pump desyncing	attenuator
Output beam size	Ø 12 mm	22 mm x 22 mm
Repetition rate	10 Hz	10 Hz

Table 3.4: General characteristics of the PLP and Bivoj laser systems.

3.3 LSP station

Both LSP stations, one at UC (Fig. 3.8a) and the other at HiLASE (Fig. 3.8b), share similar design. A Fanuc robotic arm is located at the end of each beamline serving as a mounting platform for peened samples. The robot models are LR MATE 200ic/5L for UC and M-20iA/20M for HiLASE with carrying capacities of 5 kg and 20 kg, respectively. A lens is located at a safe distance before the sample to focus the laser beam into a smaller laser spot. The size of the laser spot is controlled via distance between the sample and the lens. Water for laser confinement is delivered through adjustable tubing with a nozzle at the end. In case of classic IR peening, an air knife is used to protect the lens and divert the spraying water droplets away from the laser path. A water collector connected to a drain is placed underneath the sample. In case of underwater peening where SHG of the laser must be used, a removable water tank can be inserted. Laser enters the tank through a glass window located in the tank wall[4]. During the peening, the tank is filled with water and the sample attached to the robotic arm is submerged. The main difference between the two stations is that the PLP laser is located in the same room as the LSP station while Bivoj is located in a separate clean room and the beam must be transported via the distribution system. Second difference is that while both first and second harmonic share the same path in HiLASE case, they are separate in the UC station. This means that the laser for IR treatment enters the treatment area from one direction and the laser for SHG

[4]The distance between the window and the lens must be kept at minimum. Otherwise, the window may get damaged by high laser fluence.

treatment enters from a direction rotated by 90°. Both systems have their own separate focusing lens for each wavelength.

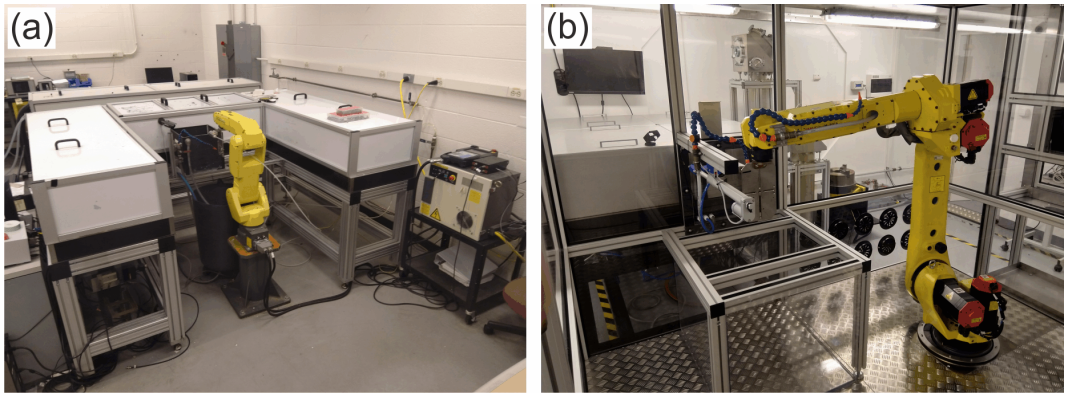

Figure 3.8: Layout of the LSP stations located (a) at UC and (b) at HiLASE.

3.3.1 Laser-robot synchronization

The desired peening pattern is achieved through robot programming when a number of lines consisting of individual laser spots are placed next to each other. Typical parameters for peening of flat samples are scanning speed, line spacing, line length and number of lines. For a given spot size, the scanning speed determines the spot overlap within individual lines, line spacing determines the spot overlap between lines and line length and line number determine the overall size of the patch. The scanning pattern starts in one of the lower corners and the lines have horizontal orientation. This is because when the tape overlay tears during the process, the laminar water flow is not disturbed as the sample moves downward when moving towards the next patch line.

A problem arises when both the laser and robot have their own independent timing. The laser timing is given by the TCU while the robot executes its programming one command after another in a closed loop. When the robot reaches the supposed beginning of the peening line, a signal is send to open the Q-switch gate (PLP) or the fast flipper (Bivoj). Pulses start coming in but with some arbitrary delay. In case of 10 Hz repetition frequency, the delay can be between 0-100 ms. The result is distorted peening pattern in horizontal direction (see Fig. 3.9a) as the constant delays produced by each cycle add up.

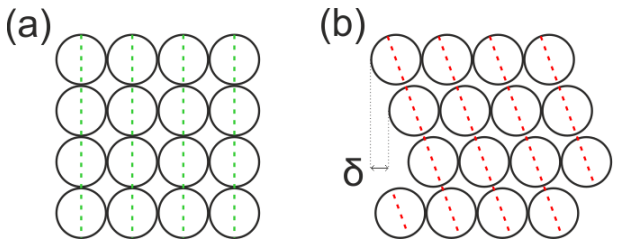

Figure 3.9: Peening pattern of (a) a synchronized process and (b) out of sync process with an arbitrary delay δ between individual lines.

To solve this problem, the laser and robot must be coupled together. In case of PLP laser it is done via the TCU unit and in case of Bivoj via laser diode trigger. The whole cycle follows these steps:

1. The peening program is started and the robot moves into position to execute the first peening line.

2. The robot waits for a timing signal from the laser to start moving. In practice, the signal is either an ascending or descending edge of the periodically changing voltage on the robot digital input module.

3. The signal arrives and the robot starts moving. Due to the robot acceleration, a short line segment is used to achieve constant speed.

4. The robot reaches the beginning of the line and sends a signal to switch on the laser pulses. For the PLP laser, the TCU gate opens and for Bivoj, the fast flipper opens. There is still some delay before the first shot arrives but it gets reset at the beginning of each line.

5. The robot reaches the end of the line and, without stopping, sends a signal to switch the laser pulses off.

6. The robot slows down, comes to a halt and moves to the start of the next peening line and the cycle repeats itself.

When the scanning finishes, each peening line is perfectly positioned with respect to other lines. The process is schematically depicted in Fig. 3.10.

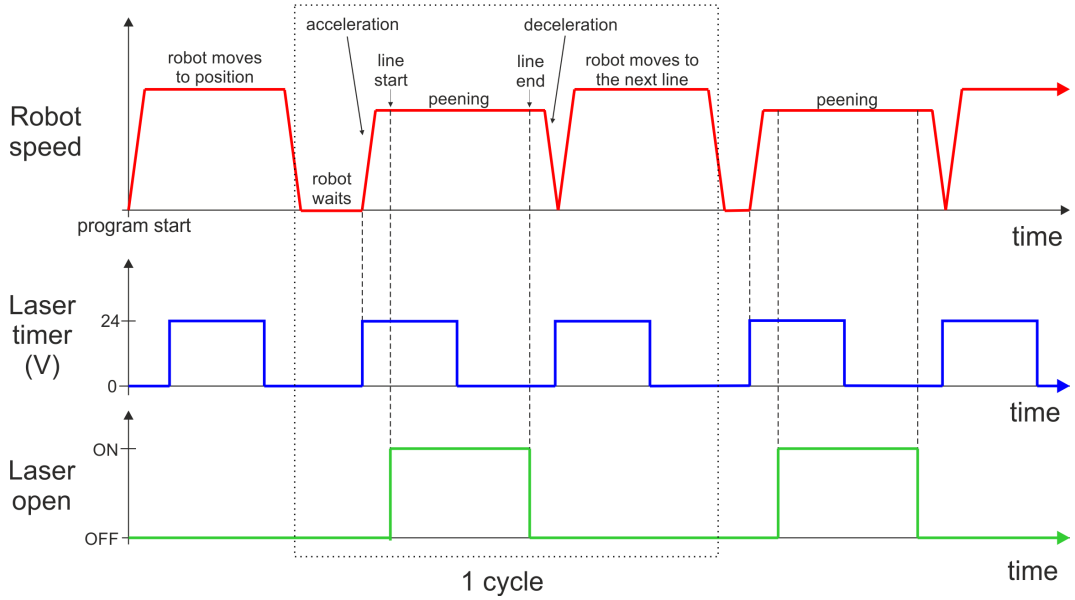

Figure 3.10: Schematic representation of the laser-robot synchronization loop.

3.4 Electrochemical analysis

The majority of corrosion related processes occurs via electrochemical reactions at the interface between a metal and an electrolyte solution. The corrosion rate is determined by an equilibrium between two opposing electrochemical reactions – anodic and cathodic. During anodic reaction, a metal is oxidized and electrons flow away from the anode

which may cause corrosion to occur. The simultaneously present cathodic reaction involves reduction of metal where electrons flow into the cathode. When these two reactions are in equilibrium, the electron flow from each reaction is balanced, and no net electrical current occurs. Fig. 3.11 shows a typical current dependency during potential sweep measured by a potentiostat. The vertical axis represents electrical potential measured with respect to a reference electrode and the horizontal axis represents the logarithm of absolute current or current density. Plotting along logarithmic axis is necessary due to a wide range of current values (commonly over 6 orders of magnitude) that are recorder during a corrosion measurement. While the theoretical current for the anodic and cathodic reactions is represented as straight lines, the current that is actually measured is denoted by the curved pink line which represents the sum of both the anodic and cathodic currents. The sharp point represents a potential value where the current direction shifts from negative to positive as the potential sweep starts in the cathodic region. This value is known as corrosion potential E_{corr} and it represents a potential where the cathodic and anodic currents are in equilibrium. When more than one electron transfer reaction takes place at the sample surface, E_{corr} becomes a mixed potential defined by the kinetics of all simultaneous electrochemical reactions. When the potential is forced away from E_{corr}, the sample is referred to as being polarized. In a time stabilized situation, E_{corr} overlaps with Open Circuit Potential (OCP) which is another important electrochemical value which marks the point when no current is flowing through the sample.

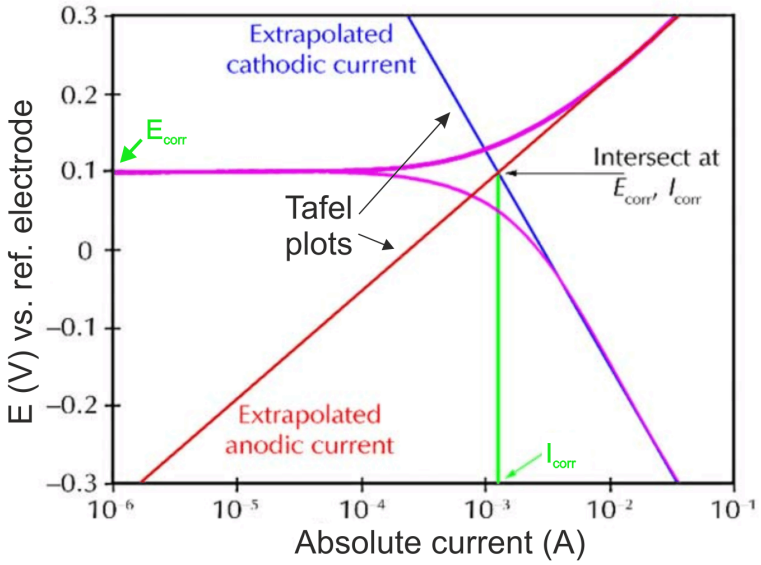

Figure 3.11: Total net current flowing through the sample measured (pink line) as a combination of anodic and cathodic reactions [204].

The current value corresponding to E_{corr} is called corrosion current I_{corr}. I_{corr} cannot be measured directly and is usually obtained via Tafel plots as depicted in Fig. 3.11. The use of Tafel plots, however, is possible only when both the anode and cathode parts follow a single exponential in the corrosion potential. That is, the system in this potential has a unique time constant. If more time constants are present, other methods such as Linear Polarization Resistance method (LPR) have to be used [205]. During LPR, small voltage variations (±10 mV) are applied around E_{corr} and the slope of current response

is measured which is used to determine polarization resistance R_p. I_{corr} is then obtained using the Stern-Geary equation [206]. Another characteristic value is the breakdown or pitting potential E_b which marks the point of sharp increase in anodic current, typically after a passivation period. Many metals form a thin oxide layer in their anodic region which lowers or even inhibits the corrosion rate. At higher potentials the passive film breaks down locally and significant point corrosion develops (pitting). When no passive region is present, E_b overlaps with E_{corr}. It is also worth mentioning the switch potential, denoted E_{sw}, which is the potential corresponding to when maximum allowed current is reached and the sweep is reversed. Similarly, when a reverse potential sweep is employed after the forward sweep has already taken place, the potential where lowest current is measured is called the protection potential E_{prot}. It is very common for E_{prot} to be lower than E_{corr} since the resultant curve often displays some form of hysteresis, especially when irreversible corrosion damage such as pitting occurs during the upward potential sweep. E_{prot} is then the potential at which the pits are re-passivated.

In electrochemical measurements, electrochemical cells of various designs are used to simulate the corrosion environment in the system being studied. The sample surface is exposed to an electrolytic solution together with additional immersed electrodes. In total, there are 3 electrodes. One of them represented by the sample, a counter-electrode and a reference electrode. The reference electrode cannot be polarized and precisely monitors the potential on the working electrodes. All of the electrodes are then connected to a potentiostat which, in this case, was supplied by Gamry instruments. The potentiostat allows to change the potential of the sample in a controlled manner and monitor the current that flows as a function of the applied potential. The specific layout of the cell used is shown in Fig. 3.12.

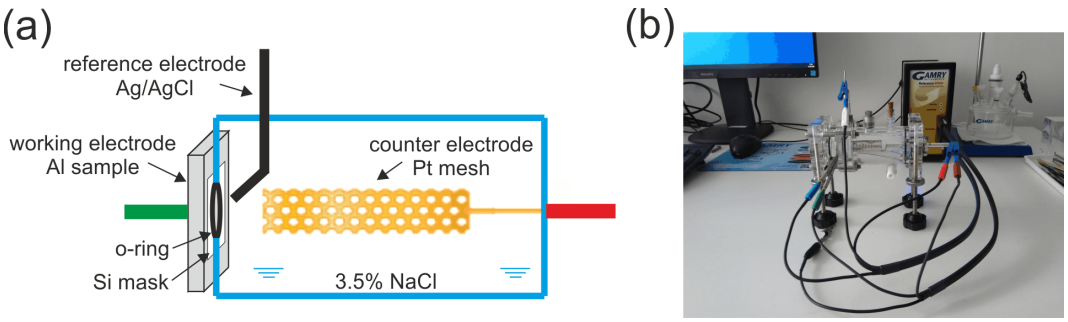

Figure 3.12: Schematic representation of (a) the Gamry electrochemical cell and (b) a real measurement in progress.

Three types of measurements have been used in this study: cyclic polarization (CP), electrochemical impedance spectroscopy (EIS) and potentiostatic test (POTSTAT). The CP test runs a potential sweep from the cathodic to the anodic region either in a given potential range or until a pre-set maximum current flow is reached. The sweep then reverses its direction and the potential starts dropping again to a specified value. From the test, one can determine E_{corr}, I_{corr}, E_b, E_{sw}, E_{prot} and trends in the corrosion behaviour such as passivation. The EIS test measures the complex impedance of a sample over a pre-set AC frequency range. The measurement is performed at a fixed potential central point with the potential periodically alternating around this point at a fixed amplitude. Impedance at each frequency point is recorded and the data is represented in a Bode and Nyquist plot where the former plots absolute impedance and phase shift against frequency while the latter plots imaginary part of the impedance against its real part.

And lastly, during the POTSTAT test, the sample is polarized at a fixed potential level and current or current density is measured over a period of time. Both the EIS and POTSTAT tests are complementary to the CP test which predetermines the areas of interest with respect to the current flowing through the sample with changing electric potential.

3.5 X-ray diffractometry

X-ray diffractometer (XRD) is a device which uses x-ray radiation to measure the distance of atomic planes in crystalline materials. When a narrow beam of x-rays irradiates periodic atomic structure, it gets diffracted due to the wavelength of the incident radiation being comparable to the typical spacing between atomic planes in materials. The direction into which the beam gets diffracted is determined by the Bragg law

$$n\lambda = 2d_{hkl}\sin\theta \tag{3.1}$$

where λ denotes the wavelength, d_{hkl} the distance between atomic planes given by the [h k l] Miller indices and θ the angle of incidence. The condition states that in order for a wave to be diffracted, the path difference between the incident and reflected wave has to be a multiple of the radiation wavelength so that constructive interference between two reflected beams occurs. The situation is shown in Fig. 3.13.

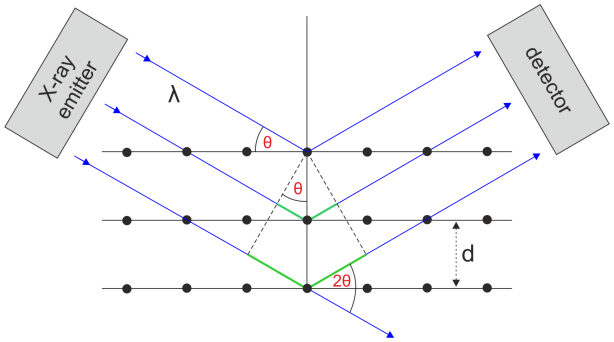

Figure 3.13: Diffraction of x-rays on atomic planes where green line represents the path difference between the incident and diffracted beams.

Since λ and d are fixed, the condition will be met only for a discrete set of angles which are referred to as Bragg angles. Depending on the structure, each crystalline material has a unique diffraction pattern characterized by an angular spectrum of Bragg peaks each associated with different atomic plane differentiated by [h k l]. The measurement of residual stresses is based on monitoring of the shift of Bragg peak position 2θ with respect to Ψ which is the angle between the normal of the sample and the normal of the diffracting plane. A typical polycrystalline material such as steel or aluminium consists of many grains, each with its own random plane orientation. When a thin x-ray beam irradiates the sample, there will always be some statistical amount of grains in the irradiated volume oriented in the right way as to satisfy the Bragg equation (3.1). If the atomic structure of all the grains is the same with grains being just randomly oriented, the same peak position will always be measured regardless of Ψ. Stresses, however, both external or residual, introduce anisotropy to the grain structure. Grains whose atomic planes are perpendicular to stresses will have their atomic planes either stretched or pressed depending on whether the stresses are tensile or compressive, respectively. Fig. 3.14 shows the grain structure changing when stresses are introduced.

The top side symbolizes the material surface. When near surface plastic deformation is created, by peening for instance, the response of the surrounding material is stronger in the direction parallel to the surface rather than in the perpendicular direction as there is no pressing surrounding material above the surface. This results in atomic planes being more compressed in the parallel direction. Tensile residual stresses which can often be introduced by heating processes, such as welding, affect the grains in similar way, only now the atomic planes in the direction parallel to the surface are stretched.

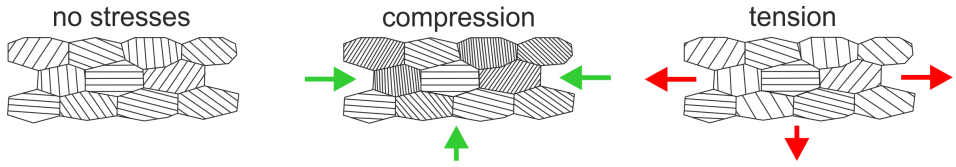

Figure 3.14: Change in atomic plane distance in subsurface volume affected by stress in relation to the grain orientation.

Since d_{hkl} is now a function of Ψ, the angle θ that fulfils (3.1) becomes also Ψ dependent[5]. Residual stresses can then be calculated based on the Bragg peak original position, its shifting with respect to Ψ and elastic constants of a specific material. The elastic constants involve Young modulus E and Poisson ratio σ. The most common calculation technique is based on the $\sin^2\Psi$ model which plots the 2θ peak position against $\sin^2\Psi$ resulting in a linear plot. Residual stresses are then calculated from the plot gradient and the elastic constants. Positive gradient is associated with compression and negative with tension.

Besides the peak position, peak broadening can be measured simultaneously. The natural peak width results from several factors. First, the x-ray beam is not perfectly monochromatic and collimated. Second, the model assumes infinite amount of atomic planes that reflect the incident beam. In reality, finite size of grains causes that the destructive interference of beams coming at angles near to, but not equal to, the exact Bragg angle is not perfect due to the finite number of atomic planes contained within the grain contributing to the interference. Next to grain size, other factors affecting the peak broadening are dislocations, stacking faults, twinning, microstresses etc. These phenomena can be used to study the effect of LSP on the material microstructure.

In this work, residual stresses were measured in 2 perpendicular directions. These directions are referred to as scanning (σ_S) and transversal (σ_T) and are defined in relation to the scanning and transversal (or advancing) directions of the peening pattern (Fig. 3.15). These stresses may differ significantly depending on the peening strategy.

Two diffractometers were used - Proto LXRD instrument at UC (Fig. 3.16a) and RIGAKU AutoMATE II at HiLASE (Fig. 3.16b). The LXRD machine had a dual detector configuration while the AutoMATE had one larger detector. The second structural difference was that the LXRD machine had an in-built stage able to rotate the sample around its normal. While the AutoMATE machine could not mechanically rotate the sample, it instead could set the inclination angle Ψ in two perpendicular directions. These directions were referred to as iso-inclination and side-inclination and corresponded to the (σ_S) and (σ_T) directions mentioned earlier. Parameters that were used for the measurements are summarized in Table 3.5 and the elastoplastic material constants can be found in Table 3.3.

[5]The shifts in the Bragg peak position are usually in the tenths of a degree.

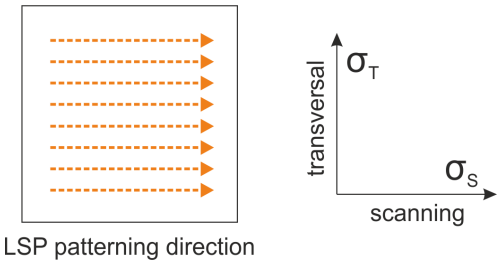

Figure 3.15: Residual stresses principal directions. The scanning direction is parallel to the peening lines while transversal direction is perpendicular to them.

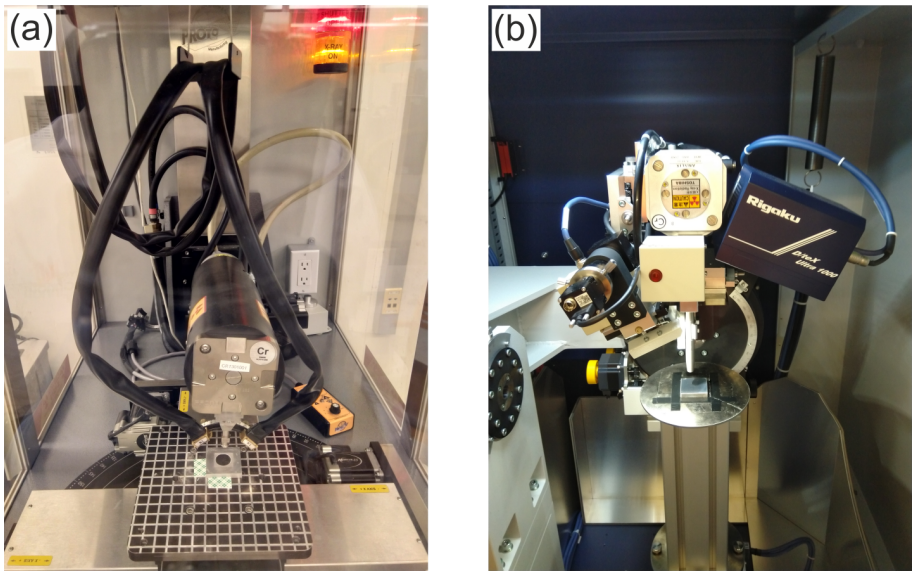

Figure 3.16: X-ray diffractometers used for residual stress measurements: (a) Proto LXRD with dual detector configuration and (b) RIGAKU AutoMATE II with a single detector.

	Proto LXRD	**Rigaku AutoMATE II**
Radiation	Cr $K\alpha_1$ (λ=2.2897 Å)	Cr $K\alpha_1$ (λ=2.2897 Å)
Filter	Vanadium	Vanadium
Tilt angles	0°, ±2.58°, ±9.07°, ±12,45°, ±18.8°, ±23.0°	0°, 18.4°, 26.6°, 33.2°, 39.2°, 45°
Aperture size	2 mm	2 mm
Bragg's angle	139° [311]	139° [311]
Exposure	10 s	20 s
Oscillation	3°	3°

Table 3.5: XRD measurement parameters.

When it comes to in-depth residual stress measurements, one must consider the attenuation length, or skin depth, which is the depth at which the x-ray intensity falls to $1/e$ of its value. The skin depth is defined at perpendicular beam incicidence. For instance, the attenuation length of x-ray radiation from Cr cathode with the K_{α_1} wave-

length of 2.29 Å in aluminium is less than 20 μm [207]. For angles where $\theta \neq 90°$, it is even less. Therefore, in order to create residual stress depth profile, layers of the sample must be removed consecutively. However, the removal of the material must be done in such a way as not to affect the residual stresses. An example of a bad technique would be mechanical polishing after which a thin surface layer (few microns) typically contains high compressive stresses caused by the polishing friction which would compromise the measurement. Instead, electro-polishing is used which utilizes electrochemical processes to remove material without affecting the already existing residual stresses. Despite the frictionless process, removal of material still intrinsically affects the measurement since removal of mass causes the material to relax and deform. This is most noticeable at higher depths. As a result, a depth correction algorithm has to be used. The Proto LXRD has such algorithm directly included in its evaluation software. The AutoMATE II machine is missing this function and therefore an approximate correction formula can be used

$$\sigma_{corrected} = \sigma_{corrected}(z) - 4\sigma(0)\frac{z}{H} \tag{3.2}$$

where z is the measurement depth and H is the sample total thickness. This approximation is however only valid for small depth increments (a few percent of the specimen thickness) [208]. Therefore, the AutoMATE machine was used for surface and shallow depth measurements only. The electropolishers used were ElectroMet 4 from Buehler at UC (Fig. 3.17a) and LectroPol-5 from Struers at HiLASE (Fig. 3.17b). The electrolyte was a mixture of 87.5 vol% methanol (CH_3OH) and 12.5 vol% sulphuric acid (H_2SO_4). The electropolishing voltage was set to 28 V with a steady current density of 1 A/cm^2 at a constant temperature of 30 °C. The average polishing rate was about 10 μm/min. After polishing, the sample thickness was measured using a precise digital thickness gauge meter with 1 μm precision.

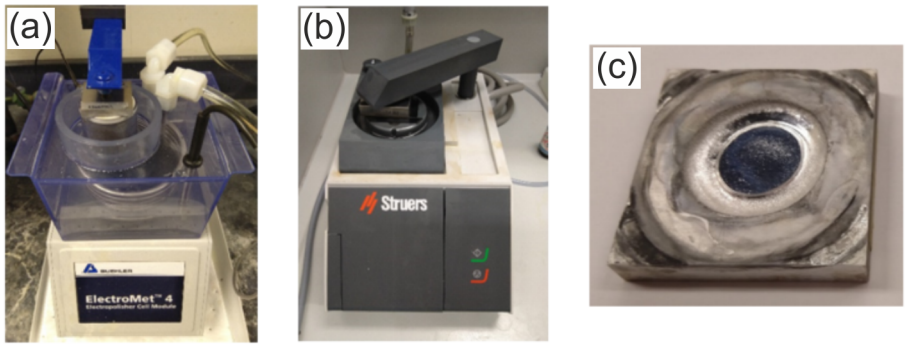

Figure 3.17: Electropolishers (a) Electromet 4 and (b) LectroPol-5. (c) Aluminium sample after electropolishing.

3.6 Nitric Acid Mass Loss Test

The NAMLT is the primary testing tool to quantitatively determine the susceptibility of 5XXX series aluminium alloys to intergranular corrosion (IGC). The test consists of immersing test samples in a concentrated nitric acid (70 %wt) in a temperature controlled environment of 30 °C for a period of 24 hours. The strong acid preferentially dissolves β-phase located at the grain boundaries over the solid solution α-phase in the aluminium

matrix. If the grain boundary is populated with continuous β-phase, the acid attacks causes grain fall-off resulting in a mass loss. The test follows the ASTM G67 standard [41] with a detailed, step-by-step procedure provided in the following list:

1. Specimens are prepared with dimensions 50 mm by 6 mm by product thickness. If the thickness of the product is greater than 25 mm it is reduced by one half or to 25 mm, whichever is less, while retaining one original as-fabricated surface. For each testing condition, at least 2 samples are used.

2. Specimens are polished with a 600 grit paper.

3. All specimen edges are smoothened using 1200 grit paper.

4. Specimen dimensions are measured using precise digital thickness gauge meter with 1 μm precision and surface area is calculated.

5. Surface cleaning procedure - specimens are immersed in 5% NaOH solution at 80 °C for 1 min, rinsed in deionized (DI) water , immersed in 70% HNO_3 (desmut) for 30 s followed by another DI water rinse and final air drying with an electric hair dryer.

6. Specimens are weighed on digital analytical scales with 0.1 mg precision.

7. Specimen are immersed in a marked glass test tube with 70% HNO_3. A minimum of 3 ml/cm^2 of HNO_3 is used.

8. Test tubes with immersed specimens (in a stand) are placed in a water bath pre-heated to 30 °C for 24 hours. The water bath is located in a fume hood[6].

9. Specimens are removed from the acid and rinsed with DI water while being brushed off with a tooth brush using consistent force. The brushing removes all the loose grains. Specimens are then left to air dry.

10. Specimens are weighed again to 0.1 mg precision.

11. Mass loss per unit area is calculated and the Degree of Sensitization (DoS) is determined.

The specific chemicals used were Nitric Acid 70% w/w (Certified ACS Plus) and Sodium Hydroxide 50% w/w (Certified) both supplied by Fisher Chemical. The general purpose water bath with 10 l volume and ±0.1 °C temperature stability was supplied by PolyScience.

3.6.1 Modified NAMLT

Later in Chapter 4, it will be showed that when it comes to the rolled AA5083-H116 plate, the mass loss contributions of individual sample faces vastly differ due to the orientation dependent grain morphology which is a result of the rolling manufacturing process. LSP is a singular surface treatment procedure and ideally would require acid exposure of the treated surface only. However, the standard NAMLT involves full immersion of the test specimen into the acid which means that all the specimen faces contribute to the grain

[6] It is not recommended to fully cover the bath if it is metallic. The HNO_3 fumes condensate on the cover and trickle down the metallic walls, corroding them.

fall-off. For this reason, a modified version of the standard NAMLT targeting singular surface has been developed. The test will be referred to as modified NAMLT.

Isolating one surface from the rest of the sample proved to be rather difficult as common masks used in electrochemical measurements do not withstand the aggressive environment of concentrated nitric acid. Eventually, a solution was found using glass flanges purchased from Chemglass with an o-ring groove at one end. The special acid resistant o-rings are produced by VITON[7] [209]. The flange is pressed against the sample in a 3D printed contraption so that the acid comes into contact with the studied surface only (Fig. 3.18). The preparation and measurement procedure is the same as before with 2 modifications. First, the affected area of the specimen is now calculated using the o-ring diameter. Second, When the contraption is placed in the water bath, it is placed in its separate water filled beaker. A part of the specimen in this configuration is exposed to the water environment which means that when more samples at once are measured, any acid leak could come into contact with other specimens and compromise the results. With an extra beaker, only the leaking sample would be invalidated.

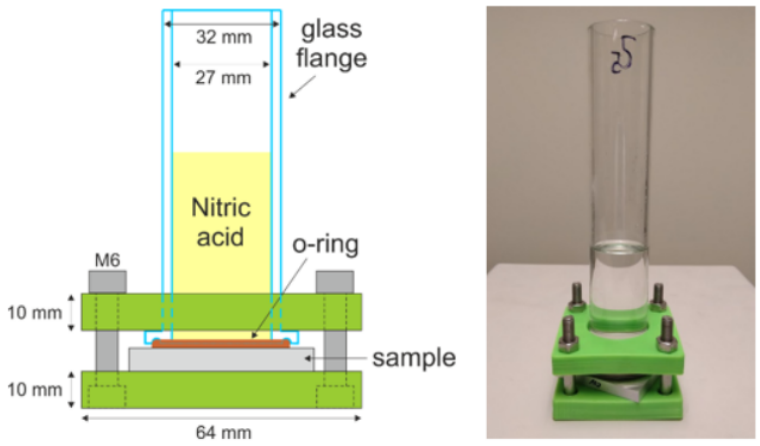

Figure 3.18: Modified nitric acid mass loss test for singular surface measurements. A glass flange placed in a special 3D printed contraption is pressed against a sample to keep only one surface exposed to the acid attack.

3.7 Hardness

Hardness testing is based on probing a material with a defined tool – indentor and measuring the material response in terms of load applied and penetration depth. The indentor tip is made of very hard material, most commonly diamond. The indentor shape in combination with the penetration depth is used to calculate the area of the tip that was in contact with the material during the measurement which is in turn used to calculate the hardness given by

$$H = \frac{P_{max}}{A_r} \tag{3.3}$$

[7] It has been experimentally determined that regular o-rings will dissolve rapidly in the acid and promptly ruin the measurement. Also, the VITON o-rings will deteriorate and expand over time (months) and at some point no longer fit the flange and need to be replaced.

where P_{max} is the maximum load applied and A_r the residual indentation area. In more rigorous measurements, hardness as a function of penetration depth can be obtained. In this work, however, only one value per measurement is obtained related to the maximum load. The unloading portion of the load-depth data contains information about stiffness of the material being tested (Fig. 3.19).

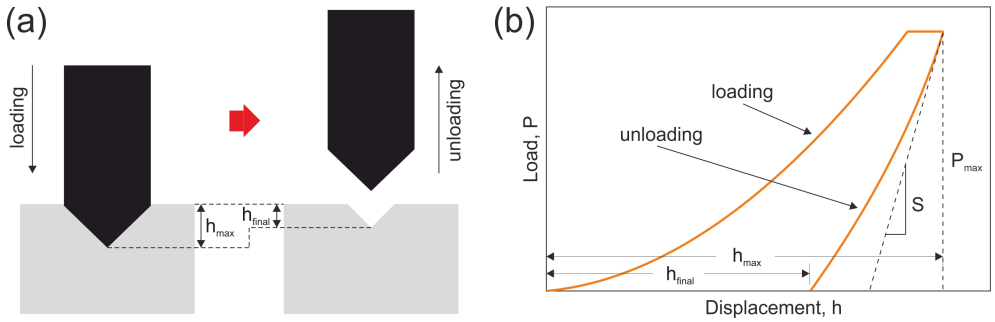

Figure 3.19: (a) Hardness measurement with a diamond indentor probing the material and (b) resultant load vs displacement curve.

There are two basic types of hardness testing: nano-indentation and micro-hardness testing. Both methods differ in a couple of ways, but the results are expected to be comparable as long as the tip geometries used provide similar strains in the tested material. These tips are Berkovich shaped tip for nano-indentation and Vickers tip for micro-hardness. Both of these tips exhibit the same projected contact area of 8% with respect to the penetration depth and the strain induced. The difference in shape is that Berkovich is a 3-sided pyramid while Vickers is 4-sided pyramid. The Berkovich shape allows the indentor to be theoretically sharpened to an atomic point. Typical loads applied with micro-hardness testing are up to 10 N and with nano-indentation up to 1 N. In this work, CSM instruments at UC (Fig. 3.20) was used to carry out the nano-indentation measurements.

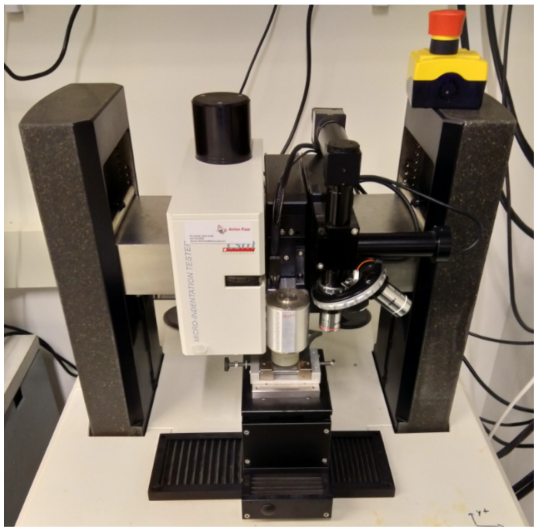

Figure 3.20: CSM instrument used for nano-indentation measurements.

3.8 Tensile testing

Tensile testing is a destructive irreversible test for metallic materials in which a sample of defined shape is subjected to controlled tension. The test provides information about the ultimate tensile strength, yield strength, breaking strength, maximum elongation and reduction in area. The measurements are most commonly used to determine basic material properties such as Young's modulus, Poisson's ratio, yield strength, and strain hardening characteristics. Typical tensile specimen can either have circular or rectangular cross-section consisting of 2 broader sections (shoulders) for gripping and a narrower section in between (gauge). The smaller cross-section of the gauge guarantees that the deformation will be localized into this area as higher stress will be applied compared to the rest of the specimen. Owing to their shape, the tensile specimens are often referred to as 'dog-bone' samples. The samples can be mounted either by simple firm gripping of the shoulders or using threaded shoulders.

After each measurement, a stress/strain plot is obtained showing relationship between the force applied (stress) and the elongation observed (strain) in the material during the test (Fig. 3.21). At first, linear behaviour is observed where the strain is directly proportional to the stress applied. The linear behaviour continues until a Yield point is reached at which point the material begins to deform plastically. The value of the stress developed at this point is called the Yield strength of the material. The now non-linear elongation continues until the Ultimate tensile strength is reached which is the maximum amount of force per unit area that a material can withstand. At this point, localized narrowing of the sample occurs called necking and the stress starts dropping. Finally, a fracture occurs and the sample breaks into two.

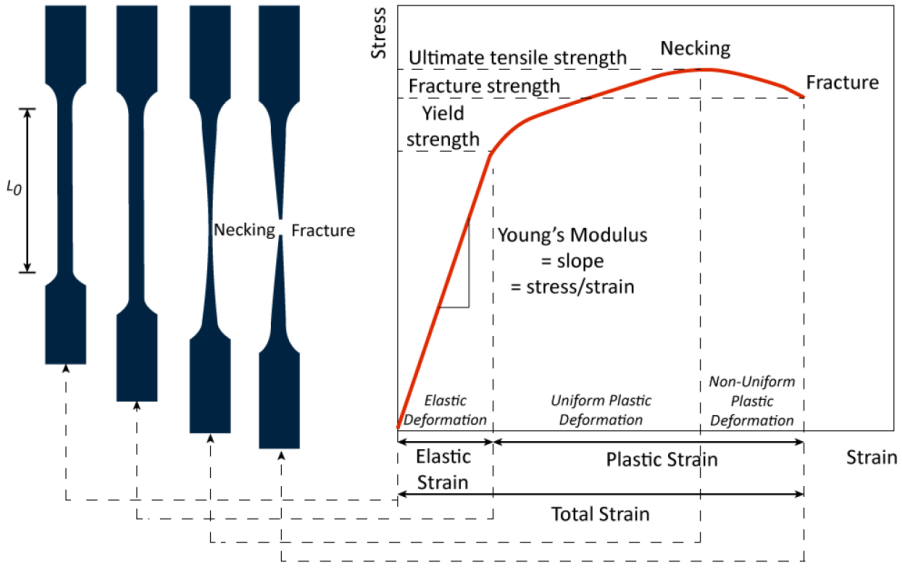

Figure 3.21: Typical stress/strain curve obtained from tensile testing.

During the test, the sample can be placed in a specially designed cell filled with an gaseous or liquid environment, which makes it one of the primary tools to study material response to SCC[8]. In order for the corrosion phenomena to take effect, however, the test

[8]Another test suitable for SCC testing is the Constant Load Test where a sample is placed in a corrosive environment at constant load until it breaks due to the corrosion induced cracks. A single test, however, can take several months to finish which was the reason it was not included in this work.

must be carried out at low strain rates (in the range from 10^{-8} to 10^{-3}) when compared to classical tensile test. Due to its importance, this subgroup of tensile testing has its own name – Slow Strain Rate Testing (SSRT). Proper selection of strain rate is very important because the susceptibility to cracking may not be evident from testing not only with too high strain rates but also with too low. The fastest strain rate that will still promote SCC for a given material-environment system is called the critical strain rate. For aluminium alloys in aqueous chloride solutions, it is 10^{-7}/s to 10^{-4}/s [210]. For AA5083 specifically, the optimal strain rate was determined to be 10^{-6} to 10^{-7}/s [211, 212, 213].

The tensile testing in this work was performed on Kappa 100 SS-CF electromagnetic creep testing machine with a load rating of 50 - 100 kN dynamic in both compression and tension in CVR – Research centre Rez in Pilsen.

3.9 Bending test

A simple uniaxial tension, such as one provided by tensile testing, may not provide all necessary information. A bending test, also referred to as flexure or transverse beam test, subjects the tested material to a complex combination of forces including tension, compression, and shear. The test is performed by placing a specimen in a fixture on two support anvils while one or two anvils apply force from the top. If the force is applied by a single upper anvil at the specimen midpoint, it is a 3-point bend test (Fig. 3.22a) while two anvils equidistant from the centre make a 4-point bend test (Fig. 3.22b). The main difference between the two is the stress distribution. In a 3-point bend test, the area of uniform stress is concentrated under the centre loading point and is quite small. In a 4-point test, uniform stress covers the whole area between the inner loading points. Also, test specimens for 3-point test are easier to prepare.

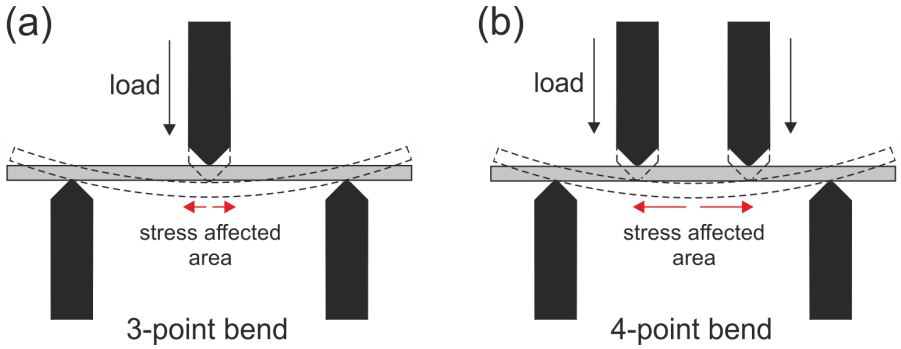

Figure 3.22: (a) 3-point bend test with area of highest stress concentration under the loading point. (b) 4-point bend test with uniform stresses distributed over larger area.

A bend test produces tensile stress in the convex side of the specimen and compression stress in the concave side which creates an area of shear stress along the midline. To ensure that primary failure comes from tensile or compression stress, the shear stress must be minimized by controlling the span to depth ratio S/d; the length of the outer span (S) divided by the height (depth) of the specimen (d). For most materials, S/d=16 is acceptable [214]. The loading amplitude is expressed as the R ratio which is the minimum peak stress divided by the maximum peak stress. Similar to tensile testing, the specimen can be immersed in a corrosive environment using a specially designed liquid container. This type of setup is suitable for corrosion fatigue (CF) testing which is the mechanical degradation of a material under the joint action of corrosion and cyclic

loading. Corrosion fatigue tests were performed on Electromagnetic pulsator RUMUL Testronic for high cycle fatigue testing situated in CVR – Research centre Rez in Pilsen.

3.10 Microscopy and near-surface chemical analysis

3.10.1 Confocal microscope

A confocal microscope is a special type of non-contact device used for 3D imaging and surface profiling. Unlike conventional microscope where the entire specimen is flooded evenly in light coming from a light source, confocal microscope uses point illumination which is achieved by placing a pinhole into a laser focal point. Another pinhole is placed in an optically conjugate plane in front of the detector. The setup is shown in Fig. 3.23a. Only light coming from the narrow in-focus plane of the illuminated sample will pass through the pinhole and be recorded while out of focus rays will be eliminated. Moving the sample in Z direction shifts the focal plane on the sample surface. A step by step scanning of the whole surface then allows 3D reconstruction of the surface profile. As only light produced by fluorescence at or close to the focal plane gets detected, the process requires longer exposures to collect high resolution images. Here, a confocal microscope Olympus LEXT OLS5000 was used supplemented by ZEISS optical microscope.

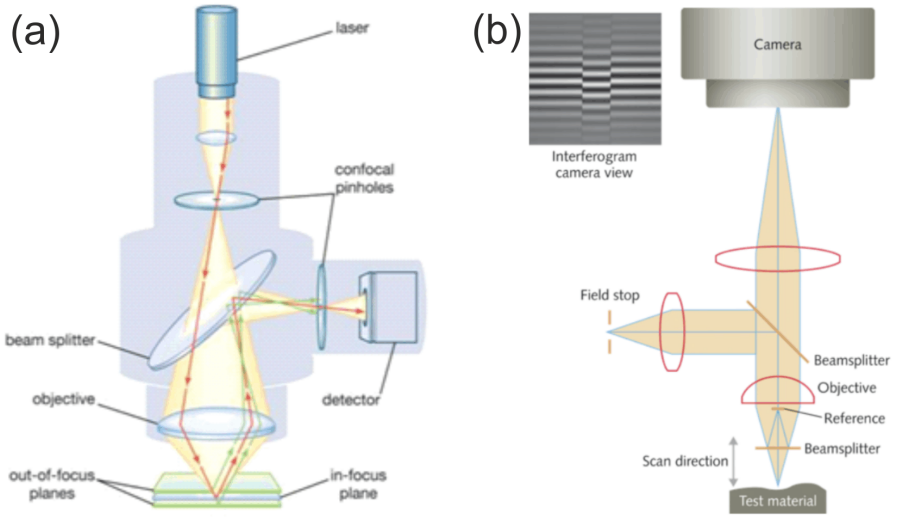

Figure 3.23: A schematic of (a) a confocal microscope [215] and (b) an interference microscope [216].

3.10.2 Interference microscope

Interference microscopes provide yet another method of non-contact optical profiling for 3D and roughness measurements. The system contains two beamsplitters. One beamsplitter is placed between the objective and the camera and the second beamsplitter is placed between the objective and the sample surface (Fig. 3.23b). Part of the light sent toward the sample coming from the first beamsplitter is transmitted to the sample surface and part gets reflected by the second beamsplitter on a reference plane. The two reflected beams then travel back through the system, recombine at the first beamsplitter and then continue to the camera. Any sample surface deviation from a flat plane is

represented as a phase shift in the interference pattern with a resolution given by half wavelength of the light used. With white light illumination, the height spacing is typically 280 nm. The use of white light results in interference fringes not covering the whole image but only a limited surface height range due to limited coherence length. Alternatively, the use of a coherent monochromatic source (laser) with fringes covering the whole field of view can be used which is called phase-shifting interferometry. White light sources are more suited for surfaces exhibiting a large height range which is also our case. The system used for measurement was WYKO NT1100 Optical Profiling System at UC.

3.10.3 Scanning electron microscope

SEM, as the name suggests, scans a focused electron beam over sample surface to create high resolution images. The theoretical limit for resolution of standard optical microscopes is given not only by the number and quality of lenses but also by the wavelength of the illumination light. White light with an approximate wavelength range of 400-700 nm and a central wavelength of 550 nm results in a maximum achievable resolution of about 200 – 250 nm. Electrons used by SEM typically have energies between 0.2 keV to 40 keV which correspond to a wavelength range of 0.03 nm to 6 nm. As a result, modern full-sized SEMs provide resolution between 1-20 nm. Electrons are generated via a thermionic emission using an electron gun and then focused and accelerated down through a combination of lenses and apertures to form an energetic tightly focused beam on the sample surface. The sample is mounted on a stage in an evacuated chamber area. The vacuum level depends on the microscope design. The scanning or sweeping of the beam is achieved by two sets of electromagnetic coils, each controlling one of the X or Y coordinates. When the electron beam hits the sample surface, a large number of products are generated. These are secondary electrons (SE), backscattered electrons (BSE) and characteristic X-rays along with continuous X-ray spectrum. The interaction volume extends from less than 100 nm to approximately 5 um into the surface depending on the accelerating voltage and the sample density. The signals are collected by one or more detectors. The image contrast is achieved in several ways. One of them is the compositional contrast generated by BSE. These high-energy electrons from the beam undergo elastic collisions when interacting with the atoms of the irradiated surface. The heavier the atoms (high atomic number) the stronger the backscattering and the brighter the resultant image (Fig. 3.24a).

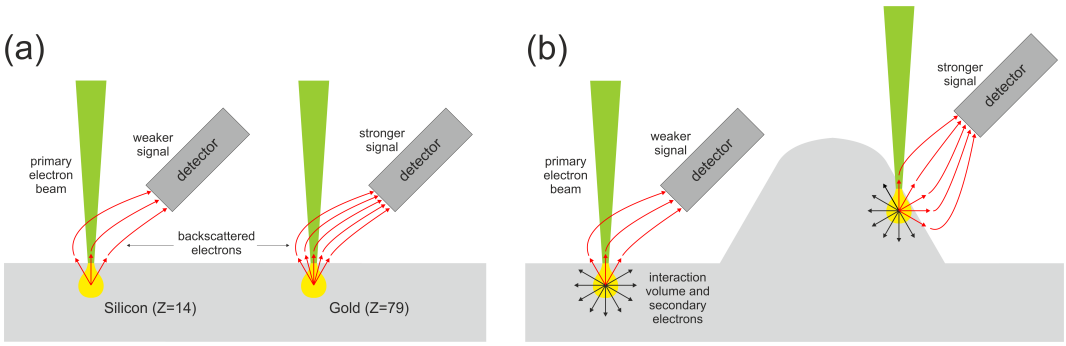

Figure 3.24: (a) SEM backscattered electrons creating contrast based on the atomic number of the irradiated elements and (b) SEM secondary electron generation creating contrast based on the surface topology.

BSE are therefore mainly used for detecting contrast between areas with different chemical composition. Second is the topographic contrast which arises due to the number of BSE and SE being dependent on the surface inclination. SE have much lower energy than the primary beam, about 50 eV, which means low penetration depth. When generated deeper inside the material which would correspond to perpendicular primary beam impact, SE do not have enough energy to leave the interaction volume resulting in lower number of detections. On an inclined surface, the interaction volume is spread closer to the surface meaning less material for the SE to penetrate and thus higher signal count (Fig. 3.24b). The resultant SEM images are characteristic in showing bright edges of objects similar to dark field illumination. The SEM devices used in this work were ZEISS Auriga Compact instruments (Fig. 3.25a) and Tescan Mira 3 (Fig. 3.25b).

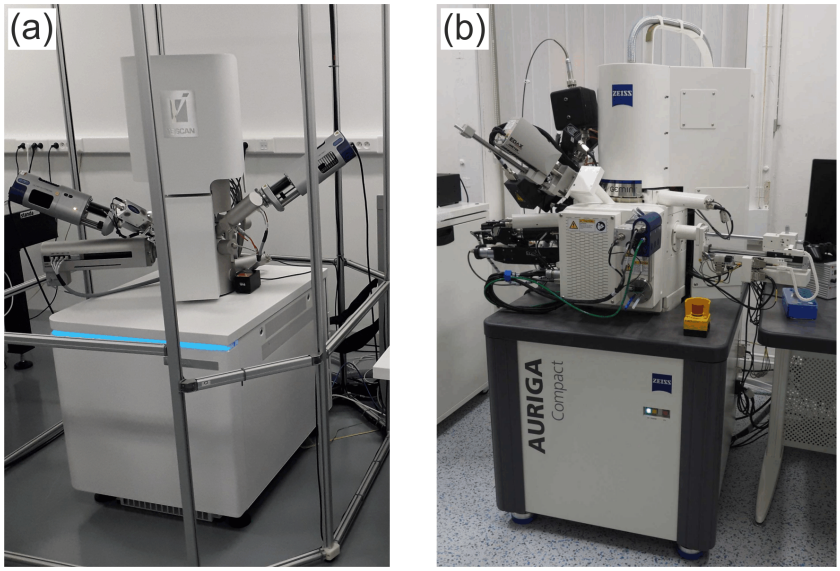

Figure 3.25: Scanning electron microscopes: (a) ZEISS Auriga Compact and (b) Tescan Mira 3.

3.10.4 X-Ray Photoelectron Spectroscopy

X-ray photoelectron spectroscopy (XPS), also known as electron spectroscopy for chemical analysis (ESCA), is a technique used for analyzing surface chemistry of various materials. One of the main advantages of the technique is that not only it can be used to measure elemental composition but also the chemical and electronic state of the atoms corresponding to different bonding energies.

During the measurement, solid surface is irradiated with an X-ray beam and electrons are ejected from the top 1-10 nm of the material. The range of electron kinetic energies is recorded creating a photoelectron spectrum or an XPS spectrum. The intensities and energies of the photoelectron peaks then allow identification and quantification of all surface elements with the exception of hydrogen. A basic scheme of the technique is shown in Fig. 3.26. The XPS spectra in this work were acquired using a KRATOS AXIS Supra XPS instrument (sputtering by Ar^+ ion clusters) using a monochromatic Al Kα (1486.6 eV) X-ray source.

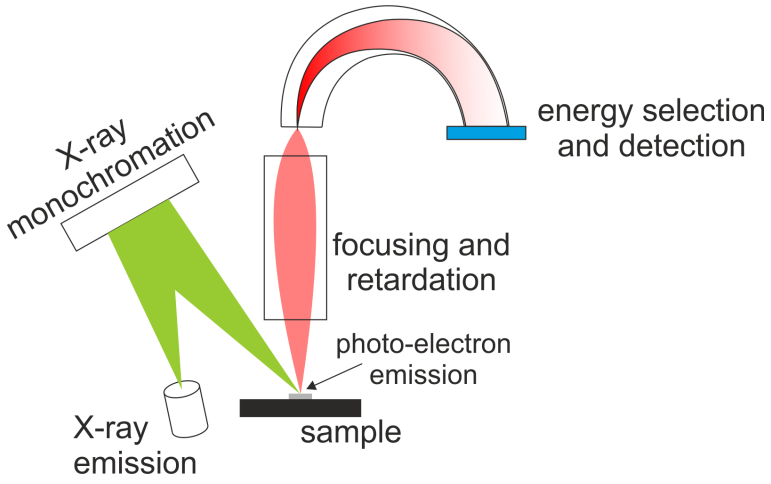

Figure 3.26: XPS scheme.

Chapter 4

Experimental results and discussion

4.1 Laser parameter optimization

Determining optimal peening parameters for a given component is a particularly uneasy task due to the large amount of variables involved. One may change the pulse energy, spot size, pulse duration, beam profile, laser spot overlap, peening strategy, protective overlay type and thickness, angle of incidence, laser wavelength, water delivery and others. Every material responds differently to the treatment but even within the scope of one material, geometry plays a very significant role. The parameters will also vary depending on the specific mechanical problem which is to be addressed by LSP. Moreover, peening parameters are not very well transferable between different laser systems as each system tends to be unique with its own parameters and the possibilities for tuning are usually limited. Therefore, the only way to properly optimize the peening parameters is computer modelling and simulations. For real components with more complex geometry such as turbine blades, modelling is a necessity. Computer simulations, however, are outside the scope of this work. The sample geometry used in this work was kept simple so that the peening parameters could be determined through a set of experimental guidelines which will be presented in the following sections. Due to multiple laser sources available, one of the main goals of this study was to cover as much variety in the peening process as possible and determine which approach yields the best results for the problem of SCC and CF of AA5083-H116. The three selected peening categories were:

1. LSP IR - conventional Laser Shock Peening (LSP) with protective tape using infrared laser (IR)

2. LPwC IR - Laser Peening without Coating (LPwC) with infrared laser (IR)

3. LPwC SHG - Laser Peening without Coating (LPwC) with second harmonic generation (SHG) laser underwater

4.1.1 Peening strategies

Two laser systems (3.2) were used in the experiments and the corresponding laser parameters for each of the peening categories are shown in Table 4.1. The parameters were selected to be as much comparable as possible despite the non-identical spatial and temporal beam profiles which were predetermined by the laser system designs (3.7). Additionally, as a part of the optimization process, the Bivoj laser was subjected to VISAR measurements (2.5.1) which was done in a collaboration of HiLASE and French LSP

group lead by Laurent Berthe and Remi Fabbro. The laser induced pressure on the specimen surface as a function of the laser power density is shown in Fig. 4.1. Up to a point of about 4.5 GPa, the plot shows a stable rise of pressure with power density which supports the analytical result for confined regime (2.21). The red line at 4.5 GPa marks the dielectric breakdown threshold after which the pressure becomes unstable. The power densities were therefore selected safely below this threshold to allow good result repeatability.

Laser	LSP condition	Wavelength (nm)	Energy (J)	Pulse length (ns)	Repetition frequency (Hz)	Beam profile	Spot size (mm)	Power density (GW/cm^2)
PLP	LSP IR	1064	3	30	10	top-hat circular	2.0	3.2
	LPwC IR	1064	1	22	10	top-hat circular	1.5	2.6
	LPwC SHG	532	1	23	10	top-hat circular	1.5	2.5
Bivoj	LSP IR	1030	3	14	10	top-hat square	2.5	3.4
	LPwC IR	1030	1	14	10	top-hat square	1.5	3.2
	LPwC SHG	515	1	14	10	top-hat square	1.5	3.2

Table 4.1: Selected laser pulse parameters for 3 treatment conditions and 2 laser systems.

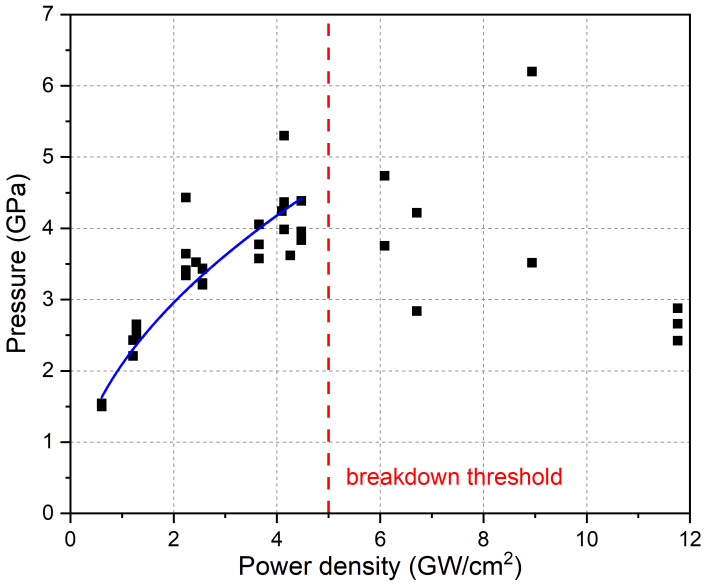

Figure 4.1: VISAR measurements of Bivoj laser system showing the dielectric breakdown threshold [217].

The first peening category, LSP IR, represents the standard way to apply LSP where protective overlay, in this case 120 μm thick black vinyl tape is being used on top of the peened surface to prevent it from melting during the laser pulse absorption. The experimental setup of the LSP IR condition is shown in Fig. 4.2a.

To prevent tearing of the tape after multiple laser hits, the sequencing technique was used (2.5.6) where full laser coverage of the surface (layer) was achieved with 4 mutually offset peening sequences with the tape being replaced between each. To better illustrate

the sequencing, changes in surface topography after application of each sequence were recorded and are shown in Fig. 4.3. The number of layers, specifically 1 and 2, was used as a variable in the following measurements to study the influence of number of laser impacts on the residual stresses and DoS.

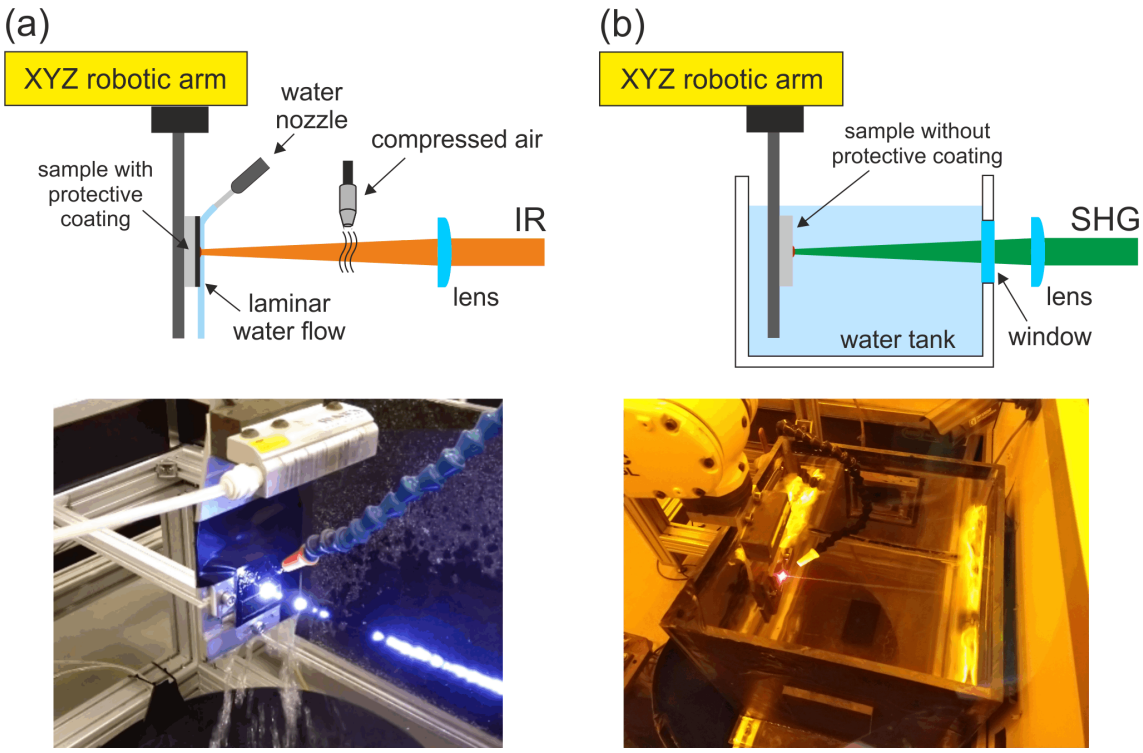

Figure 4.2: Experimental setup using the PLP laser for (a) peening with protective tape (LSP IR) and (b) peening without protective tape underwater (LPwC SHG). Plasma breakdown in the beam path can be observed in the LSP IR setup as the laser gets focused by small sprayed water droplets. The orange colour of the photo showing the underwater peening setup is caused by safety goggles equipped with 532 nm filter which were placed in front of the camera objective to protect it against intense green light.

The experimental setup for the LPwC IR samples was the same as in Fig. 4.2a except for the missing protective coating and different lens-to-sample distance to accommodate the different laser spot size. The experimental setup fot the LPwC SHG condition is shown in Fig. 4.2b. The sample is submerged in a water tank where the laser beam enters through a laser-grade glass window in the tank wall. With no tape to replace, a straightforward scanning strategy can be adopted. The whole treatment can now be carried out in a single laser pass where pulses are placed next to each other with high overlap from the very start. The peening patterns are summarized in Fig. 4.4.

Rather than the number of layers, the deciding parameter in the LPwC treatment is the pulse density which is controlled via scanning speed and spacing between lines. Specific pulse densities have been selected based on the Fanuc robotic arm speed which did not allow for decimal number values. The processing parameters in both LPwC categories were selected the same so that a direct comparison between the IR applied in air with thin water film and SHG laser applied underwater could be made.

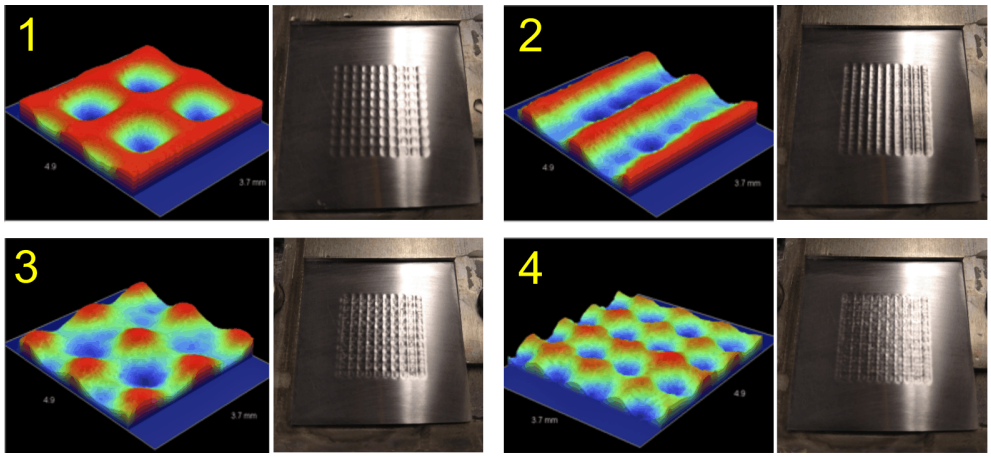

Figure 4.3: Plastic deformation of sample surface after 1,2,3 and 4 LSP sequences being applied. The left part of each sequence represents the surface profile scanned by Wyko profilometer and the right part shows the real surface after particular LSP sequence.

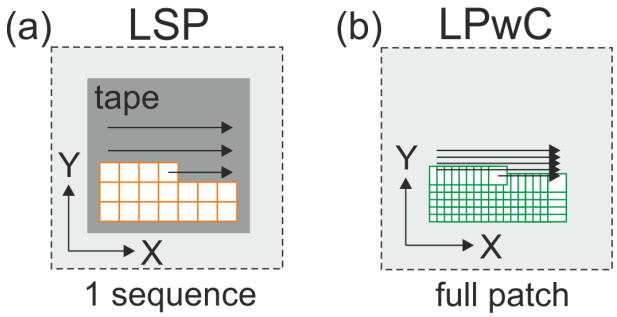

Figure 4.4: Laser scanning strategy (a) with and (b) without protective tape applied.

4.1.2 Residual stress analysis

The 6.35 mm plate of AA5083-H116 was sectioned using EDM to 40 mm x 40 mm x 6.35 mm flat coupons. The surface has been progressively grinded to 600 grit polish. A 20 mm x 20 mm patch was peened in the coupon centre using the PLP laser system. The laser and processing parameters are shown in Table 4.1 and Table 4.2, respectively. Prior to the treatment, the coupons were in a non-sensitized state (as received) without any previous heat treatment outside the manufacturing process. The coupons after the treatment are shown in Fig. 4.5. After the LSP IR treatment, the surface retains its polish with the laser induced plastic deformation well visible. Surfaces of the LPwC coupons are partially molten which in this case manifests as white patches of rougher surface.

For the in-depth residual stress analysis (3.5), the material was removed by electropolishing in small increments closer to the surface (~30 μm) where stress changes are most rapid. Deeper inside the material, the intervals were increased to 100-200 μm. For each depth, the stresses were measured both in scanning and transversal directions, denoted σ_S and σ_T, respectively. Fig. 4.6 shows in-depth residual stress measurement results in all three peening setups. Multiple pulse densities are investigated for LPwC similar to the number of layers in the LSP treatment. Additionally, the data measured is compared to the baseline (as received) material, i.e. material where no laser peening was applied. The standard deviation of any of the XRD measurements did not exceed ± 18

LSP Condition	Protective Coating	Water confinement	Scanning speed (mm/sec)	Line Spacing (mm)	Pulse density per pass (p/cm^2)	Total laser passes	Total pulse density (p/cm^2)	Total fluence (J/cm^2)
LSP IR 1L	yes	laminar flow	20	2	25	4	100	300
LSP IR 2L	yes	laminar flow	20	2	25	8	200	600
LPwC IR 204	no	laminar flow	7	0.7	204	1	204	204
LPwC IR 400	no	laminar flow	5	0.5	400	1	400	400
LPwC IR 1089	no	laminar flow	3	0.3	1089	1	1089	1089
LPwC IR 2500	no	laminar flow	2	0.2	2500	1	2500	2500
LPwC SHG 204	no	underwater	7	0.7	204	1	204	204
LPwC SHG 400	no	underwater	5	0.5	400	1	400	400
LPwC SHG 1089	no	underwater	3	0.3	1089	1	1089	1089
LPwC SHG 2500	no	underwater	2	0.2	2500	1	2500	2500

Table 4.2: Processing parameters for residual stress measurement analysis.

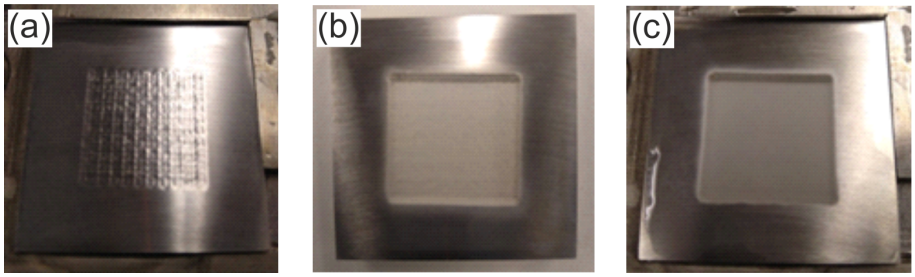

Figure 4.5: Square coupons of AA5083 after (a) LSP IR 2L, (b) LPwC IR 1089 and (c) LPwC SHG 1089 after being treated with the PLP laser.

MPa. The LSP IR condition is represented on top row of 4.6. The left and right columns show stresses σ_S and σ_T, respectively. In comparison with the baseline, the LSP treatment with protective tape applied clearly generates significant compressive residual stresses, around -200 MPa on the surface and maximum compressive stresses reached at a depth of about 200 μm. More laser pulse impacts represented by the 2L plot cause a constant increase of about 50 MPa in the compressive stresses. The stresses induced in both σ_S and σ_T are very similar and no significant variations are observed. The compression depth in both directions is about 1.5-1.6 mm which is higher than in the LPwC cases. This can be explained by larger spot size used where shock waves generated by laser impacts with larger spot size attenuate slower and thus deeper residual stresses are produced (2.5.5). The middle row graphs in Fig. 4.6 represent the LPwC IR condition. Unlike the LSP IR plots, there is a clear distinction between σ_S and σ_T. In scanning direction, the compressive residual stresses peak almost immediately at pulse density as low as 204 p/cm^2. The maximum compressive stress reached is -150 MPa and the compression depth is about 1.5 mm regardless of the pulse density. In the transversal direction, the stress curve changes as higher pulse densities are applied. A maximum compression of about -325 MPa was achieved corresponding to pulse density of 1089 p/cm^2. The ultimate tensile strength of the material is 317 MPa which means a saturation point was reached. The compression depth reached was in the range of 1.2 mm to 1.4 mm with the highest depth corresponding to 204 p/cm^2 and lowest to 2500 p/cm^2. The stress plots for the LPwC SHG condition are displayed at the bottom row of Fig. 4.6. The results are similar to the LPwC IR case, showing the same distinction between σ_S and σ_T measurements. The maximum compressive stresses reached in the scanning direction were about -180 MPa with very fast saturation. The compression depth ranged between 1.1 mm to 1.4 mm.

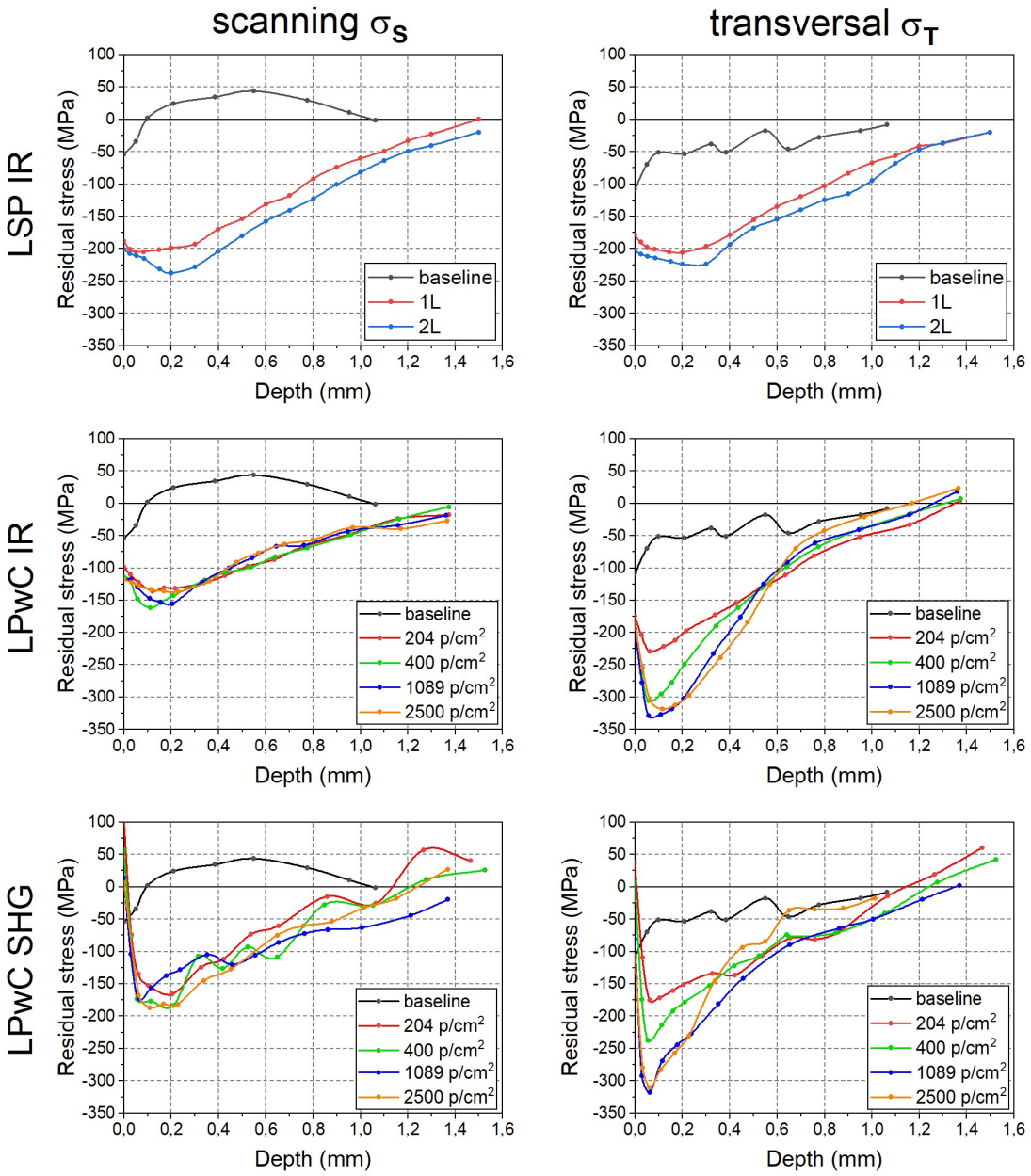

Figure 4.6: In-depth residual stress measurements of AA5083 after various LSP treatments: LSP IR (top line), LPwC IR (middle line) and LPwC SHG (bottom line). The measurements were taken both in scanning σ_S (left column) and transversal σ_T (right column) directions.

The σ_T measurements show the same trends as their LPwC IR counterpart with saturation reached at -325 MPa at 1089 p/cm^2. The plots show, however, that the saturation point is reached faster in the LPwC IR case which is evident from the higher stress values of the 204 p/cm^2 and 400 p/cm^2 plots. The peaks in the LPwC SHG case are also sharper and the subsequent drop-off is faster. The depths reached are once again between 1.1 mm to 1.4 mm depending on the pulse density. The resultant stress anisotropy with LPwC treatments can be explained by stress field interaction of overlapping laser pulses in a single pass peening pattern [195]. As a result, the residual stresses are higher in the

advancing transversal direction as opposed to the scanning direction. Furthermore, the stress anisotropy only occurs when the pulse overlap occurs within one laser pass. This is evidenced here in top row of Fig. 4.6 where despite the final overlap being 50% in the LSP IR case, the overlap within each separate sequence was 0% and as a result, no residual stress anisotropy was detected. On the contrary, high stress anisotropy was found in both LPwC IR and LPwC SHG where high laser pulse overlap was achieved within a single laser pass.

Special attention is paid to the surface residual stresses where the biggest difference between the treatment with and without tape should be found (2.3.1). With the LSP IR treatment involving protective tape, the surface stresses are rather straightforward, about -175 MPa for 1L and -200 MPa for 2L in both directions. Without the tape, the results start to vary based on the environment. The surface stress values for LPwC IR and LPwC SHG are separately plotted against pulse density in Fig. 4.7.

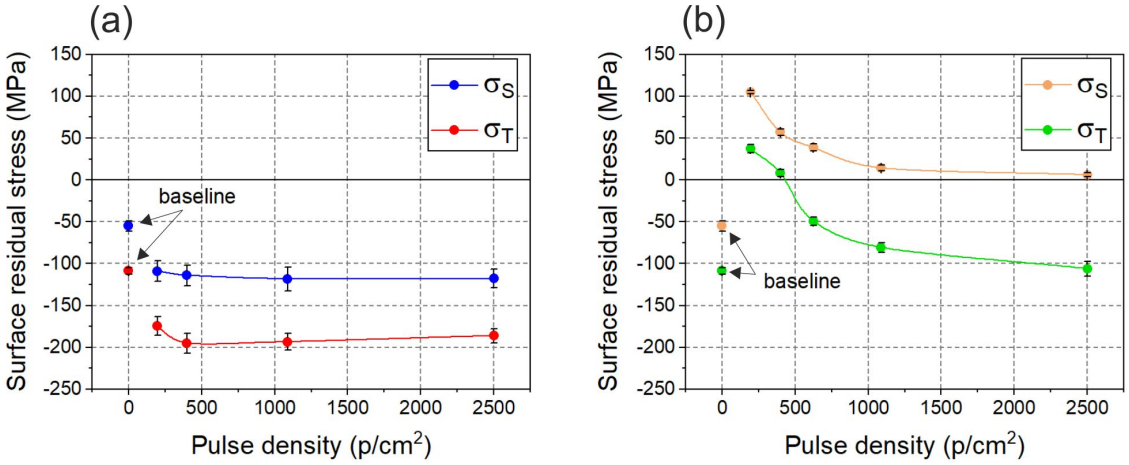

Figure 4.7: Surface residual stresses in LPwC treatments as a function of laser pulse density: (a) LPwC IR and (b) LPwC SHG.

The LPwC IR data in Fig. 4.7a show that despite the heat effects present in the treatment, the stresses moved towards compression both in σ_S and σ_T measurements when compared to baseline. The stresses peak rather fast around 400 p/cm^2 and then level off. The difference between σ_S and σ_T is about 60-80 MPa and is kept constant over the whole data range. The surface stress measurement in LPwC SHG (Fig. 4.7b) shows similar trend but everything is shifted in the tensile direction. The underwater peening at the lowest pulse density causes an abrupt shift of roughly 150 MPa towards tensile stresses in both scanning and transversal direction, creating tensile residual stresses of 105 MPa and 37 MPa as opposed to baseline values of -55 MPa and -109 MPa, respectively. The stresses then start to move toward compression as the pulse density rises. Compared to the LPwC IR data, however, it does not level off and keeps dropping at a low rate within the data range. While the initial baseline value in σ_T is regained at 2500 p/cm^2, the data suggests that the baseline value will not be reached in the σ_S plot. As the laser energy should be absorbed readily regardless of wavelength by the plasma layer that forms near instantaneously compared to the nanosecond scale pulse duration, the difference in laser wavelengths is expected to be largely inconsequential, assuming that energy delivered per pulse remains constant. The differences between the LPwC IR and LPwC SHG conditions are therefore more likely to arise from changes in the confinement and resulting interactions between the plasma and the metal surface. Further analysis, however, is

required and is currently beyond the scope of this study. Nevertheless, it was reported that compressive residual surface stresses can be achieved underwater when lower pulse energies (<250 mJ) with very high pulse densities (~10000 p/cm^2) are used (2.3.1).

Based on the results presented in this section, several conclusions can be made:

1. Both LSP and LPwC imparts deep compressive residual stresses into the studied material. The magnitude of the stresses rises with the number of laser pulse impacts until a saturation point is reached. Slightly deeper stresses were obtained with LSP treatment which is explained by slower shock wave attenuation when larger laser spot is used.

2. Residual stress anisotropy was observed in case of LPwC treatments where larger compressive stresses up to a point of material saturation were measured in the laser advancing direction with respect to the peening pattern. The anisotropy is explained by stress field interaction during pulse overlapping and is completely absent in the LSP case where 0% pulse overlap within individual sequences was used.

3. Comparable compressive residual stresses were found on surface of both LSP IR and LPwC IR conditions. In both cases, the surface stress magnitude was mostly independent on the number of laser impacts. In case of LPwC SHG, tensile surface stresses were measured which turned into compressive in the transversal direction for higher pulse densities. The baseline compression was however never exceeded.

4. At certain pulse density during the LPwC treatment, a saturation point is reached and the compressive stresses no longer increase with increasing pulse density. This saturation point for both LPwC treatments was determined as 1089 p/cm^2. Together with the LSP IR 2L, the specific conditions LPwC IR 1089 and LPwC SHG 1089 were determined as primary treatment conditions for the following measurements presented in this work.

4.2 Nano-Hardness measurement

Square coupons with dimensions 40 mm x 40 mm x 6.35 mm were sectioned using EDM and polished to 1200 grit. Peening in the form of 20 mm x 20 mm patch was applied using the PLP laser. Based on the residual stresses measured, the processing parameters have been narrowed down to 3 conditions: LSP IR 2L, LPwC IR 1089 and LPwC SHG 1089. In this section from now on, the distinct samples will be marked with the first two labels only; that is LSP IR, LPwC IR and LPWC SHG. After the treatment, the specimens were cross-sectioned and cold mounted using epoxy resin with the cross-section pointing up (Fig. 4.8a). The exposed surface was further polished to 1200 fine grit to remove surface damage from sectioning. The measurement strategy involved 2 rows of indentations starting at the surface and reaching 2 mm in depth (Fig. 4.8b). The two rows were 50 μm apart and the spacing between the indentations was 30 μm for the first 800 μm and 50 μm for the rest of the depth. Berkovich indentor (3.7) was used at a maximum load of 100 mN and holding time of 10 sec. The results of the hardness measurements are displayed in Fig. 4.9.

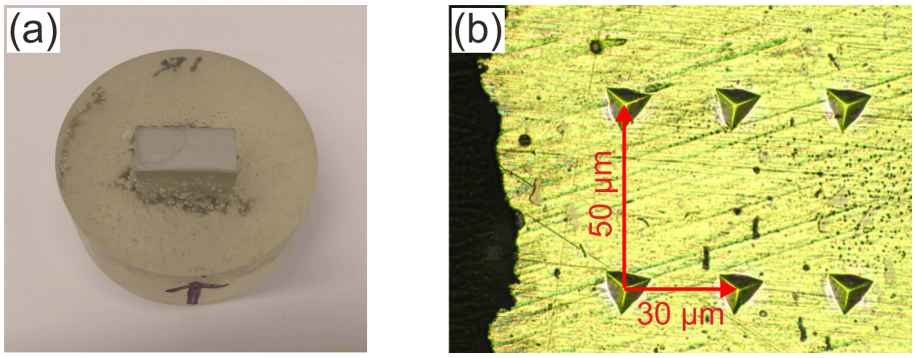

Figure 4.8: (a) Cross-sectioned LPwC IR specimen cold mounted in epoxy resin and (b) three sided pyramid shaped nano indentions in two rows starting at surface of LPwC IR sample.

The highest surface nano-hardness of roughly 155 HV was achieved with the LSP IR condition where protective coating and pulse energy of 3 J was used. This represents an increase of 25% when compared to the non-treated sample which showed a constant hardness level of 120 HV. The second highest surface nano-hardness of about 148 HV was reached with the LPwC IR treatment which represents an increase of 23%. The LPwC SHG treatment also lead to an increase of 18% with the surface nano-hardness value of 142 HV. In all three peening cases, the increased nano-hardness decreases exponentially with depth until the baseline level is restored. The depths reached are around 1.6 mm, 1.5 mm and 1.2 mm for the LSP IR, LPwC IR and LPwC SHG, respectively. When compared to the residual stress data, we can see that the increased hardness depth roughly copies the compression depth of the corresponding processing parameters from Fig. 4.6.

Furthermore, the hardness increase for each investigated condition qualitatively correlates with the degree of plastic deformation induced during the peening process represented by single laser pulse surface changes displayed in Fig. 4.10. The largest deformation is caused by the LSP IR condition as quantified by the dimple depth in Fig 4.10a which stretches over 41.3 μm from the highest to the lowest point of the scanned dimple area. The LPwC IR dimple is shown in Fig. 4.10b and its depth is 30.2 μm. Lastly, the lowest deformation is caused by LPwC SHG (Fig. 4.10c) with only 9.9 μm dimple depth.

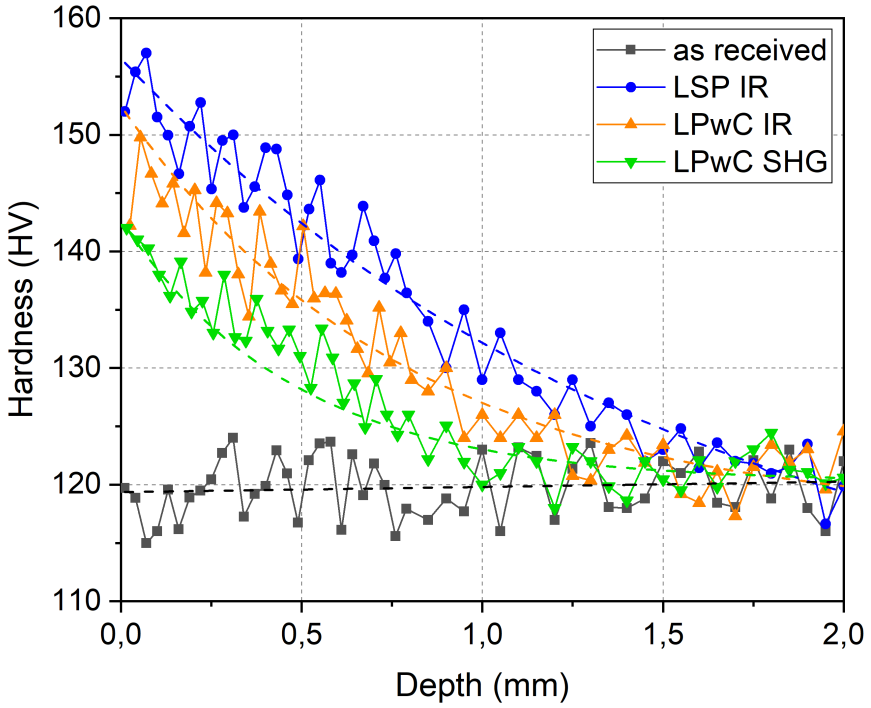

Figure 4.9: Nano-indentation hardness measurements of AA5083 samples subjected to various LSP treatments compared to the as received condition.

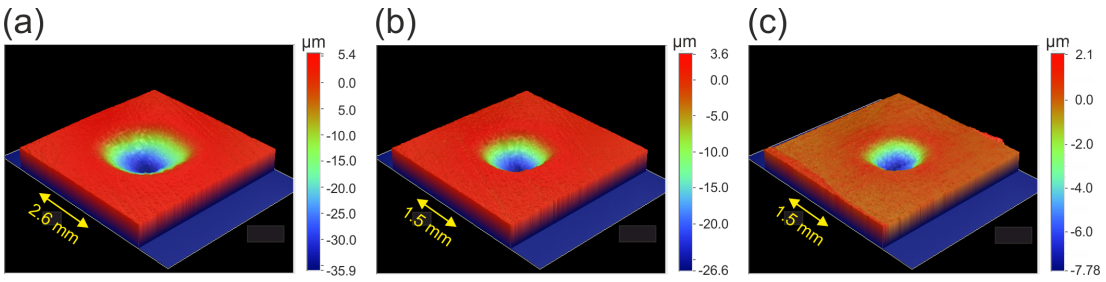

Figure 4.10: Plastic deformation of AA5083 surface after single laser pulse impact: (a) LSP IR, (b) LPwC IR and (c) LPwC SHG.

4.3 Nitric Acid Mass Loss Test analysis

4.3.1 Degree of Sensitization as a function of grain orientation

Due to the rolling process involved in the manufacturing, the alloy grains are pancake shaped with an elongation in the rolling direction (RD) and narrowest dimension in the normal direction (ND). A 3D image of the grain morphology obtained using the EBDS technique is displayed in Fig. 4.11.

It has already been established that when the AA5083 alloy is sensitized, Mg rich β-phase precipitates on grain boundaries (1.2). To better understand the sensitization process and what effect heat processing has on the DoS, the samples were divided into 3

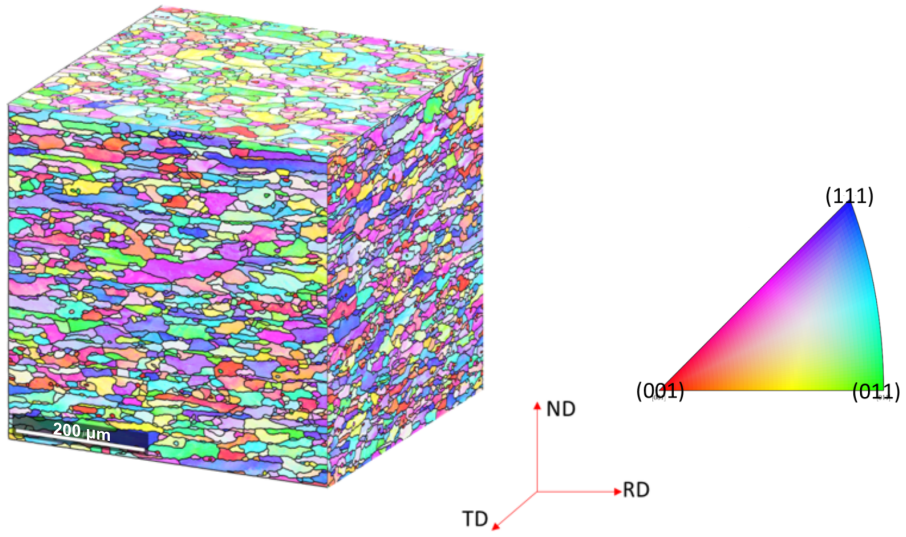

Figure 4.11: EBSD image of grain structure from AA5083-H116 3/8" thick plate from the same supplier used in this study. The grains are flattened in normal direction (ND) and elongated in the rolling direction (RD).

heat related categories. The first category comprises samples in their received condition directly from the manufacturer with no additional heat processing (as received). The second category involves sensitized samples which were put into heat oven for a period of 60 days at 100 °C and air cooled upon removal (sensitized). And lastly, the third category comprises samples that have been solutionized at 450 °C for a period of 2 hours and water cooled upon removal (solutionized). Fig. 4.12 then shows images taken by a confocal microscope of different specimen faces of solutionized, as received and sensitized specimens with β-phase visualized. The β-phase was revealed by etching the specimens in 8.5 vol% H_3PO_4 at 60 °C for a 1 min period based on the work of Jones et al. [218].

First, we notice no β-phase precipitates visible on none of the solutionized faces which was expected as all the precipitates were dissolved during the high temperature treatment. While both as received and sensitized specimens show signs of β-phase precipitation, only small discontinuous traces can be visible in the as received specimen regardless of orientation. In contrast, the sensitized condition shows nearly continuous network of precipitated grain boundary β-phase. Due to the varying amount of grain boundaries available on each face (Fig. 4.11), different amount of β-phase precipitation is exposed to outside chemical attack. The grains are large on the RD-TD face which means the least amount of grain boundary and β-phase present. The highest amount of β-phase is present in the ND-TD plane where the grain dimensions are small and the boundary to grain size ratio is the highest.

Fig. 4.13 shows all three sensitized faces after being subjected to the nitric acid attack using standard NAMLT. Almost no grains falling off can be observed on the RD-TD face despite network of heavily corroded grain boundaries. In contrast, both the RD-ND and ND-TD faces show loosely attached and completely exposed grains. In order to determine how much each face contributes to the mass loss specifically, two sets of 5 sensitized specimens with one fixed face area (RD-ND and ND-TD) and decreasing thickness were subjected to the standard NAMLT. The specimen dimensions were 50 mm x 6.35 mm x 5.7-1.5 mm. As the thickness got smaller, the face with fixed area became more dominant. The mass loss test results are shown in Fig. 4.14.

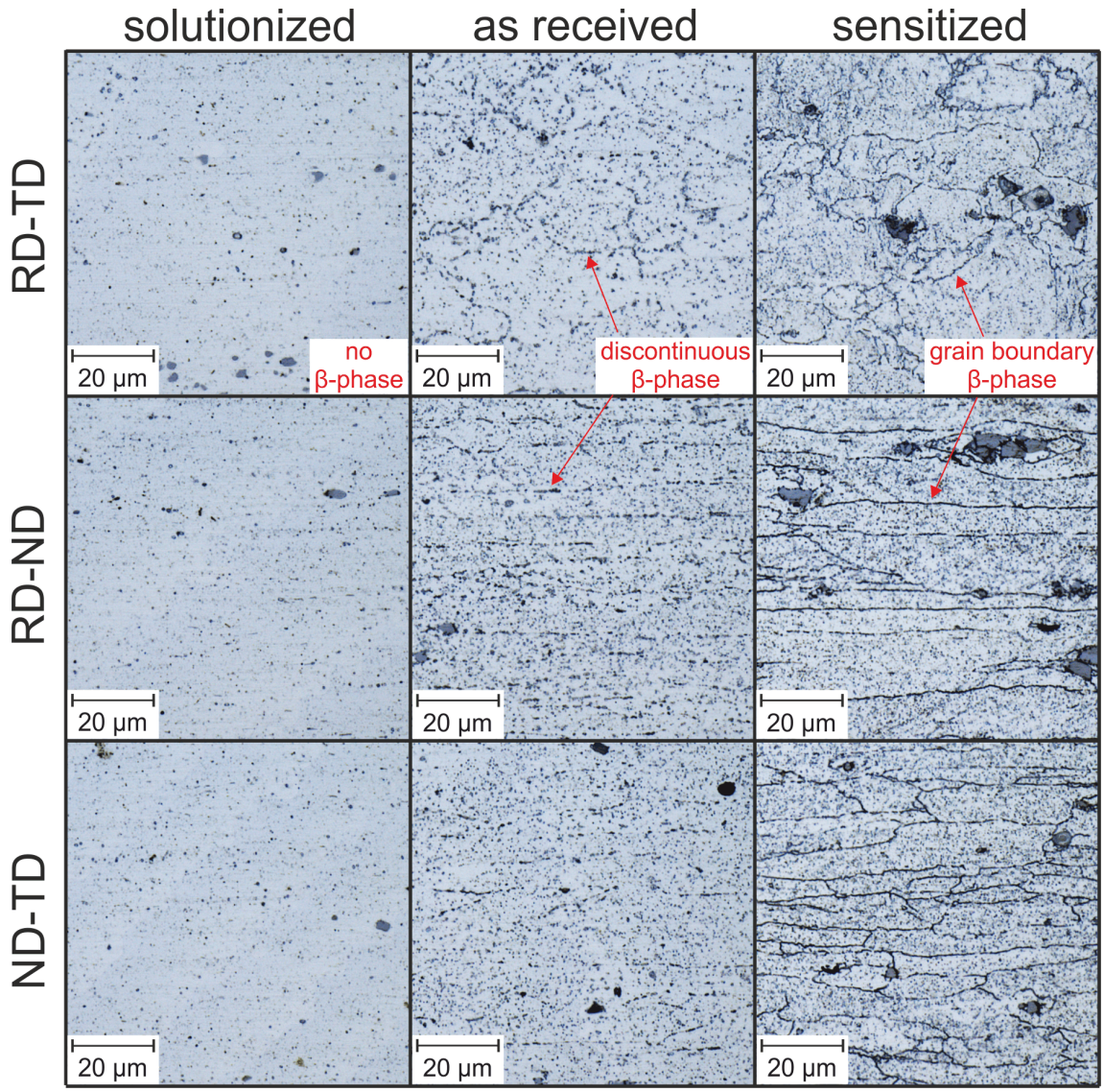

Figure 4.12: Optical microscope images of β-phase on various faces of solutionized, as received and sensitized samples on various specimen faces.

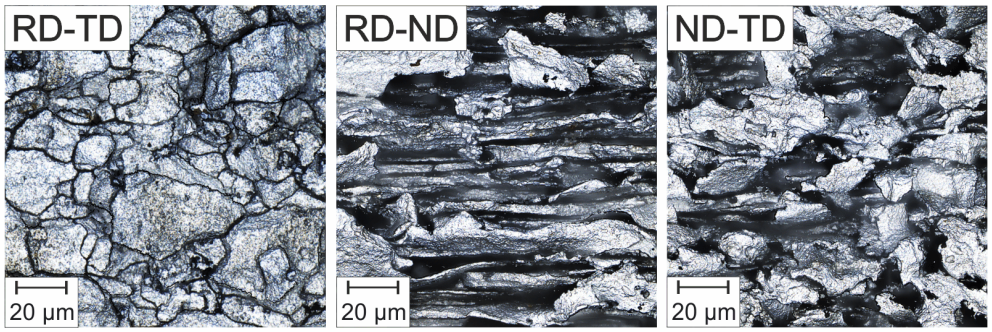

Figure 4.13: Optical microscope images of AA5083 faces after being subjected to 24 hour attack of concentrated nitric acid during NAMLT.

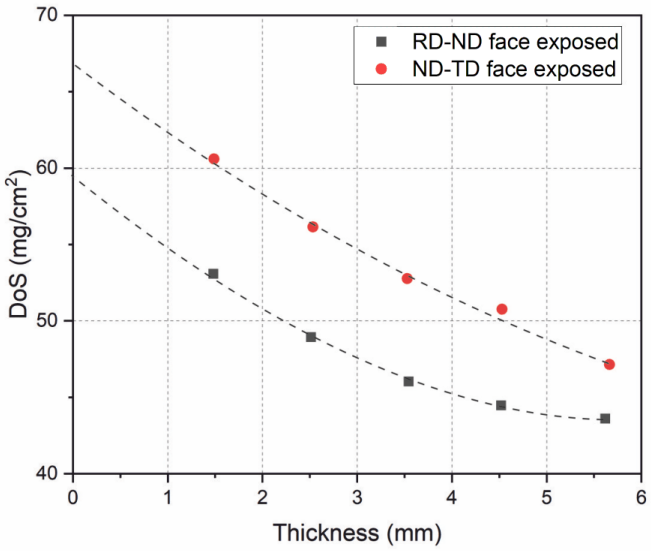

Figure 4.14: Degree of sensitization of specimens with one face area fixed and the area of the other two faces progressively decreasing.

The DoS of isolated RD-TD face was determined to be 10.6 mg/cm^2 using the modified NAMLT (3.6.1). The increasing trend of DoS observed with decreasing thickness can therefore be explained by the decreasing area share of the RD-TD face with low DoS. Specific DoS of the RD-ND and ND-TD can then be determined approximately by extrapolation to the limit case of 0 mm thickness where only a singular face theoretically contributes to the DoS. Finally, the estimated specific contribution of each face to the total mass loss is depicted in Fig. 4.15.

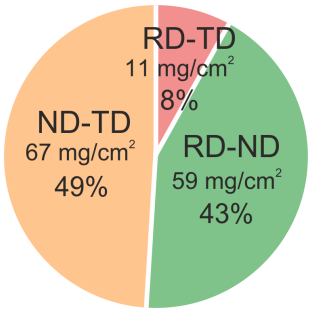

Figure 4.15: Estimated mass loss contribution of various faces of sensitized AA5083 plate when subjected to NAMLT.

By far the lowest contribution of 8% from the total mass loss comes from the RD-TD face. The ND-TD and RD-ND faces then yield comparable ratios of 49% and 43%, respectively. The highest mass therefore comes from the face with the highest grain boundary to grain size ratio Fig. 4.11. More detailed explanation is provided in (1.3.4).

Fig. 4.16 shows the sensitization progress of the AA5083 samples as measured both by the standard NAMLT and modified NAMLT. The DoS of the RD-TD face as opposed

to the combined DoS of all three faces was around 50% on day 0 and it kept decreasing down to 24% by day 60. It is interesting to note that that the DoS in case of modified NAMLT maximizes around day 42 while it keeps rising for standard NAMLT all the way to day 60. Based on the data, the modified test shows more consistency than the standard one. This is attributed to the absence of specimen edges which introduce larger degree of uncertainty into the measurement since these are the source of highest grain fall-off.

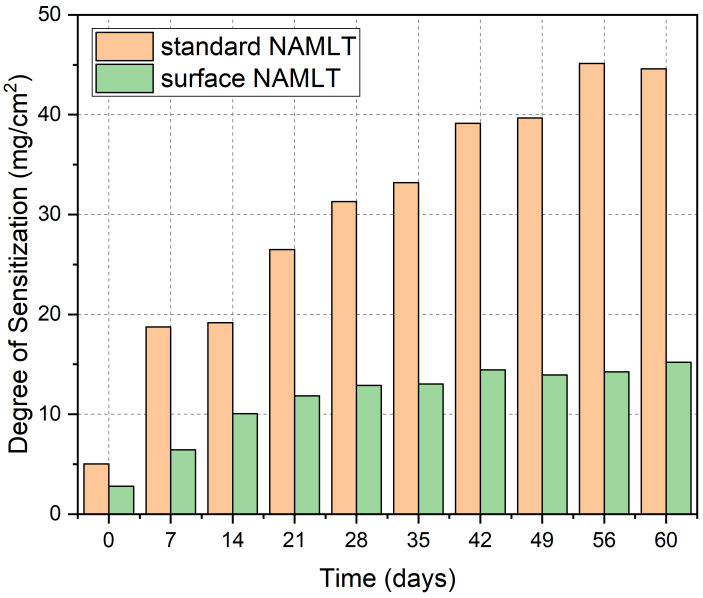

Figure 4.16: Sensitization progress of AA5083 measured by standard NAMLT and modified NAMLT applied on the RD-TD face.

4.3.2 The effect of LSP on DoS

To better demonstrate the insufficiencies of the standard NAMLT when it comes to laser peening, the results obtained with both tests will be shown and compared. For the standard test, specimens with dimensions 50 mm x 6 mm x 6.2 mm (after polishing) were cut out from the sensitized plate. Due to the nature of laser peening, the specimens were treated only from two opposing sides (Fig. 4.17a) which corresponded to the ND-TD faces following the previous conclusion that the ND-TD face contributes the most to the DoS. Because of that, the specimens had to be first cut out and then treated as independent blocks rather than peening the whole plate and then cutting out the blocks afterwards. For the modified NAMLT, square coupons with dimension 50 mm x 50 x by 6.2 mm were used (Fig 4.17b). Here, laser peening was applied to the largest face with RD-TD orientation. PLP laser was used for the peening and the treatment applied follows the notation from Table 4.2.

During the treatment, the standard NAMLT samples were placed next to each other and attached to the base holder using two sided tape. The peened patch overreached the specimen edges so that the exposed face was completely covered (Fig. 4.18a). The larger square coupons for modified NAMLT used standard mechanical attachment and

the treated area was 45 mm x 45 mm to cover the whole area exposed to the acid attack (Fig. 4.18b).

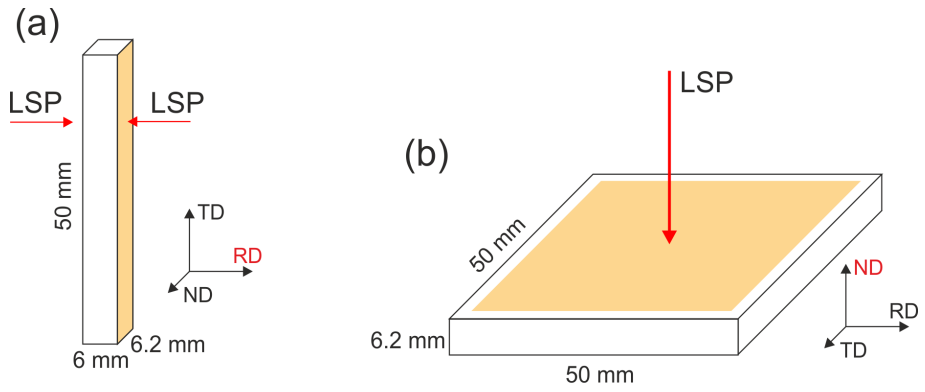

Figure 4.17: Specimen dimensions and orientation for (a) standard NAMLT and (b) modified NAMLT.

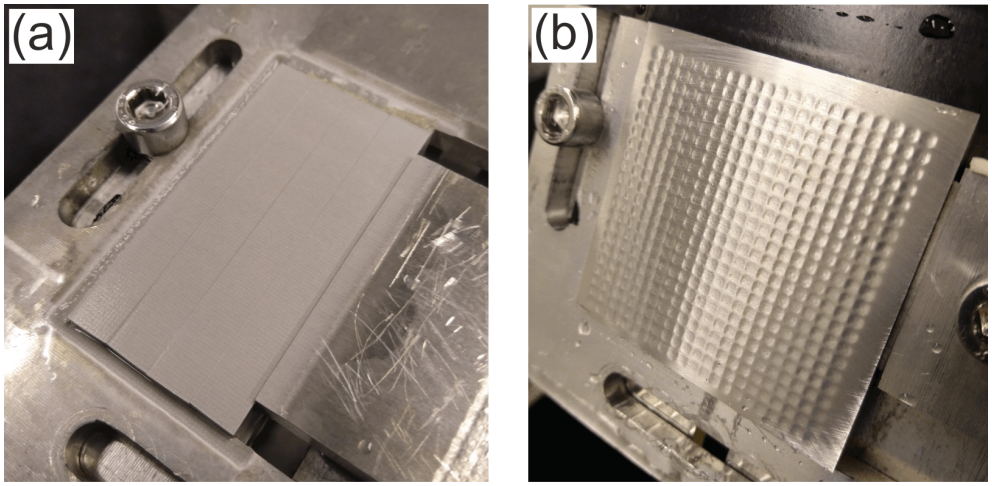

Figure 4.18: Laser peening of NAMLT specimens: (a) LPwC SHG for standard NAMLT and (b) LSP IR (1st sequence) for modified NAMLT.

Once the peening was finished, the specimens were subjected to the DESMUT procedure as described in (3.6) and weight measurements were taken. For the standard NAMLT, each sample including the control group was placed into a separate glass tube with 40 ml of 70% HNO_3. The tubes were then placed into a holder submerged in water bath with temperature control (Fig. 4.19b). The glass tube with sensitized specimen before and after 24 h of acid attack is shown in Fig. 4.19a. For the modified NAMLT, the samples were mounted in the developed contraption (Fig. 4.19c) so that the acid attack affected the treated face only. Once again, the exposed area was cca 12 cm^2 and 40 ml of 70% HNO_3 was used. The actual test in progress with specimens submerged in the water bath is shown in Fig. 4.19d.

For better interpretation, the final results are displayed both in the form of a table and a column graph in Fig. 4.20. While the standard test comprises all the LSP and LPwC treatment conditions, the modified test focuses only on the LSP IR 2L, LPwC IR 1089 and LPwC SHG 1089. The standard NAMLT results show improvement with most of the

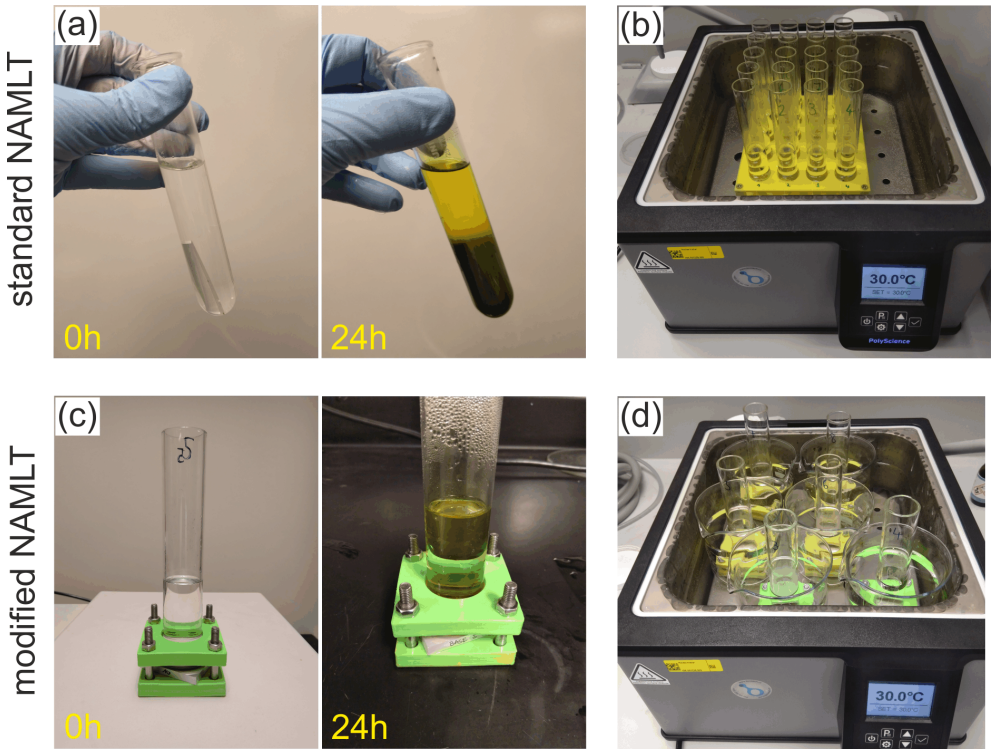

Figure 4.19: Implementation of the NAMLT: (a) standard NAMLT before and after 24h of 70% nitric acid attack, (b) glass tubes with specimens placed in a water bath during standard NAMLT, (c) modified NAMLT before and after 24h of 70% nitric acid attack and (d) 3D printed contraptions with specimens placed in separate beakers in a water bath during modified NAMLT.

peening conditions but most of the time, the improvement is negligible, represented only by a few percentage points. These results are within the margin of error of the measurement and are statistically insignificant. The only recognizable trend can be seen in the LPwC IR condition which shows steady improvement in DoS with rising pulse density down to 40.66 mg/cm^2 as opposed to 44.6 mg/cm^2 of the control sample. Overall however, the results are unconvincing. The modified NAMLT results fortunately give a much clearer picture. With only the treated area involved in the weight loss measurement, we now see a clear improvement of 17.6% and 20.1% with the LSP IR 2L and LPwC IR 1089 samples, respectively. On the other hand, the LPwC SHG 1089 condition showed a slight increase of 5.4% in DoS.

(a) Standard NAMLT

LSP condition	DoS [mg/cm^2]	Change vs control
Control	44.60	
LSP IR 1L	44.61	-0.03%
LSP IR 2L	43.16	3.23%
LPwC IR 400	43.45	2.57%
LPwC IR 1089	41.76	6.38%
LPwC IR 2500	40.66	8.83%
LPwC SHG 400	44.19	0.92%
LPwC SHG 1089	43.09	3.38%
LPwC SHG 2500	45.43	-1.85%

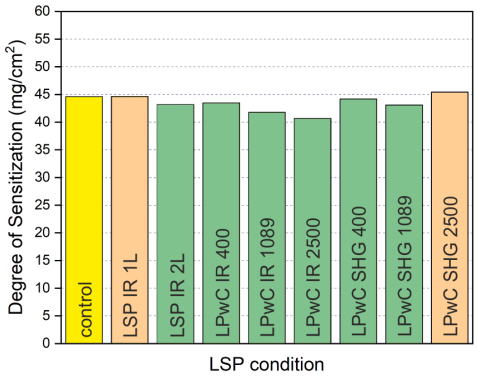

(b) Modified NAMLT

LSP condition	DoS [mg/cm^2]	Change vs control
Control	10.60	
LSP IR 2L	8.73	17.63%
LPwC IR 1089	8.47	20.10%
LPwC SHG 1089	11.17	-5.36%

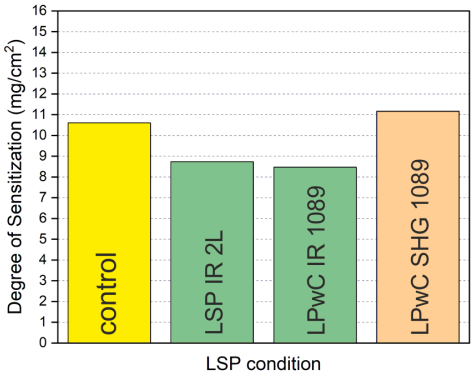

Figure 4.20: (a) Standard NAMLT results and (b) modified NAMLT results. Green fill implies improvement over the control sample as opposed to orange that implies higher DoS.

Based on the results presented in this section, the following conclusions can be made:

1. The DoS of AA5083 is strongly grain orientation dependent. The difference between weight loss contribution of grains in the rolling direction is six time higher than in the normal direction due to denser grain boundary network and more direct depth penetration.

2. The NAMLT test, as defined by the ASTM G67, is not a valid method to determine the effect of LSP and LPwC on the DoS of rolled AA5083 plates.

3. The modified NAMLT showed clear drop in DoS for LSP and LPwC samples treated with infrared laser and thin water layer and a slight increase in DoS for LPwC samples treated underwater.

4.4 Electrochemical analysis

Similar to the previous section (4.3), the specimens were divided into three heat related categories: as received, sensitized and solutionized. This was done to better understand the effect heat treatment has on the electrochemical properties before any LSP or LPwC treatments were applied. Square coupons of 40 mm x 40 mm x 6.35 mm sectioned from the AA5083 plate using EDM were used. Before testing, all samples were polished to 1200 grit with silicon carbide paper followed by 1 μm mirror polish using diamond suspensions. After DI water rinsing, the samples were ultrasonically cleaned for 30 s, followed by ethanol (C_2H_5OH) rinse and air drying. The LSP and LPwC treatments were applied to the sensitized samples only. In this case, samples were peened by the Bivoj laser system using laser parameters from Table 4.1. Based on the previous measurements, only one set of processing parameters was chosen per each peening condition. These were LSP IR 2L, LPwC IR 1089 and LPwC SHG 1089 as specified in Table 4.2. Once again for simplicity, the name of the samples in this section will be shortened to LSP IR, LPwC IR and LPwC SHG. A summary of all labels used in this section is shown in Table 4.3. Samples after the peening treatment with Bivoj laser are shown in Fig. 4.21.

Specimen label	Sensitization	Treatment	Protective coating	Wavelength	Water confinement
as received	no	x	x	x	x
sensitized	yes	x	x	x	x
solutionized	no	x	x	x	x
sens + LSP IR	yes	LSP	yes	1030 nm	1 mm water layer
sens + LPwC IR	yes	LPwC	no	1030 nm	1 mm water layer
sens + LPwC SHG	yes	LPwC	no	515 nm	water tank

Table 4.3: Sample categorization for electrochemical analysis.

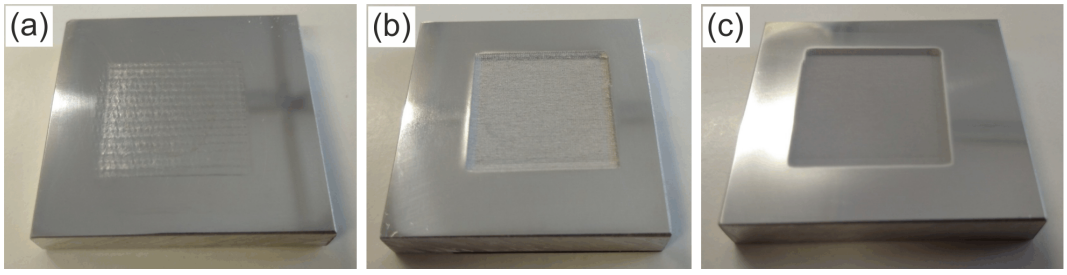

Figure 4.21: Sensitized square coupons of AA5083 after laser peening using Bivoj laser: (a) LSP IR, (b) LPwC IR and (c) LPwC SHG.

The electrochemical testing was carried out in 3.5 wt% NaCl naturally aerated water environment at a room temperature of 25 °C in a flat-cell with a platinum mesh counter electrode and a standard Ag/AgCl reference electrode (3.4). Prior to testing, specimens were covered with a Si mask with 15 mm circular opening in the middle to prevent crevice corrosion around the o-ring contact area. The total surface area exposed to the electrolyte was 1.77 cm^2. A fresh sample was used for each measurement with at least 3 measurements performed per sample condition. The plots presented are representative results of these replicated measurements.

4.4.1 Cyclic Polarization

The potential was scanned at 10 mV/min in the anodic direction and 20 mV/min in the cathodic direction with a sampling period of 0.33 seconds. The current density was capped at 1 mA/cm^2. The scan started at 0.5 V below steady E_{corr} after 30 minute stabilization period. Fig. 4.22 shows cyclic polarization (CP) curves of as received, sensitized and solutionized material with no peening treatment applied.

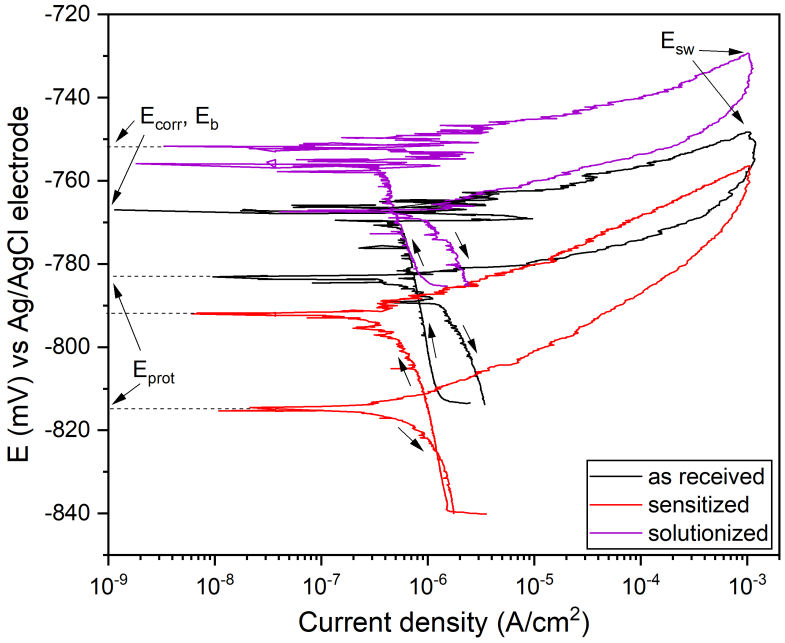

Figure 4.22: Cyclic polarization curves of as received, sensitized and solutionized AA5083 samples in 3.5 wt% NaCl solution.

The arrows point in the direction of the potential sweep. All three curves exhibit similar shape with a notable potential offset. The highest E_{corr} of -752 mV is displayed by the solutionized material, followed by -767 mV of the as received samples and -792 mV of the sensitized material. The anodic region in all three cases is characterized by sharp increase in current density with rising potential. The difference in E_{corr} is correlated with the amount of β-phase precipitation present on the sample surface and exposed to the electrolyte as evidenced by Fig. 4.12. Sensitized samples show the highest amount of continuous β-phase grain boundary while the solutionized samples show no β-phase on the surface. Birbilis et al. [31] showed that E_{corr} of the bulk β-phase (-950 mV$_{SCE}$) is lower than the polarization potential of the aluminium matrix. With the β-phase precipitation present, the result is a mixed potential between the two components which would explain the differences in E_{corr}. After the measurement, all three samples exhibited severe pitting attacks although no traces of IGC were observed (Fig. 4.23). All surfaces display localised pitting attack which is more widespread in the case of sensitized samples. The reverse potential sweep in Fig. 4.22 shows hysteresis which is caused by the pitting damage to the surface.

Fig. 4.24 shows CP measurements of sensitized samples under various treatment

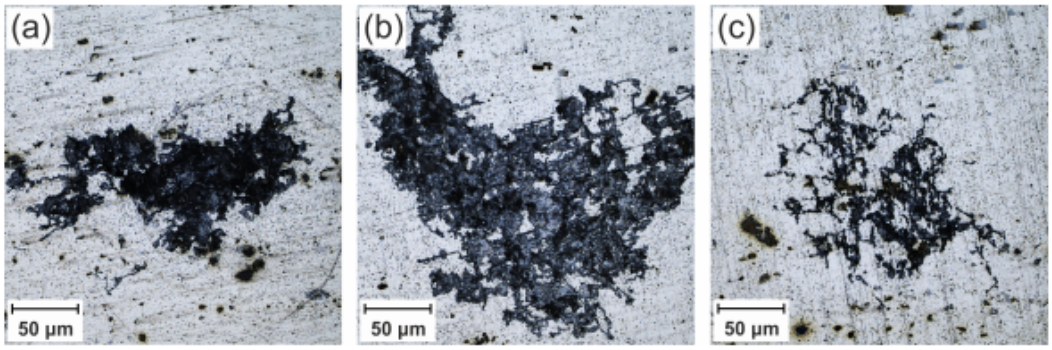

Figure 4.23: Optical microscope images of pitting attacks after CP measurement on the surface of (a) as received, (b) sensitized and (c) solutionized AA5083 samples.

conditions. E_{corr} dropped in all cases when compared to the non-treated sample with the highest drop of 47 mV for the LSP IR sample. Both LPwC treatments, however, display extended passivity region with reduced anodic current. In these cases, E_b is shifted further away from E_{corr}, exceeding E_b of the non-treated sensitized sample by more than 20 mV. In contrast, the anodic region stayed relatively flat for LSP IR although slight indication of passivity may also be observed. This suggests that the kinetics of the process is controlled by oxygen diffusion through the porous oxygen film which is more developed after the LPwC treatment. It is also worth noting the different behaviour of LPwC samples during the reversed potential sweep where E_{prot} is completely outside the potential range applied. The widespread pitting attack on the LSP IR surface (Fig. 4.25a) was similar to the non-treated sensitized sample (Fig. 4.23b). In contrast, the surfaces of both LPwC IR and LPwC SHG samples in Fig. 4.25b and Fig. 4.25c, respectively, show more localized pitting which penetrates the transformed recast layer.

The polarization resistance R_p of the investigated samples was determined using the LPR method. Small voltage variations (±5 mV) were applied around E_{corr} and the slope of current response was measured. The resultant R_p values are summarized in Table 4.4 along with other characteristic dissolution parameters. Smaller electrical current variations and rapid increase in R_p were observed for the LPwC samples. Most notably nearly 50 times higher R_p was measured for LPwC SHG sample when compared to the non-treated sensitized sample (202.5 kΩ versus 4.3 kΩ). An increase in R_p, although much smaller, was also measured with the LSP IR sample.

	E_{corr} (mV)	E_{prot} (mV)	E_b (mV)	E_{sw} (mV)	R_p (kΩ)
as received	-767	-783	-767	-748	1.7
sensitized	-792	-815	-792	-757	4.3
solutionized	-752	-767	-752	-729	2.5
sens + LSP IR	-814	-851	-814	-763	20.9
sens + LPwC IR	-805	N/A	-772	-715	70.1
sens + LPwC SHG	-803	N/A	-781	-680	202.5

Table 4.4: Characteristic dissolution parameters obtained from CP measurement in naturally aerated 3.5 wt% NaCl solution.

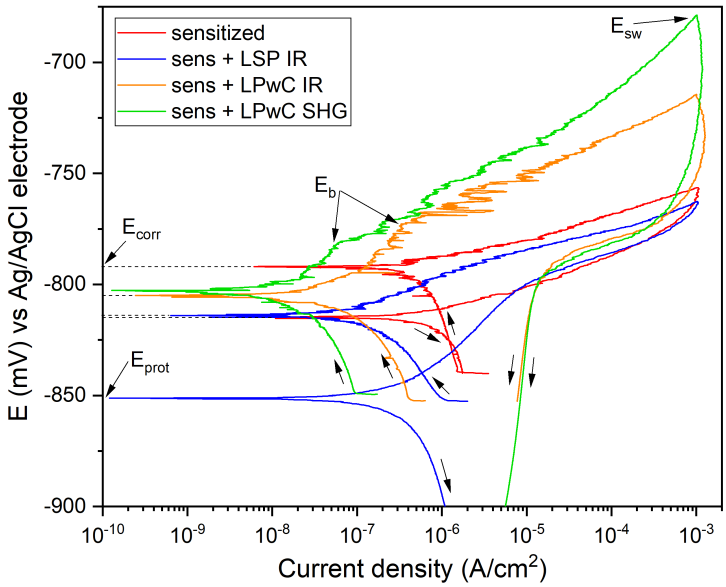

Figure 4.24: Cyclic polarization curves of laser peened samples of sensitized AA5083 in 3.5 wt% NaCl solution.

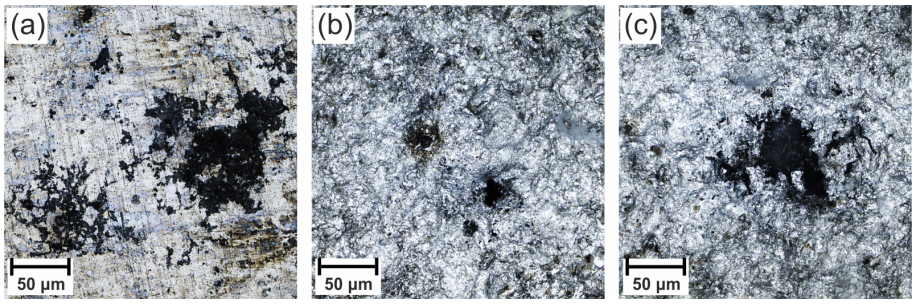

Figure 4.25: Optical microscope images of pitting attacks after CP measurement on the surface of: (a) LSP IR, (b) LPwC IR and (c) LPwC SHG samples.

4.4.2 Potentiostatic polarization

The core aspect of sensitized AA5083 revolves around the phenomenon of IGC which subsequently leads to IGSCC. However, to investigate the role laser peening plays in it we must first isolate IGC from other prevalent corrosion mechanisms such as pitting which proved to be dominant in the CP measurements. Seong et al. [81] achieved that by polarizing the sample in its cathodic region just below E_{corr}. They considered that the E_b of -950 mV_{SCE} of the bulk β-phase is lower than the E_{corr} of -780 mV_{SCE} of the sensitized material. Polarizing the sensitized material at -800 mV_{SCE} then led to clear manifestation of IGC without the pitting corrosion being present. In this case, the E_{corr} of sensitized AA5083 was established at -792 mV vs Ag/AgCl reference electrode. The samples were therefore polarized at -800 mV vs Ag/AgCl. The current density measured over time for the untreated conditions is shown in Fig. 4.26. From now on, the potential

will always refer to the Ag/AgCl reference electrode unless specified otherwise.

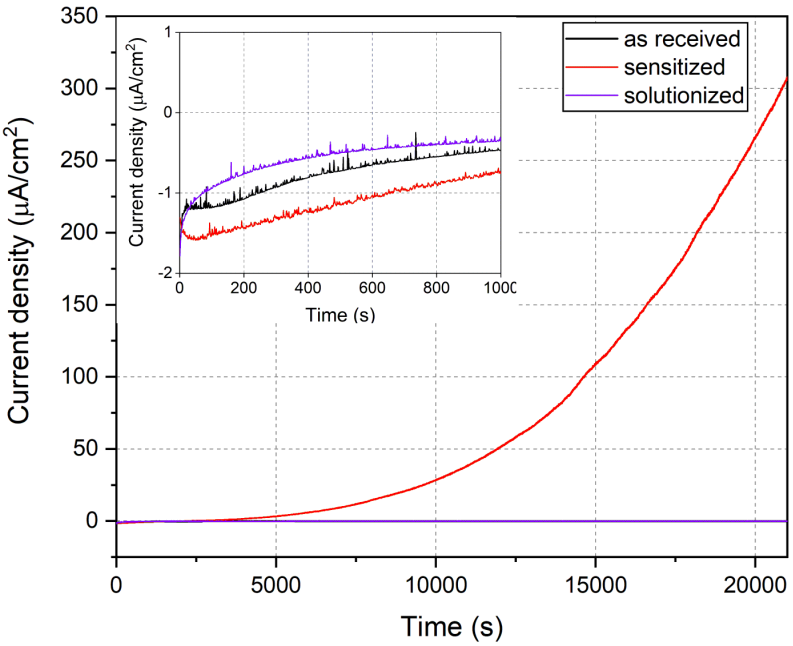

Figure 4.26: Current density during potentiostatic polarization at -800 mV of non-treated AA5083 in 3.5 wt% NaCl solution.

In all cases, the current density starts in negative values as expected due to the cathodic polarization. After some time, the current density of the sensitized sample starts rising exponentially, reaching a value of 330 μA/cm^2 over a period of 6 hours. In contrast, the current density of both the as received and solutionized samples stays close to zero and does not change over time. The surface condition after the measurement is shown in Fig. 4.27. The as received (Fig. 4.27a) and solutionized (Fig. 4.27b) conditions show no signs of IGC or pitting corrosion after 6 h of immersion in the 3.5 wt% NaCl solution. In contrast, the sensitized sample in Fig. 4.27c exhibits a large interconnected network of IGC all over the exposed surface area. No traces of pitting corrosion are observed this time as the polarization pushes the reaction below E_b.

Potentiostatic measurements at -800 mV of sensitized samples subjected to LSP and LPwC are presented in Fig. 4.28. Both LPwC treatments show significant drop in current density. For LPwC IR, the current density after 6 h is 80 μA/cm^2 which is more than four times lower than in case of the non-treated sensitized sample. For LPwC SHG, the current density after 6 h is 5 μA/cm^2, which is nearly the same as for the as received sample. We can however assume that the current density will keep on rising albeit at an extremely slow rate when compared to the non-treated sensitized condition. LSP IR sample with protective coating showed only a slight improvement with final current density of 267 μA/cm^2 although for more than 3 h the curve copied that of the control sample which indicates that no significant change took place. Optical microscope images of the surface of treated samples after the potentiostatic measurement are shown in Fig. 4.29. The surface of LSP IR shows developing IGC network with most severely corroded area in the middle indicated by the blue spot. The LPwC samples on the other hand

show no observable intergranular features. Instead, the corrosion manifests in the form of localized surface perturbations.

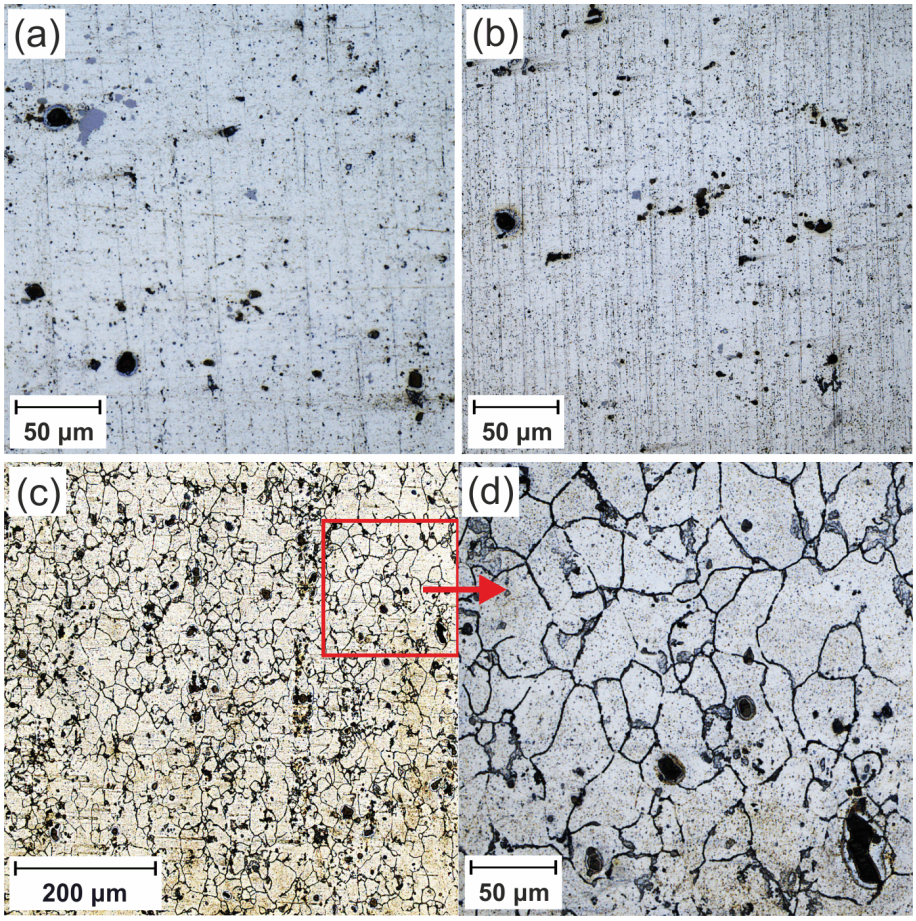

Figure 4.27: Optical microscope images of AA5083 after potentiostatic polarization at -800 mV for 6 h: (a) as received sample, (b) solutionized sample and (c) IGC network and its close up developed on sensitized sample.

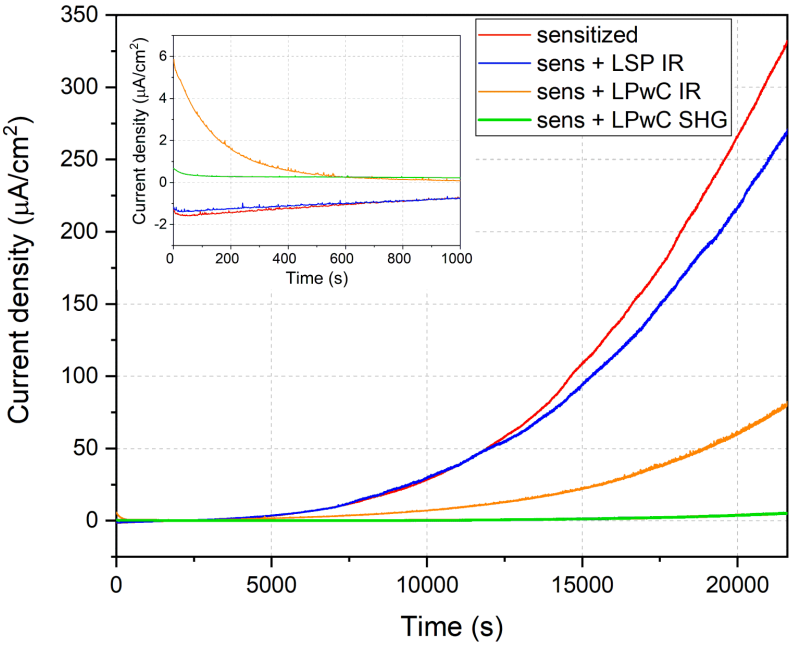

Figure 4.28: Current density during potentiostatic polarization at -800 mV of laser peened sensitized AA5083 in naturally aerated 3.5 wt% NaCl solution.

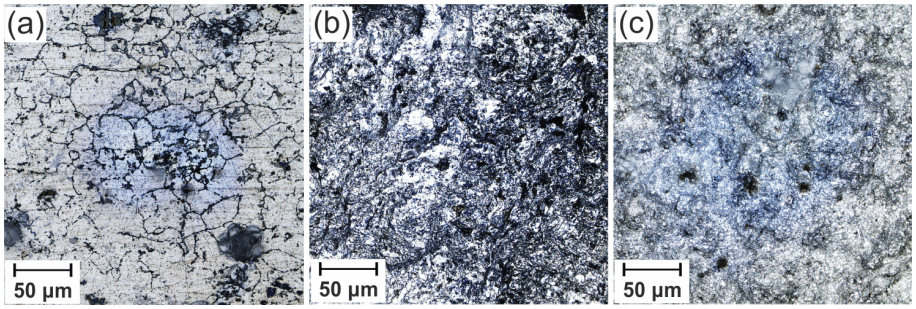

Figure 4.29: Optical microscope images of laser peened sensitized AA5083 after potentiostatic polarization at -800 mV for 6 h: (a) LSP IR, (b) LPwC IR and (c) LPwC SHG.

4.4.3 Electrochemical Impedance measurements

The results of Electrochemical Impedance Spectroscopy (EIS) are presented in the form of Bode and Nyquist plots. Based on the potentiostatic measurements (4.4.2), samples were polarized at -800 mV vs Ag/AgCl which showed to be successful in isolating IGC from pitting corrosion. The testing was carried out in 3.5 wt% NaCl solution with 5 mV RMS voltage oscillation and frequency range from 100 kHz down to 100 mHz. For clarity, the data is divided into a separate category of different heat conditions applied to the non-treated plate and a second category of sensitized treated samples. The Bode and Nyquist plots of the non-treated samples are shown in Fig. 4.30 and Fig. 4.32, respectively. Similarly, the Bode and Nyquist plots of the sensitized treated samples are shown in Fig. 4.31 and Fig. 4.33, respectively. Two time constants can be distinguished; one in the high frequency range (~20-100 Hz) and one in the low frequency range (0.1-0.3 Hz). In the high frequency range, the plots indicates higher |Z| for treated samples with protective coating (Fig. 4.31) as well as non-treated samples (Fig. 4.30). However, as we approach lower frequencies (<5 Hz), the trend is reversed and higher |Z| is achieved with both LPwC conditions, LPwC SHG in particular. In contrast, specimens processed by LSP IR fall more than an order of magnitude behind. The phase angle shift data shows significant phase angle peak broadening for both LPwC conditions while the regular LSP IR peak narrows in comparison with the non-treated conditions. The peak broadening is indicative of a stable protection barrier spread across wider frequency range [219]. The Nyquist plots presented in Fig. 4.32 and Fig. 4.33 are in the form of semicircles with centres depressed below the x-axis. Treated samples in Fig. 4.33 show that the LPwC specimens display higher resistance, represented by wider arc, when compared to the non-treated specimens. The LSP IR condition with protective coating shows the smallest arc, indicating lower resistance when compared to the rest of the tested conditions.

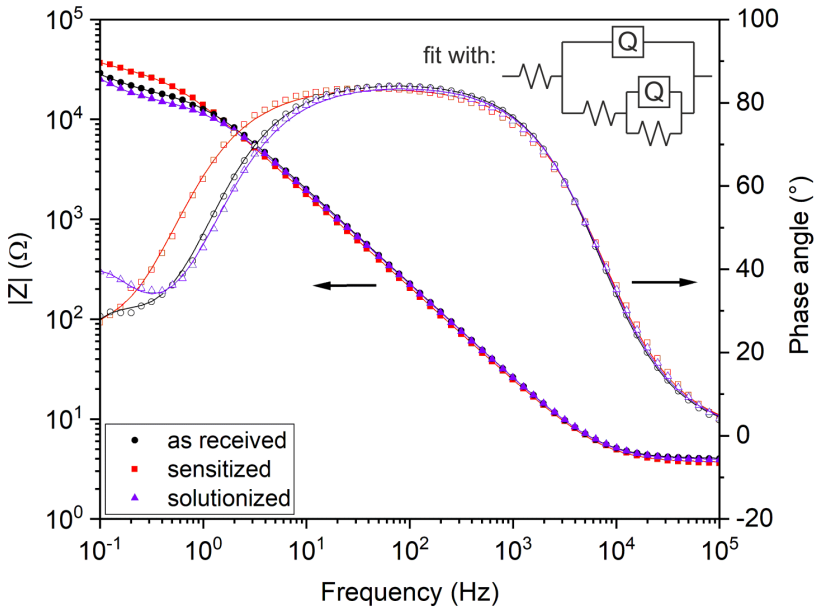

Figure 4.30: Bode plot of as received, sensitized and solutionized samples recorded in 3.5 wt% NaCl solution. The data is fitted using the displayed equivalent electrical circuit.

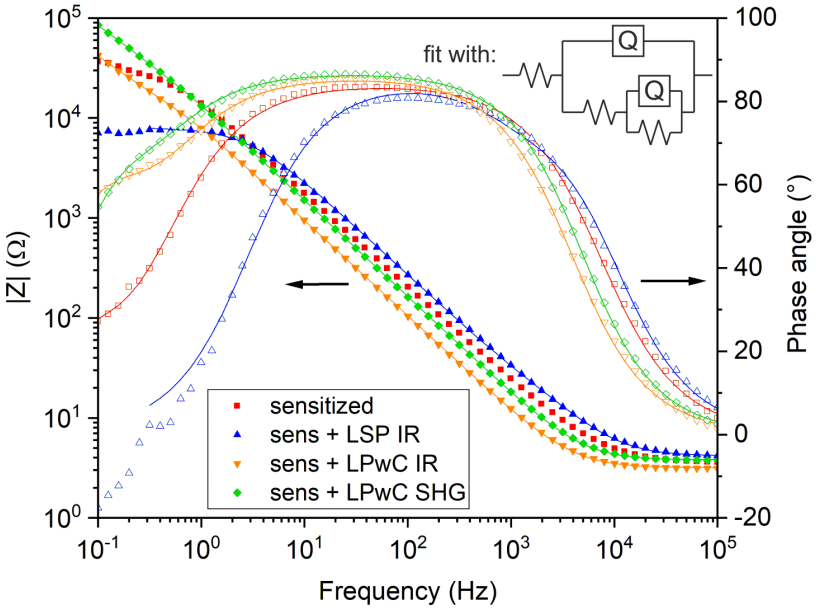

Figure 4.31: Bode plot of laser peened sensitized samples recorded in 3.5 wt% NaCl solution. The data is fitted using the displayed equivalent electrical circuit.

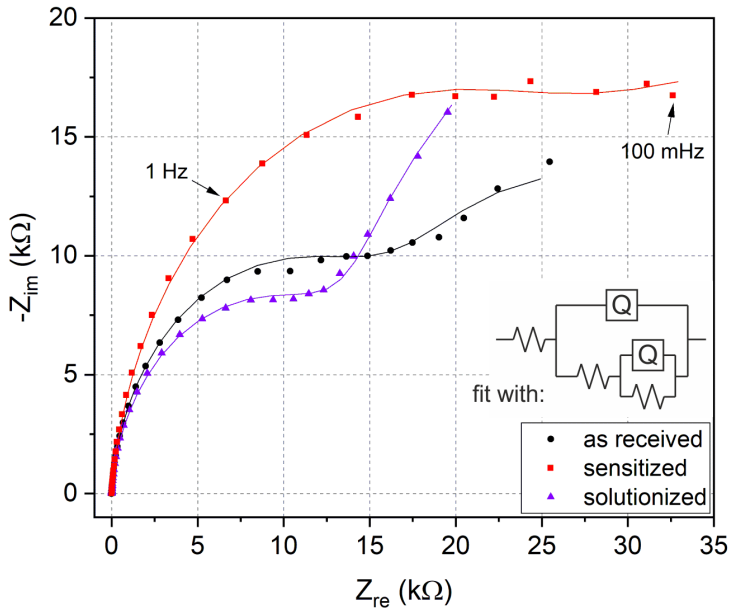

Figure 4.32: Nyquist plots of as received, sensitized and solutionized samples recorded in 3.5 wt% NaCl solution. The data is fitted using the displayed equivalent electrical circuit.

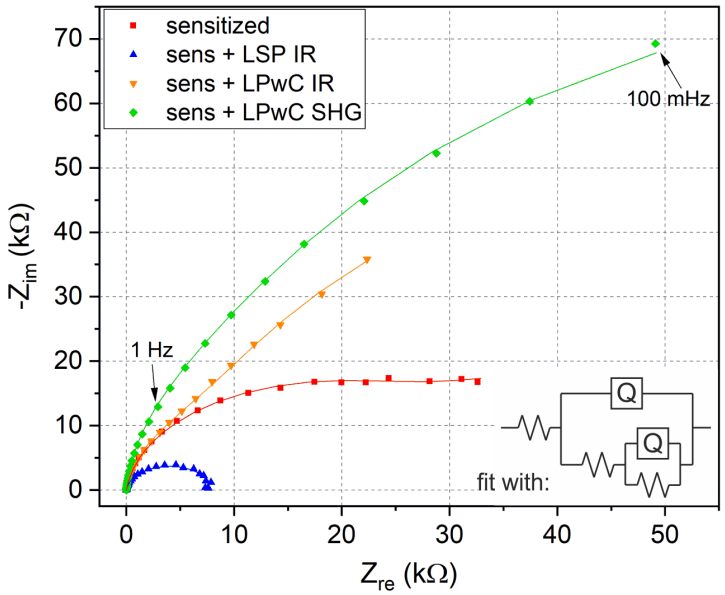

Figure 4.33: Nyquist plots of laser peened sensitized samples treated wih LSP recorded in 3.5 wt% NaCl solution. The data is fitted using the displayed equivalent electrical circuit.

An impedance plot obtained for a given electrochemical system can be modelled by one or more equivalent electrical circuits [220] where the appropriate model gives a reasonable fit with the least amount of circuit components. In this case, an equivalent electrical circuit model $R_s(Q_c(R_{po}(Q_{dl}R_{ct})))$ was used based on the work of several authors [158, 221, 222] who proved it to be adequate for modelling of aluminium corrosion. The model comprises two time constants as previously indicated by the potentiodynamic measurements and by the Bode and Nyquist plots. The high-frequency time constant is related to the reactions at the outer interface ($R_{po}Q_c$), i.e. the porous oxide film and electrolyte where R_{po} represents the film pore resistance and Q_c the film capacitance or constant phase element (CPE). CPE is used to signify the possibility of a non-ideal capacitance with a varying n. The factor n is within the range of $0 \leq n \leq 1$. When $n = 1$, Q describes an ideal capacitor. The value of n is related to the electrode roughness and heterogeneities [223]. The second time constant at low frequencies ($R_{ct}Q_{dl}$) is attributed to the charge-transfer reaction at the metal surface (inner barrier), in the base of the oxide film pores where R_{ct} and Q_{dl} represent the charge transfer resistance and double layer capacitance, respectively. The electrolyte resistance is denoted by R_s. A good fit of the experimental data was achieved and the results are shown in Table 4.5.

According to the data, the combined resistance $R_s + R_{po} + R_{ct}$ of the LPwC SHG treatment increased more than 3 times (178 ± 16 kΩ) when compared to non-treated sensitized sample (58 ± 24 kΩ). This suggests that the underwater treatment increased both the quality of the oxide film (R_{po}) as well as the passivity of the transformed layer below (R_{ct}). Lower R_{ct} of the non-treated and LSP IR specimens generally indicates an increase in the metal area in contact with the electrolyte, denoting the penetration of water molecules, oxygen anions through the porous film, and the corrosion activity on the metal surface [224]. The large difference between LPwC IR (33 ± 5 kΩ) and LPwC

Sample	R_s (Ω cm^2)	R_{po} (kΩ cm^2)	R_{ct} (kΩ cm^2)	Q_c (μF cm^{-2})	n-Q_c	Q_{dl} (μF cm^{-2})	n-Q_{dl}
as received	4	21 ± 1	20 ± 5	5.4 ± 0.1	0.95	53.4 ± 4.1	1.00
sensitized	3.7	36 ± 2	21 ± 24	6.6 ± 0.2	0.94	75.1 ± 21.9	1.00
solutionized	3.9	18 ± 1	40 ± 12	5.6 ± 0.1	0.95	48.9 ± 2.3	1.00
sens + LSP IR	4.2	0.1 ± 0.1	7.9 ± 0.2	3.7 ± 1.5	0.95	0.9 ± 1.5	0.94
sens + LPwC IR	3.2	33 ± 5	87 ± 38	11.4 ± 0.3	0.96	14.7 ± 1.7	0.95
sens + LPwC SH	3.8	80 ± 8	98 ± 14	6.8 ± 0.1	0.97	7.0 ± 1.2	0.96

Table 4.5: Electrochemical parameters obtained from EIS spectra.

SHG (87 ± 38 kΩ) in R_{po} is attributed to the surface oxide film quality which tends to be more uniform in case of underwater treatment. These results are in good agreement with the potentiodynamic measurements from Fig. 4.24. On the other hand, LSP IR underperformed heavily when compared with the non-treated sensitized condition, with the combined resistance of only 8.0 ± 0.2 kΩ. This result suggests that the treatment with protective coating in this case does have a negative effect on the oxide film. The discrepancy between this result and the higher R_p value compared to SE sample (Table 4.4) can be attributed to the anodic dissolution of LSP IR polarized at -800 mV during EIS.

The highest Q_c was achieved with LPwC IR which suggests increased surface porosity and heterogeneity. In contrast, lower Q_c of LSP IR compared to the non-treated sensitized sample points to more homogeneous surface layer after laser treatment with protective coating. In addition, Q_{dl} of the treated samples was significantly lower when compared to the non-treated samples. The decrease in Q_{dl} of the metal surface/solution interface after laser treatment is probably an outcome of lower ion adsorption due to more difficult penetration of water molecules, oxygen, and Cl^- ions [158, 225]. The values of $n-Q_c$ and $n-Q_{dl}$ are in the range of 0.94–1.00; hence Q_c and Q_{dl} can be considered approximately as a pure capacitors.

4.4.4 XPS analysis

Spectra of Al 2p were measured and fitted with Gaussian functions to distinguish between states corresponding to different bonding energies. The ratio of areas inside the recorded peaks then represents the ratio of corresponding components present in the material. The two main components revealed were Al-oxide Al_2O_3 at 75.7 eV and Al-metallic at 72.5 eV. In order to reach larger depth, the samples were subjected to 20 min of ion sputtering with an estimated sputtering depth of about 10 nm [226]. The number of Ar atoms in a cluster was 1000 and the energy of a cluster was 5 keV. The size of sputtered area was 2 mm x 2 mm. One of the measured spectra, specifically LPwC SHG at 10 nm, is shown in Fig. 4.34a. Other spectra are similar, with varying ratios of the Gaussian areas. The ratios of calculated areas of Al_2O_3 oxide to metallic Al in Al 2p spectra are plotted in Fig. 4.34b. Each sample condition is represented by 2 columns, one at 0 nm and the other at 10 nm depth. Both non-treated conditions show a similar ratio of the oxide and metallic Al on the surface. At the estimated depth of 10 nm, the amount of Al_2O_3 decreases with depth due to less oxygen molecules being present further away from the surface. This drop is more pronounced with the as received sample at 85% to 78% as opposed to the 83% to 81% of the sensitized sample. In the case of treated samples, the largest difference can be observed with the LPwC samples. The amount of Al-metallic was halved when compared to the non-treated conditions while the amount

of Al_2O_3 increased correspondingly. LSP IR showed no increase in Al-oxide but rather the lowest amount of all the conditions tested with 82% on the surface and 76% at 10 nm.

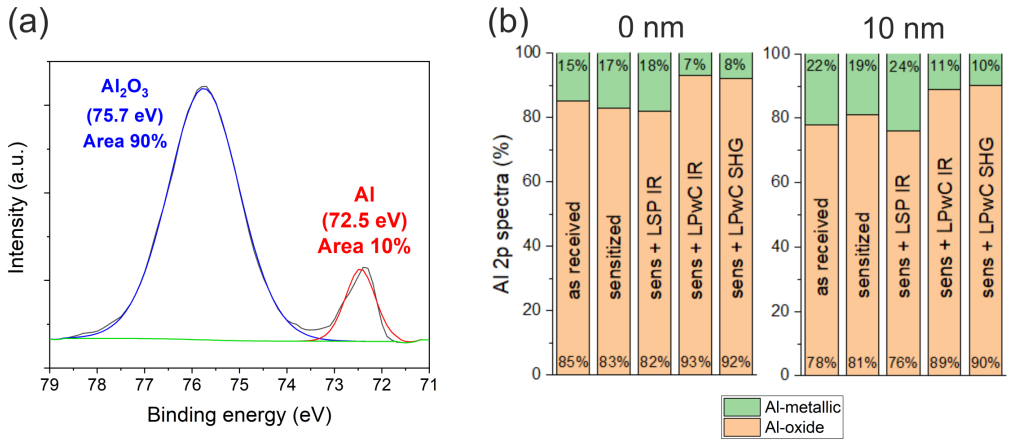

Figure 4.34: XPS analysis of bonding energies: (a) Al 2p spectrum of LPwC SHG at a 10 nm depth and (b) the ratio of Al-metallic and Al-oxide of non-treated and treated specimens at 0 nm and 10 nm depth.

4.4.5 Microstructure analysis

Near-surface cross-section SEM images of the treated specimens are shown in Fig. 4.35. The smooth LSP IR surface in Fig. 4.35a contrasts with the LPwC SHG surface in Fig. 4.35b where a recast layer approximately 2-3 μm thick with a modified oxide layer on top can be observed. The etched cross-section of the LSP IR sample (Fig. 4.35c) further reveals β-phase sensitized grain boundaries in very close proximity to the surface. In case of the etched LPwC SHG sample (Fig. 4.35d), however, the sensitized boundaries are shielded from the surface by the recast layer that was generated during the laser pulse interaction when no protective coating was applied.

Fig. 4.36 provides a closer look at the near-surface cross-section of the sensitized material without treatment. The TEM image in Fig 4.36a shows that the polishing process creates fine flat grains up to a depth of about 100 nm. These grains are divided into several subgrains containing high dislocation density. Underneath, larger grains are also heavily deformed as a result of the manufacturing process. Fig. 4.36b and 4.36c then show the Mg precipitates distribution both in coarse isolated particles as well as dense coverage on the grain boundary. The subgrains are subjected to large stress with high dislocation density homogeneously distributed in the volume with Fe and Mn precipitates present.

When the plate was treated with the protective coating applied (LSP IR), most of the grains near the surface were refined to a grain size of 100-200 nm (Fig. 4.37a). The newly formed subgrains contain high dislocation density (Fig. 4.37c) and the affected zone reaches up to 300 nm below the surface. There is no grain boundary β-phase in this region (Fig. 4.37b), however, below this region the structure is the same as in the initial sensitized state. This means that the shock wave induced plastic deformation can dynamically change the microstructure only to a limited depth. The presence of Mg enrichment at the boundary of this refined layer is interesting, as well as the morphological transition of the β-phase to what appears to be a smooth film, as opposed to the less uni-

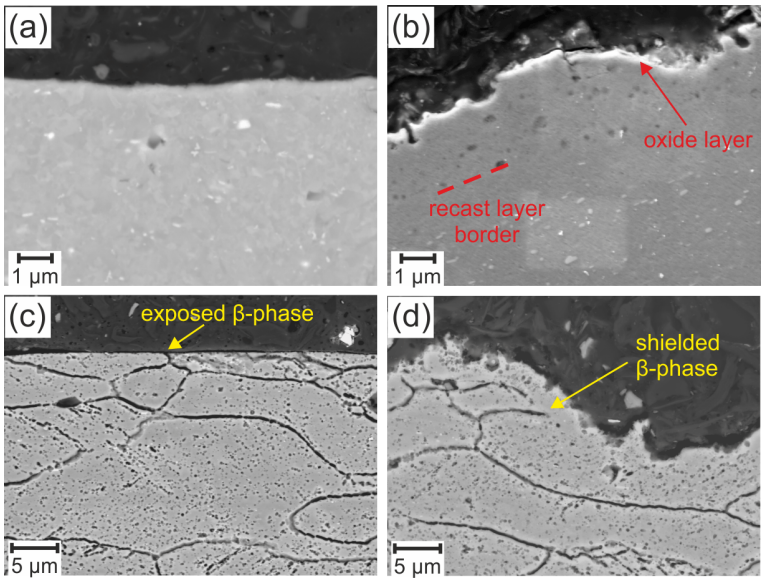

Figure 4.35: SEM cross-section images of treated sensitized AA5083: (a) LSP IR, (b) LPwC SHG with recast layer and modified oxide layer visible, (c) LSP IR with β-phase visualized, (d) LPwC SHG with β-phase visualized and shielded from the surface.

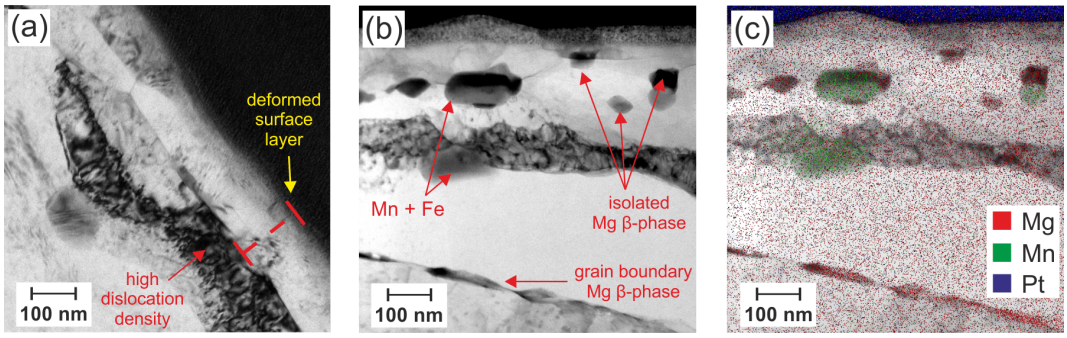

Figure 4.36: Cross-section images of near-surface area of sensitized AA5083 with no treatment applied: (a) TEM of the surface layer deformed by polishing, (b) STEM image of particles near the surface and (c) distribution map of selected elements.

form thickness observed in Fig. 4.36b that is typical of a densely populated but largely discrete β-phase coverage viewed in transmission. The limited area of the TEM sample, however, makes it hard to discern how prevalent this phenomenon is.

The microstructure observed in the surface region of the LPwC SHG sample (Fig. 4.38) is very different from that of both non-treated and LSP IR samples. First, a nearly 2-3 μm wide recast surface layer is present (Fig. 4.38a) which is quite different from that of the base material beneath this region indicated below the white dashed line in the TEM image. The β-phase precipitates that appear dark in the BF image and brighter in STEM EDS Mg map in Fig. 4.38b have been taken back into solution in the melted and recast layer that appears in a uniform grey contrast; the STEM EDS map in Fig. 4.38b reveals the β-phase distinctively, but also that the Mg is evenly distributed in the recast layer. The second remarkable feature is the presence of numerous nanoparticles of varying size embedded within this layer. Very recent work on LPwC of Al7075-T6 alloy

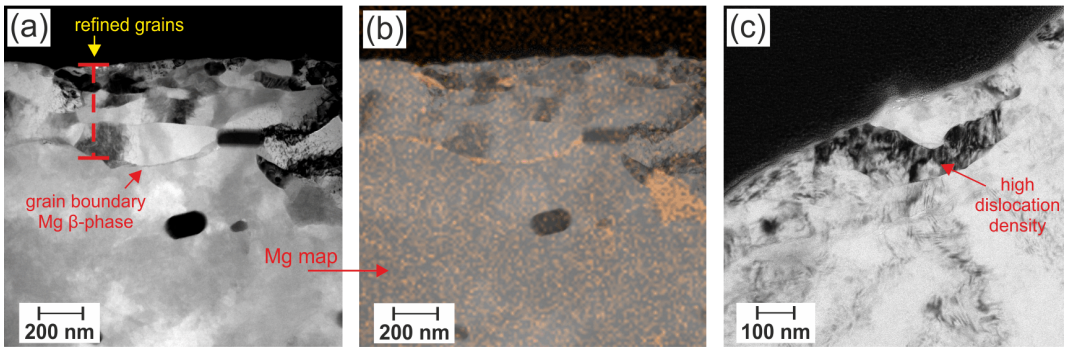

Figure 4.37: Cross-section images of near-surface area of sensitized AA5083 after LSP IR treatment: (a) STEM of LSP induced subgrains, (b) Mg distribution in the surface region and (c) TEM showing detail of the subgrains with high dislocation density.

has determined that these are oxygen-rich aluminium nanoparticles [227], and possible mechanisms for their formation have been discussed. The recast layer and the layer below are also marked by a heavily deformed structure with high dislocation density and subgrain boundaries (Figs. 4.38a and 4.38c). This microstructure reaching into the depth is the result of shock-assisted deformation. Overlapping laser spots result in heterogeneous thermal and mechanical conditions, which consequently lead to further increase in dislocation density and less defined subgrains. These subgrains are kept under stress caused by rapid solidification and by compressive residual stresses. Since the LPwC SHG sample was processed in water environment without protective coating, the aluminium nanoparticles in Fig. 4.38a are enriched in oxygen. The melting/solidification and thermomechanical deformation mechanism during LPwC led to dissolution of β-phase precipitates at original grain boundaries and more uniform distribution of Mg in solution in the recast surface layer (Fig. 4.38b), as well as their break-up into coarser precipitates in the matrix regions below (Fig. 4.38c).

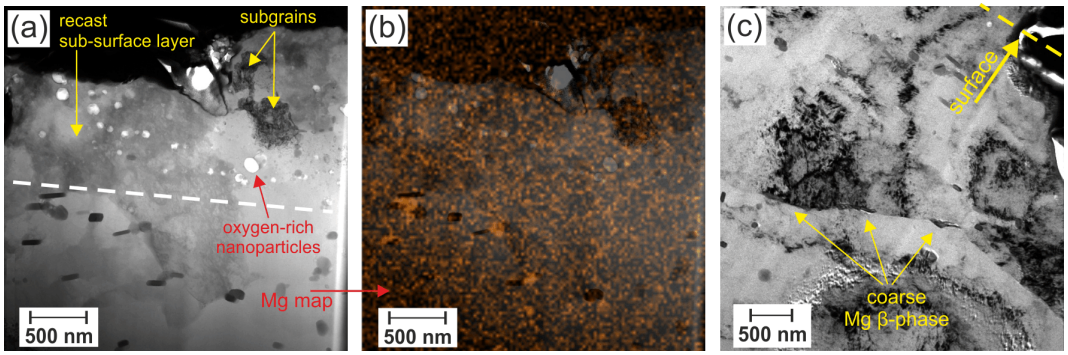

Figure 4.38: Cross-section images of near-surface area of sensitized AA5083 after LPwC SHG treatment: (a) TEM showing the uniform solid solution recast layer with embedded oxygen-rich Al nanoparticles, (b) Mg map of the recast layer and (c) STEM of coarse β-phase precipitates under the recast layer.

4.5 Slow strain rate test

Specimens for SSRT were EDM sectioned from 25.4 mm thick rolled plate of AA5083 sensitized at 100 °C for a period of 60 days. A 'dog-bone' sample geometry was chosen based on the work of Ogoucha et al. [49] with up-scaled dimensions for this work (Fig. 4.39a). Based on the unequal contribution of various specimen faces to the DoS (4.3.1), the specimens were sectioned in such a way that the ND-TD plane with highest IGC susceptibility coincided with the dominant plane on the SSRT specimen which would be later laser treated (Fig. 4.39b). The grains were elongated along the long axis of the sample as the plate geometry did not allow for perpendicular grain orientation. Prior to peening, the gauge (narrowed central part) of the specimens was polished to 600 grit from both sides.

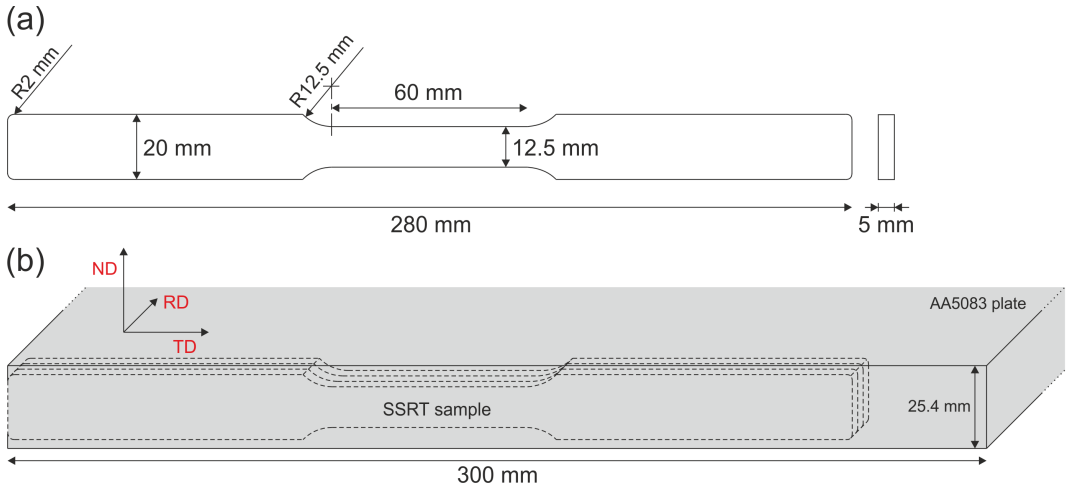

Figure 4.39: Dog-bone shaped specimens for SSRT: (a) specimen dimensions and (b) sectioning of specimens from AA5083 plate.

A customized plastic sample holder was 3D printed to allow laser access to both sample sides without manual repositioning of the sample. Moreover, side insertions made of AISI304 steel were used to facilitate the peening near the specimen edges (Fig. 4.40a). The insertions had the same thickness and copied the shape of the specimen. Smooth plane transition lessens the likelihood that the laser impact tears the tape at the edge and burns the underlying surface in the LSP process. Similarly the insertions help to shield the side planes of the LPwC samples so that the peening takes place on the designated front and back surfaces only. The specimens were treated with Bivoj laser using processing parameters that were determined to give the highest residual stresses (4.1.2). The parameters are summarized in Table 4.6. A specimen during the peening process is shown in Fig. 4.40b.

A special patterning strategy was employed to prevent the sample from excessive bending. In general, aluminium alloys are relatively soft and tend to easily bend away from the peened area when relatively small and thin samples are used. There are several ways to deal with this. First, one can use thicker samples so that more bulk material prevents the bending. This was not possible here due to technical limitations of the SSRT machine. Second, double side peening, i.e. simultaneous peening from both specimen sides, can be used. Such option was also not available for this work. Lastly, the specimen can be peened from both sides consecutively in several smaller connected patches. This strategy was utilized here. Every time a line was peened on one side of the specimen, the

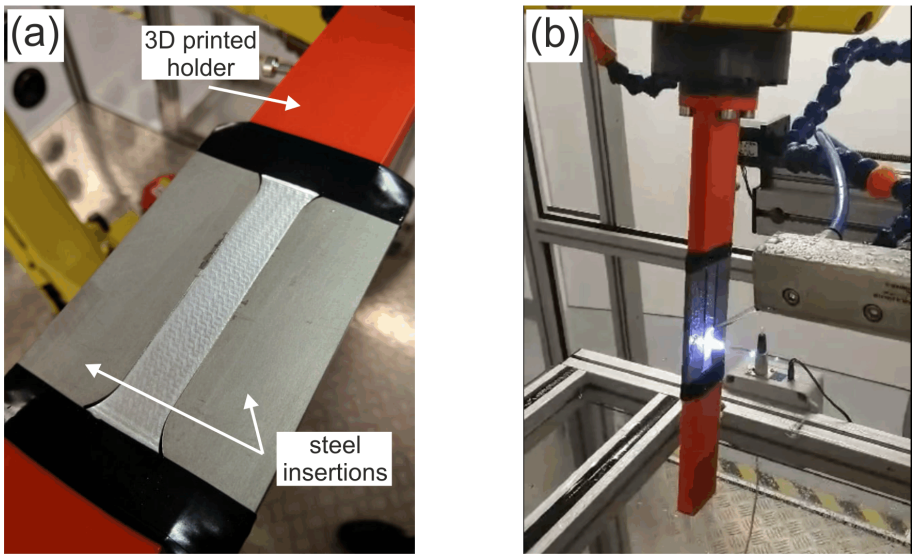

Figure 4.40: (a) SSRT LSP IR specimen with tape removed placed in a holder and surrounded by steel insertions to smoothen edge transitions and (b) SSRT LPwC IR specimen being peened by Bivoj laser.

Sample	Laser energy (J)	Spot size (mm)	Power density (GW/cm^2)	Pulse coverage	Wavelength (nm)	Confinement	Protective coating
LSP IR	3	2.5	3.4	2 layers	1030	1 mm water	tape
LPwC IR	1	1.5	3.2	1089 p/cm^2	1030	1 mm water	none
LPwC SHG	1	1.5	3.2	1089 p/cm^2	515	water tank	none

Table 4.6: Selected laser treatment parameters for SSRT using Bivoj laser system.

specimen would rotate 180° around its long axis and the same line would be peened on the other side to counteract the bending of the opposite line. Eventually, line after line, the whole sample would be peened from both sides without any bending occurring. The strategy is shown step by step in Fig. 4.41. The total size of the laser patch was 75 mm x 20 mm, i.e. the whole gauge of the sample was peened from each side. Samples after peening, before being subjected to the tensile testing, are shown in Fig. 4.42. In total, 3 samples were processed for each peening condition with a representative sample being shown in the stress/strain plots.

The tensile tests were performed with a uniaxial strain rate of 10^{-6} which was determined to be within the ideal range of SCC testing for AA5083 (3.8). It is also within the parameters set forth in ASTM G 129-00, Standard Practice for Slow Strain Rate Testing to Evaluate the Susceptibility of Metallic Materials to Environmentally Assisted Cracking [228]. All stresses and strains were computed as engineering stresses and strains using the original and final dimensions of the specimen. The samples were placed into a specially designed cell (Fig. 4.43) which contained circulating 3.5% NaCl solution. The circulatory system kept the temperature constant at 40 °C throughout the whole test. Prior to the test, the upper and lower wide parts of the specimen were coated with silicon to ensure that only the gauge was in contact with the electrolyte.

First, sensitized samples without any additional treatment were tested both in air and

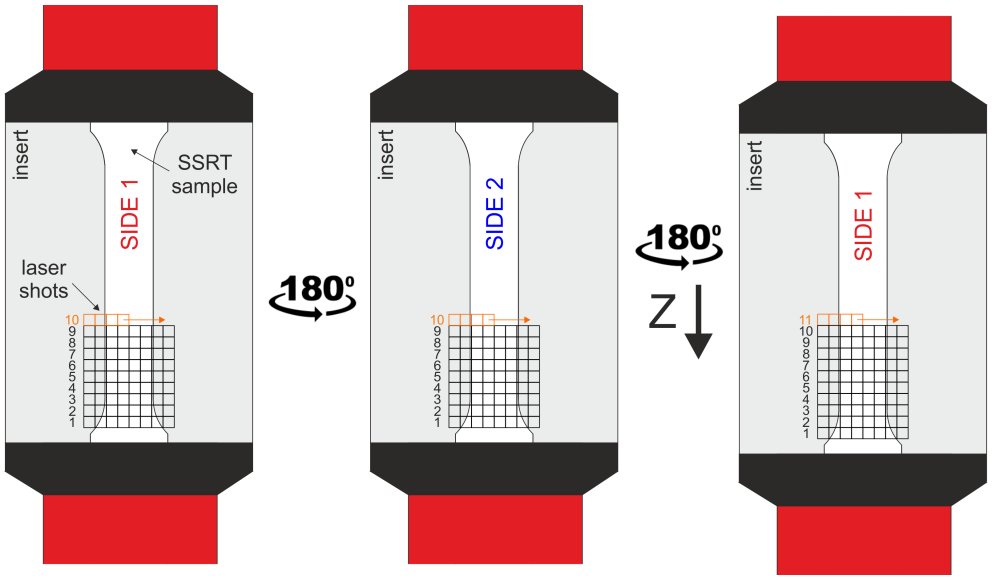

Figure 4.41: Peening strategy for the SSRT samples. Sample would rotate after every laser pattern line to counteract bending of the sample.

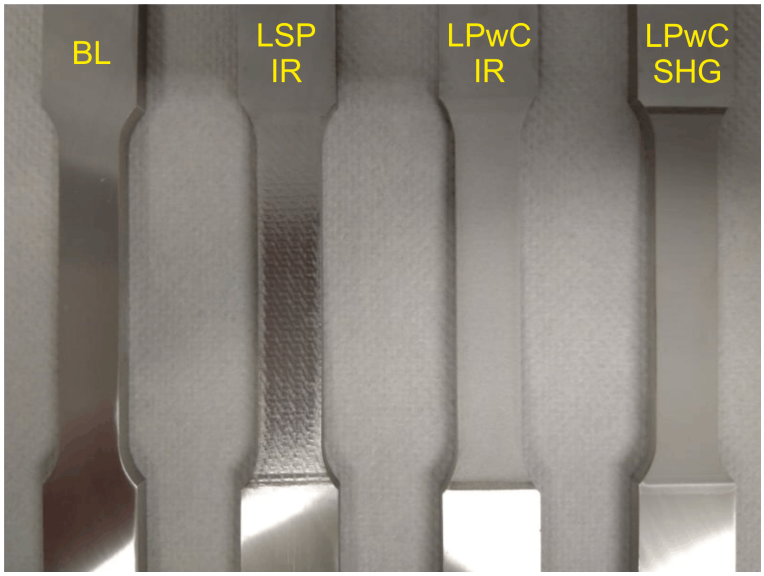

Figure 4.42: SSRT samples after laser peening including a baseline (BL) sample as a reference.

the NaCl solution to determine what effect the environment has on the tensile properties of the samples. The stress/strain curves are shown in Fig. 4.44. The sensitized sample in solution shows drastic decrease both in maximum stress and strain to failure. The literature shows that similar discrepancy can also be observed between non-sensitized and sensitized samples tested in NaCl solution [9]. In contrast, measurements of non-sensitized and sensitized samples in air [229] does not show any significant difference with only a slightly higher strain to failure for the sensitized sample. This is most likely due to increased ductility of the aluminium once the magnesium transitioned from solid solution in the material matrix to the grain boundaries. We can therefore conclude that

the decrease in maximum stress and strain to failure is a direct result of the environmental influence of the NaCl solution on the sensitized material.

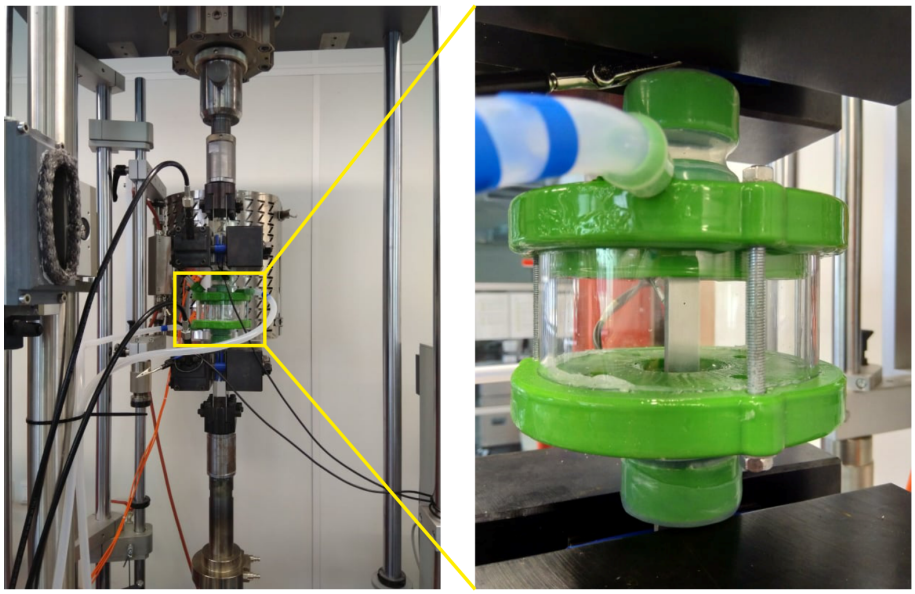

Figure 4.43: Specimens mounted in SSRT machine and surrounded by plastic chamber with circulating NaCl solution at constant temperature.

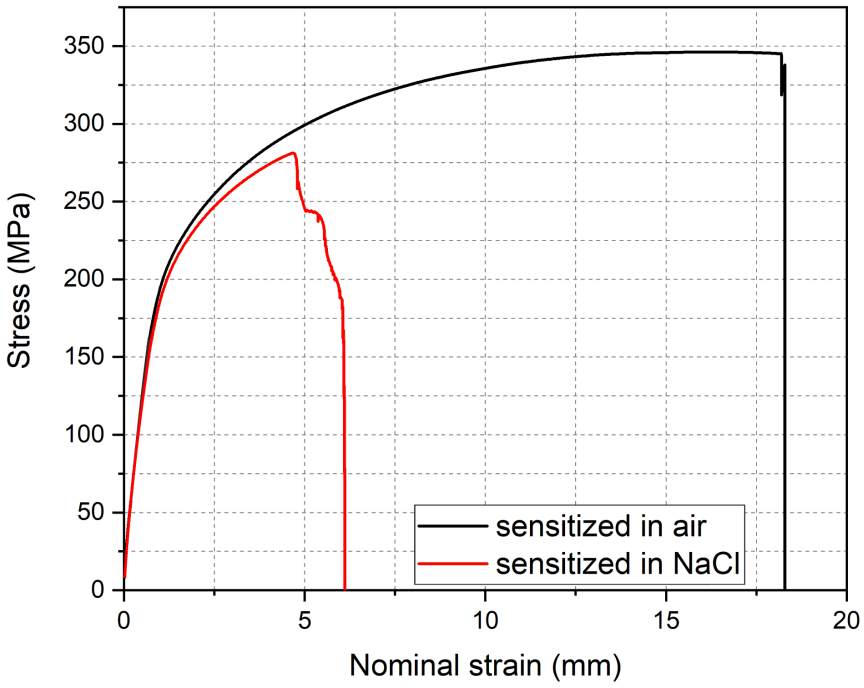

Figure 4.44: Stress/strain curves of sensitized samples in air and 3.5% NaCl solution.

The results of SSRT of sensitized specimens after LSP and LPwC treatments are shown in Fig. 4.45. It is immediately clear the material was cold worked by the laser treatment, resulting in its strengthening and raising of maximum stress before breaking. At the same time, the strain hardening lowered the ductility as the nominal strain at break decreased significantly in all laser treated cases. The results are summarized in Table 4.7. The maximum stress at failure was achieved with the LSP IR condition with ~8% increase when compared to the baseline although the strain at break dropped by 45%. LPwC SHG had a similar increase in maximum stress of 6% but the strain at break decreased by 18% only. The LPwC IR samples performed the worst both in maximum stress and strain at break.

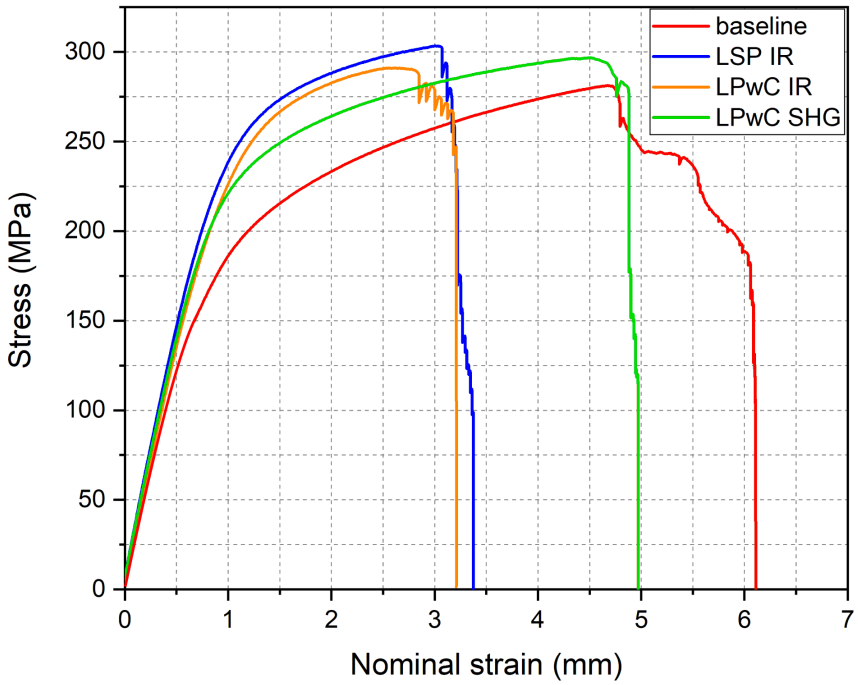

Figure 4.45: Stress/strain curves of sensitized samples in 3.5% NaCl solution after LSP and LPwC treatments.

Sample	Test medium	Time to failure (h)	Nominal strain at break (mm)	Max stress σ_{max} (MPa)
sensitized air	air	94	18.3	346
sensitized NaCl	3.5% Nacl	34	6.1	281
sens + LSP IR	3.5% Nacl	16	3.4	303
sens + LPwC IR	3.5% Nacl	20	3.2	291
sens + LPwC SHG	3.5% Nacl	25	5	297

Table 4.7: SSRT result summary.

4.5.1 Fracture analysis

The fracture analysis consists of fracture plane stereomicroscopy and SEM followed by metallography analysis. All the images are displayed in Fig. 4.46 to allow for direct comparisons between different sample conditions.

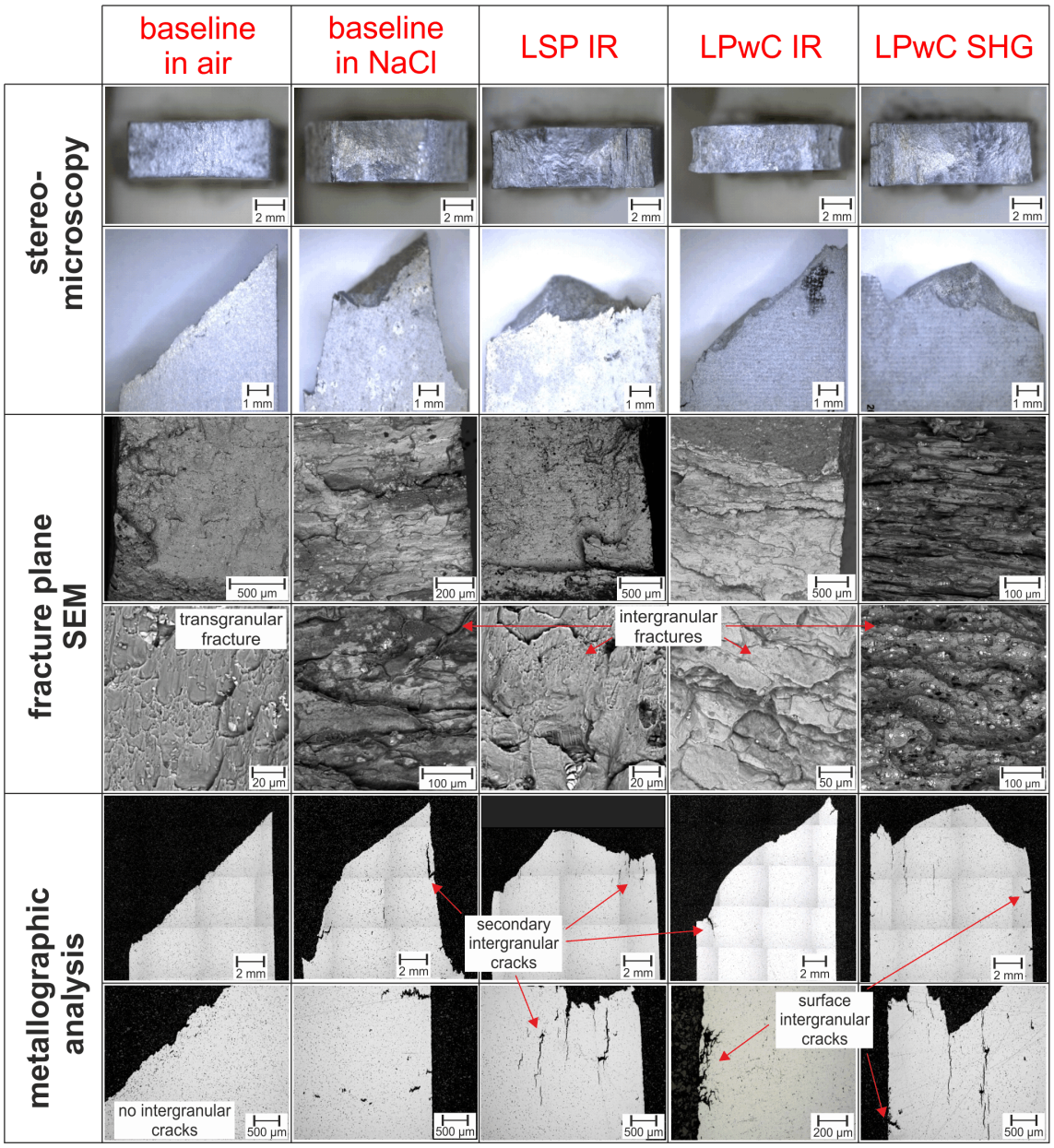

Figure 4.46: Fracture analysis results. Rows correspond to analytical method and columns to specific sensitized condition.

The stereomicroscopic images (Fig. 4.46 top row) show that the fracture progressed differently in different environments. Sensitized specimens in air show straight fracture under 45° angle where the highest shear stresses can be found. On the other hand, specimens tested in NaCl environment show irregular fracture roughly perpendicular to the loading stresses. These fractures comprise several smaller fracture areas where the specimen body was breached under the influence of the highest shear stresses. The closest

any sensitized specimen in NaCl got to the fracture shape in air was the LPwC IR condition. Upon closer investigation, however, the LPwC IR fracture morphology much more resembles the other sensitized samples in NaCl. The images also show no distinct plastic deformation around the fractures in the corrosive environment which is in agreement with the stress/strain curves in Fig. 4.45 where the strain at failure was relatively low. The SEM images in middle row of Fig. 4.46 show two different crack propagation mechanisms. Sensitized samples in air show transgranular crack features while all sensitized samples in NaCl show distinct intergranular cracking. The metallographic analysis in bottom row of Fig. 4.46 further reveals that cracks in the NaCl solution were initiated at the specimen surface, specifically at the edges. At first, the intergranular cracks propagated perpendicular to the applied stress due to material weakening in the corrosive environment. As the cracks progressed, the fracture morphology changed to ductile until the specimens fractured completely. Furthermore, as the primary crack propagated, secondary corrosion cracks split off into the specimen volume. These cracks were also intergranular as evidenced by a close up image in Fig. 4.47 with β-phase boundary visible. Moreover, next to the primary crack, more smaller perpendicular cracks can be observed on the edge surfaces of specimens in NaCl solution which lead to weakening of specimen cross-section. The size and length of these smaller cracks varied among different testing conditions. The average crack length of the NaCl baseline sample was 2 ± 1.14 mm while the LSP IR specimens showed 0.97 ± 0.33 mm. The LPwC conditions displayed even shorter cracks, specifically 0.25 ± 0.20 mm for LPwC IR and 0.80 ± 0.43 mm for LPwC SHG.

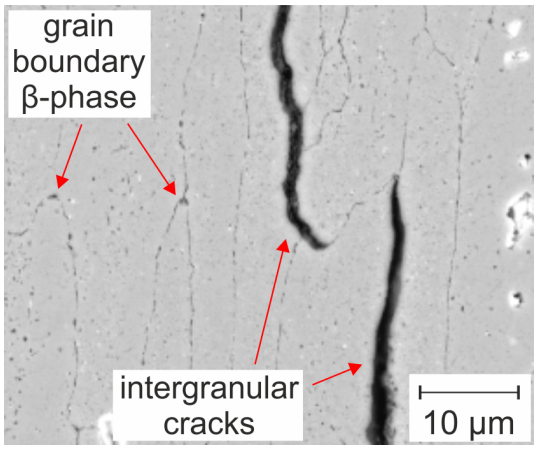

Figure 4.47: Secondary intergranular cracks following β-phase grain boundary.

In conclusion, we have shown that the SSRT parameters lead to IGSCC of AA5083 in 3.5% NaCl. The LSP and LPwC treatments induced strain hardening of the treated specimens which made the material stronger but less ductile. It is however unclear what effect the treatment had on the SCC process itself since the base material was essentially changed by the process and it is difficult to distinguish between the strain hardening and potential SCC suppression. An indicator of an actual improvement could be the length of the smaller intergranular surface cracks that were found on the sensitized samples. These cracks were smaller in case of LPwC treatments, most notably in the case of LPwC IR. This assessment, however, is very rough since laser treated strain hardened specimens failed sooner than non-treated specimens and the surface cracks did not have the same amount of time to develop. Nevertheless, LSP IR specimens with about half the time

to failure displayed side intergranular cracks about twice as short which implies linear propagation of the surface cracks in time. Based on this estimate and longer times to failure, we would expect longer surface cracks for LPwC specimens compared to the LSP IR but the crack length was in fact shorter. This qualitative result therefore supports the hypothesis that modified surface layer created during LPwC treatment does have a positive impact on IGSCC.

4.6 Fatigue testing

Samples for CF were in the form of 60 mm x 12 mm x 4 mm blocks sectioned from a 25.4 mm thick rolled plate and polished to 600 grit on all sides. Fig. 4.48a shows that the samples were sectioned in a way such that the plane experiencing the cyclic loading corresponded to the ND-TD face, i.e. the face with the highest DoS (4.3.1). The samples were once again sensitized at 100 °C for a period of 60 days. The peening parameters were the same as in the previous section and their summary can be found in Table 4.6. Only the 12 mm x 10 mm middle section of each sample was peened from both sides. Due to the patch short length, the samples were first fully peened from one side and then from the other to counteract the bending coming from the first side. No special patterning strategy was needed as opposed to the SSRT. Samples after LSP and LPwC treatments before fatigue testing are shown in Fig. 4.48b.

The 3-point bend test was load controlled and took place at room temperature at 45 Hz with R value 0.1. The supports were 20 mm apart and the specimen was submerged in 3.5% NaCl solution to simulate marine environment. The terminating condition was either when 10^7 cycles were reached or when the frequency dropped by 20 Hz due to lowered toughness as a crack developed and started to propagate. The testing setup is shown in Fig. 4.49.

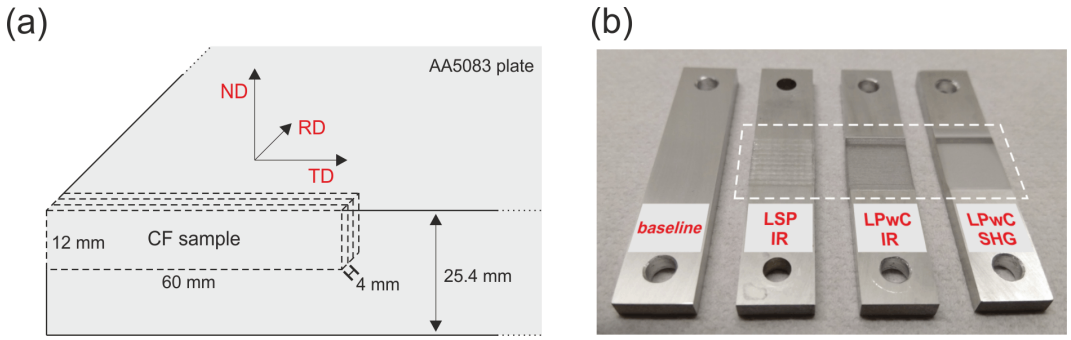

Figure 4.48: (a) Sectioning of CF samples in relation to the parental plate orientation and (b) CF samples before fatigue testing.

The results of the 3-point bend test are shown in Fig. 4.50. Data points with arrows mark samples which did not break during the test and were halted after 10^7 cycles. The baseline material not treated by laser peening without and with sensitization is represented by the black and red plots, respectively. The sensitized sample displays the S-N curve shifted down which shows a clear negative effect of IGC on the CF of AA5083. The fatigue strength at 10^7 cycles of the as received material was 127 MPa which is 44 MPa higher compared to the sensitized baseline sample. At the same time, it is lower than the fatigue strength value given in (3.3) and the discrepancy is attributed to the corrosive environment. Both the LSP and LPwC treatments had a positive impact on the fatigue,

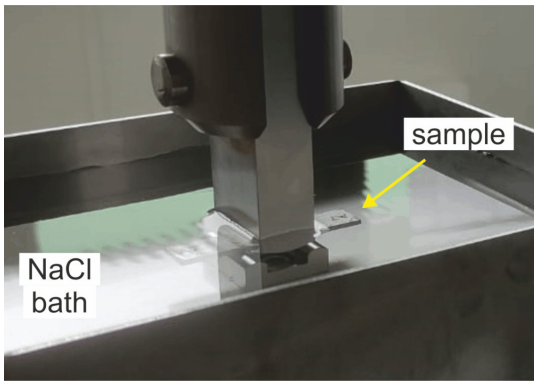

Figure 4.49: Corrosion fatigue 3-point bend testing setup.

bringing the S-N curves back up and possibly surpassing the original non-sensitized fatigue strength. Better improvements were achieved with the LPwC IR and LPwC SHG treatments where the fatigue strength improved by 63% and 69%, respectively. The LSP IR showed the least improvement out of the treatments tested but still reached a slightly higher fatigue resistance than the non-sensitized sample. Fatigue strength improved by 57% when compared to the control sensitized samples. The results are summarized in Table. 4.8.

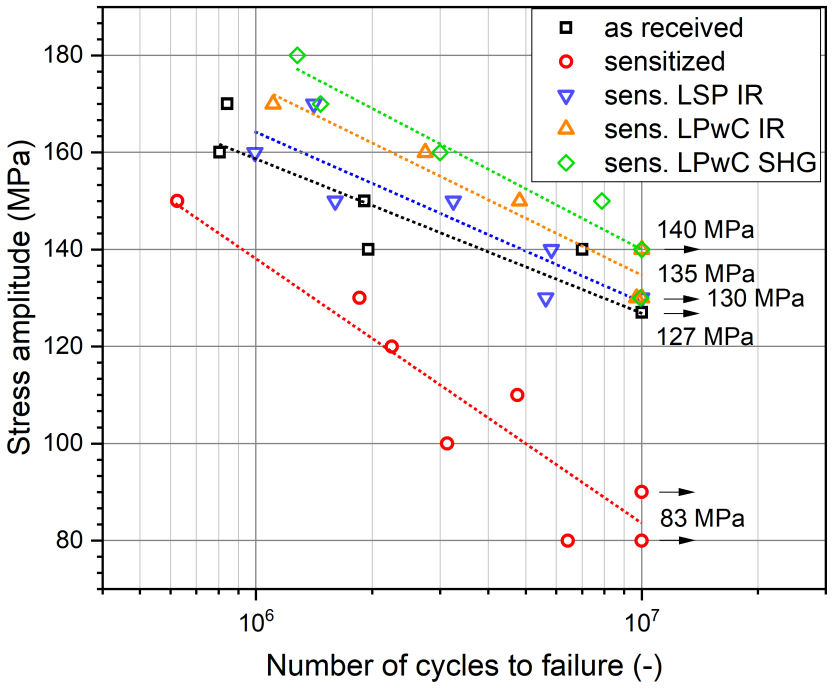

Figure 4.50: S-N curves of sensitized AA5083 after 3-point bend test in 3.5% NaCl solution after LSP and LPwC treatments. Plot for as received samples is provided for comparison.

Sample	Fatigue strength [MPa]	Improvement vs sensitized
as received	127	53%
sensitized	83	-
sens + LSP IR	130	57%
sens + LPwC IR	135	63%
sens + LPwC SHG	140	69%

Table 4.8: Fatigue strength of non-treated and laser peened samples in 3.5 wt% NaCl solution.

SEM images of cracked samples are shown in Fig. 4.51. In all cases, the fatigue crack was initiated in the central part of the loaded section, specifically at one of the sample edges, and the crack propagation was perpendicular to the tensile loading vector. The crack propagation mechanism of transgranular cracking was the same for all tested conditions which can be observed in the bottom part of Fig. 4.51. The highest corrosion damage was observed on the fracture plane of the sensitized baseline sample (Fig. 4.51b) with pitting as the dominant corrosion mechanism. Laser peened samples showed significantly lower pitting damage.

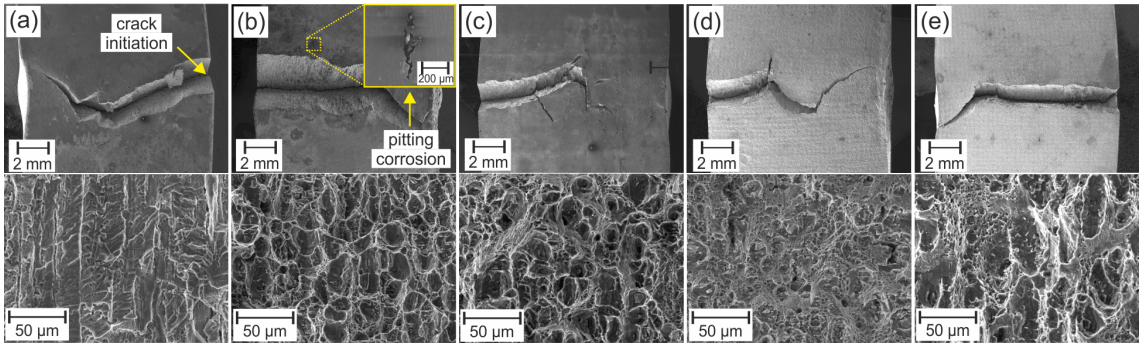

Figure 4.51: SEM images of cracked samples (top) and detail of the fracture surface (bottom) after 3-point bend testing: (a) as received, (b) sensitized, (c) sensitized LSP IR, (d) sensitized LPwC IR and (e) sensitized LPwC SHG.

In conclusion, sensitization has a negative impact on CF of the material which manifests as a 35% drop in fatigue strength. LSP and LPwC treatment restored and even possibly improved the original fatigue resistance of the non-sensitized samples. The improvement over the sensitized material appears to be over 60% (Fig. 4.50), especially with the LPwC underwater treatment, although more data points would be required for higher statistical certainty.

4.7 Discussion

In the experimental section we tried to answer the question what effect LSP and LPwC treatments have on stress corrosion cracking and corrosion fatigue of marine grade aluminium alloys which are weakened due to sensitization. Generally speaking, there are three key components for SCC to take place which are corrosive environment (sea water), weakened material (sensitization) and tensile stresses. While LSP as a post-processing method is predominantly used to remove the tensile stresses and replace them with compressive, the direct effect on the corrosion behaviour was also investigated.

From the mechanical standpoint, all three peening scenarios (LSP IR, LPwC IR and LPwC SHG) lead to generation of deep compressive residual stresses. Both magnitude and depth increased with number of laser impacts until a saturation was reached (Fig. 4.6). The largest differences observed were on the material surface which was heated and transformed during the LPwC treatments resulting in drop in compressive stresses (Fig. 4.7). However, higher compressive stresses were achieved with higher laser pulse density which is in agreement with LPwC literature [4, 156, 157, 158]. The second difference in the LPwC treatments was in stress anisotropy which is associated with single pass patterning strategy combined with high pulse density used in the LPwC treatments. This was later used in the CF and SSRT measurements to orient higher compressive stresses in the direction of tensile loading. The nano-hardness measurements showed an increase in surface hardness as a result of the cold working process applied via the LSP and LPwC treatments (Fig. 4.9). The amount of cold working and hardness increase was correlated to the degree of plastic deformation induced by individual treatments, with the highest deformation caused by LSP IR and the lowest with LPwC SHG (Fig. 4.10).

The electrochemical measurements show that the effect on corrosion resistance varies depending on whether an ablative overlay is applied or not, with other processes that affect the near-surface microstructure such as melting, solidification, surface oxide formation and grain refinement also playing significant role. In general, corrosion behaviour of aluminium alloys is determined by the behaviour of the surface oxide film, notably its degree of hydration and porosity [230]. The film forms either naturally or through thermodynamic processes. In spite of the LSP IR sample displaying the highest combined compressive stresses, the process is purely mechanical and thus no modified oxide layer is generated. Although some improvement was observed in R_p (Table 4.4), the data suggests that the character of the oxide film stayed mostly unchanged when compared to the LPwC treatments. This is further supported by the XPS analysis (Fig. 4.34b) where similar or slightly lower amount of aluminium oxide compared to non-treated samples was detected. Instead, the grains to about 300 nm depth are refined to ultra-fine nano-grains 100-200 nm in size (Fig. 4.37a). This result is consistent with other publications which showed LSP refined aluminium microstructure with grain size in the 60-200 nm range [15, 105, 106]. Despite no β-phase being present around the newly formed grain boundaries (Fig. 4.37b), the potentiostatic measurement in Fig. 4.28 suggest that this newly refined layer does not have an effect on IGC. This could be possibly due to low thickness of the refined layer since according to Seong et al. [81], 1 μm thick altered layer with refined grains is already sufficient to affect IGC. During the LPwC treatment, on the other hand, the direct interaction between the nanosecond laser pulse and the aluminium alloy surface under a water confinement creates a modified oxide layer and underlying transformed recast layer with a microstructure composed of a supersaturated Al solid solution free of β-phase precipitates, combined with a high dislocation density. These features are the result of the combined effect of thermal (melting/solidification) and high pressure severe plastic deformation as the pressure and temperature present are in the order of GPa

[1, 231] and thousands of °C [170], respectively. The presence of the modified oxide layer is supported by the XPS analysis (4.34b) where higher amount of aluminium oxide was detected as well as by potentiodynamic measurements (Fig. 4.24) where larger regions of passivity were observed. R_p after LPwC treatment was significantly increased which is in accordance with literature [17, 18, 232] where the improved corrosion characteristics of aluminium were attributed to modified oxide layer resulting from the LPwC process. Furthermore, the microstructure analysis gave evidence for β-phase free Al solid solution with high dislocation density layer beneath (Fig. 4.38). The 2-3 μm thick recast layer acts as a shielding barrier between the underlying β-phase and the electrolyte (Fig. 4.35d). This resulted in significantly lower IGC current measured during the potentiostatic test (Fig. 4.28) and higher resistance in the EIS analysis (Table 4.5). Furthermore, the recast layer being a uniform solid solution free of β-phase precipitates along the grain boundaries considerably minimizes galvanic coupling effects, mitigating early pitting by the electrolyte. Lastly, the increased roughness of treated samples means that the area exposed to the electrolyte is actually higher than area of the non-treated samples. This means that the corrosion current density of treated samples should objectively be even lower than presented here which further supports the conclusion of positive impact of LPwC.

The NAMLT measurements, on the other hand, do not show any significant change in DoS for the LPwC SHG sample (Fig. 4.20) even though DoS is the primary indicator of IGC susceptibility. Instead, an improvement in DoS is observed with the LSP IR and LPWC IR. This improvement becomes statistically significant when modified NAMLT was used. These results suggest that the IGC susceptibility as measured by NAMLT is more closely related to the amount of cold work which is the highest in the LSP IR and LPwC IR samples. Other studies also indicate that deformation processing methods such as rolling reductions, cryo-milling and extrusion have a positive effect on DoS of sensitized 5xxx alloys [233, 56]. The modified oxide layer seems to be ineffective when subjected to the aggressive attack of concentrated Nitric acid. However, we showed it to be effective in less aggressive environments such as 3.5% NaCl solution as demonstrated in the electrochemical analysis (4.4).

The tensile testing showed a clear negative effect of the corrosive sea water environment which resulted in premature failure of sensitized samples (Fig. 4.44). The fracture analysis revealed this was due to IGSCC while the fracture of specimen in air had a ductile character. The LSP and LPwC treated samples, however, did not show a clear SCC behaviour improvement but rather a high amount of cold work induced into the material (Fig. 4.45). We observed a slight increase in maximum stress and a significant reduction in strain-to-failure as the specimens became less ductile. The reduction was more pronounced for LSP IR and LPwC IR samples where more cold working took place as evidenced by the nano-hardness measurements (4.2). The investigation of smaller surface intergranular crack length suggests, however, that some improvement in IGSCC resistance could take place. The LPwC surface cracks were less than half in length compared to the baseline non-treated material while adjusting for different test durations. In contrast, the LSP IR condition with protective coating showed almost no crack length reduction. These results are in agreement with the electrochemical analysis which revealed the 3 μm thick modified oxide layer suppressing IGC in LPwC samples and no effect for the LSP samples. There is however a high degree of uncertainty due to the mechanical cold working of the material. Despite its popularity in the stress corrosion literature, the SSRT test might therefore not be the best option to investigate the effect of laser peening on IGSCC. The LSP and LPwC treatments basically transform the whole thin SSRT specimen into a different material which makes it hard to evaluate the SCC behaviour. A

tensile bending test would be more suitable since only a single surface of the sample is exposed to the tensile forces rather than the whole volume. Moreover, the sample can in such case be thicker so that the laser treatment would not affect the whole volume.

The CF testing on the other hand gives very clear idea of the LSP and LPwC influence. All laser treated samples outperformed the sensitized control samples and even surpassed the original non-sensitized fatigue strength (Fig. 4.50). The CF improvement is attributed to the compressive residual stresses imparted by the LSP and LPwC treatments. Higher fatigue life of the LPwC samples could be explained by the residual stress anisotropy. The LPwC fatigue samples had the transversal axis oriented parallel to the stress loading which means higher compression was achieved. Other authors also report positive impact of the enhanced oxide layer created during the LPwC process which improved corrosion resistance of various aluminium alloys [17, 18]. Compared to the SSRT, the bending test is much more suitable to test the LSP and LPwC influence. The tensile loading takes place on one surface only which could be specifically targeted by the treatment. That is the strength and primary use of the LSP technology - targeted treatment of critical areas.

Conclusion

In this work, the effect of Laser Shock Peening (LSP) treatment on marine grade aluminium alloys, specifically AA5083-H116, was investigated. A series of mechanical and electrochemical tests was carried out and evaluated in the context of material sensitization and intergranular corrosion (IGC) which have been shown to lead to stress corrosion cracking (SCC) and corrosion fatigue (CF). In order to cover more variation within the LSP process itself, three distinct peening configurations were used, one with protective overlay (LSP IR) and two without which were further separated by different water confinement and laser wavelength used (LPwC IR and LPwC SHG). Throughout the work, two laser systems were used; one at the University of Cincinnati, Ohio, USA, and the other at HiLASE research center in the Czech Republic. The laser parameters used were chosen as similar as possible so that shared conclusions could be made.

First, a residual stress parametric study was carried out that showed that LSP introduces deep compressive residual stresses into the material which increase with the number of laser impacts. Lower compressive stresses were measured on the surface in treatment without protective coating as a result of material heating during the laser absorption. A set of optimal parameters was picked for each peening configuration which was used for the rest of the study. Hardness testing showed a general increase in nano-hardness after leser peening with the highest increase up to 25% for the LSP IR samples. There was a correlation between the nano-hardness increase and the amount of cold working the laser treatment induced.

For the following tests, the material was sensitized at 100 °C for a period of 2 months. Nitric acid mass loss test (NAMLT) confirmed that after the heat treatment the samples were highly susceptible to IGC. It was also shown that the degree of sensitization (DoS) strongly depended on the grain orientation which were elongated in the AA5083 plate rolling direction. In order to accommodate NAMLT for LSP, a modified version of NAMLT was developed which was able to target a singular surface of the measured specimen. The modified NAMLT then showed that LSP treatment does have an impact on the DoS with up to 20% decrease for the LSP IR and LPwC IR speciemens whereas the LPwC SHG treatment showed no significant change. This result is attributed to plastic deformation caused by the LSP process which is the weakest in the LPwC SHG case. The modified oxide layer after the LPwC treatments does not seem to play any role in the aggressive nitric acid environment.

The electrochemical tests showed that the laser plasma interaction with the aluminum surface associated with the LPwC process creates β-phase free, supersaturated Al solid solution recast layer with a modified oxide layer on top in the treated area. This leads to the creation of a passive region with significantly lower anodic current in the potentiodynamic measurement. The modified oxide layer and the 2–3 μm thick β-phase free recast layer from the LPwC treatment shield the underlying β-phase regions from the electrolyte which results in significantly reduced IGC current during potentiostatic measurements, most notably for LPwC performed underwater. Despite 300 nm of re-

fined microstructure caused by LSP with no grain boundary β-phase present, the low thickness is not sufficient to protect the specimen against IGC.

The SSRT measurements clearly showed the cold working effect of the LSP treatment on the aluminium samples. We have observed an increase in maximum stress but at the same time significant decrease in nominal strain at failure as the samples lost some ductility. The effect of LSP on SCC is not clear since the cold working essentially transforms the base material into a different material although some evidence suggests that LPwC treatment slows down the crack propagation. Nevertheless, SSRT might not be an ideal ideal for determining the influence of LSP on SCC in general. Instead, constant strain test or bending tensile test might be more suitable. In contrast, the CF tests clearly showed large improvement in fatigue strength up to 69% for all laser treated samples. Simultaneously, sensitized control samples show about 50% drop in fatigue strength when compared to the non-sensitized samples. We can therefore conclude that the LSP and LPwC treatments recovered the fatigue strength loss caused by sensitization and it even improved the original fatigue strength of the non-sensitized material.

Although more work needs to be done in better designing the SCC tests, this thesis overall showed that LSP can be successfully applied to treat corrosion related phenomena in marine aluminium alloys. When compared to conventional shot peening or ultrasonic impact peening, LSP offers additional benefits such as deep compressive residual stresses and a unique recast oxide surface layer that significantly slows down the rate of IGC in sea water environment and increases pitting breakdown potential. This layer is produced in the LPwC treatment when no protective coating is used and the effect is stronger with underwater peening that uses green laser. The absence of protective coating additionally brings the economical benefit of lower time consumption for the treatment. We believe that in future, LPwC could become a commonly used tool in combating material sensitization and other stress related phenomena problems in the marine industry.

For future research, the author proposes these following steps: First step would be to investigate the stability of the beneficial recast layer. The recast layer is key for combating the IGC process and it needs to be able to withstand real ship service conditions. Secondly, a concrete application should be developed where real ship parts are treated and the process is further optimized. Thirdly, process capability should be assessed in terms of variability of the output which should then be compared with a proposed specification or product tolerance. And lastly, modelling should be used to simulate the process within the verification model.

Contribution to the scientific community

According to the author's opinion, this doctoral thesis will help to expand the field of LSP applications which were historically associated primarily with aerospace. Besides the traditional approach through compressive residual stresses, this work also shows more underutilized aspects of the LPwC method which modifies the material surface through thermomechanical effects. We have shown that this modified oxide layer alone can act as a barrier against IGC in sea water environment. This result is unique as current literature reporting on naked peening predominantly focuses on pitting as a main corrosion mechanism. The positive effect of LSP and LPwC and CF of sensitized AA5083 is also new and not published anywhere else. This work also features wide variety of LSP techniques including treatment both with and without protective coating as well as somewhat rare peening underwater utilizing second laser harmonic. Although the amount of cold working induced in the underwater peening is lower, the oxide layer modification is stronger which could make underwater peening more suitable for corrosion related applications

featuring aluminium alloys. The various LSP techniques are further supplemented with rigorous summary of the LSP technology. And lastly, we have also developed a modified nitric acid mass loss test which is able to target singular sample surface. This technique could be useful in number of applications outside the scope of this work or LSP technology.

Bibliography

[1] R. Fabbro, P. Peyre, L. Berthe, and X. Scherpereel, "Physics and applications of laser-shock processing," *Journal of laser applications*, vol. 10, no. 6, pp. 265–279, 1998.

[2] N. Anderholm, "Laser-generated stress waves," *Applied physics letters*, vol. 16, no. 3, pp. 113–115, 1970.

[3] S. Atluri, C. Harris, A. Hoggard, N. Miller, and S. Sampath, "Durability of metal aircraft structures," in *Proceeding of the FAA/NASA Conference on Aging Airplanes, Atlanta*, 1992.

[4] Y. Sano, K. Akita, K. Masaki, Y. Ochi, I. Altenberger, and B. Scholtes, "Laser peening without coating as a surface enhancement technology," *Pulse*, vol. 100, no. 40, p. 250mJ, 2006.

[5] W. J. Golumbfskie, K. T. Tran, J. M. Noland, R. Park, D. J. Stiles, G. Grogan, and C. Wong, "Survey of detection, mitigation, and repair technologies to address problems caused by sensitization of Al-Mg alloys on navy ships," *Corrosion*, vol. 72, no. 2, pp. 314–328, 2016.

[6] R. Zhang, S. P. Knight, R. L. Holtz, R. Goswami, C. H. Davies, and N. Birbilis, "A survey of sensitization in 5xxx series aluminum alloys," *Corrosion*, vol. 72, no. 2, pp. 144–159, 2016.

[7] K. Sridharan, T. R. Allen, Y.-K. Yang, B. R. Maier, and B. J. Hauch, "Mitigation of corrosion in 5xxx series al-mg alloys in marine environments: Grain boundary engineering and cold spray coating approaches," tech. rep., WISCONSIN UNIV-MADISON DEPT OF MATERIALS SCIENCE AND ENGINEERING, 2014.

[8] M. Ammon, "Nps student-professor team assists commander u.s. third fleet with 'splitting' dilemma," *NPS News*, 2011.

[9] H. R. Mattern, "Laser peening for mitigation of stress corrosion cracking at welds in marine aluminum," *Laser*, p. 3, 2011.

[10] C. Cavas, "Cracks plague ticonderoga-class cruisers," *Navy Times*, vol. 9, 2010.

[11] Y. Sano, M. Obata, T. Kubo, N. Mukai, M. Yoda, K. Masaki, and Y. Ochi, "Retardation of crack initiation and growth in austenitic stainless steels by laser peening without protective coating," *Materials Science and Engineering A*, vol. 417, no. 1-2, pp. 334–340, 2006.

[12] P. Peyre, C. Braham, J. Lédion, L. Berthe, and R. Fabbro, "Corrosion reactivity of laser-peened steel surfaces," *Journal of Materials Engineering and Performance*, vol. 9, no. 6, pp. 656–662, 2000.

[13] J. T. Wang, Y. K. Zhang, J. F. Chen, J. Y. Zhou, M. Z. Ge, Y. L. Lu, and X. L. Li, "Effects of laser shock peening on stress corrosion behavior of 7075 aluminum alloy laser welded joints," *Materials Science and Engineering A*, vol. 647, pp. 7–14, 2015.

[14] Y. Zhang, J. You, J. Lu, C. Cui, Y. Jiang, and X. Ren, "Effects of laser shock processing on stress corrosion cracking susceptibility of AZ31B magnesium alloy," *Surface and Coatings Technology*, vol. 204, no. 24, pp. 3947–3953, 2010.

[15] H. Wang, C. Ning, Y. Huang, Z. Cao, X. Chen, and W. Zhang, "Improvement of abrasion resistance in artificial seawater and corrosion resistance in NaCl solution of 7075 aluminum alloy processed by laser shock peening," *Optics and Lasers in Engineering*, vol. 90, no. July 2016, pp. 179–185, 2017.

[16] H. Amar, V. Vignal, H. Krawiec, C. Josse, P. Peyre, S. N. da Silva, and L. F. Dick, "Influence of the microstructure and laser shock processing (LSP) on the corrosion behaviour of the AA2050-T8 aluminium alloy," *Corrosion Science*, vol. 53, no. 10, pp. 3215–3221, 2011.

[17] U. Trdan and J. Grum, "Evaluation of corrosion resistance of AA6082-T651 aluminium alloy after laser shock peening by means of cyclic polarisation and ElS methods," *Corrosion Science*, vol. 59, pp. 324–333, 2012.

[18] U. Trdan and J. Grum, "SEM/EDS characterization of laser shock peening effect on localized corrosion of Al alloy in a near natural chloride environment," *Corrosion Science*, vol. 82, pp. 328–338, 2014.

[19] M. Abdulstaar, M. Mhaede, M. Wollmann, and L. Wagner, "Investigating the effects of bulk and surface severe plastic deformation on the fatigue, corrosion behaviour and corrosion fatigue of aa5083," *Surface and Coatings Technology*, vol. 254, pp. 244–251, 2014.

[20] R. L. Holtz, P. S. Pao, R. A. Bayles, T. M. Longazel, and R. Goswami, "Corrosion fatigue of al 5083-h131 sensitized at 70, 100, and 175 c relation to microstructure and degree of sensitization," in *DoD Corrosion Conference*, NACE/DoD Houston, TX, 2011.

[21] S. Benedictus-deVries, A. Bakker, G. Janssen, and H. de Wit, "Fatigue crack initiation behavior of welded aa5083 in a seawater environment," *J. Eng. Mater. Technol.*, vol. 126, no. 2, pp. 199–203, 2004.

[22] M. Abdulstaar, M. Mhaede, M. Wollmann, and L. Wagner, "Investigating the effects of bulk and surface severe plastic deformation on the fatigue, corrosion behaviour and corrosion fatigue of AA5083," *Surface and Coatings Technology*, vol. 254, pp. 244–251, 2014.

[23] P. H. Wirsching and Y.-N. Chen, "Considerations of probability-based fatigue design for marine structures," *Marine Structures*, vol. 1, no. 1, pp. 23–45, 1988.

[24] W. Cui, "A state-of-the-art review on fatigue life prediction methods for metal structures," *Journal of marine science and technology*, vol. 7, no. 1, pp. 43–56, 2002.

[25] A. Groysman, *Corrosion for everybody*, p. 102. Springer, 2010.

[26] R. Parkins, W. Blanchard Jr, and B. Delanty, "Transgranular stress corrosion cracking of high-pressure pipelines in contact with solutions of near neutral ph," *Corrosion*, vol. 50, no. 5, pp. 394–408, 1994.

[27] NACE, "Stress Corrosion Cracking." Available at https://www.nace.org/resources/general-resources/corrosion-basics/group-3/stress-corrosion-cracking (6.6.2020).

[28] U. Chatterjee, "Stress corrosion cracking and component failure: Causes and prevention," *Sadhana*, vol. 20, no. 1, pp. 165–184, 1995.

[29] R. K. Gupta, R. Zhang, C. H. Davies, and N. Birbilis, "Influence of Mg content on the sensitization and corrosion of Al-xMg(-Mn) alloys," *Corrosion*, vol. 69, no. 11, pp. 1081–1087, 2013.

[30] R. L. Holtz, R. Goswami, and P. S. Pao, "Sensitization of naturally aged aluminum 5083 armor plate," tech. rep., NAVAL RESEARCH LAB WASHINGTON DC MATERIALS SCIENCE AND TECHNOLOGY DIV, 2015.

[31] N. Birbilis and R. G. Buchheit, "Electrochemical characteristics of intermetallic phases in aluminum alloys an experimental survey and discussion," *Journal of The Electrochemical Society*, vol. 152, no. 4, pp. B140–B151, 2005.

[32] E. McCafferty, "Sequence of steps in the pitting of aluminum by chloride ions," *Corrosion science*, vol. 45, no. 7, pp. 1421–1438, 2003.

[33] T. Nguyen and R. Foley, "The chemical nature of aluminum corrosion iii. the dissolution mechanism of aluminum oxide and aluminum powder in various electrolytes," *Journal of the Electrochemical Society*, vol. 127, no. 12, pp. 2563–2566, 1980.

[34] A. Aballe, M. Bethencourt, F. Botana, M. Cano, and M. Marcos, "Localized alkaline corrosion of alloy aa5083 in neutral 3.5% nacl solution," *Corrosion science*, vol. 43, no. 9, pp. 1657–1674, 2001.

[35] M. L. C. Lim, R. G. Kelly, and J. R. Scully, "Overview of intergranular corrosion mechanisms, phenomenological observations, and modeling of AA5083," *Corrosion*, vol. 72, no. 2, pp. 198–220, 2016.

[36] H. C. Lab, "Aluminium exfoliation." Available at https://http://hawaiicorrosionlab.org/photos/photos.html (13.1.2022).

[37] R. Zhang, M. Steiner, S. Agnew, S. Kairy, C. Davies, and N. Birbilis, "Experiment-based modelling of grain boundary β-phase (mg 2 al 3) evolution during sensitisation of aluminium alloy aa5083," *Scientific reports*, vol. 7, no. 1, pp. 1–14, 2017.

[38] C. B. Crane and R. P. Gangloff, "Stress corrosion cracking of Al-Mg alloy 5083 sensitized at low temperature," *Corrosion*, vol. 72, no. 2, pp. 221–241, 2016.

[39] N. Birbilis, R. Zhang, M. L. C. Lim, R. K. Gupta, C. H. J. Davies, S. P. Lynch, R. G. Kelly, and J. R. Scully, "Quantification of sensitization in aa5083-h131 via imaging ga-embrittled fracture surfaces," *Corrosion*, vol. 69, no. 4, pp. 396–402, 2013.

[40] E. Bumiller, "Intergranular corrosion in aa5xxx aluminum alloys with discontinuous precipitation at the grain boundaries," *Ph. D. Thesis*, 2011.

[41] "Determining the Susceptibility to Intergranular Corrosion of 5XXX Series Aluminum Alloys by Mass Loss After Exposure to Nitric Acid (NAMLT Test)," standard, ASTM International, West Conshohocken, PA, USA, May 2013.

[42] F. S. Bovard, "Sensitization and environmental cracking of 5xxx aluminum marine sheet and plate alloys," *Corrosion in Marine and Saltwater Environments II*, pp. 232–243, 2005.

[43] ElectraWatch, "DoS probe." Available at `https://http://electrawatch.com/product/dosprobe/` (9.6.2020).

[44] R. Goswami and R. L. Holtz, "Transmission electron microscopic investigations of grain boundary beta phase precipitation in al 5083 aged at 373 k (100 c)," *Metallurgical and Materials Transactions A*, vol. 44, no. 3, pp. 1279–1289, 2013.

[45] R. Goswami, G. Spanos, P. Pao, and R. Holtz, "Precipitation behavior of the ß phase in al-5083," *Materials Science and Engineering: A*, vol. 527, no. 4-5, pp. 1089–1095, 2010.

[46] M. A. Steiner and S. R. Agnew, "Modeling sensitization of Al-Mg alloys via β-phase precipitation kinetics," *Scripta Materialia*, vol. 102, pp. 55–58, 2015.

[47] G. Yi, Y. Zhu, E. Sundberg, A. T. Derrick, and M. L. Free, "Sensitization prediction and validation for Al 5xxx alloys exposed to long-term cyclical and constant heating at low temperatures," *Corrosion*, vol. 72, no. 2, pp. 177–186, 2016.

[48] J. R. Davis *et al.*, *Aluminum and aluminum alloys*. ASM international, 1993.

[49] I. Oguocha, O. Adigun, and S. Yannacopoulos, "Effect of sensitization heat treatment on properties of al–mg alloy aa5083-h116," *Journal of Materials Science*, vol. 43, no. 12, pp. 4208–4214, 2008.

[50] R. Z. Valiev, N. Krasilnikov, and N. Tsenev, "Plastic deformation of alloys with submicron-grained structure," *Materials Science and Engineering: A*, vol. 137, pp. 35–40, 1991.

[51] H. Fujita and T. Tabata, "The effect of grain size and deformation sub-structure on mechanical properties of polycrystalline aluminum," *Acta metallurgica*, vol. 21, no. 4, pp. 355–365, 1973.

[52] A. Halap, T. Radetić, M. Popović, and E. Romhanji, "Influence of the thermomechanical treatment on the intergranular corrosion susceptibility of zn-modified al-5.1 wt pct mg-0.7 wt pct mn alloy sheet," *Metallurgical and Materials Transactions A*, vol. 45, no. 10, pp. 4572–4579, 2014.

[53] A. J. Davenport, Y. Yuan, R. Ambat, B. J. Connolly, M. Strangwood, A. Afseth, and G. M. Scamans, "Intergranular corrosion and stress corrosion cracking of sensitised aa5182," in *Materials science forum*, vol. 519, pp. 641–646, Trans Tech Publ, 2006.

[54] D. S. D'Antuono, J. Gaies, W. Golumbfskie, and M. Taheri, "Grain boundary misorientation dependence of β phase precipitation in an al–mg alloy," *Scripta Materialia*, vol. 76, pp. 81–84, 2014.

[55] Y. Zhao, M. N. Polyakov, M. Mecklenburg, M. E. Kassner, and A. M. Hodge, "The role of grain boundary plane orientation in the β phase precipitation of an al–mg alloy," *Scripta Materialia*, vol. 89, pp. 49–52, 2014.

[56] R. Zhang, R. K. Gupta, C. H. Davies, A. M. Hodge, M. Tort, K. Xia, and N. Birbilis, "The influence of grain size and grain orientation on sensitization in AA5083," *Corrosion*, vol. 72, no. 2, pp. 160–168, 2016.

[57] W. Zhang and G. S. Frankel, "Anisotropy of localized corrosion in aa2024-t3," *Electrochemical and Solid State Letters*, vol. 3, no. 6, p. 268, 2000.

[58] M. Robinson and N. Jackson, "The influence of grain structure and intergranular-corrosion rate on exfoliation and stress corrosion crackingof high strength al–cu–mg alloys," *Corrosion Science*, vol. 41, no. 5, pp. 1013–1028, 1999.

[59] M. Robinson and N. Jackson, "Exfoliation corrosion of high strength al-cu-mg alloys: effect of grain structure," *Corrosion Engineering, Science, and Technology*, vol. 34, no. 1, p. 45, 1999.

[60] T. Hunt, A. Laspe, J. Rojas, Y. Yang, and T. Allen, "Quantification of mass loss dependence on sample orientation in 5xxx series aluminum alloys," *Corrosion*, vol. 72, no. 2, pp. 187–197, 2016.

[61] L. Kramer, M. Phillippi, W. T. Tack, and C. Wong, "Locally reversing sensitization in 5xxx aluminum plate," *Journal of Materials Engineering and Performance*, vol. 21, no. 6, pp. 1025–1029, 2012.

[62] R. Y. Chen, H. Y. Chu, C. C. Lai, and C. T. Wu, "Effects of annealing temperature on the mechanical properties and sensitization of 5083-H116 aluminum alloy," *Proceedings of the Institution of Mechanical Engineers, Part L: Journal of Materials: Design and Applications*, vol. 229, no. 4, pp. 339–346, 2015.

[63] A. P. Reynolds and J. Chrisfield, "Use of friction stir processing to eliminate sensitization in an al-mg alloy," *Corrosion*, vol. 68, no. 10, pp. 913–921, 2012.

[64] A. P. Reynolds and J. Chrisfield, "Use of friction stir processing to eliminate sensitization in an Al-Mg alloy," *Corrosion*, vol. 68, no. 10, pp. 913–921, 2012.

[65] M. Carroll, P. Gouma, M. Mills, G. Daehn, and B. Dunbar, "Effects of zn additions on the grain boundary precipitation and corrosion of al-5083," *Scripta materialia*, vol. 42, no. 4, pp. 335–340, 2000.

[66] M. Carroll, P. Gouma, G. Daehn, and M. Mills, "Effects of minor cu additions on a zn-modified al-5083 alloy," *Materials Science and Engineering: A*, vol. 319, pp. 425–428, 2001.

[67] M. Carroll, R. Buchheit, G. S. Daehn, and M. J. Mills, "Optimum trace copper levels for scc resistance in a zn-modified al-5083 alloy," in *Materials Science Forum*, vol. 396, pp. 1443–1448, Trans Tech Publications Ltd., Zurich-Uetikon, Switzerland, 2002.

[68] N. Sukiman, R. Gupta, R. Zhang, R. G. Buchheit, and N. Birbilis, "Influence of microalloying additions on al-mg alloy. part 2: Phase analysis and sensitisation behaviour," *Corrosion engineering, science and technology*, vol. 49, no. 4, pp. 263–268, 2014.

[69] R. K. Gupta, R. Zhang, C. H. J. Davies, and N. Birbilis, "Theoretical study of the influence of microalloying on sensitization of aa5083 and moderation of sensitization of a model al-mg-mn alloy via sr additions," *Corrosion*, vol. 70, no. 4, pp. 402–413, 2014.

[70] Y. Wang, R. K. Gupta, N. Sukiman, R. Zhang, C. H. J. Davies, and N. Birbilis, "Influence of alloyed nd content on the corrosion of an al–5mg alloy," *Corrosion science*, vol. 73, pp. 181–187, 2013.

[71] R. K. Gupta, Y. Wang, R. Zhang, N. Sukiman, C. H. J. Davies, and N. Birbilis, "Imparting sensitization resistance to an al-5mg alloy via neodymium additions," *Corrosion*, vol. 69, no. 1, pp. 4–8, 2013.

[72] M. Heine and M. Pryor, "Passivation of aluminum by chromate solutions," *Journal of The Electrochemical Society*, vol. 114, no. 10, pp. 1001–1006, 1967.

[73] Z. Szklarska-Smialowska, "Pitting corrosion of aluminum," *Corrosion science*, vol. 41, no. 9, pp. 1743–1767, 1999.

[74] A. K. Mishra and R. Balasubramaniam, "Corrosion inhibition of aluminum alloy aa 2014 by rare earth chlorides," *Corrosion Science*, vol. 49, no. 3, pp. 1027–1044, 2007.

[75] O. Lopez-Garrity and G. Frankel, "Corrosion inhibition of aa2024-t3 by sodium silicate," *Electrochimica Acta*, vol. 130, pp. 9–21, 2014.

[76] J. Searles, P. Gouma, and R. Buchheit, "Stress corrosion cracking of sensitized aa5083 (al-4.5 mg-1.0 mn)," *Metallurgical and Materials Transactions A*, vol. 32, no. 11, pp. 2859–2867, 2001.

[77] J. Seong, G. S. Frankel, and N. Sridhar, "Inhibition of stress corrosion cracking of sensitized AA5083," *Corrosion*, vol. 72, no. 2, pp. 284–296, 2016.

[78] J. Seong, G. S. Frankel, and N. Sridhar, "Corrosion Inhibition of Sensitized and Solutionized AA5083," *Journal of The Electrochemical Society*, vol. 162, no. 9, pp. C449–C456, 2015.

[79] I.-C. Park and S.-J. Kim, "Determination of corrosion protection current density requirement of zinc sacrificial anode for corrosion protection of aa5083-h321 in seawater," *Applied Surface Science*, p. 145346, 2020.

[80] A. Supply, "Sacrificial anode." Available at `https://www.ship-technology.com/contractors/corrosion/anode-supply/` (11.6.2020).

[81] J. Seong, F. Yang, F. Scheltens, G. S. Frankel, and N. Sridhar, "Influence of the Altered Surface Layer on the Corrosion of AA5083," *Journal of The Electrochemical Society*, vol. 162, no. 6, pp. C209–C218, 2015.

[82] X. Sauvage, N. Enikeev, R. Valiev, Y. Nasedkina, and M. Murashkin, "Atomic-scale analysis of the segregation and precipitation mechanisms in a severely deformed Al-Mg alloy," *Acta Materialia*, vol. 72, pp. 125–136, 2014.

[83] Y. L. Ma, J. J. Xie, Y. S. Hong, and Z. M. Deng, "Study on Mechanical Properties of Nanocrystal Surface Layer of an Aluminum Alloy," *International Journal of Nonlinear Sciences and Numerical Simulation*, vol. 3, no. 3-4, pp. 491–494, 2002.

[84] Curtiss-Wright, "Shot Peening." Available at `https://cwst.com/shot-peening/overview/` (11.6.2020).

[85] E. Inc., "A, N and C Certified Almen Strips." Available at https://www.electronics-inc.com/products/almen-strips/a-n-c-strips/ (11.6.2020).

[86] A. T. Vielma, V. Llaneza, and F. J. Belzunce, "Effect of coverage and double peening treatments on the fatigue life of a quenched and tempered structural steel," *Surface and Coatings Technology*, vol. 249, pp. 75–83, 2014.

[87] P. S. Prevey and J. T. Cammett, "The Effect of Shot Peening Coverage on Residual Stress, Cold Work and Fatigue in a Ni-Cr-Mo Low Alloy Steel," *Shot Peening*, pp. 295–304, 2006.

[88] N. Sidhom, A. Laamouri, R. Fathallah, C. Braham, and H. Lieurade, "Fatigue strength improvement of 5083 h11 al-alloy t-welded joints by shot peening: experimental characterization and predictive approach," *International journal of fatigue*, vol. 27, no. 7, pp. 729–745, 2005.

[89] A. V. Jebaraj, L. Ajaykumar, C. Deepak, and K. Aditya, "Enhancement of exfoliation corrosion resistance of aluminium alloy 5083 by shot peening," *Surface Review and Letters*, vol. 25, no. 07, p. 1950020, 2018.

[90] K. L. Yuan and Y. Sumi, "Modelling of ultrasonic impact treatment (UIT) of welded joints and its effect on fatigue strength," *Frattura ed Integrita Strutturale*, vol. 9, no. 34, pp. 476–486, 2015.

[91] E. Statnikov, L. Zhuravlev, A. Alekseev, Y. Bobylev, E. Shevtsov, V. Sokolenko, and V. Kulikov, "Ultrasonic head for strain hardening and relaxation treatment," *USSR inventor's certificate*, no. 472782, 1975.

[92] J. Fisher, E. Statnikov, and L. Tehini, "Fatigue Strength Enhancement by Means of Weld Design Change and the Application of Ultrasonic Impact treatment," *Proc. of Intl. Symp. On Steel Bridges*, 2001.

[93] K. N. T. Tran, *Microstructural characterization of ultrasonic impact treated Al-Mg alloy*. PhD thesis, 2012.

[94] X. An, C. A. Rodopoulos, E. S. Statnikov, V. N. Vitazev, and O. V. Komlkov, "Study of the surface nanocrystallization induced by the esonix ultrasonic impact treatment on the near-surface of 2024-T351 aluminum alloy," *Journal of Materials Engineering and Performance*, vol. 15, no. 3, pp. 355–364, 2006.

[95] M. Liao, W. R. Chen, and N. C. Bellinger, "Effects of ultrasonic impact treatment on fatigue behavior of naturally exfoliated aluminum alloys," *International Journal of Fatigue*, vol. 30, no. 4, pp. 717–726, 2008.

[96] H. sang Lee, D. soo Kim, J. sung Jung, Y. shik Pyoun, and K. Shin, "Influence of peening on the corrosion properties of AISI 304 stainless steel," *Corrosion Science*, vol. 51, no. 12, pp. 2826–2830, 2009.

[97] B. N. Mordyuk and G. I. Prokopenko, "Ultrasonic impact peening for the surface properties' management," *Journal of Sound and Vibration*, vol. 308, no. 3-5, pp. 855–866, 2007.

[98] C. S. Montross, T. Wei, L. Ye, G. Clark, and Y. W. Mai, "Laser shock processing and its effects on microstructure and properties of metal alloys: A review," *International Journal of Fatigue*, vol. 24, no. 10, pp. 1021–1036, 2002.

[99] O. Hatamleh, J. Lyons, and R. Forman, "Laser peening and shot peening effects on fatigue life and surface roughness of friction stir welded 7075-T7351 aluminum," *Fatigue and Fracture of Engineering Materials and Structures*, vol. 30, no. 2, pp. 115–130, 2007.

[100] B. N. Mordyuk, Y. V. Milman, M. O. Iefimov, G. I. Prokopenko, V. V. Silberschmidt, M. I. Danylenko, and A. V. Kotko, "Characterization of ultrasonically peened and laser-shock peened surface layers of AISI 321 stainless steel," *Surface and Coatings Technology*, vol. 202, no. 19, pp. 4875–4883, 2008.

[101] Z. D. Wang, G. F. Sun, Y. Lu, M. Z. Chen, K. D. Bi, and Z. H. Ni, "Microstructural characterization and mechanical behavior of ultrasonic impact peened and laser shock peened AISI 316L stainless steel," *Surface and Coatings Technology*, vol. 385, 2020.

[102] S. S. Hassan, M. N. Hamzah, and R. M. Abed, "Comparison between ultrasonic and laser shock peening treatment on fatigue life performance of al-alloy 7075," *Advances in Natural and Applied Sciences*, vol. 11, no. 9, pp. 159–166, 2017.

[103] C. Dane, F. Harris, E. Lao, J. Rankin, and R. Hurd, "Advanced beam delivery formobile laser peening." Presentation at the 2nd International Conference on Laser Peening, San Francisco CA, Apr 19 2010.

[104] J. Wang, Y. Zhang, J. Chen, J. Zhou, M. Ge, Y. Lu, and X. Li, "Effects of laser shock peening on stress corrosion behavior of 7075 aluminum alloy laser welded joints," *Materials Science and Engineering: A*, vol. 647, pp. 7–14, 2015.

[105] J. Z. Lu, K. Y. Luo, Y. K. Zhang, C. Y. Cui, G. F. Sun, J. Z. Zhou, L. Zhang, J. You, K. M. Chen, and J. W. Zhong, "Grain refinement of LY2 aluminum alloy induced by ultra-high plastic strain during multiple laser shock processing impacts," *Acta Materialia*, vol. 58, no. 11, pp. 3984–3994, 2010.

[106] U. Trdan, M. Skarba, and J. Grum, "Laser shock peening effect on the dislocation transitions and grain refinement of Al-Mg-Si alloy," *Materials Characterization*, vol. 97, pp. 57–68, 2014.

[107] U. Trdan and J. Grum, "Evaluation of corrosion resistance of AA6082-T651 aluminium alloy after laser shock peening by means of cyclic polarisation and ElS methods," *Corrosion Science*, vol. 59, pp. 324–333, 2012.

[108] Y. Sano, K. Akita, K. Masaki, Y. Ochi, I. Altenberger, and B. Scholtes, "Laser peening without coating as a surface enhancement technology," *Journal of Laser Micro Nanoengineering*, vol. 1, no. 3, pp. 161–166, 2006.

[109] A. U. Tsao, *The Effect of Laser Shock Peening on Dislocation Morphology and Microstructural Evolution of AA5083-H116*. PhD thesis, 2019.

[110] C.-K. Lin and S.-T. Yang, "Corrosion fatigue behavior of 7050 aluminum alloys in different tempers," *Engineering Fracture Mechanics*, vol. 59, no. 6, pp. 779–795, 1998.

[111] A. Mohamed, "Intergranular corrosion fatigue fracture surface analysis of nickel alloy," *Procedia Engineering*, vol. 114, pp. 754–759, 2015.

[112] A. Gingell and J. King, "The effect of frequency and microstructure on corrosion fatigue crack propagation in high strength aluminium alloys," *Acta materialia*, vol. 45, no. 9, pp. 3855–3870, 1997.

[113] P. Pao, S. Gill, C. Feng, and K. Sankaran, "Corrosion–fatigue crack growth in friction stir welded al 7050," *Scripta Materialia*, vol. 45, no. 5, pp. 605–612, 2001.

[114] R. M. Bay, D. J. Schrock, A. M. Akman, L. G. Bland, R. Thodla, and J. S. W. Locke, "The effect of sensitization and fatigue loading frequency on corrosion fatigue of aa5083-h131," *International Journal of Fatigue*, vol. 124, pp. 1–9, 2019.

[115] D. Bäuerle, *Laser processing and chemistry*. Springer Science & Business Media, 2013.

[116] O. Benavides, L. De la Cruz May, and A. F. Gil, "A comparative study on reflection of nanosecond nd-yag laser pulses in ablation of metals in air and in vacuum," *Optics express*, vol. 21, no. 11, pp. 13068–13074, 2013.

[117] D. Bergström, J. Powell, and A. Kaplan, "The absorption of light by rough metal surfaces—a three-dimensional ray-tracing analysis," *Journal of Applied Physics*, vol. 103, no. 10, p. 103515, 2008.

[118] Z. Zhang, Q. Nian, C. C. Doumanidis, and Y. Liao, "First-principles modeling of laser-matter interaction and plasma dynamics in nanosecond pulsed laser shock processing," *Journal of Applied Physics*, vol. 123, no. 5, p. 054901, 2018.

[119] C. Stenz and V. Tikhonchuk, "Lecture notes in ultraintense laser-plasma interaction," 2008.

[120] R. Stoian, D. Ashkenasi, A. Rosenfeld, and E. Campbell, "Coulomb explosion in ultrashort pulsed laser ablation of al 2 o 3," *Physical review B*, vol. 62, no. 19, p. 13167, 2000.

[121] B. N. Chichkov, C. Momma, S. Nolte, F. Von Alvensleben, and A. Tünnermann, "Femtosecond, picosecond and nanosecond laser ablation of solids," *Applied physics A*, vol. 63, no. 2, pp. 109–115, 1996.

[122] A. Pukhov, "Strong field interaction of laser radiation," *Reports on progress in Physics*, vol. 66, no. 1, p. 47, 2002.

[123] C. Thaury, F. Quéré, J.-P. Geindre, A. Levy, T. Ceccotti, P. Monot, M. Bougeard, F. Réau, P. d'Oliveira, P. Audebert, *et al.*, "Plasma mirrors for ultrahigh-intensity optics," *Nature Physics*, vol. 3, no. 6, pp. 424–429, 2007.

[124] A. Lévy, T. Ceccotti, P. D'Oliveira, F. Réau, M. Perdrix, F. Quéré, P. Monot, M. Bougeard, H. Lagadec, P. Martin, *et al.*, "Double plasma mirror for ultrahigh temporal contrast ultraintense laser pulses," *Optics letters*, vol. 32, no. 3, pp. 310–312, 2007.

[125] J. J. Duderstadt and G. A. Moses, *Inertial confinement fusion*. John Wiley & Sons, 1982.

[126] T. H. Maiman *et al.*, "Stimulated optical radiation in ruby," *Nature*, vol. 187, pp. 493–494, 1960.

[127] G. Askar'Yan and E. Moroz, "Pressure on evaporation of matter in a radiation beam," *Soviet Journal of Experimental and Theoretical Physics*, vol. 16, p. 1638, 1963.

[128] F. Neuman, "Momentum transfer and cratering effects produced by giant laser pulses," *Applied physics letters*, vol. 4, no. 9, pp. 167–169, 1964.

[129] D. W. Gregg and S. J. Thomas, "Momentum transfer produced by focused laser giant pulses," *Journal of Applied Physics*, vol. 37, no. 7, pp. 2787–2789, 1966.

[130] R. M. White, "Elastic wave generation by electron bombardment or electromagnetic wave absorption," *Journal of Applied Physics*, vol. 34, no. 7, pp. 2123–2124, 1963.

[131] C. Skeen and C. York, "Laser-induced"blow-off"phenomena," *Applied Physics Letters*, vol. 12, no. 11, pp. 369–371, 1968.

[132] B. Fairand, B. Wilcox, W. Gallagher, and D. Williams, "Laser shock-induced microstructural and mechanical property changes in 7075 aluminum," *Journal of Applied Physics*, vol. 43, no. 9, pp. 3893–3895, 1972.

[133] A. H. Clauer, B. P. Fairand, and B. A. Wilcox, "Pulsed laser induced deformation in an fe-3 wt pct si alloy," *Metallurgical Transactions A*, vol. 8, no. 1, pp. 119–125, 1977.

[134] B. Fairand and A. Clauer, "Laser generation of high-amplitude stress waves in materials," *Journal of Applied Physics*, vol. 50, no. 3, pp. 1497–1502, 1979.

[135] A. H. Clauer, C. T. Walters, and S. C. Ford, "The effects of laser shock processing on the fatigue properties of 2024-t3 aluminum," *Lasers in materials processing*, pp. 7–22, 1983.

[136] A. H. Clauer, B. P. Fairand, and B. A. Wilcox, "Laser shock hardening of weld zones in aluminum alloys," *Metallurgical Transactions A*, vol. 8, no. 12, pp. 1871–1876, 1977.

[137] A. Clauer and B. Fairand, "Interaction of laser-induced stress waves with metals," in *Proc. ASM Conference Applications of Lasers in Materials Processing*, 1979.

[138] A. Clauer and J. Koucky, "Laser shock processing increases the fatigue life of metal parts," *Materials and Processing Report*, vol. 6, no. 6, pp. 3–5, 1991.

[139] R. Fabbro, J. Fournier, P. Ballard, D. Devaux, and J. Virmont, "Physical study of laser-produced plasma in confined geometry," *Journal of applied physics*, vol. 68, no. 2, pp. 775–784, 1990.

[140] L. Berthe, R. Fabbro, P. Peyre, L. Tollier, and E. Bartnicki, "Shock waves from a water-confined laser-generated plasma," *Journal of Applied Physics*, vol. 82, no. 6, pp. 2826–2832, 1997.

[141] L. Berthe, R. Fabbro, P. Peyre, and E. Bartnicki, "Wavelength dependent of laser shock-wave generation in the water-confinement regime," *Journal of applied physics*, vol. 85, no. 11, pp. 7552–7555, 1999.

[142] J. Ocaña, C. Molpeceres, J. Porro, G. Gómez, and M. Morales, "Experimental assessment of the influence of irradiation parameters on surface deformation and residual stresses in laser shock processed metallic alloys," *Applied Surface Science*, vol. 238, no. 1-4, pp. 501–505, 2004.

[143] U. Trdan, J. A. Porro, J. L. Ocaña, and J. Grum, "Laser shock peening without absorbent coating (lspwc) effect on 3d surface topography and mechanical properties of 6082-t651 al alloy," *Surface and Coatings Technology*, vol. 208, pp. 109–116, 2012.

[144] M. Yoda and B. Newton, "Underwater laser peening," in *Proceedings of the Welding and Repair Technology for Power Plants Eighth International EPRI Conference, Fort Myers, FL, USA*, pp. 18–20, 2008.

[145] Y. B. Zel'Dovich and Y. P. Raizer, *Physics of shock waves and high-temperature hydrodynamic phenomena*. Courier Corporation, 2002.

[146] C. Phipps Jr, T. Turner, R. Harrison, G. York, W. Osborne, G. Anderson, X. Corlis, L. Haynes, H. Steele, K. Spicochi, *et al.*, "Impulse coupling to targets in vacuum by krf, hf, and co2 single-pulse lasers," *Journal of Applied Physics*, vol. 64, no. 3, pp. 1083–1096, 1988.

[147] P. Ballard, J. Fournier, R. Fabbro, and J. Frelat, "Residual stresses induced by laser-shocks," *Le Journal de Physique IV*, vol. 1, no. C3, pp. C3–487, 1991.

[148] P. Peyre, R. Fabbro, P. Merrien, and H. Lieurade, "Laser shock processing of aluminium alloys. application to high cycle fatigue behaviour," *Materials Science and Engineering: A*, vol. 210, no. 1-2, pp. 102–113, 1996.

[149] P. Peyre, L. Berthe, X. Scherpereel, and R. Fabbro, "Laser-shock processing of aluminium-coated 55c1 steel in water-confinement regime, characterization and application to high-cycle fatigue behaviour," *Journal of materials science*, vol. 33, no. 6, pp. 1421–1429, 1998.

[150] P. Peyre, L. Berthe, V. Vignal, I. Popa, and T. Baudin, "Analysis of laser shock waves and resulting surface deformations in an al–cu–li aluminum alloy," *Journal of Physics D: Applied Physics*, vol. 45, no. 33, p. 335304, 2012.

[151] B. Fairand and A. Clauer, "Effect of water and paint coatings on the magnitude of laser-generated shocks," *Optics Communications*, vol. 18, no. 4, pp. 588–591, 1976.

[152] C. Rubio-González, G. Gomez-Rosas, J. Ocaña, C. Molpeceres, A. Banderas, J. Porro, and M. Morales, "Effect of an absorbent overlay on the residual stress field induced by laser shock processing on aluminum samples," *Applied Surface Science*, vol. 252, no. 18, pp. 6201–6205, 2006.

[153] A. Vorobyev, V. Kuzmichev, N. Kokody, P. Kohns, J. Dai, and C. Guo, "Residual thermal effects in al following single ns-and fs-laser pulse ablation," *Applied Physics A*, vol. 82, no. 2, pp. 357–362, 2006.

[154] C. Montross, V. Florea, and M. Swain, "The influence of coatings on subsurface mechanical properties of laser peened 2011-t3 aluminum," *Journal of materials science*, vol. 36, no. 7, pp. 1801–1807, 2001.

[155] N. Mukai, N. Aoki, M. Obata, A. Ito, Y. Sano, and C. Konagai, "Laser processing for underwater maintenance in nuclear plants," 1995.

[156] Y. Sano, K. Masaki, T. Gushi, and T. Sano, "Improvement in fatigue performance of friction stir welded a6061-t6 aluminum alloy by laser peening without coating," *Materials & Design (1980-2015)*, vol. 36, pp. 809–814, 2012.

[157] C. Rubio-González, C. Felix-Martinez, G. Gomez-Rosas, J. Ocaña, M. Morales, and J. Porro, "Effect of laser shock processing on fatigue crack growth of duplex stainless steel," *Materials Science and Engineering: A*, vol. 528, no. 3, pp. 914–919, 2011.

[158] U. Trdan and J. Grum, "Evaluation of corrosion resistance of aa6082-t651 aluminium alloy after laser shock peening by means of cyclic polarisation and els methods," *Corrosion Science*, vol. 59, pp. 324–333, 2012.

[159] E. Maawad, Y. Sano, L. Wagner, H.-G. Brokmeier, and C. Genzel, "Investigation of laser shock peening effects on residual stress state and fatigue performance of titanium alloys," *Materials Science and Engineering: A*, vol. 536, pp. 82–91, 2012.

[160] B. Mordyuk, Y. V. Milman, M. Iefimov, G. Prokopenko, V. Silberschmidt, M. Danylenko, and A. Kotko, "Characterization of ultrasonically peened and laser-shock peened surface layers of aisi 321 stainless steel," *Surface and coatings technology*, vol. 202, no. 19, pp. 4875–4883, 2008.

[161] J. E. Bertie and Z. Lan, "Infrared intensities of liquids xx: The intensity of the oh stretching band of liquid water revisited, and the best current values of the optical constants of h2o (l) at 25 c between 15,000 and 1 cm- 1," *Applied Spectroscopy*, vol. 50, no. 8, pp. 1047–1057, 1996.

[162] C. Ye, Y. Liao, and G. J. Cheng, "Warm laser shock peening driven nanostructures and their effects on fatigue performance in aluminum alloy 6160," *Advanced Engineering Materials*, vol. 12, no. 4, pp. 291–297, 2010.

[163] Z. Hong and Y. Chengye, "Laser shock processing of 2024-t62 aluminum alloy," *Materials Science and Engineering: A*, vol. 257, no. 2, pp. 322–327, 1998.

[164] D. Lin, C. Ye, Y. Liao, S. Suslov, R. Liu, and G. J. Cheng, "Mechanism of fatigue performance enhancement in a laser sintered superhard nanoparticles reinforced nanocomposite followed by laser shock peening," *Journal of Applied Physics*, vol. 113, no. 13, 2013.

[165] Y. Shadangi, K. Chattopadhyay, S. Rai, and V. Singh, "Effect of laser shock peening on microstructure, mechanical properties and corrosion behavior of interstitial free steel," *Surface and Coatings Technology*, vol. 280, pp. 216–224, 2015.

[166] J. Chu, J. Rigsbee, G. Banaś, and H. Elsayed-Ali, "Laser-shock processing effects on surface microstructure and mechanical properties of low carbon steel," *Materials Science and Engineering: A*, vol. 260, no. 1-2, pp. 260–268, 1999.

[167] Q. Liu, K. Ding, L. Ye, C. Rey, S. Barter, P. Sharp, and G. Clark, "Spallation-like phenomenon induced by laser shock peening surface treatment on 7050 aluminum alloy," 2004.

[168] Q. Liu, S. Barter, P. Sharp, C. Rey, K. Ding, L. Ye, and G. Clark, "Effect of internal cracking on fatigue life of 7050 aluminum alloy treated by laser shock processing," in *Proceedings of the 11th International Conference on Fracture (ICF11'05)*, pp. 6093–6098, 2005.

[169] Y. Cao and Y. C. Shin, "Shock wave propagation and spallation study in laser shock peening," *Journal of engineering materials and technology*, vol. 132, no. 4, 2010.

[170] A. Sollier, L. Berthe, P. Peyre, E. Bartnicki, and R. Fabbro, "Laser-matter interaction in laser shock processing," in *First International Symposium on High-Power Laser Macroprocessing*, vol. 4831, pp. 463–467, International Society for Optics and Photonics, 2003.

[171] D. Devaux, R. Fabbro, L. Tollier, and E. Bartnicki, "Generation of shock waves by laser-induced plasma in confined geometry," *Journal of Applied Physics*, vol. 74, no. 4, pp. 2268–2273, 1993.

[172] RP Photonics Encyclopedia, "Frequency Doubling." Available at https://www.rp-photonics.com/frequency_doubling.html (11.10.2021).

[173] RP Photonics Encyclopedia, "Frequency Tripling." Available at https://www.rp-photonics.com/frequency_tripling.html (11.10.2021).

[174] B. Stuart, M. Feit, S. Herman, A. Rubenchik, B. Shore, and M. Perry, "Nanosecond-to-femtosecond laser-induced breakdown in dielectrics," *Physical review B*, vol. 53, no. 4, p. 1749, 1996.

[175] X. Wu, C. Huang, X. Wang, and H. Song, "A new effective method to estimate the effect of laser shock peening," *International Journal of Impact Engineering*, vol. 38, no. 5, pp. 322–329, 2011.

[176] J. Cuq-Lelandais, M. Boustie, L. Berthe, T. De Rességuier, P. Combis, J.-P. Colombier, M. Nivard, and A. Claverie, "Spallation generated by femtosecond laser driven shocks in thin metallic targets," *Journal of Physics D: Applied Physics*, vol. 42, no. 6, p. 065402, 2009.

[177] T. Sano, T. Eimura, R. Kashiwabara, T. Matsuda, Y. Isshiki, A. Hirose, S. Tsutsumi, K. Arakawa, T. Hashimoto, K. Masaki, *et al.*, "Femtosecond laser peening of 2024 aluminum alloy without a sacrificial overlay under atmospheric conditions," *Journal of Laser Applications*, vol. 29, no. 1, p. 012005, 2017.

[178] H. Nakano, S. Miyauti, N. Butani, T. Shibayanagi, M. Tsukamoto, and N. Abe, "Femtosecond laser peening of stainless steel," *Laser Micro/Nanoeng*, vol. 4, no. 1, pp. 35–38, 2009.

[179] X. Zhang, Y. Zhang, J. Lu, F. Xuan, Z. Wang, and S. Tu, "Improvement of fatigue life of ti–6al–4v alloy by laser shock peening," *Materials Science and Engineering: A*, vol. 527, no. 15, pp. 3411–3415, 2010.

[180] M. Shepard, P. Smith, and M. S. Amer, "Introduction of compressive residual stresses in ti-6al-4v simulated airfoils via laser shock processing," *Journal of materials engineering and performance*, vol. 10, no. 6, pp. 670–678, 2001.

[181] C. Ziwen, X. Haiying, Z. Shikun, and C. Zhigang, "Investigation of surface integrity on tc17 titanium alloy treated by square-spot laser shock peening," *Chinese Journal of Aeronautics*, vol. 25, no. 4, pp. 650–656, 2012.

[182] P. Peyre, X. Scherpereel, L. Berthe, C. Carboni, R. Fabbro, G. Béranger, and C. Lemaitre, "Surface modifications induced in 316l steel by laser peening and shot-peening. influence on pitting corrosion resistance," *Materials Science and Engineering: A*, vol. 280, no. 2, pp. 294–302, 2000.

[183] C. S. Montross, T. Wei, L. Ye, G. Clark, and Y.-W. Mai, "Laser shock processing and its effects on microstructure and properties of metal alloys: a review," *International journal of fatigue*, vol. 24, no. 10, pp. 1021–1036, 2002.

[184] Y. Hu, Z. Yao, and J. Hu, "3-d fem simulation of laser shock processing," *Surface and Coatings Technology*, vol. 201, no. 3-4, pp. 1426–1435, 2006.

[185] J. Bolger, C. Montross, and A. V. Rode, "Shock waves in basalt rock generated with high-powered lasers in a confined geometry," *Journal of Applied Physics*, vol. 86, no. 10, pp. 5461–5466, 1999.

[186] A. Warren, Y. Guo, and S. Chen, "Massive parallel laser shock peening: simulation, analysis, and validation," *International Journal of Fatigue*, vol. 30, no. 1, pp. 188–197, 2008.

[187] N. Kalentics, E. Boillat, P. Peyre, S. Ćirić-Kostić, N. Bogojević, and R. E. Logé, "Tailoring residual stress profile of selective laser melted parts by laser shock peening," *Additive Manufacturing*, vol. 16, pp. 90–97, 2017.

[188] Z.-w. Cao, Z.-g. Che, S.-k. Zou, and Q.-x. Fei, "Numerical simulation of residual stress field induced by laser shock processing with square spot," *Journal of Shanghai University (English Edition)*, vol. 15, no. 6, pp. 553–556, 2011.

[189] S. Zabeen, M. Preuss, and P. Withers, "Residual stresses caused by head-on and 45 foreign object damage for a laser shock peened ti–6al–4v alloy aerofoil," *Materials Science and Engineering: A*, vol. 560, pp. 518–527, 2013.

[190] B. Lin, C. Lupton, S. Spanrad, J. Schofield, and J. Tong, "Fatigue crack growth in laser-shock-peened ti–6al–4v aerofoil specimens due to foreign object damage," *International journal of fatigue*, vol. 59, pp. 23–33, 2014.

[191] O. Hatamleh and A. DeWald, "An investigation of the peening effects on the residual stresses in friction stir welded 2195 and 7075 aluminum alloy joints," *Journal of Materials Processing Technology*, vol. 209, no. 10, pp. 4822–4829, 2009.

[192] I. Nikitin, B. Scholtes, H. Maier, and I. Altenberger, "High temperature fatigue behavior and residual stress stability of laser-shock peened and deep rolled austenitic steel aisi 304," *Scripta materialia*, vol. 50, no. 10, pp. 1345–1350, 2004.

[193] M. Achintha and D. Nowell, "Eigenstrain modelling of residual stresses generated by laser shock peening," *Journal of Materials Processing Technology*, vol. 211, no. 6, pp. 1091–1101, 2011.

[194] N. Hfaiedh, P. Peyre, H. Song, I. Popa, V. Ji, and V. Vignal, "Finite element analysis of laser shock peening of 2050-t8 aluminum alloy," *International Journal of Fatigue*, vol. 70, pp. 480–489, 2015.

[195] C. Correa, D. Peral, J. Porro, M. Díaz, L. R. de Lara, A. García-Beltrán, and J. Ocaña, "Random-type scanning patterns in laser shock peening without absorbing coating in 2024-t351 al alloy: a solution to reduce residual stress anisotropy," *Optics & Laser Technology*, vol. 73, pp. 179–187, 2015.

[196] F. C. Campbell, *Elements of metallurgy and engineering alloys*, pp. 487–508. ASM International, 2008.

[197] L. Katgerman and D. Eskin, "Hardening, annealing, and aging," *Handbook of Aluminum, Physical Metallurgy and Processes, edited by GE Totten, DS MacKenzie, CRC Taylor and Francis, London, New York*, pp. 259–303, 2003.

[198] ASM Aerospace Specification Metals Inc., "Aluminum 5083-H116; 5083-H321." Available at http://asm.matweb.com/search/SpecificMaterial.asp?bassnum=MA5083H116 (16.6.2020).

[199] RP Photonics Encyclopedia, "Q Switching." Available at https://www.rp-photonics.com/q_switching.html (16.6.2020).

[200] RP Photonics Encyclopedia, "Pockels Cells." Available at https://www.rp-photonics.com/pockels_cells.html (17.6.2020).

[201] Amplitude, "Powerlite DLS Plus." Available at https://amplitude-laser.com/produit/powerlite-dls-plus/ (17.6.2020).

[202] P. Mason, M. Divokỳ, K. Ertel, J. Pilař, T. Butcher, M. Hanuš, S. Banerjee, J. Phillips, J. Smith, M. De Vido, *et al.*, "Kilowatt average power 100 j-level diode pumped solid state laser," *Optica*, vol. 4, no. 4, pp. 438–439, 2017.

[203] HiLASE, "A new World record for BIVOJ laser." Available at https://www.hilase.cz/wp-content/uploads/HiLASE-_BIVOJ_world-record-2021_Press-Release.pdf (6.10.2021).

[204] GAMRY instruments, "Getting Started with Electrochemical Corrosion Measurement." Available at https://www.gamry.com/application-notes/corrosion-coatings/basics-of-electrochemical-corrosion-measurements/ (19.6.2020).

[205] GAMRY Instruments, "Polarization Resistance Tutorial - Getting Started." Available at https://www.gamry.com/application-notes/corrosion-coatings/corrosion-techniques-polarization-resistance/ (7.10.2021).

[206] M. Stern and A. L. Geary, "Electrochemical polarization: I. a theoretical analysis of the shape of polarization curves," *Journal of the electrochemical society*, vol. 104, no. 1, p. 56, 1957.

[207] CXRO, "X-Ray Attenuation Length." Available at https://henke.lbl.gov/optical_constants/atten2.html (20.6.2020).

[208] M. Fitzpatrick, T. Fry, P. Holdway, *et al.*, "Npl good practice guide no. 52: determination of residual stresses by x-ray diffraction—issue 2," *NPL, Great Britain*, 2005.

[209] Chemglass Life Sciences, "O-RINGS, VITON." Available at https://chemglass.com/o-rings-viton (20.6.2020).

[210] S. D. Cramer and B. S. C. Jr., *ASM Metals Handbook: Corrosion: Fundamentals, Testing, and Protection*. ASM International, 1997.

[211] N. Holrody and G. Scamans, "Slow-strain-rate stress corrosion testing of aluminum alloys," in *Environment-Sensitive Fracture: Evaluation and Comparison of Test Methods*, ASTM International, 1984.

[212] J. Seong, G. S. Frankel, and N. Sridhar, "Inhibition of stress corrosion cracking of sensitized AA5083," *Corrosion*, vol. 72, no. 2, pp. 284–296, 2016.

[213] R. E. Ricker, E. Lee, R. Taylor, C. Lei, B. Pregger, and E. Lipnickas, "Chloride ion activity and susceptibility of al alloys 7075-t6 and 5083-h131 to stress corrosion cracking," *Metallurgical and Materials Transactions A*, vol. 44, no. 3, pp. 1353–1364, 2013.

[214] INSTRON, "What is Bend Testing?." Available at https://www.instron.us/our-company/library/test-types/flexure-test (20.6.2020).

[215] Encyclopædia Britannica, "Confocal microscopes." Available at https://www.britannica.com/technology/microscope/Confocal-microscopes (24.6.2020).

[216] LaserFocusWorld, "OPTICAL SURFACE PROFILING: Profilometer advances benefit surface analysis, film-thickness measurement." Available at https://www.laserfocusworld.com/test-measurement/test-measurement/article/16552227/optical-surface-profiling-profilometer-advances-benefit-surface-analysis-filmthickness-measurement (24.6.2020).

[217] M. Scius-Bertrand, L. Videau, A. Rondepierre, E. Lescoute, Y. Rouchausse, J. Kaufman, D. Rostohar, J. Brajer, and L. Berthe, "Laser induced plasma characterization in direct and water confined regimes: new advances in experimental studies and numerical modelling," *Journal of Physics D: Applied Physics*, vol. 54, no. 5, p. 055204, 2020.

[218] R. Jones, D. Baer, M. Danielson, and J. Vetrano, "Role of mg in the stress corrosion cracking of an al-mg alloy," *Metallurgical and Materials Transactions A*, vol. 32, no. 7, pp. 1699–1711, 2001.

[219] U. Trdan and J. Grum, "Sem/eds characterization of laser shock peening effect on localized corrosion of al alloy in a near natural chloride environment," *Corrosion Science*, vol. 82, pp. 328–338, 2014.

[220] J. Macdonald *et al.*, "Emphasizing solid materials and systems," *Impedance Spectroscopy; John Wiley & Sons Inc.: New York, NY, USA*, 1987.

[221] A. Kocijan, D. K. Merl, and M. Jenko, "The corrosion behaviour of austenitic and duplex stainless steels in artificial saliva with the addition of fluoride," *Corrosion Science*, vol. 53, no. 2, pp. 776–783, 2011.

[222] H. Shi, E.-H. Han, and F. Liu, "Corrosion protection of aluminium alloy 2024-t3 in 0.05 m nacl by cerium cinnamate," *corrosion science*, vol. 53, no. 7, pp. 2374–2384, 2011.

[223] J. Sui and W. Cai, "Formation of diamond-like carbon (dlc) film on the niti alloys via plasma immersion ion implantation and deposition (piiid) for improving corrosion resistance," *Applied Surface Science*, vol. 253, no. 4, pp. 2050–2055, 2006.

[224] J. Bajat, I. Milošev, Ž. Jovanović, R. Jančić-Heinemann, M. Dimitrijević, and V. Mišković-Stanković, "Corrosion protection of aluminium pretreated by vinyltriethoxysilane in sodium chloride solution," *Corrosion Science*, vol. 52, no. 3, pp. 1060–1069, 2010.

[225] R. Foley, "Localized corrosion of aluminum alloys—a review," *Corrosion*, vol. 42, no. 5, pp. 277–288, 1986.

[226] V. S. Smentkowski, "Trends in sputtering," *Progress in Surface Science*, vol. 64, no. 1-2, pp. 1–58, 2000.

[227] A. Sharma, J. Song, D. Furfari, S. R. Mannava, and V. K. Vasudevan, "Remarkable near-surface microstructure of nanoparticles and oxide film in laser shock peened al-zn-mg-cu alloy," *Scripta Materialia*, vol. 202, p. 114012, 2021.

[228] A. G129, "Standard practice for slow strain rate testing to evaluate the susceptibility of metallic materials to environmentally assisted cracking," 2013.

[229] I. N. Oguocha, O. J. Adigun, and S. Yannacopoulos, "Effect of sensitization heat treatment on properties of Al-Mg alloy AA5083-H116," *Journal of Materials Science*, vol. 43, no. 12, pp. 4208–4214, 2008.

[230] M. Pourbaix, *Lectures on electrochemical corrosion*. Springer Science & Business Media, 2012.

[231] L. Berthe, R. Fabbro, P. Peyre, L. Tollier, and E. Bartnicki, "Shock waves from a water-confined laser-generated plasma," *Journal of Applied Physics*, vol. 82, no. 6, pp. 2826–2832, 1997.

[232] U. Trdan and J. Grum, "Investigation of corrosion behaviour of aluminium alloy subjected to laser shock peening without a protective coating," *Advances in Materials Science and Engineering*, vol. 2015, 2015.

[233] T. Radetić, A. Halap, M. Popović, and E. Romhanji, "Effect of the thermomechanical treatment on igc susceptibility of aa 5083 alloy," in *Light Metals 2014*, pp. 297–302, Springer, 2014.

Publications of the author related to the doctoral thesis

Articles in peer-reviewed journals

[A] **J. Kaufman**, J. Racek, M. Cieslar, P. Minárik, M.A. Steiner, S.R. Mannava, V.K. Vasudevan, A. Sharma, M. Böhm, J. Brajer, J. Pilař, L. Pína, and T. Mocek, "The effect of laser shock peening with and without protective coating on intergranular corrosion of sensitized AA5083," *Corrosion Science*, vol. 194, 2022.

[B] **J. Kaufman**, Z. Špirit, V.K. Vasudevan, M.A. Steiner, S.R. Mannava, J. Brajer L. Pína, and Tomáš Mocek,"Effect of Laser Shock Peening Parameters on Residual Stresses and Corrosion Fatigue of AA5083," *Metals*, vol. 11, no. 10, 2021.

[C] **J. Kaufman**, M. Böhm, J. Brajer, and S. Zulic, "Laser Shock Peening of aluminium alloys to enhance surface properties," *MM Science Journal*, 2019.

[D] S. Zulic, D. Rostohar, **J. Kaufman**, S. Pathak, J. Kopeček, and M. Böhm, "Fatigue life enhancement of additive manufactured 316l stainless steel by LSP using a DPSS laser system," *Surface Engineering*, pp. 1-8, 2022.

[E] Z. Špirit, **J. Kaufman**, M. Chocholoušek, and J. Strejcius, "Mechanical Tests Results of Laser Shock Peening-Treated Austenitic Steel," *Journal of Nuclear Engineering and Radiation Science*, vol. 7, no. 2, 2021.

[F] M. Scius-Bertrand, L. Videau1, A. Rondepierre, E. Lescoute, Y. Rouchausse, **J. Kaufman**, D. Rostohar, J. Brajer, and Laurent Berthe, "Laser induced plasma characterization in direct and water confined regimes: new advances in experimental studies and numerical modelling," *Journal of Physics D: Applied Physics*, vol. 54, 2021.

[G] J. Kubásek, O. Molnárová, J. Čapek, K. Bartha, J. Čížek, P. Doležal, J. Racek, **J. Kaufamn**, J. Řídký, and P. Lejček, "Laser shock peening of copper poly- and single crystals," *Materials Characterization*, vol. 174, 2021.

[H] M. Böhm, **J. Kaufman**, J. Brajer, and D. Rostohar, "Robotic arm human-machine interface for Laser Shock Peening applications," *MM Science Journal*, 2019.

Conference contributions

[I] **J. Kaufman**, J. Racek, M. Cieslar, P. Minárik, M.A. Steiner, S.R. Mannava, V.K. Vasudevan, J. Brajer, J. Pilař, L. Pína, T. Mocek, "Laser Shock Peening to enhance stress corrosion cracking and corrosion fatigue resistance in marine aluminium alloys," in *14th International Conference on Shot Peening*, Milan, Italy, 2022.

[J] A. Cunha, R.O. Giacomelli, **J. Kaufman**, J. Brajer, and T.S. Pereira, "An Overview on Laser Shock Peening Process: From Science to Industrial Applications," in *SBFoton International Optics and Photonics Conference*, Sao Carlos, Brazil, 2021.

[K] **J. Kaufman**, J. Brajer, L. Pína, and Tomáš Mocek, "Laser Shock Peening," in *EPIC Online Technology Meeting on Industrial Laser Manufacturing for Naval and Aeronautic Applications*, online, 2020.

[L] **J. Kaufman**, M. Böhm, O. Stránský, S. Zulic, S. Pathak, J. Brajer, "Low-power Laser Peening without Coating to combat Stress Corrosion Cracking and Corrosion Fatigue in AA5083," in *XXIII International Symposium on High-Power Laser Systems and Applications*, Prague, Czech Republic, 2022.

[M] M. Kattoura, **Jan Kaufman**, B.T. Donkor, J. Song, S.R. Mannava, and V.K.Vasudevan, "Effect of Laser Shock Peening Processing Parameters on the Microstructure, Residual Stress, and Fatigue Behavior of Additive Manufactured CoCrMo Alloy," in *ALT International Conference*, Prague, Czech Republic, 2019.

[N] Z. Špirit, **J. Kaufman**, J. Brajer, J. Strejcius, and M. CHocholoušek, "Zvýšení únavové životnosti materiálů metodou Laser Shock Peening," in *Konference Srní VZU: Životnost komponent energetických zařízení*, Srní, Czech Republic, 2019.

[O] **J. Kaufman**, V.K. Vasudevan, M.A. Steiner, S.R. Mannava, J. Brajer L. Pína, and Tomáš Mocek, "Influence of different laser systems on LSP treatment of Aluminum alloys ," in *7th International Conference on Laser Peening and Related Phenomena*, Singapore, 2018.

[P] **J. Kaufman**, M. Böhm J. Brajer, and Tomáš Mocek, "Development of LSP station in HiLASE laser center," in *6th International Conference on Laser Peening and Related Phenomena*, Pretoria, South African Republic, 2016.